PACIFIC EARTHQUAKE ENGINEERING RESEARCH CENTER

Performance Modeling Strategies for Modern Reinforced Concrete Bridge Columns

Michael P. Berry
Montana State University, Bozeman

and

Marc O. Eberhard
University of Washington, Seattle

PEER 2007/07
APRIL 2008

Performance Modeling Strategies for Modern Reinforced Concrete Bridge Columns

Michael P. Berry

Department of Civil Engineering

Montana State University, Bozeman

Marc O. Eberhard

Department of Civil and Environmental Engineering

University of Washington, Seattle

PEER Report 2007/07

Pacific Earthquake Engineering Research Center

College of Engineering

University of California, Berkeley

April 2008

ABSTRACT

It is important to characterize the performance of bridges during earthquakes because they are integral components of transportation networks. Loss of bridge function can have severe economic consequences, and consequences to life safety when bridges are critical links in lifelines to emergency facilities, which are particularly important after a disasters. Although damage to other elements can have economic and life-safety impacts, reinforced concrete columns are often the most vulnerable elements in a bridge, and column failure can have catastrophic consequences.

The objective of this project was to develop column-modeling strategies to accurately model column behavior under seismic loading, including global and local forces and deformations, as well as progression of damage. The models were calibrated using the observed cyclic force-deformation responses and damage progression observations of 37 tests of spiral-reinforced columns representative of modern bridge construction. This research resulted in (1) a standardized discretization scheme for fiber cross sections; (2) a calibrated distributed-plasticity column modeling strategy including deformation components for bond-slip and shear deformations; (3) a calibrated lumped-plasticity column modeling strategy with recommendations for effective elastic-stiffness properties and plastic-hinge lengths; (4) the identification of inaccuracies of standard cyclic material models; (5) the implementation and evaluation of improved cyclic material models; (6) a series of damage equations to predict two flexural damage states with three engineering demand parameters; (7) the evaluation of the proposed modeling strategies when applied to complex structural models (two-column bent, and biaxial shake-table specimen).

This effort is an important step toward implementing performance-based earthquake engineering for modern reinforced concrete bridges.

ACKNOWLEDGMENTS

This work was supported primarily by the Earthquake Engineering Research Centers Program of the National Science Foundation under award number EEC- 9701568 through the Pacific Earthquake Engineering Research Center (PEER). Any opinions, findings, and conclusions or recommendations expressed in this material are those of the author(s) and do not necessarily reflect those of the National Science Foundation.

The authors would like to thank Professors Dawn Lehman, John Stanton, Laura Lowes, and Greg Miller for their invaluable advice and assistance.

Finally, the author would like to thank his friends Dylan Freytag, Aaron Sterns, Nilanjan Mitra, Nathan McBride, Mark Gallik, and Tyler Ranf; his family, Sandy, Tim, Tim Jr., Shelley, Dave, Wendell, Candy, Mark, Casey, and Tony; and his wife Deanna for their patience and support throughout this research project.

CONTENTS

LIST OF FIGURES

LIST OF TABLES

1 Introduction

1.1 CONTEXT

Current building codes and modern engineering practice address the issues of collapse prevention and life safety by conservatively predicting nominal demands and strengths of structural members, but provide little indication of the actual state of a structure after an earthquake. After an earthquake, a building or bridge may still be standing, but structural and nonstructural members may be damaged, resulting in costly repairs. The economic losses due to downtime may even be larger.

In contrast to current codes, performance-based earthquake engineering (PBEE) attempts to explicitly predict damage states and assess the probability of reaching multiple levels of damage. PBEE has the potential to improve structural engineering practice by providing engineers the capability of designing structures to achieve a variety of performance levels. The impact of implementing PBEE goes beyond improving engineering practice and extends to a wide range of decision making. The potential impact of PBEE is summarized in Pacific Earthquake Engineering Research Center's (PEER) mission statement.

> *This approach is aimed at improving decision-making about seismic risk by making the choice of performance goals and the tradeoffs that they entail apparent to facility owners and society at large. The approach has gained worldwide attention in the past ten years with the realization that urban earthquakes in developed countries - Loma Prieta, Northridge, and Kobe - impose substantial economic and societal risks above and beyond potential loss of life and injuries. By providing quantitative tools for characterizing and managing these risks, performance-based earthquake engineering serves to address diverse economic and safety needs. (http://peer.berkeley.edu)*

Reinforced concrete structures are particularly vulnerable to earthquakes. Excessive deformations can result in spalling of cover concrete, buckling of longitudinal reinforcement, reduction of flexural capacity, bar fracture, and eventually, structural collapse. Although damage to other elements can have economic and life-safety impacts, columns are often the most vulnerable elements in a structure, and column failure can have catastrophic consequences.

To quantitatively implement PBEE for reinforced concrete columns, it is necessary to predict deformation demands on columns at the onset of particular damage states. Berry and Eberhard (2003) developed practical empirical models that predict the drift ratios at which cover concrete spalls and longitudinal bars buckle in reinforced concrete columns, given a column geometry, transverse reinforcement, and axial load. The models were calibrated with existing experimental results from the UW-PEER reinforced concrete column performance database, which documents the performance of over 400 columns (Berry et al. 2004).

The drift-ratio approach provides a simple means of estimating damage displacements (which is essential to engineering practice), but it has significant limitations. This approach neglects the effects of cycling on damage and it is difficult to implement for columns with biaxial bending, variable axial loads or variable shear spans. More versatile and detailed models are needed to overcome these limitations.

The availability of increasingly powerful computers provides researchers and engineers with the opportunity to implement numerically intensive modeling strategies that could not have been considered until recently. In particular, enhanced fiber beam-column elements have been developed to model the nonlinear behavior of reinforced concrete structures under cyclic loads. Previous researchers have used these simulation models to predict the response of ductile reinforced concrete columns, but none of these modeling strategies have been calibrated with a large database to reproduce force-deformation behavior and damage progression. The absence of model calibration has made it difficult to evaluate the impact of proposed improvements in modeling methodologies.

1.2 OBJECTIVE

The objective of this project is to develop, calibrate, and evaluate column-modeling strategies that are capable of accurately modeling column behavior under seismic loading, including global and local deformations, as well as progression of damage. The focus of this research will be on ductile spiral-reinforced bridge columns, for which shear failure is not a consideration.

1.3 BRIDGE COLUMN DATA

The UW-PEER reinforced concrete column test database (Berry et al. 2004) provides a unique opportunity to evaluate and calibrate column-modeling strategies. The database documents column geometry, material properties, and reinforcement details. It also includes the digital force-displacement histories, and the observed displacements at the onset of multiple damage states.

For this study on ductile spiral-reinforced columns, the columns from the database were screened to eliminate columns that are not representative of modern bridge construction. The database was screened using the following criteria.

- $P/A_g f'_c \leq 0.30$
- $\rho_{eff} = \rho_s f_{ys}/f'_c \geq 0.05$
- $\rho_l \leq 0.04$
- $S/d_b \leq 6$
- $cover/D \leq 0.10$
- Availability of observed displacements at onset of cover spalling, bar buckling, or bar fracture

where: P is the axial load, A_g is the gross cross-sectional area, f'_c is the concrete compressive strength, ρ_s is the transverse reinforcement ratio, f_{ys} is the yield stress of the spiral reinforcement, ρ_l is the longitudinal-reinforcement ratio, S is the spacing of the spiral reinforcement, d_b is the diameter of the longitudinal reinforcement, *cover* is the distance from column face to the transverse reinforcement, and D is the diameter of the column.

The 37 column tests considered in this study are listed in Table 1.1. The reported drift ratios at the onset of cover spalling (Δ_{sp}/L), bar buckling (Δ_{bb}/L), bar fracture (Δ_{bf}/L) are included in the table along with key properties of the columns.

Table 1.1 Bridge column dataset

Reference	Designation	L (mm)	L/D	ρ_{eff}	$P/A_g f'_c$	ρ_l	S/d_b	Δ_{sp}/L (%)	Δ_{bb}/L (%)	Δ_{bf}/L (%)
Munro et al. (1976)	No. 1	2730	5.5	0.13	0.00	0.026	1.85	1.39	-	-
Ghee et al. (1981)	No. 1	1600	4.0	0.09	0.20	0.024	2.50	0.94	3.75	3.75
Pontangaroa et al. (1979)	No. 1	1200	2.0	0.08	0.23	0.024	3.13	0.83	-	-
Wong et al. (1990)	No. 1	800	2.0	0.11	0.19	0.032	3.75	0.75	5.18	-
Stone and Cheok (1989)	Flexure	9140	6.0	0.09	0.07	0.020	2.07	1.96	5.89	5.89
Stone and Cheok (1989)	Shear	4570	3.0	0.19	0.07	0.020	1.26	-	6.24	7.79
Cheok and Stone (1986)	N1	750	3.0	0.26	0.10	0.020	1.27	2.57	11.00	10.29
Cheok and Stone (1986)	N2	750	3.0	0.27	0.21	0.020	1.27	-	6.21	7.45
Cheok and Stone (1986)	N3	1500	6.0	0.13	0.10	0.020	2.07	3.41	7.38	6.83
Cheok and Stone (1986)	N4	750	3.0	0.26	0.10	0.020	1.27	2.84	7.11	7.11
Cheok and Stone (1986)	N5	750	3.0	0.26	0.20	0.020	1.27	2.58	6.96	6.44
Cheok and Stone (1986)	N6	1500	6.0	0.14	0.10	0.020	2.07	2.24	4.77	6.72
Kunnath et al. (1997)	No. A2	1372	4.5	0.14	0.09	0.020	2.00	-	4.70	-
Kunnath et al. (1997)	No. A3	1372	4.5	0.14	0.09	0.020	2.00	1.97	-	-
Kunnath et al. (1997)	No. A7	1372	4.5	0.13	0.09	0.020	2.00	1.46	5.83	-
Kunnath et al. (1997)	No. A8	1372	4.5	0.13	0.09	0.020	2.00	2.33	5.83	-
Kunnath et al. (1997)	No. A9	1372	4.5	0.13	0.09	0.020	2.00	-	4.59	-
Kunnath et al. (1997)	No. A10	1372	4.5	0.15	0.10	0.020	2.00	2.33	6.61	-
Kunnath et al. (1997)	No. A11	1372	4.5	0.15	0.10	0.020	2.00	3.64	-	7.65
Kunnath et al. (1997)	No. A12	1372	4.5	0.15	0.10	0.020	2.00	3.64	5.90	-
Hose et al. (1997)	No. SRPH1	3660	6.0	0.09	0.15	0.027	2.56	1.64	8.74	8.74
Vu et al. (1998)	No. NH3	910	2.0	0.13	0.15	0.024	3.78	2.06	5.49	-
Kowalsky et al. (1999)	No. FL3	3656	8.0	0.12	0.30	0.036	4.79	-	9.08	9.08
Lehman and Moehle (2000)	No.415	2438	4.0	0.14	0.07	0.015	2.00	1.56	5.29	7.30
Lehman and Moehle (2000)	No.815	4877	8.0	0.14	0.07	0.015	2.00	2.73	9.12	9.12
Lehman and Moehle (2000)	No.1015	6096	10.0	0.14	0.07	0.015	2.00	3.13	10.42	10.42
Lehman and Moehle (2000)	No.407	2438	4.0	0.14	0.07	0.008	2.00	1.56	5.21	5.21
Lehman and Moehle (2000)	No.430	2438	4.0	0.14	0.07	0.030	2.00	1.56	7.30	-
Lehman and Moehle (2000)	No.328	1829	3.0	0.16	0.09	0.027	1.33	1.64	7.27	7.22
Lehman and Moehle (2000)	No.828	4877	8.0	0.16	0.09	0.027	1.33	3.65	12.30	-
Lehman and Moehle (2000)	No.1028	6096	10.0	0.16	0.09	0.027	1.33	4.17	14.58	-
Henry and Mahin (1999)	No. 415p	2438	4.0	0.12	0.12	0.015	2.00	-	5.21	5.54
Henry and Mahin (1999)	No. 415s	2438	4.0	0.06	0.06	0.015	4.00	-	5.21	-
Moyer and Kowalsky (2001)	No.1	2438	5.3	0.12	0.04	0.020	4.00	3.02	6.15	7.66
Moyer and Kowalsky (2001)	No.2	2438	5.3	0.11	0.04	0.020	4.00	2.29	10.73	12.29
Moyer and Kowalsky (2001)	No.3	2438	5.3	0.12	0.04	0.020	4.00	3.02	10.74	-
Moyer and Kowalsky (2001)	No.4	2438	5.3	0.11	0.04	0.020	4.00	3.02	13.14	-
Statistics	n	37	37	37	37	37	37	31	33	31
	Mean	2458	4.8	0.14	0.11	0.021	2.35	2.33	7.39	7.62
	COV	0.75	0.4	0.35	0.57	0.25	0.42	0.39	0.37	0.26
	Min	750	2.0	0.06	0.00	0.008	1.26	0.75	3.75	3.75
	Max	9140	10.0	0.27	0.30	0.036	4.79	4.17	14.58	12.29

1.4 SCOPE OF PROJECT

Two column-modeling strategies are developed, calibrated, and evaluated in this report. One method utilizes the combination of a force-based beam-column element (flexural deformations) with elastic shear deformations and a zero-length bond-slip section. A second method utilizes lumped-plasticity theory in which nonlinear deformations are concentrated in a plastic hinge. The following describes the key aspects of the section modelling strategy, the distributed-plasticity modeling strategy, and the lumped-plasticity modeling strategy addressed in this research.

1.4.1 Discretization Strategies for Fiber Cross Sections

Both column-modeling strategies use fiber sections to model section response. Two aspects of fiber-section modeling are discussed in Chapter 2.

Material Models. Numerous material constitutive models are available to model the monotonic and cyclic responses of the concrete and steel components of a reinforced concrete column. In this study, key modeling parameters are calibrated for the Giuffre-Menegotto-Pinto steel model (Taucer et al. 1991), the Mander et al. (1988) concrete model, and a new steel model proposed by Mohle and Kunnath (2006), which includes softening due to fracture and cycling.

Fiber-Section Discretization. Column cross sections can be discretized into small fibers using a variety of schemes (e.g., unilateral discretization, radial discretization) to varying degrees of mesh density. Two discretization strategies are evaluated, and recommendations are made on the number of fibers needed to accurately model column section behavior.

1.4.2 Distributed-Plasticity Modeling Strategy

The distributed-plasticity modeling strategy is described and calibrated in chapters 3 and 4, respectively. The following are key aspects of the proposed spread-plasticity column-modeling strategy addressed by this study.

Number of integration points. The spread-plasticity column-modeling strategy requires the user to select the number of integration points to use in the analysis. The effect of the number of integration points on column model accuracy is studied and documented, and recommendations are made that balance model accuracy and efficiency.

Bond Slip Deformations and Shear Deformations. A standard fiber beam-column element formulation assumes perfect bond between concrete and steel. To address this issues, a new zero-length bond-slip model is developed for use with the spread-plasticity modeling strategy.

Shear Deformations. Shear deformations are neglected with a standard fiber beam-column element formulation. Additional flexibility was added to the cross sections of the fiber beam-column element to address this issue.

Strain Localization. The distributed-plasticity formulation is susceptible to strain localizations, which lead to model inaccuracies when the column being modeled has a perfectly-plastic or softening behavior. The limitations of this modeling strategy are highlighted, and recommendations are made to assist in overcoming them.

1.4.3 Lumped-Plasticity Modeling Strategy

The lumped-plasticity column model is considered in chapters 5 and 6. The following are key aspects of the lumped-plasticity column-modeling strategy addressed by this study.

Elastic Properties of Lumped-Plasticity Model. The use of lumped-plasticity models requires the selection of effective section properties for the elastic portion of the column (e.g., EI). Recommendations are made for estimating these elastic properties, based on the accuracy of the calculated column stiffness.

Plastic-Hinge Length of Lumped-Plasticity Model. Lumped-plasticity theory assumes that nonlinear deformations are concentrated in plastic hinges. With this methodology, the length of the plastic hinge is assumed to account for bond slip and shear deformations. A plastic-hinge length that accurately predicts column force-deformation response as well as damage progression is developed and evaluated.

1.4.4 Evaluation of Cyclic Response

The calculated cyclic response of the modeling strategies depend on the cyclic response of the concrete and steel material constitutive models. The cyclic response of the proposed column-modeling strategies, utilizing standard concrete and steel material models, are evaluated in Chapter 7. The cyclic response of the concrete was modeled according to a model proposed by Karsan and Jirsa, whereas the steel was modeled according to a model proposed by Giuffre-Menegotto-Pinto.

1.4.5 Improved Cyclic Material Models

The cyclic modeling inaccuracies identified in Chapter 7 are addressed in Chapter 8. A steel material model proposed by Mohle and Kunnath (2006), which accounts for degradation due to cycling, is presented, calibrated, and evaluated. A concrete model that accounts for imperfect crack closure is also developed and evaluated in this chapter.

1.4.6 Column Flexural Damage

A necessary step in implementing performance-based design in bridge columns is relating engineering demand parameters (e.g., drift ratio, plastic rotation, longitudinal strain) to damage measures (e.g., cover spalling, longitudinal bar buckling, and bar fracture). Several methods for estimating the progression of damage in flexural columns are developed, evaluated, and compared in Chapter 9. This chapter presents accuracy statistics and fragility curves for the various damage states and engineering demand parameters.

1.4.7 Application of Column-Modeling Strategy to More Complex Structures

In chapters 4 and 6, the proposed column-modeling strategies were calibrated and evaluated by comparing measured and calculated responses of single cantilever columns subjected to pseudo-static, unidirectional loads. In Chapter 10, the proposed modeling strategies are implemented and evaluated in the following situations.

Bridge-Bent. The proposed column-modeling strategies are used to model the response of a pseudo-static, unidirectional bridge bent test (Makido 2006).

Shake-Table Tests. The proposed column-modeling strategies are utilized to model four columns subjected to unidirectional and bidirectional dynamic loading (Hachem et al. 2003). The modeling strategies will be evaluated based on their ability to model, among other things, maximum displacement, maximum shear force, maximum moment, and residual displacement.

1.4.8 Summary and Conclusions

Chapter 11 summarizes the report and provides key conclusions.

2 Discretization Strategies for Fiber Sections

In order to accurately model the behavior of a reinforced concrete column, the response of the column cross section must be captured. In this chapter, the fiber model and material models employed in this report are presented, and a section discretization scheme is calibrated. Recommendations are then made to accurately and efficiently model moment-curvature behavior.

2.1 FIBER MODEL

For this report, column cross sections were discretized into small fibers in which each fiber had a prescribed uniaxial stress-strain relationship. For example, a typical circular column cross-section discretization is shown in Figure 2.1. This cross section is discretized with a radial discretization scheme with 7 radial core divisions ($n_c^r = 7$), 18 transverse core divisions ($n_c^t = 18$), 2 radial unconfined cover divisions ($n_u^r = 2$), and 18 transverse cover divisions ($n_u^t = 18$). The core concrete, cover concrete, and longitudinal steel fibers each have a uniaxial stress-strain model associated with them corresponding to the material they represent.

2.2 MATERIAL CONSTITUTIVE RELATIONSHIPS

Accurate material models are needed to predict reinforced concrete column behavior. The following sections discuss the material models used in this study to model the longitudinal reinforcing steel, the confined concrete, and the unconfined concrete.

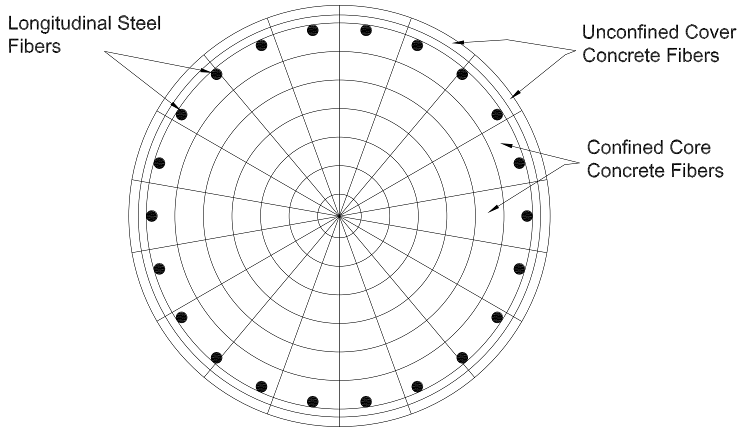

Fig. 2.1 Typical fiber discretization, $n_c^r = 7, n_c^t = 18, n_u^r = 2, n_u^t = 18$

2.2.1 Reinforcing Steel

The reinforcing steel is modeled using the Giufre-Menegotto-Pinto constitutive model (Taucer et al. 1991) available in OpenSees (OpenSees Development Team 2002). The model has a bilinear backbone curve with a post-yield stiffness proportional to the modulus of elasticity of the steel, $E_{sh} = b \cdot E$, and accounts for the Bauschinger effect in the cyclic response of the material. Figure 2.2a compares the monotonic analytical model (for b = 0.01 and b = 0.001) to the measured stress-strain response of a typical reinforcing bar (Lehman and Moehle 2000). The calculated cyclic response of the steel is shown in Figure 2.2b.

Despite the simplicity of the model, the bilinear model predicts the measured material response accurately over most of the strain range, but it does not account for the yield plateau of the reinforcing steel or the degradation of the steel strength due to bar buckling or rupture. The post-yield slope factor 0.001 underestimates the amount of strain hardening. The slope factor of 0.01 overestimates the stress at strains below 0.03.

The strain-hardening ratio (b) affects the accuracy of the column-modeling strategy proposed in this report. This parameter is calibrated in Chapter 4.

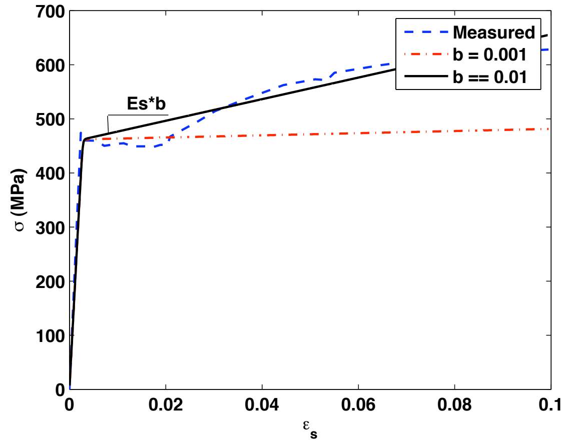

Fig. 2.2 Reinforcing steel material model

2.2.2 Concrete

The Popovics curve with model parameters proposed by Mander et al. (1988) was used to model the responses of both the confined and unconfined concrete in compression. Mander et. al. proposed that the maximum compressive stress of the concrete (f'_{cc}) and the strain at the maximum compressive stress (ε_{cc}) should be calculated as follows.

$$f'_{cc} = f'_c \left(2.254\sqrt{1 + 7.94\frac{f_{pl}}{f'_c}} - 2\frac{f_{pl}}{f'_c} - 1.254 \right) \tag{2.1}$$

$$\varepsilon_{cc} = 0.002 \left(1 + 5 \left(\frac{f'_{cc}}{f'_c} - 1 \right) \right) \tag{2.2}$$

where:

$$f_{pl} = \frac{1}{2}\rho_{sc} f_{yt} k_e \tag{2.3}$$

$$k_e = 1 - \frac{\frac{s'}{2d_c}}{1 - \rho_{lc}} \tag{2.4}$$

$$s' = s - d_{trans} \tag{2.5}$$

$$\rho_{sc} = 4\left(\frac{A_{ts}}{d_c s}\right) \tag{2.6}$$

where f'_c is the compressive strength of the concrete, d_c is the diameter of the core, and A_{ts}, d_{trans}, s and f_{yt} are the area, diameter, spacing and yield stress of the spiral reinforcement. The calculated stress-strain responses of the confined and unconfined concrete for a typical column are shown in Figure 2.3.

The concrete was assumed to have strength in tension up to the cracking strength f_t. Beyond this, the strength of the concrete was assumed to decay exponentially to $0.1 f_t$ at ε_{tu}. A detailed view of the response of the concrete in tension is shown in Figure 2.3b, and the equation governing the response is as follows.

$$\sigma(\varepsilon) = \begin{cases} E_c \varepsilon & \varepsilon \leq \varepsilon_t \\ f_t \frac{1}{10}^{\frac{(\varepsilon-\varepsilon_t)}{(\varepsilon_{tu}-\varepsilon_t)}} & \varepsilon_t < \varepsilon \leq \varepsilon_{tu} \\ 0.0 & \varepsilon > \varepsilon_{tu} \end{cases} \tag{2.7}$$

where $\varepsilon_t = \frac{f_t}{E_c}$. This response was developed as part of this project with collaboration with Nilanjan Mitra.

For the purpose of the development of a cross-section discretization scheme, the concrete was assumed to crack at a tensile stress of 0.0. For the calibration of the proposed column-modeling strategies (sections 4 and 6), the concrete was assumed to crack at a tensile stress of $f_t = 0.625\sqrt{f'_c}$ (f'_c in MPa).

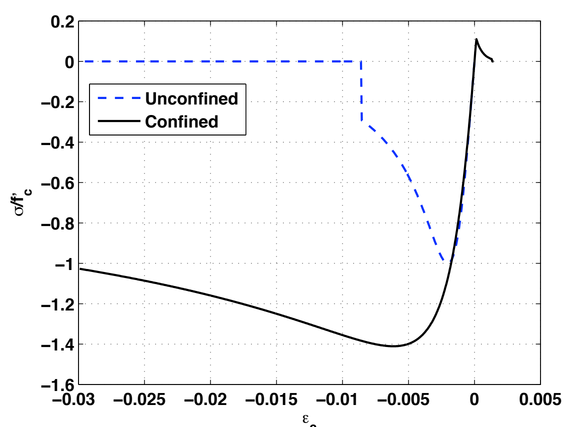

(a) Monotonic Response Normalized by Cylinder Strength

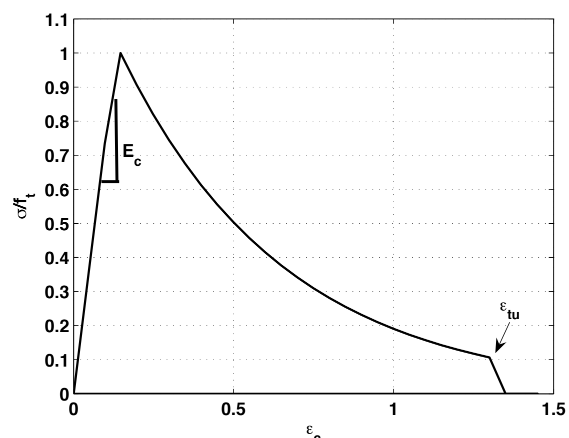

(b) Tensile Response Detail Normalized by Tensile Strength

Fig. 2.3 Concrete material models

2.3 UNIFORM RADIAL SECTION-DISCRETIZATION STRATEGY

The accuracy and efficiency of moment-curvature analyses depend heavily on the discretization of the core and cover concrete. A parametric study was performed in order to select the optimal number of radial and tangential subdivisions of both the confined core concrete (n_c^r and n_c^t) and unconfined cover concrete (n_u^r and n_u^t). In this study, the moment-curvature relationships generated with the fiber model were compared to the results of a typical moment-curvature analysis program developed at the University of Washington (Parish 2001). The UW moment-curvature program uses a unidirectional strip discretization scheme in which the concrete is divided into numerous unidirectional strips, as seen in Figure 2.4. The results of the UW program (utilizing a highly refined mesh, 100 strips) was used to represent the optimal solution.

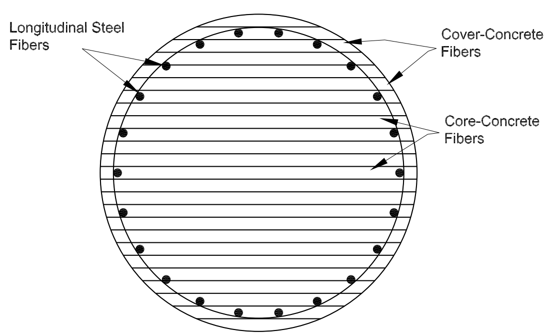

Fig. 2.4 Unidirectional section discretization

Increasing the number of fibers increases the accuracy of the moment-curvature analysis but increases the computational demand. A discretization scheme in which accuracy and efficiency are balanced is needed. Because there is not a unique solution to this problem, typical optimization methods cannot be applied without assigning an arbitrary cost to computational time. In order to find a balanced discretization scheme, a highly refined uniform radial discretization scheme was compared to the highly refined unidirectional discretization scheme, then the number of radial section divisions (i.e. n_c^r, n_c^t, n_u^r, n_u^t) were decreased until a balanced scheme was determined.

The uniform radial discretization scheme was compared to the unidirectional scheme by comparing the calculated moment-curvature responses of 75 columns from the UW-PEER column database (Berry et al. 2004). The 75 circular columns were all the columns in the database that failed in shear or flexure-shear, and had circular spiral reinforcement. This study used a bilinear steel model ($b = 0.01$, Section 2.2.1) and the Mander concrete model for both the confined and unconfined concrete (Section 2.2.2). The moment-curvature response was evaluated based on three parameters.

ϕ_y **Ratio,** The ratio of curvature at first yielding of the tension steel calculated with the unidirectional scheme to those calculated with the uniform radial scheme, $\frac{\phi_y^{unid}}{\phi_y^{radial}}$

$M_{5\varepsilon_y}$ **Ratio,** The ratio of calculated moment at a tensile strain of 5 times ε_y calculated with the unidirectional scheme to the moment calculated with the uniform radial scheme, $\frac{M_{5\varepsilon_y}^{unid}}{M_{5\varepsilon_y}^{radial}}$

$M_{10\varepsilon_y}$ **Ratio,** The ratio of calculated moment at a tensile strain of 20 times ε_y calculated with the unidirectional scheme to the moment calculated with the uniform radial scheme, $\frac{M_{20\varepsilon_y}^{unid}}{M_{20\varepsilon_y}^{radial}}$

Based on the results of this analysis, the following recommendations are made in order to efficiently and accurately model the moment-curvature response of a column cross section using a uniformly distributed radial discretization scheme,

- 20 core transverse subdivisions, $n_c^t = 20$
- 10 core radial subdivisions, $n_c^r = 10$
- 20 cover transverse subdivisions, $n_u^t = 20$
- 1 cover radial subdivision $n_u^r = 1$

The mean ϕ_y ratio using this scheme is 1.000 with a coefficient of variation (c.o.v.) of 0.110%. The mean $M_{5\varepsilon_y}$ ratio is 0.996 with a coefficient of variation of 0.128% and the mean $M_{20\varepsilon_y}$ ratio is 0.996 with a coefficient of variation of 0.233%. This configuration is shown in Figure 2.5.

A parametric study was performed to verify that the recommended discretization scheme accurately and efficiently models moment-curvature response. The parametric study used a bilinear steel model ($b = 0.01$) and the Mander concrete model for both the confined and unconfined concrete. The recommended scheme was used as the base discretization scheme, and the number of radial divisions were systematically varied to demonstrate the analyses dependency on the varied parameter.

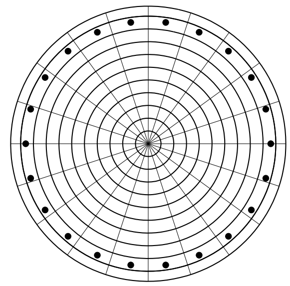

Fig. 2.5 Recommended configuration, $n_c^t = 20$**,** $n_c^r = 10$**,** $n_u^t = 20$ **and** $n_u^r = 1$

Figures 2.6 and 2.7 show the effects of varying the number of confined concrete radial and tangential subdivisions. The mean values of the ϕ_y, $M_{5\varepsilon_y}$, and $M_{10\varepsilon_y}$ ratios are plotted versus n_c^r in Figure 2.6 and n_c^t in Figure 2.7. Also shown in the figures are the maximum and minimum values and the coefficient of variation of the ratios. Figure 2.6 shows that an unbiased results can be obtained by using at least 10 radial subdivisions and that using more than 10 does not significantly improve results. It can be seen in Figure 2.7 that although the mean values vary slightly between 20 and 40 tangential subdivisions, the coefficients of variation of the ratios are the same. Using more than 20 subdivisions is unnecessary, since the mean value of the ratios using 20 subdivisions is 0.996 and the coefficient of variation does not improve by using more divisions.

Similarly, the effects of varying the number of unconfined concrete radial and tangential subdivisions on moment-curvature accuracy is illustrated in figures 2.8 and 2.9. Figure 2.8 shows that varying the number of radial unconfined subdivisions does not affect the accuracy of the moment-curvature analysis significantly. In Figure 2.9, it can be seen that the solutions converge when $n_u^t = 20$ and that using a finer mesh does not significantly improve the accuracy of the moment-curvature analyses.

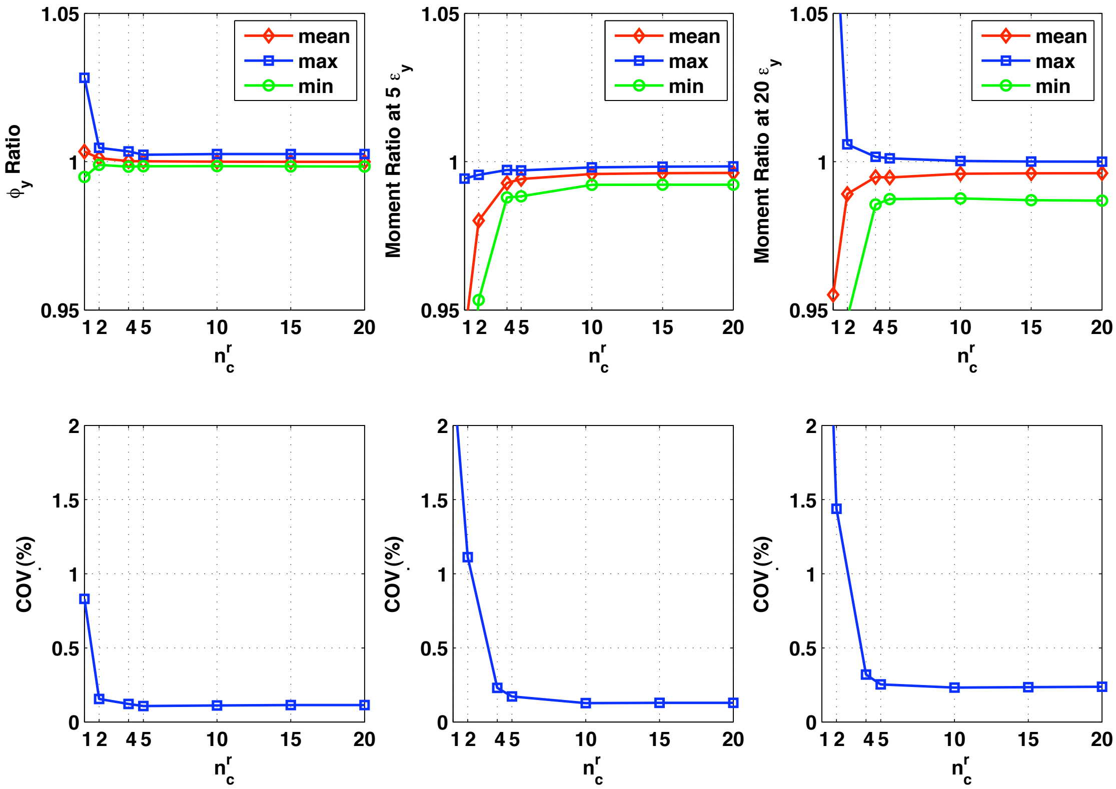

Fig. 2.6 Effect of n_c^r on m-ϕ accuracy

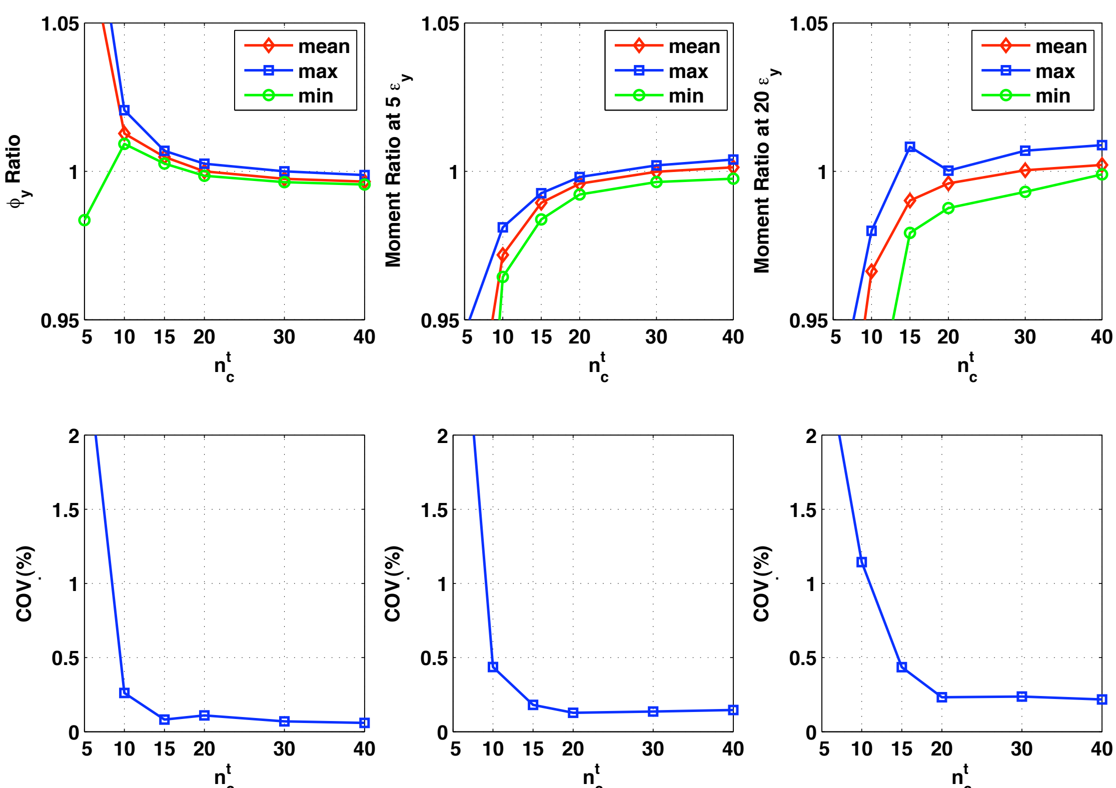

Fig. 2.7 Effect of n_c^t on m-ϕ accuracy

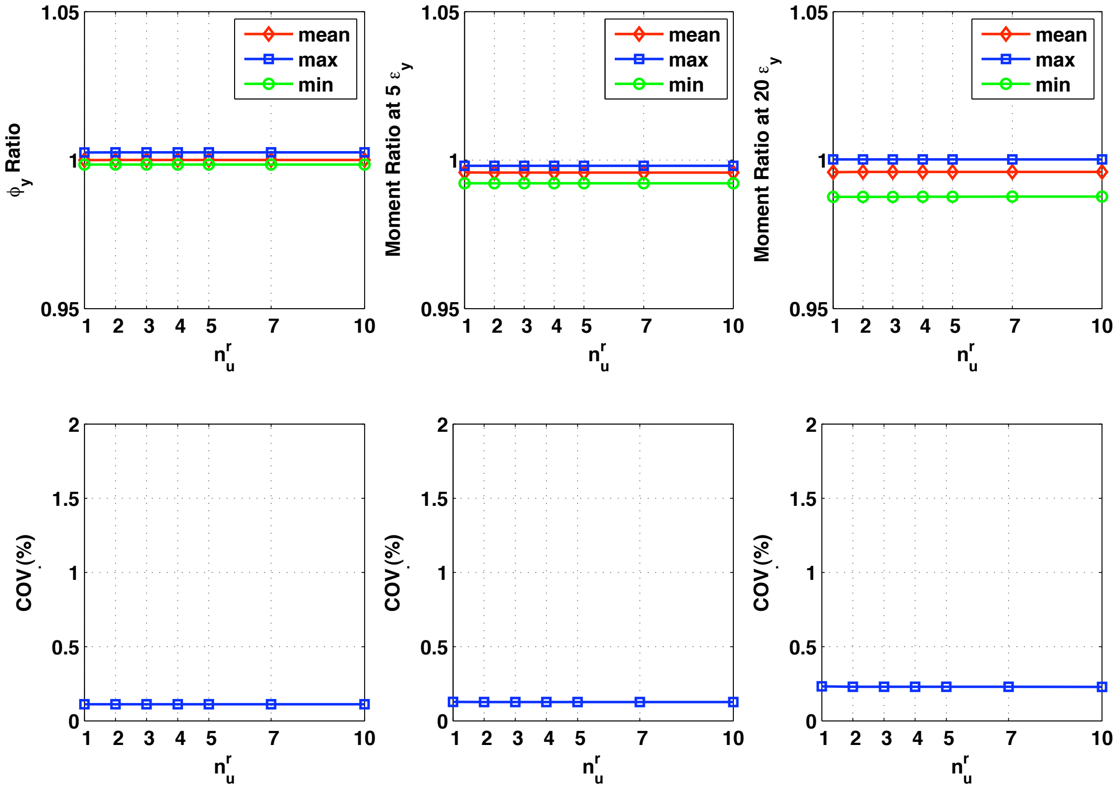

Fig. 2.8 Effect of n_u^r on m-ϕ accuracy

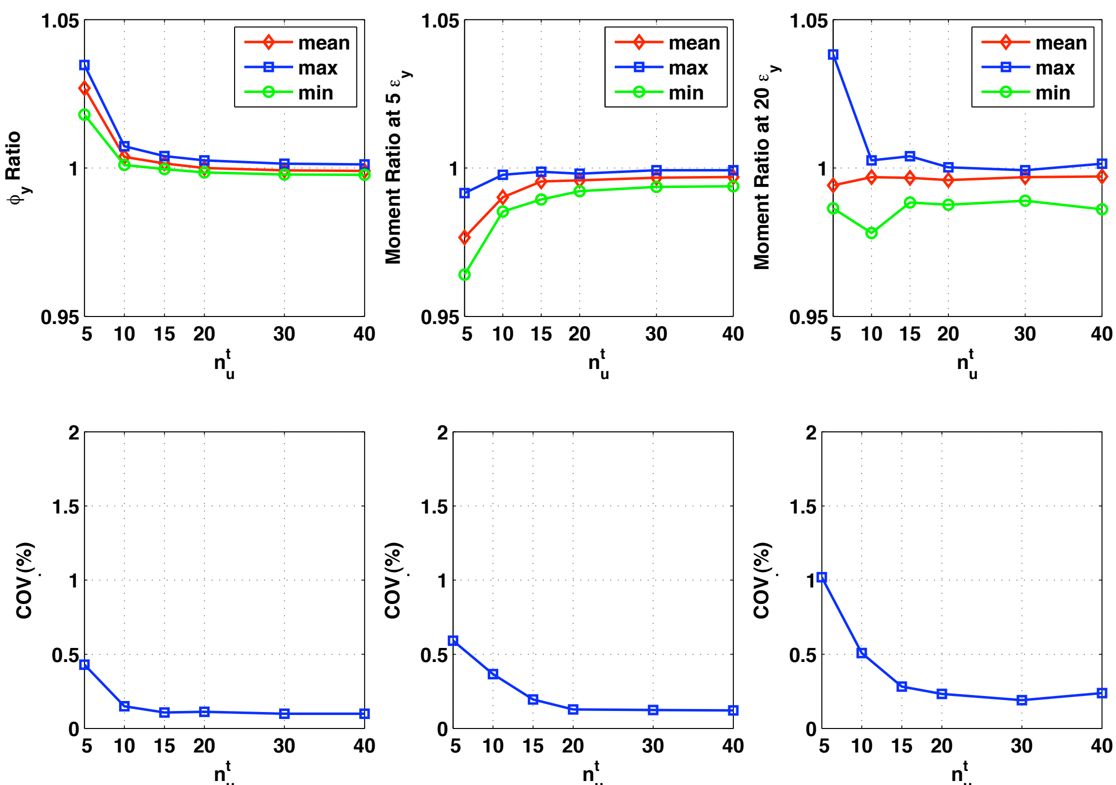

Fig. 2.9 Effect of n_u^t on m-ϕ accuracy

2.4 NONUNIFORM RADIAL DISCRETIZATION STRATEGY

Because the area nearest the column-neutral axis does not significantly affect moment-curvature response, it may sometimes be efficient to use a coarser fiber mesh in this region. Utilizing this scheme would reduce the number of fiber sections required to model the moment-curvature response significantly, thus reducing the computational demand of the analysis. It should be noted that the amount of axial load will affect the location of the neutral axis, and the location will not always be at the center of the column. The dataset used in the following analysis contained columns with a wide range of axial-load ratios ($\frac{P}{A_g f'_c} = 0$ to 70%). In this section the effect of using a coarser mesh near the center of the cross section is studied and recommendations are proposed for utilizing this methodology.

A parametric study was performed in which the diameter of a coarse mesh in the center of a cross section was varied from 50% - 70% of the core diameter (i.e., $\frac{d_{coarse}}{d_{core}} = 0.5$, 0.6 and 0.7) and the number of coarse mesh fibers (n_{coarse}) was varied between 10 and 20 fibers. The density of the fine mesh near the exterior of the core remained the same regardless of the coarse mesh diameter; therefore an increase in the diameter of coarse mesh resulted in a decrease in the total number of core fibers (n_{total}). The nonuniform configurations were also compared to the recommended uniform configuration from the previous section (Figure 2.5). Table 2.1 describes the parameter study matrix and Figure 2.10 illustrates the various configurations. As seen in the table and the figures, the total number of core fibers was varied from 200 to 70.

The accuracy of the moment-curvature analysis was evaluated using the ϕ_y, $M_{5\varepsilon_y}$ and $M_{20\varepsilon_y}$ ratios as defined in the previous section, and the same 75 columns from the UW-PEER database. The study used a bilinear steel model ($b = 0.01$, Section 2.2.1) and the Mander concrete model for both the confined and unconfined concrete (Section 2.2.2).

As expected, the accuracy of the moment-curvature analysis decreases as the size of the coarse mesh increases. Decreasing the number of coarse fibers has a similar effect. Utilizing any of these schemes reduces the number of fibers, but some accuracy is lost. The accuracy lost by utilizing configuration 1 is within acceptable bounds. With configuration 1, the mean, minimum, and maximum values of the ϕ_y, $M_{5\varepsilon_y}$, and $M_{20\varepsilon_y}$ ratios are all within 0.01 of 1.00 and the coefficients of variation are all less than 0.25%. The loss in accuracy from configurations 2-6 are significant enough to outweigh the resulting gains in efficiency.

Table 2.1 Discretization study matrix

Configuration	Unif.	1	2	3	4	5	6
$\frac{d_{coarse}}{d_{core}}$	0	0.5	0.5	0.6	0.6	0.7	0.7
n^t_{fine}	20	20	20	20	20	20	20
n^r_{fine}	10	5	5	4	4	3	3
n^t_{coarse}	0	10	10	10	10	10	10
n^r_{coarse}	0	2	1	2	1	2	1
n_{total}	200	120	110	100	90	80	70

2.5 SUMMARY

The constitutive material models used in this report were presented. The reinforcing steel was modeled using the Giufre-Menegotto-Pinto constitutive model, and the confined and unconfined concrete was modeled using a model proposed by Mander, Priestley, and Park. The following parameter was identified for calibration with experimental results.

Strain-Hardening Ratio (b). The ratio of post-yield stiffness of the reinforcing steel to the modulus of elasticity of the steel, $b = \frac{E_{sh}}{E}$.

This parameter is calibrated in Chapter 4. A second parameter was identified, but will not be part of the optimization study. The effect of the following parameter is studied in 4.6.

Transverse Reinforcement Effectiveness Ratio (η). The ratio of the effective core transverse reinforcement ratio to the calculated transverse reinforcement ratio to be used in the calculation of f'_{cc} and e_{cc}, $\eta = \frac{\rho_{sc}^{eff}}{\rho_{sc}}$.

A parametric study was performed to determine the best uniform radial discretization scheme to use for modeling column cross-section response. Based on the results of these analyses, the following recommendations are made in order to efficiently and accurately model the moment-curvature response of a column cross section using a fiber model: $n^t_c = 20$, $n^r_c = 10$, $n^t_u = 20$ and $n^r_u = 1$. This configuration is shown in Figure 2.5.

Because the area nearest the center of the column influences the column section response little, a coarser mesh may be used near the center of the column. The effect of using a coarser

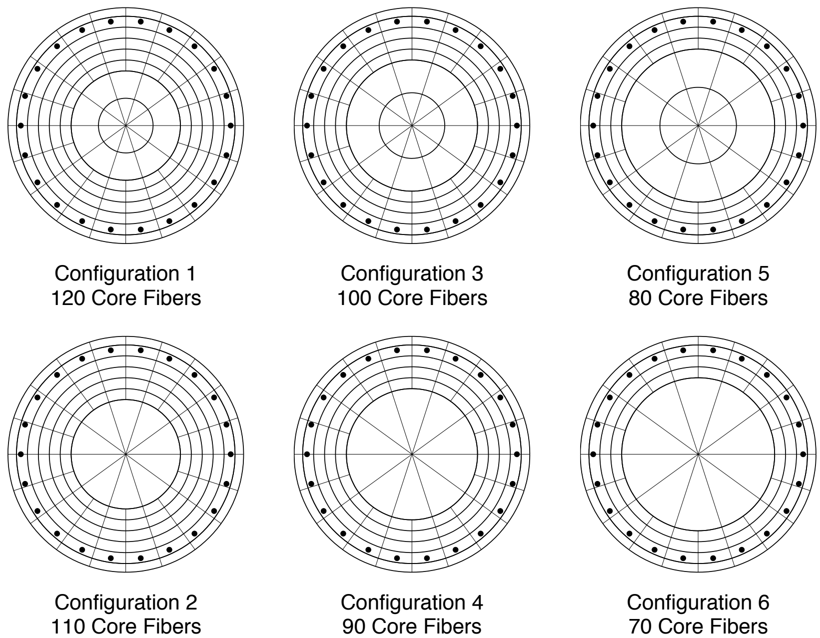

Fig. 2.10 Configuration types

mesh near the center of the cross section was also studied in this chapter. Since some accuracy is lost by utilizing this methodology, it is recommended that a uniform discretization with 200 core fibers (Fig. 2.5) be used when accuracy is the top priority. In cases where efficiency is a concern, configuration 1 (120 core fibers) could be used also.

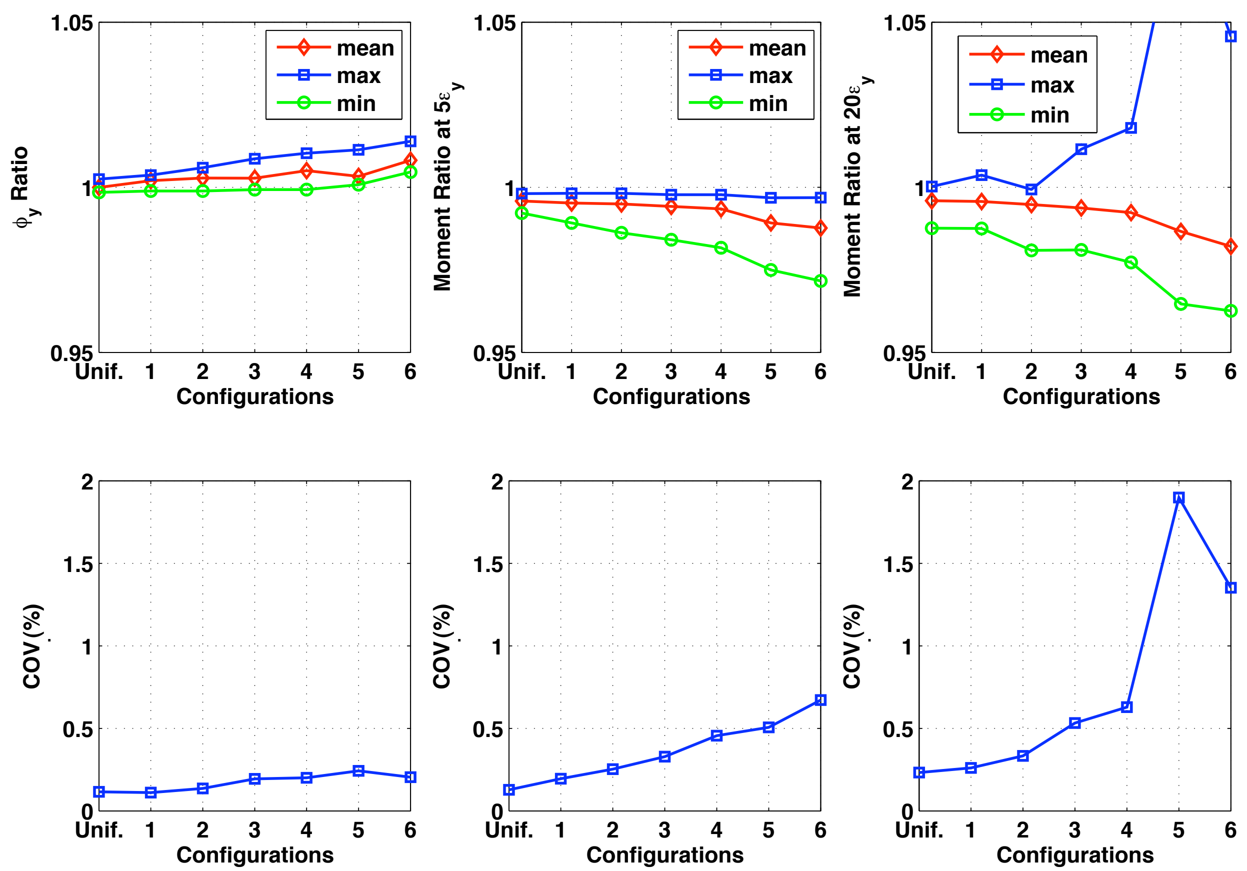

Fig. 2.11 Effect of discretization scheme on $m-\phi$ accuracy

3 Development of Distributed-Plasticity Column Model

In this chapter, a column-modeling strategy is presented, and key modeling parameters are identified for calibration. In the proposed modeling strategy, a force-based fiber beam-column element, a zero-length bond section, and an elastic shear component are combined to model the flexural, bond slip, and shear components of the total column deflection. A graphical interpretation of the model is shown in Figure 3.1. The following sections describe each of these components in detail.

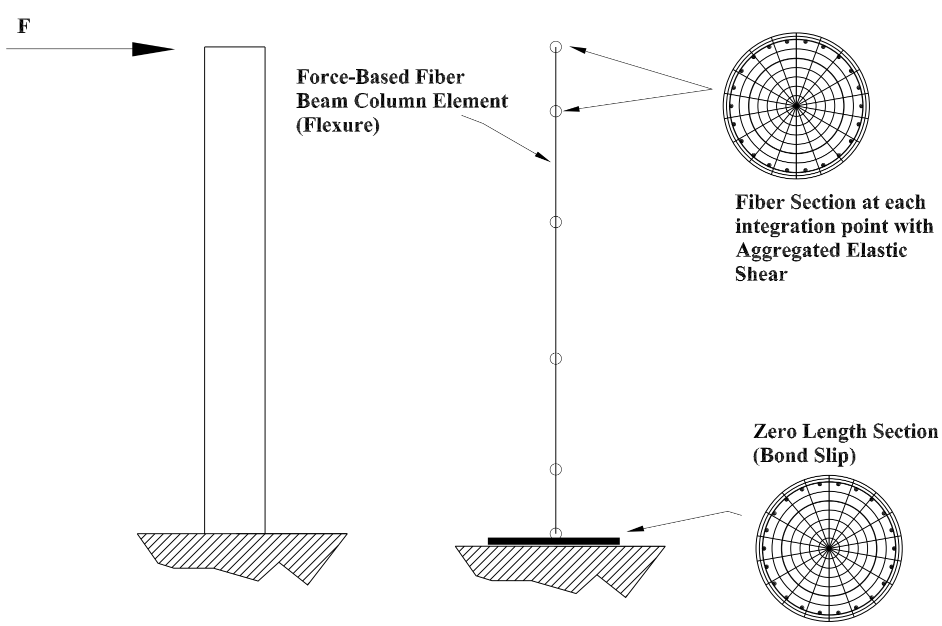

Fig. 3.1 Distributed-plasticity model with bond slip and shear components

3.1 NONLINEAR FORCE-BASED BEAM-COLUMN ELEMENT (FLEXURE)

The flexural component of the column deflection was modeled with a distributed-plasticity, flexibility-based, fiber beam-column element. A fiber beam-column element is a line element in which the moment-curvature response at each integration point is determined from the fiber section assigned to that integration point.

A flexibility-based formulation assumes a moment-distribution along the length of the column, and the curvatures at each integration point are subsequently estimated for the moment at that section. The column response is then obtained through weighted integration of the section responses (Taucer et al. 1991). Because most inelastic behavior occurs near the base of the column, the element used in this report utilizes the Gauss-Labotto integration scheme, in which the integration points are placed at the ends of the element, as well as along the column length.

A force-based fiber beam-column element utilizing a Gauss-Labotto integration scheme was implemented in MATLAB (2005) to evaluate the effects of strain localization (Section 3.1.1) and to verify the implementation of the force-based beam-column element in OpenSees (OpenSees Development Team 2002) (Section 3.4). The MATLAB implementation utilized the section discretization scheme and material constitutive models discussed in sections 2.1 and 2.2, in which each fiber was assigned a particular stress-strain response.

3.1.1 Concentration of Local Deformations

The force-based formulation is attractive because it can model the spread of plasticity along the length of the column using only one element and a number of integration points (N_p). However, force-based elements lose objectivity at the local and/or global level depending on the section hardening behavior (Coleman and Spacone 2001).

For example, figures 3.2 and 3.3 show the calculated force-deformation responses and the calculated strain distribution along the height of the column for a column with a hardening section behavior ($b = 0.015$). The included plot shows the strain distribution at various levels of deformation. For these figures, pushover analyses were performed on a typical column from the UW-PEER database (Lehman et. al. 2000, No. 415). One force-based fiber element was used, and the number of integration points and the strain-hardening ratios were varied systematically. Both the force-deformation envelope (Fig. 3.2) and the average strains (Fig. 3.3) are insensitive to the number of integration points used in the analysis. The inelastic strains spread up the height of the column as the deformation is increased.

In contrast, figures 3.4 and 3.5 show the calculated force-deformation responses and the calculated strain distributions along the height of the column for a column with nearly a plastic section response ($b = 0.001$). The force-deformation response (Fig. 3.4) does not vary with the number of integration points, but the local strains (Fig. 3.5) vary drastically. Inelastic strains localized at the base of the column and did not spread to any of the other integration points. This occurs because the column reaches its load carrying capacity when the when the integration point at the base reaches the yield moment. As the total deflection increases, the base curvature increases with constant moment, while the other integration points do not see any change in moment or curvature (Coleman and Spacone 2001). As seen in Figure 3.5, as the number of integration points increases, the length of the plastic hinge decreases, resulting in larger base curvatures for a given tip displacement.

Figures 3.6 and 3.7 show similar plots for a column with softening properties ($b = -0.002$). Both the global and local responses are sensitive to the number of integration points used in the analysis. As in the column with the plastic section response, strains localize at the base of the column and increasing the number of integration points decreases the length over which these strains localize. This decrease in length increases the curvature and strains for a given tip deflection. For the softening section, the increase in strain causes the column force-deformation response to degrade quickly (Coleman and Spacone 2001).

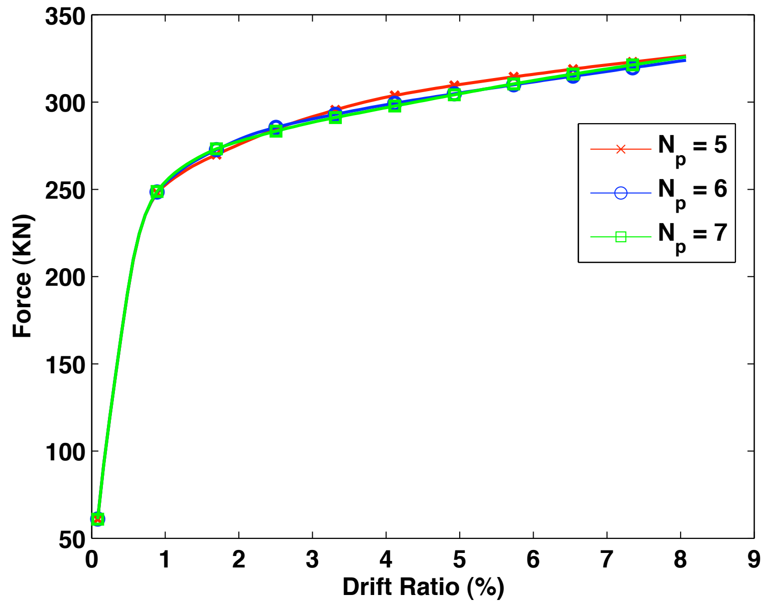

Fig. 3.2 Force-deformation envelope with varying n_p (hardening)

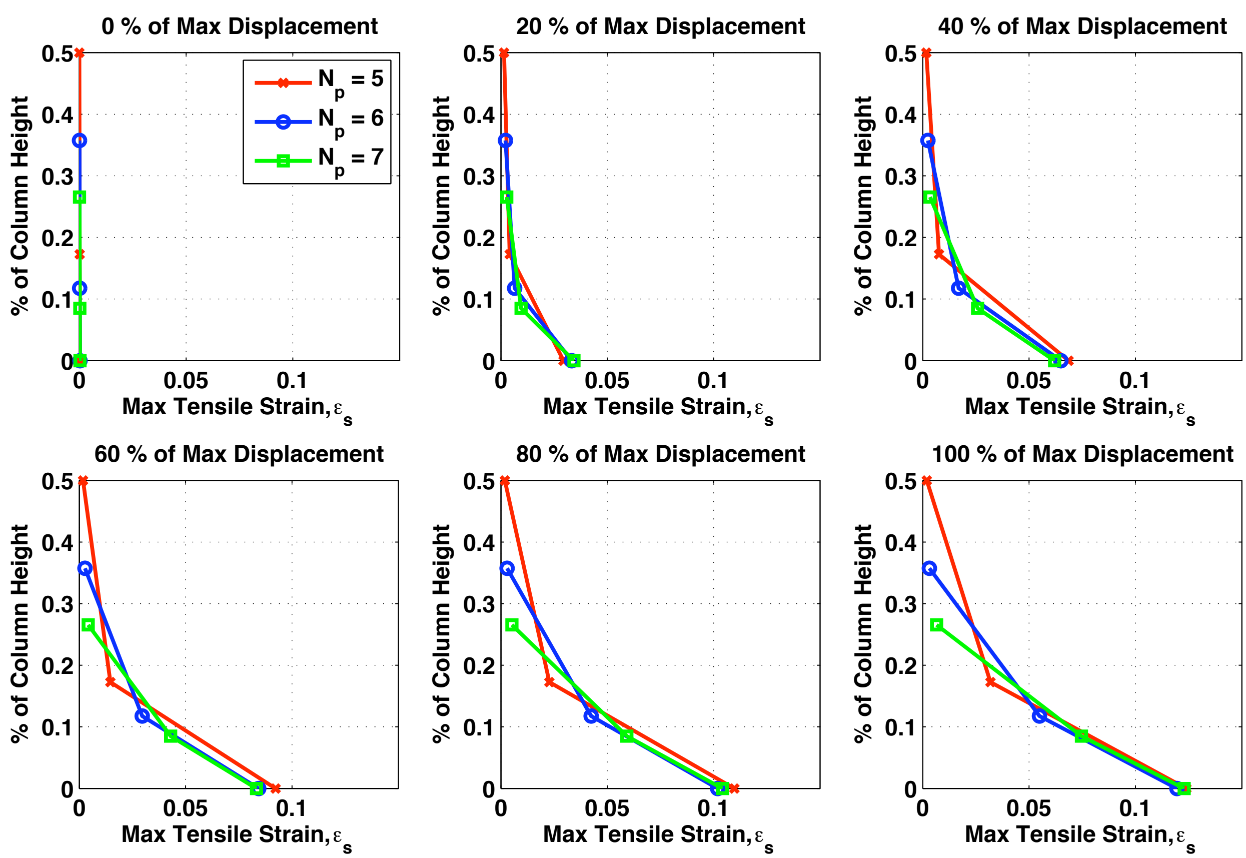

Fig. 3.3 Strain distributions for varying n_p (hardening)

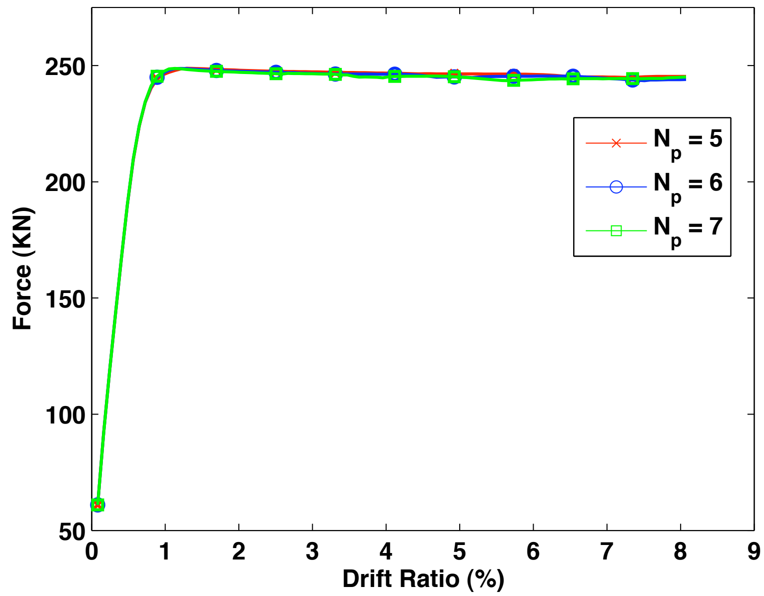

Fig. 3.4 Force-deformation envelope with varying n_p (plateau)

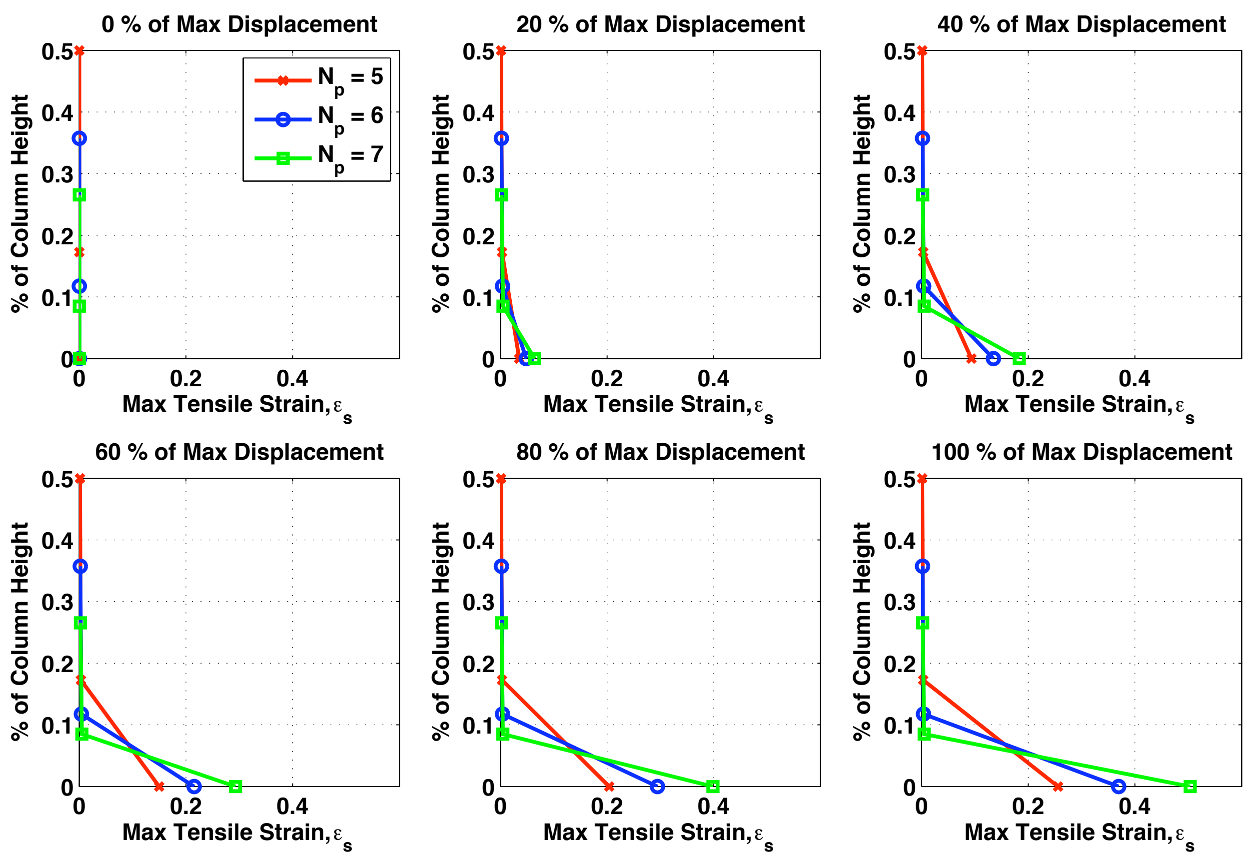

Fig. 3.5 Strain distributions for varying n_p (plateau)

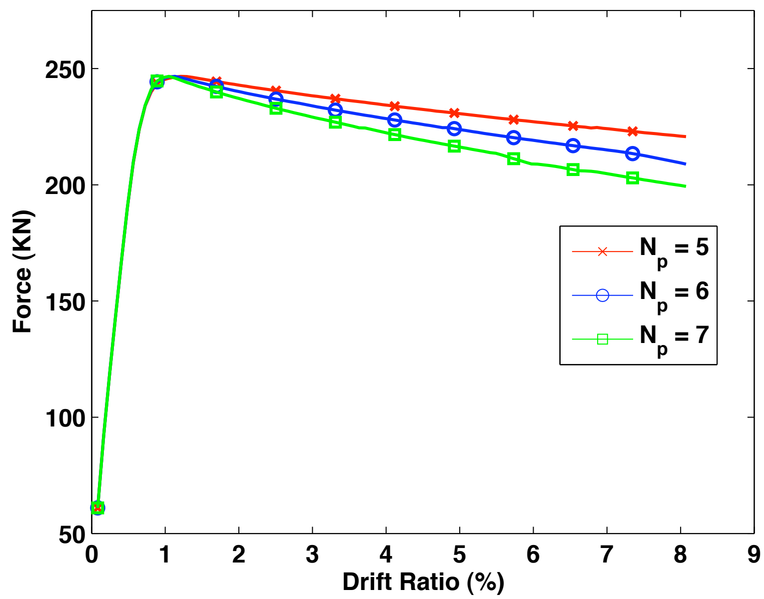

Fig. 3.6 Force-deformation envelope with varying n_p (softening)

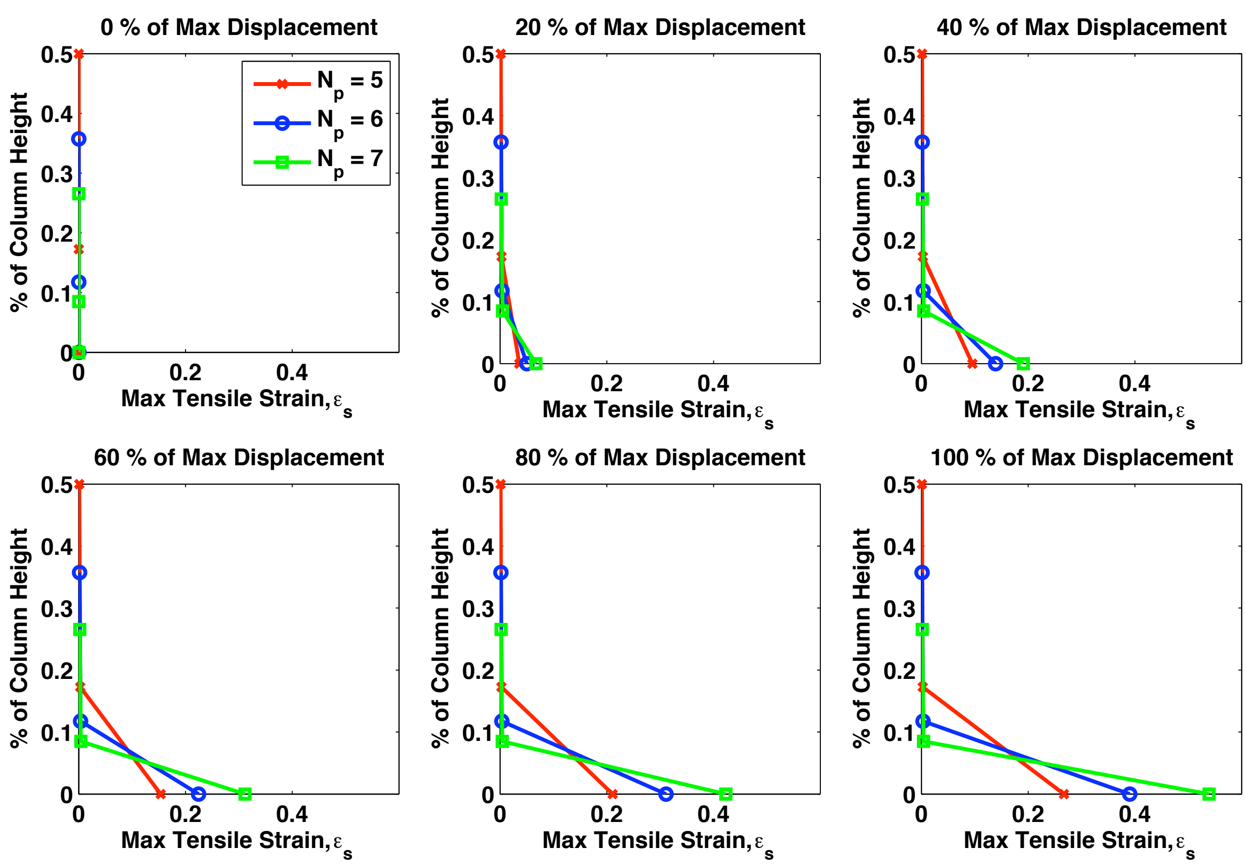

Fig. 3.7 Strain distributions for varying n_p (softening)

For elements with perfectly plastic section behavior, the calculated curvatures and strains are sensitive to the number of integration points. For elements with softening section behavior, the local and global responses of the element are sensitive to the number of integration points. Figure 3.8 summarizes these findings. For this figure, pushover analyses were performed on the 8 columns tested by Lehman and Moehle (2000). One force-based fiber element was used for each column, and the number of integration points and the strain-hardening ratios were varied systematically. In this figure, the average values of the following parameters were plotted versus N_p.

Moment at Δ_{max} Ratio. The moment at maximum displacement (Δ_{max}) for varying N_p normalized by the moment at maximum displacement for $N_p = 5$, $\left(\frac{M_{\Delta_{max}}^{N_p}}{M_{\Delta_{max}}^{5}}\right)$.

Max Strain at Δ_{max} Ratio. The maximum tensile steel strain at maximum displacement for varying N_p normalized by the maximum strain at maximum displacement for $N_p = 5$, $\left(\frac{\varepsilon_{\Delta_{max}}^{N_p}}{\varepsilon_{\Delta_{max}}^{5}}\right)$.

As seen in Figure 3.8, the global and local responses of the column with the hardening sections are insensitive to N_p if at least four integration points are used. For the column with the plastic section, the global response is insensitive to N_p, but the local response is not. As the number of integration points is increased, the strain at maximum displacement also increases. For the column with a softening section, both the global and local responses are sensitive to N_p. As N_p is increased, the moments at maximum displacement decrease and the strains increase.

Similarly, Figure 3.9 illustrates the effect of N_p on columns under double curvature for the three section behaviors. In this figure, the maximum moments and strains are normalized by the results at 6 N_p. As seen in the figure, at least 6 integration points are needed for unbiased global and local results for columns with hardening sections under double curvature.

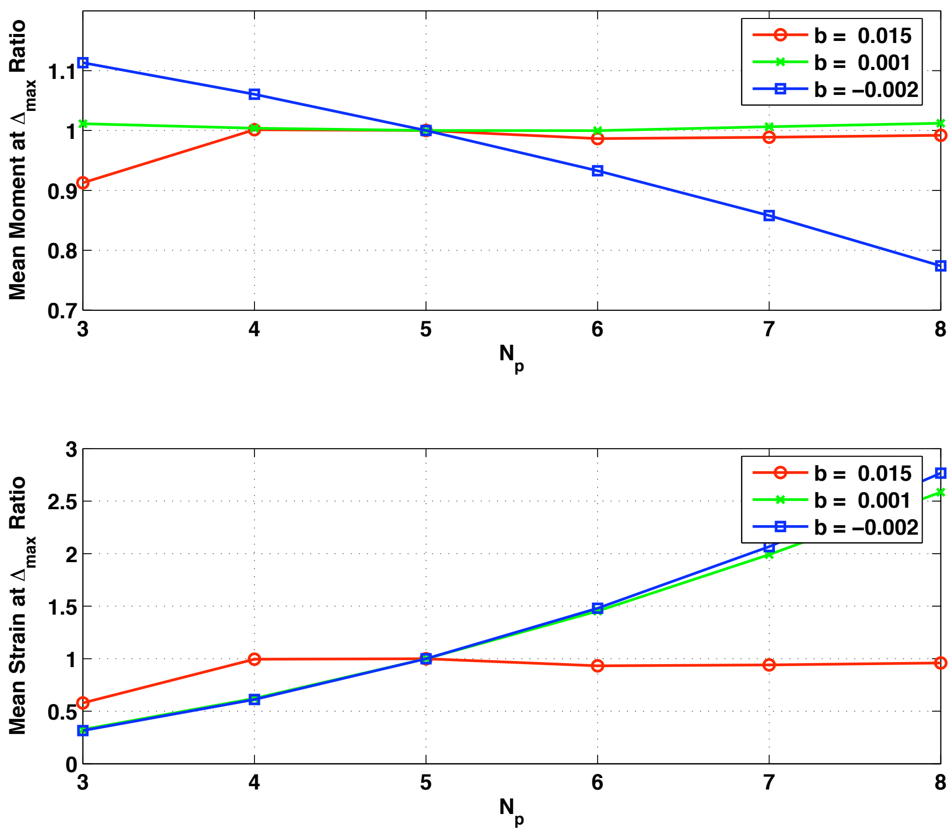

Fig. 3.8 Force-deformation and strain dependency on n_p (cantilever)

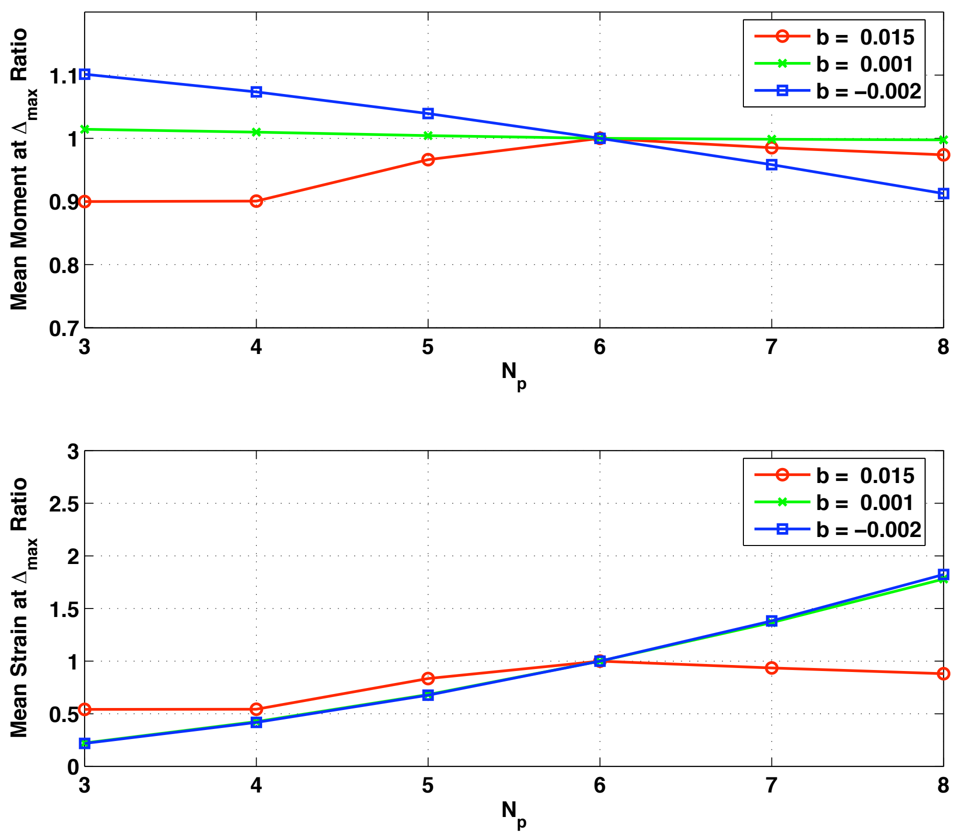

Fig. 3.9 Force-deformation and strain dependency on n_p (double curvature)

The issue of the concentration of local deformations in distributed-plasticity elements was addressed by Coleman and Spacone (2001). The researchers developed a method of post-processing plastic curvatures to obtain nonbiased curvatures based on assumed plastic-hinge lengths (L_p). The post-processing method was developed by equating equations for tip displacements from traditional plastic-hinge analysis (δ_p^{lumped}) to the tip displacements calculated from the distributed-plasticity element ($\delta_p^{distributed}$), and then adjusting the distributed-plasticity plastic curvatures to match the curvatures from the lumped-plasticity formulation. This process is described in more detail in the following discussion.

The plastic tip displacement for a cantilever column calculated from traditional plastic-hinge analysis is as follows.

$$\delta_p^{lumped} = \phi_p L_p \left(L - \frac{L_p}{2} \right) \tag{3.1}$$

where ϕ_p is the plastic curvature in the hinge, and L is the column length. The plastic-displacement for a cantilever column calculated with the distributed-plasticity element can be simplified to the following equation.

$$\delta_p^{distributed} = \phi_{p1} L_{ip1} \left(L - \frac{L_{ip1}}{2} \right) + \phi_{p2} L_{ip2} \left(L - L_{ip1} - \frac{L_{ip2}}{2} \right) + \ldots \tag{3.2}$$

where ϕ_{p1} and ϕ_{p2} are the plastic curvatures calculated at the first and second integration points in the element. L_{ip1} and L_{ip2} are the equivalent plastic-hinge lengths of the first and second integration points. In this formulation, the plastic-hinge lengths for the integration points are calculated as $L_{ip1} = w_{ip1} L$ and $L_{ip2} = wip2L$. $wip1$ and $wip2$ are the weights of the respective integration points according to the integration scheme. The traditional implementation of the force-based element uses Gauss-Labotto integration.

Equation 3.2 can be carried out to include the other integration points; however the plastic deformations rarely spread to the other integration points. In fact, in the case of a softening section response, the plastic deformations will not spread to the second integration point, and will be concentration in the first integration point at the base of the column, as illustrated in Figure 3.7.

The post-processing method developed by Coleman and Spacone (2001) was formulated for a softening section, and therefore the second integration point terms in Equation 3.2 are ignored. By equating the first integration point terms of Equation 3.2 to Equation 3.1, the following relationship is obtained for the nonbiased, adjusted plastic curvature (ϕ_p^{adj1}) as a function of the weight of the integration point, plastic-hinge length, and calculated curvature.

$$\phi_p^{adj1} = \phi_{p1}\frac{w_{ip1}L^2\left(2-w_{ip1}\right)}{L_p\left(2L-L_p\right)} \tag{3.3}$$

This formulation is correct for softening sections; however if there is any hardening in the section, and plastic deformations spread to the second integration point, it will no longer be valid. In the case of a hardening section, the calculated curvatures from the distributed-plasticity element will be nonbiased, but will not match the curvatures calculated with the traditional lumped-plasticity formulation.

A similar relationship for the nonbiased adjusted plastic curvature can be obtained for hardening sections by including the higher integration points. The following relationship is obtained by including the second integration point in 3.2.

$$\phi_p^{adj2} = \phi_{p1}\frac{w_{ip1}L^2\left(2-w_{ip1}\right)}{L_p\left(2L-L_p\right)} + \phi_{p2}\frac{w_{ip2}L^2\left(2-2w_{ip1}-w_{ip2}\right)}{L_p\left(2L-L_p\right)} \tag{3.4}$$

This relationship will be valid as long as plastic deformations do not spread to the third integration point. The following figures (figures 3.10-3.12) demonstrate the concepts discussed above.

In Figure 3.10 the post-yield strain-hardening ratio (b) of the steel in the distributed-plasticity element is varied between -1.0 % and 5.0% for a typical column in the database using 5 integration points and neglecting bar slip and shear deformations. The first axes in this figure illustrates the recorded curvatures at the first integration point. The second axes is a plot of the adjusted plastic curvatures calculated with one integration point (Equation 3.3) versus displacement ductility. The third axes is a plot of the adjusted-plastic curvature calculated with two integration points (Equation 3.4) versus displacement ductility. The fourth axes is a plot of the ratio of plastic curvature calculated at the second integration point to the curvatures at the first integration point. This axes is included to demonstrate the amount of plastic deformation that has spread to the second integration point.

As seen in the figure, the recorded curvature at the first integration point is dependent on the amount of hardening or softening in the column, and the curvatures do not match the curvatures calculated with plastic-hinge analysis. In the case of the softening section response, utilizing one integration point in the calculation of the adjusted plastic curvature is sufficient, however the method is inaccurate for the hardening section responses, as expected. As seen in the third axes, the adjusted curvatures using two integration points match the target curvatures of the lumped-plasticity formulation for both the hardening and softening section responses.

Similarly, in Figure 3.11 the number of integration points is varied between 5 and 8 for a typical column in the database with a softening section response ($b = -1.00\%$). As seen in the first axes, the curvatures recorded at the base of the column are dependent on the number of integration points used in the calculation. As shown in the second and third axes, both nonbiased curvatures calculated with both methods are identical to the target curvatures from the lumped-plasticity formulation.

In Figure 3.12, the number of integration points is varied between 5 and 8 for a typical column in the database with a hardening section response ($b = 5.00\%$). As seen in the first axes, the curvatures at the base of the column are not dependent on the number of integration points used in the calculation; however, these curvatures do not match those calculated with the lumped-plasticity formulation. The second axes illustrates the inability of Equation 3.3 to calculated unbiased curvatures for hardening sections. The third axes demonstrates that Equation 3.4 is accurate (in particular case) for 5, 6, and 7 integration points, but begins to stray at higher ductilities for 8 integration points. This is because the plastic curvatures begin to spread to the third integration point.

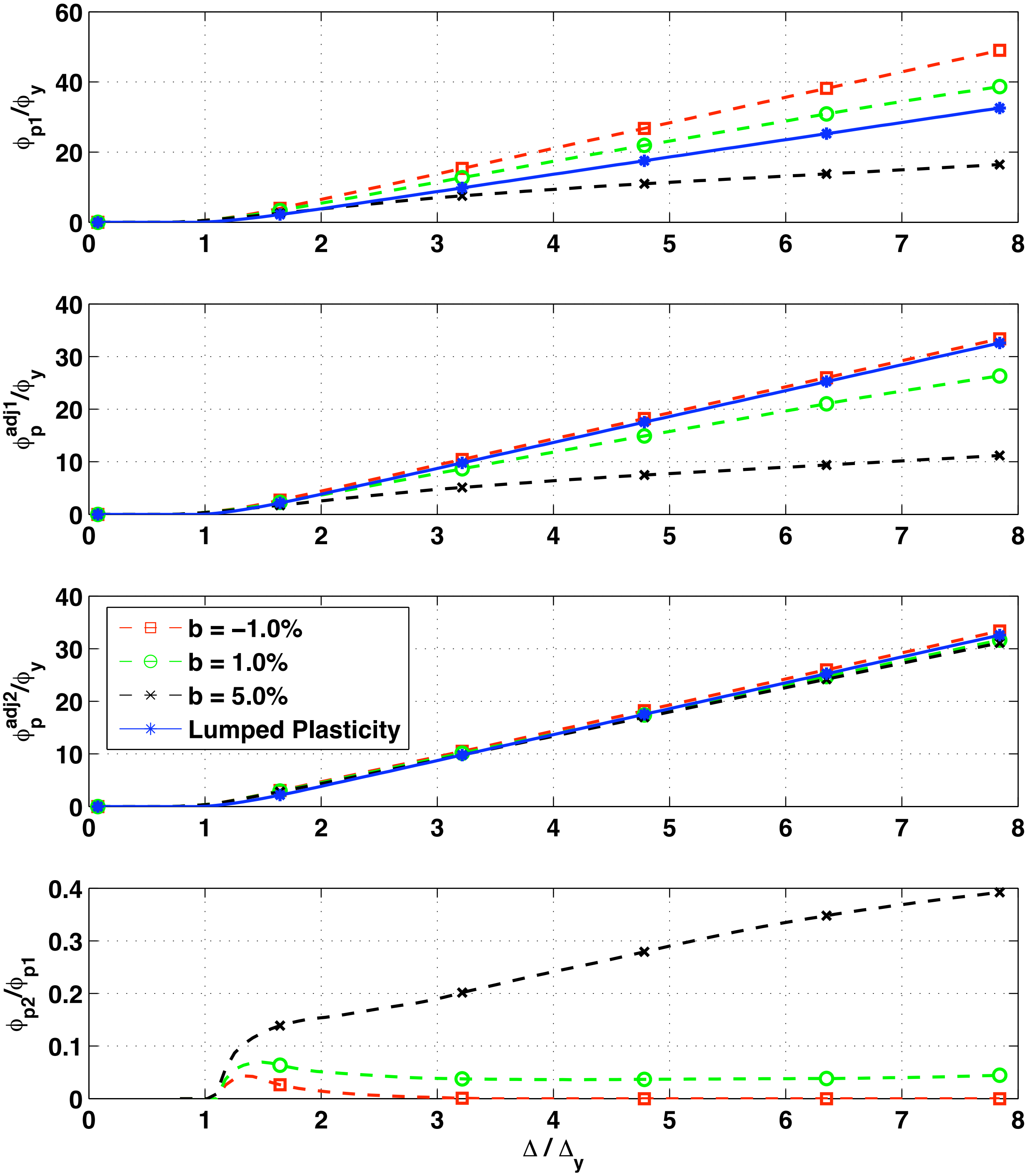

Fig. 3.10 Curvature response for typical column with varying strain-hardening ratio, $n_p = 5$

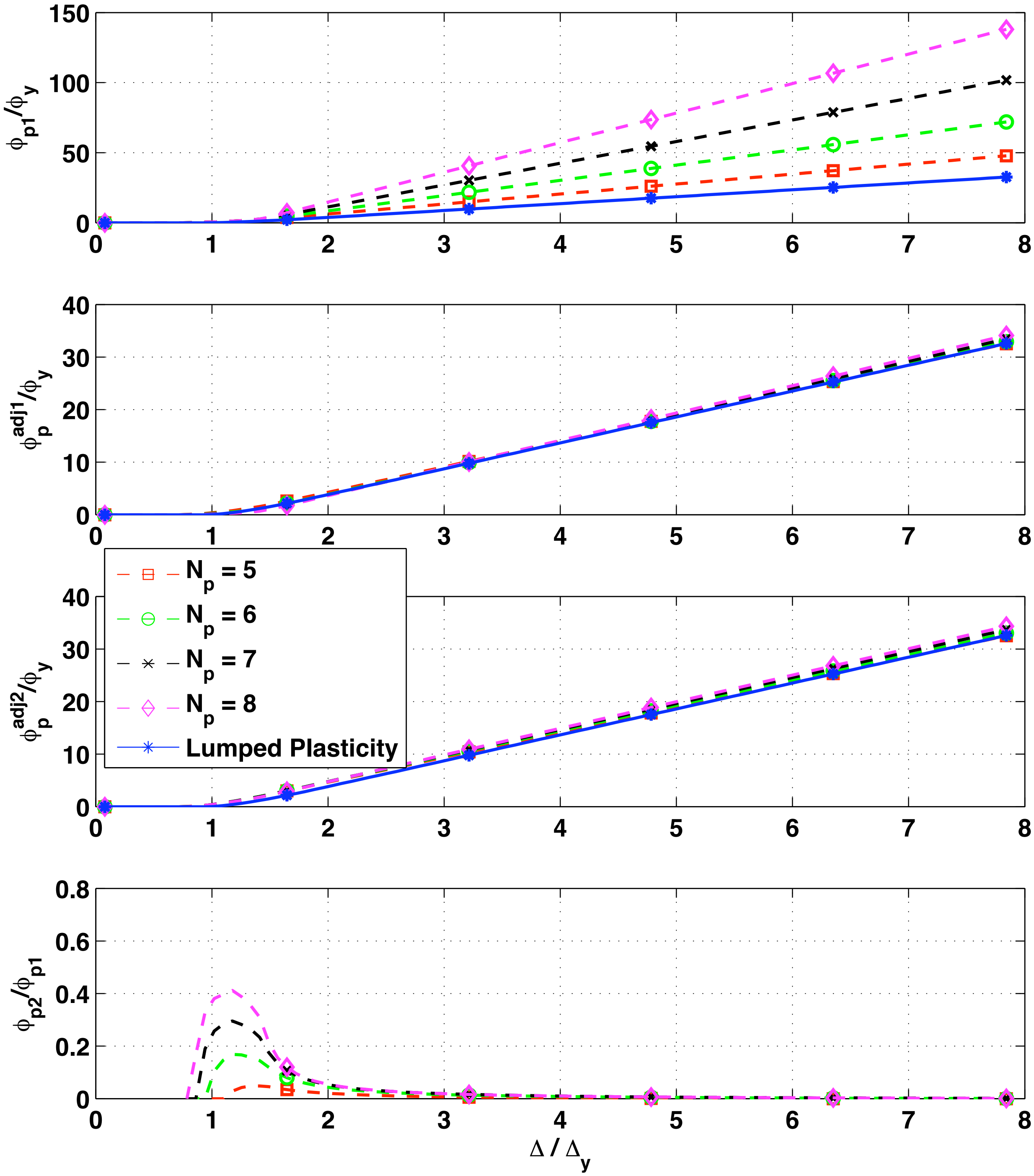

Fig. 3.11 Curvature response for typical column with degrading section response, $b = -1.00\%$

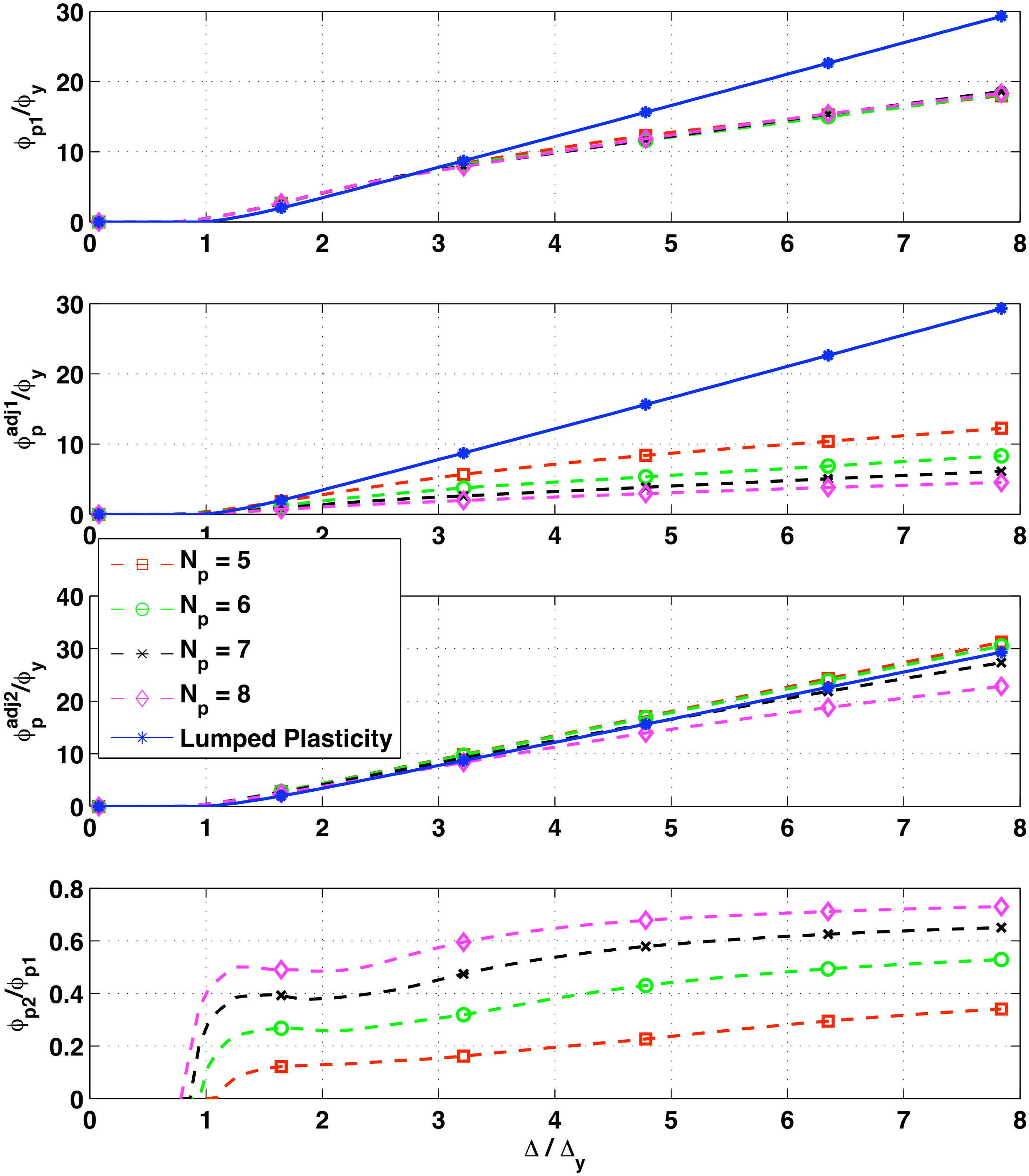

Fig. 3.12 Curvature response for typical column with hardening section response, $b = 5.00\%$

3.2 BOND SLIP DISPLACEMENT MODEL

The fiber-based beam-column element is based on the assumption that plane sections remain plane, which implies perfect bond between the longitudinal reinforcement and the surrounding concrete (Hachem et al. 2003). The force-based beam-column element does not include the component of deformation due to bond slip, and the column appears stiffer than it actually is. In the proposed modeling strategy, a zero-length section at the base of the column is used to model the bond slip of the anchorage reinforcement. The zero-length section is a fiber section in which each fiber is assigned a stress-displacement relationship instead of a stress-strain relationship. This formulation is beneficial because it allows for biaxial, cyclic lateral loading and variable axial loads.

3.2.1 Tensile Stress-Displacement Relationship of Reinforcement

The steel stress-displacement relationship was based on a two-component bond-stress model (Lehman and Moehle 2000). The model was modified by Ranf (2006) to account for development of bond stress at low bar strains. An illustration of the model is presented in Fig. 3.13. In this

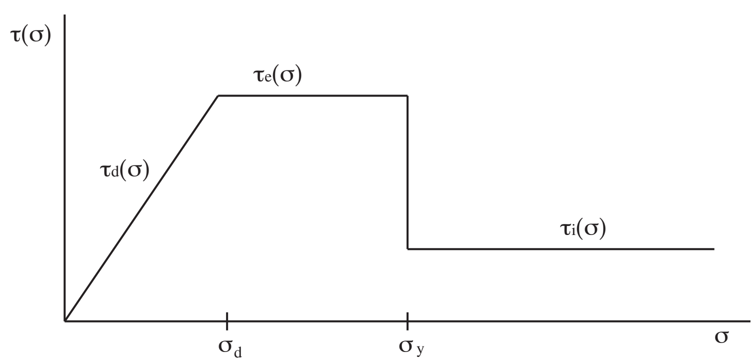

Fig. 3.13 Bond model illustration

figure, σ is the axial stress in the longitudinal reinforcement, $\tau_i(\sigma)$ is the bond stress above the yield stress of the reinforcement σ_y, $\tau_e(\sigma)$ is the bond stress above the bar stress that is needed to fully develop the bond (σ_d) but below the yield stress. $\tau_d(\sigma)$ is the bond stress for stress in the reinforcement below the development stress. For this model, the elastic and inelastic bond stresses were assumed to be constant with stress, while the development bond stress was assumed to be linearly related to the stress in the reinforcement. The components of the model are described in Equation 3.5,

$$\tau(\sigma) = \begin{cases} \tau_e \dfrac{\sigma}{\sigma_d} = a \dfrac{\sigma}{\sigma_d} \sqrt{f_c'} & \sigma \leq \sigma_d \\ \tau_e = \lambda_e \sqrt{f_c'} & \sigma_d \leq \sigma \leq \sigma_y \\ \tau_i = \lambda_i \sqrt{f_c'} & \sigma_y \leq \sigma \end{cases} \tag{3.5}$$

where λ_e and λ_i are the elastic and inelastic bond-stress coefficients respectively. Using the bond stress defined in Eq. 3.5, the change in strain (change in stress) along the length of the reinforcement is described by the differential equation, Equation. 3.6.

$$\begin{aligned} \frac{dF}{dx} &= \frac{\pi d_b^2}{4} \frac{d\sigma}{dx} = \tau(\sigma) \pi d_b \\ \frac{d\sigma}{dx} &= \frac{4\tau(\sigma)}{d_b} \end{aligned} \tag{3.6}$$

By integrating the strains along the development length, the tensile stress-displacement envelope of an anchorage bar can be calculated for a column. The stress-displacement envelope for a typical column is shown in Figure 3.14. For this study, the nonlinear stress-displacement relationships calculated with this method were simplified by assuming a linear relationship from $\sigma = 0$ to $\sigma = f_y$ and a second linear relationship between f_y and f_u as seen in the figure.

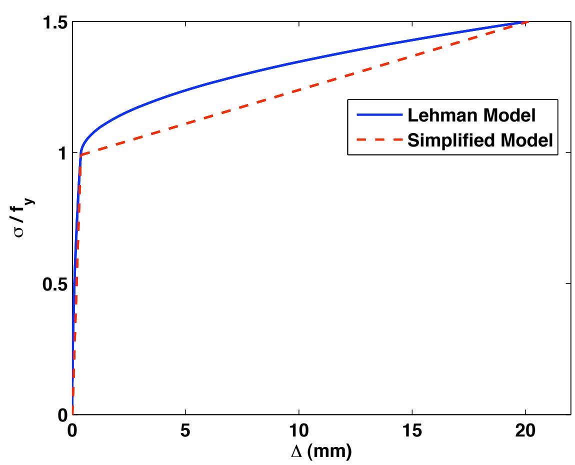

Fig. 3.14 Stress-displacement envelope for typical anchor bar

The three parameters of the bond model (σ_d, λ_e, and λ_i) are calibrated by comparing the strains measured in the columns at the anchorage-column interface with the strains measured 8 inches within the anchorage in Section 4.3.

3.2.2 Compressive Stress-Displacement Relationships

The compressive stress-displacement relationship of the concrete was calculated from the stress-strain relationship by assuming an effective depth over which the compressive strains act (d_{comp}), and multiplying the strains by this assumed depth to obtain a displacement. The assumed depth is illustrated in Figure 4.11.

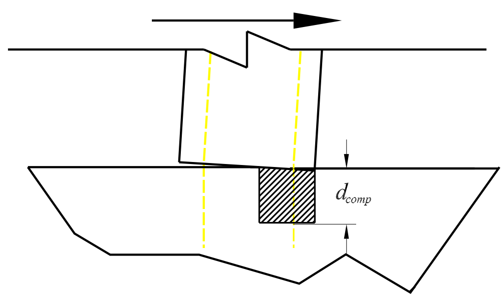

Fig. 3.15 Assumed compressive depth

3.2.3 Calibration Parameters

Because of the complexity of bond slip, the proposed bond slip model needs to be calibrated with experimental results. The key model parameters that need to be calibrated are the bond-strength ratios λ_e and λ_i, and the depth of the compressive strains d_{comp}. These parameters are calibrated in Chapter 4.

3.3 SHEAR-DISPLACEMENT MODEL

The shear component (Δ_v) of the total deflection of the column was modeled in accordance with elastic theory:

$$\Delta_v = \frac{k \cdot V \cdot L}{G \cdot A_G} \tag{3.7}$$

where k is a shape factor to account for the shape of the cross section ($k = \frac{4}{3}$ for circular sections), V is the transverse shear force, and A_G is the gross cross-sectional area. G is the modulus of rigidity of the concrete and can be estimated as the concrete modulus of elasticity multiplied by a scalar, $G = \gamma E_c$, where E_c can be calculated as $E_c = 4730\sqrt{f_c'}$, (ACI 318 2002). Park and Paulay (1975) recommend a value of $\gamma = 0.4$ (MPa).

3.4 OPENSEES IMPLEMENTATION

The MATLAB implementation of the force-based beam-column element was developed for monotonic loading. Since both the monotonic and cyclic behavior of a column are important in seismic regions, OpenSees (which is capable of modeling cyclic loading) was used to implement the proposed distributed-plasticity modeling strategy for the remainder of this report. This section discusses the implementation of the three major components of column deformation into OpenSees.

3.4.1 Flexural Component

The force-based beam-column element in OpenSees was implemented using the *nonlinearBeam-Column* command. The OpenSees implementation was verified by comparing the calculated force-deformation responses from OpenSees with the calculated force-deformation responses from the MATLAB implementation for 8 columns (Lehman and Moehle 2000) (Figure 3.16). As seen in the figure, the force-deformation envelopes calculated with OpenSees are indistinguishable with the force-deformation envelopes calculated with the stand-alone MATLAB implementation.

3.4.2 Bond Slip Deformation

The bond slip deformation model described in Section 3.2 was implemented in OpenSees using a zero-length section (*zeroLengthSection*) placed at the base of the column. The zero-length section consisted of a fiber section (Section 2.1) in which the stress-deformation response of the steel was determined in accordance with Section 3.2.1, and the compressive stress-displacement response of the concrete was determined in accordance with Section 3.2.2. The stress-displacement response of the steel was modeled with *steel02* material model in OpenSees, and the stress-displacement response of the concrete was modeled with *concrete04*.

3.4.3 Shear Deformation

The shear-deformation model was implemented in OpenSees by aggregating lateral force-deformation sections into the fiber sections of the beam-column element, as seen in Figure 3.1. The properties of the lateral force-deformation response were determined in accordance with elastic theory, as described in Section 3.3.

3.4.4 Calculation of Average Strains

The calculated average tensile strain values at two levels of column height are used in the calibration of the proposed modeling strategy (Section 4.4). Specifically, the measured and calculated average tensile steel strains are compared from the base of the column to a quarter of the column depth (0-D/4) and a quarter of the column depth to the total column depth (D/4-D/2). In a fiber beam-column element, the stresses and strains of any fiber in a section can be recorded. However, the sections are only located at integration points, and the location of the integration points are determined from the Gauss-Labotto integration scheme. In order to obtain the average strains from 0-D/4 and D/4-D/2, zero-weight integration points were added to the elements at D/4 and D/2. The added integration points do not affect the results of the analyses, but provide a means of recording section and fiber behavior at their locations. The average flexural tensile steel strain values from 0-D/4 were obtained by averaging the strain values recorded at the base of the column and at D/4. The average strain values were obtained for the D/4-D/2 segment in a similar manner.

The measured average strains from 0-D/4 also include the strains associated with bond slip of the anchorage reinforcement. In order to compare these strain values with calculated strain values, a calculated bond slip component was included in the calculated strains. The calculated vertical displacement of the anchorage steel was recorded from the zero-length bond slip section (Section 3.2). This vertical displacement was then divided by the length D/4 to obtain an average strain, and then added onto the calculated flexural steel strain.

3.5 SUMMARY

In the proposed modeling strategy, a nonlinear force-based fiber beam-column element, a zero-length bond section, and an aggregated elastic shear section are combined to model the flexural, bond slip, and shear components of the total tip deflection of a column. The following key modeling parameters were identified:

Number of Integration Points (N_p). The number of integration points used in the flexibility-based, fiber beam- column element.

Bond-Strength Ratios (λ_e and λ_i). The ratio of bond strength to the square root of the compressive strength of the concrete, $\lambda_e = \frac{\tau_{be}}{\sqrt{f'_c}}$ and $\lambda_i = \frac{\tau_{bi}}{\sqrt{f'_c}}$.

Development Bar Stress (σ_d). The bar stress required to fully develop the bond.

Bond-Model Compression Depth (d_{comp}). The effective depth of the compression strains for the concrete in the zero-length bond-slip element.

Shear-Stiffness Ratio (γ). The ratio of the modulus of rigidity of the concrete to the modulus of elasticity of the concrete, $\gamma = \frac{G}{E_c}$.

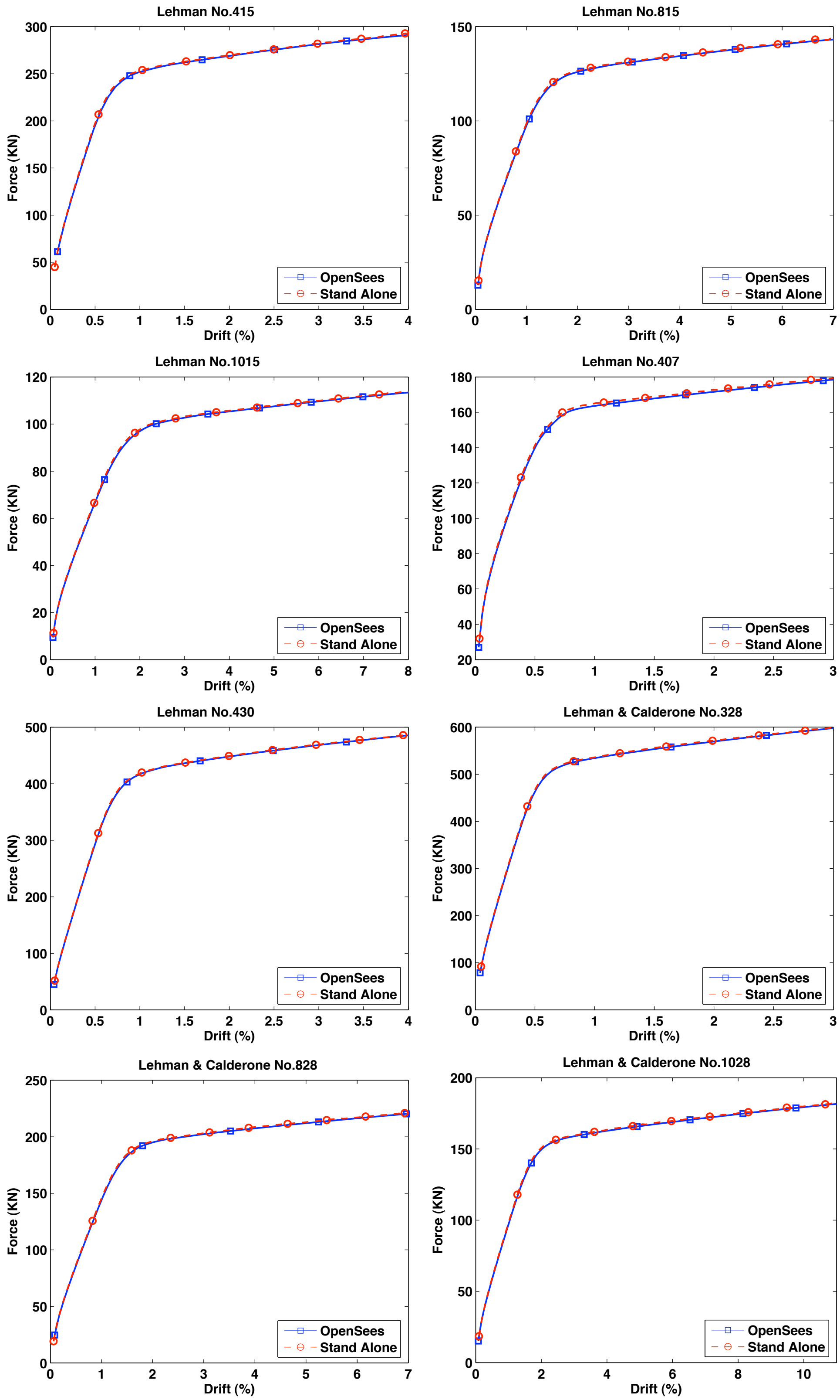

Fig. 3.16 Comparison of calculated f-Δ envelopes

4 Calibration of Distributed-Plasticity Column Model

To accurately model reinforced concrete column behavior, the distributed-plasticity modeling strategy proposed in Chapter 3 was calibrated with experimental results. The modeling parameters identified for calibration in chapters 2 and 3 are:

Strain-Hardening Ratio (b). The ratio of post-yield stiffness of the reinforcing steel to the modulus of elasticity of the steel, $b = \frac{E_{sh}}{E}$ (Section 2.2.1).

Bond-Strength Ratios (λ_e and λ_i). The ratio of bond strength to the square root of the compressive strength of the concrete, $\lambda_e = \frac{\tau_{be}}{\sqrt{f'_c}}$ and $\lambda_i = \frac{\tau_{bi}}{\sqrt{f'_c}}$.

Development Bar Stress (σ_d). The bar stress required to fully develop the bond.

Number of Integration Points (N_p). The number of integration points used in the flexibility-based, fiber beam-column element (Section 3.1).

Bond-Model Compression Depth (d_{comp}). The effective depth of the compression strains for the concrete in the zero-length bond-slip element (Section 3.2).

Shear-Stiffness Ratio (γ). The ratio of the modulus of rigidity of the concrete to the modulus of elasticity of the concrete, $\gamma = \frac{G}{E_c}$ (Section 3.3).

This chapter discusses the calibration strategy used in this report and presents the results of this analysis. The results of a sensitivity analysis are then presented to identify the effects of varying key parameters.

4.1 COLUMN DATA

A subset of eight columns from the bridge column dataset designated in Section 1.3 was used to calibrate the distributed-plasticity column-modeling strategy. The eight columns were the experiments documented in Lehman and Moehle (2000), and are included in Table 1.1. These columns were selected because they met Caltrans/AASHTO detailing requirements and the following data were available.

- Force-displacement histories
- Strain-gage histories
- Relative-rotation histories (average curvature)
- Observations of damage

This data were not available for all columns in the database, specifically the strain-gage data and average rotations.

Because estimating both global and local deformations are important, the force-displacement envelopes and the average strains in the tensile reinforcement were used in the calibration of the distributed-plasticity model. The force-displacement envelopes and average strain-displacement envelopes were extracted from the recorded digital force-displacement histories of the column with the algorithm described in Parish (2001). The average strains were calculated from the average rotations measured with the potentiometers as described in Appendix C of Lehman and Moehle (2000).

The average strains at two different levels of the column height were used in the calibration of the distributed-plasticity model, the average strains from the base of the column to one quarter of the column depth, $0-D/4$, and the strains from one quarter of the column depth to half the column depth, $D/4-D/2$. It should be noted that the average strains at the base of the column include deformations from bar slip since the potentiometers at the base of the column measure both the flexural displacement and the displacement due to bond slip of the anchorage reinforcement.

The average strains were used in this study instead of the strain gages, because potentiometers are able to accurately measure deformation at higher levels of deformation. The average strain measurements were verified with the strain gages attached to the reinforcement, and at low levels of deformation, the measurements were similar.

4.2 STEEL STRAIN-HARDENING RATIO CALIBRATION

The strain-hardening ratio was calibrated by minimizing the square root of the sum of the squares of the difference between the calculated response of the steel under monotonic loading to the measured response from coupon tests up to a strain of 0.1. The measured stress-strain response used for this calibration was the average response of the coupon tests performed by Lehman and Moehle (2000). A value of $b = 0.0097$ minimized the normalized error with a value of 3.91%. However, for simplicity, $b = 0.01$ was selected as the optimal value, (normalized error = 3.93%). The measured and calculated material responses are shown in Figure 4.1.

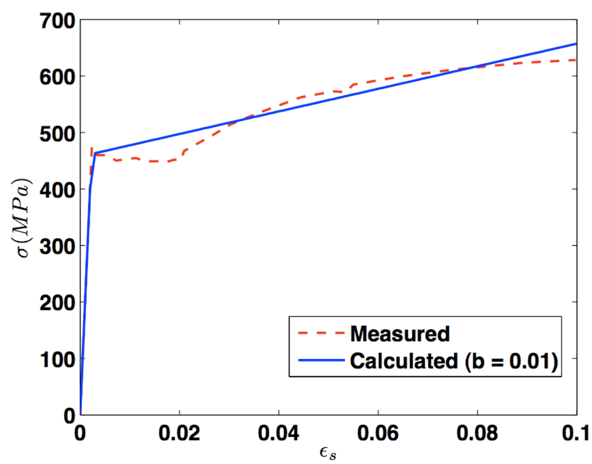

Fig. 4.1 Measured and calculated stress-strain response of steel

4.3 BOND-STRENGTH MODEL CALIBRATION

Three parameters of the bond model (σ_d, λ_e, and λ_i, defined in Figure 3.13) were calibrated by comparing the strains measured in the column tests at the anchorage-column interface with the strains measured six inches within the anchorage. Of the 16 possible strain-gage sets (north and south locations for the 8 columns), measurements from both of the strain gages were reliable up to an interface strain of 0.015 for 8 sets. The envelopes of the interface gage strains versus the anchorage gage strains for the 8 strain-gage sets are shown in Figure 4.2.

The best fit of the envelopes from the 8 strain-gage sets shown in Figure 4.2 was realized using elastic and inelastic bond-stress coefficients of $\lambda_e = 0.9$ and $\lambda_i = 0.45$, and a development stress of $\sigma_d = 0.25\sigma_y$. These values would vary if the steel were modified from the bilinear approximation, b = 0.01.

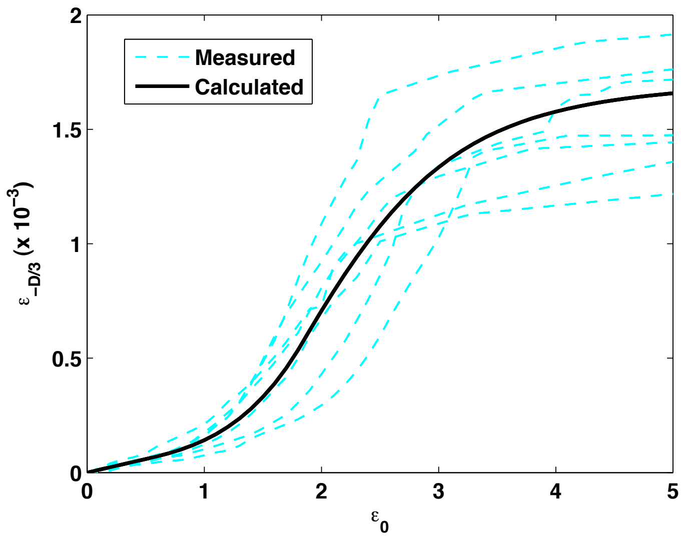

Fig. 4.2 Bond-strength calibration

4.4 OPTIMIZATION STRATEGY FOR REMAINING MODEL PARAMETERS

4.4.1 Measures of Accuracy

In order to successfully predict the response of a column under seismic loading (including damage prediction) both the global force-deformation response, and the local curvatures and strains must be predicted accurately. The calibration of the proposed modeling strategy considered the accuracy of both the global and local responses. The parameters used in this chapter to measure the accuracy of the modeling strategy are as follows.

Pushover Error (E_{push}). The accuracy of the force-displacement envelope was accounted for with the pushover error, which is defined as

$$E_{push} = \sqrt{\frac{\sum_{i=1}^{n}\left(F^i_{meas} - F^i_{calc}\right)^2}{\left(\max\left(F_{meas}\right)\right)^2 n}} \tag{4.1}$$

where F_{meas} and F_{calc} are the measured and calculated forces at corresponding displacements up to a drift ratio of 4%, and n is the number of datapoints in the envelope ($n = 100$ for this study).

Strain Error (E_{strain}). The accuracy of the models ability to predict average strains was accounted for with the strain error, which is defined as

$$E_{strain} = \sqrt{\frac{\sum_{i=1}^{n}\left(\varepsilon_{meas}^{i} - \varepsilon_{calc}^{i}\right)^2}{\left(\max\left(\varepsilon_{meas}\right)\right)^2 n}} \tag{4.2}$$

where ε_{meas} and ε_{calc} are the measured and calculated average strains at corresponding displacements up to a drift ratio of 4%. The strain error was accounted for at two ranges of column height, from the base of the column to a quarter of the column depth $\left(E_{strain}^{(0-D/4)}\right)$ and from a quarter of the column depth to half the column depth $\left(E_{strain}^{(D/4-D/2)}\right)$. The method used to calculate the average strains over the two heights is described in Section 3.4.4.

Stiffness Ratio (S.R.) is the ratio of measured stiffness to calculated stiffness $\frac{K_{meas}}{K_{calc}}$, where $K_{meas} = \frac{F_y}{\Delta_y^{meas}}$ and $K_{calc} = \frac{F_y}{\Delta_y^{calc}}$. F_y is the smaller of the calculated lateral force at first yield of the tensile reinforcement, and the lateral, effective force calculated at a concrete strain of 0.002. Δ_y^{meas} and Δ_y^{calc} are the measured and calculated displacements associated with F_y.

Moment Ratio (M.R) is the ratio of the maximum measured moment at or before 4% drift to the calculated moment at or before 4% drift, $\frac{M_{max}^{meas}}{M_{max}^{calc}}$.

Degradation Error Ratio (D.R.) is a parameter that captures the effectiveness of the model in predicting column degradation.

$$D.R. = \left(\frac{\left(F_{calc}^{4\%} - F_{calc}^{3\%}\right)}{F_{calc}^{3\%}} - \frac{\left(F_{meas}^{4\%} - F_{meas}^{3\%}\right)}{F_{meas}^{3\%}}\right) * 100 \tag{4.3}$$

A degradation error ratio close to zero means that the model accurately models degradation.

4.4.2 Optimization Procedure

The MATLAB function, *fmincon*, was originally used to perform the constrained nonlinear optimization. The function *fmincon* finds the constrained minimum of a scalar function of several variables starting at an initial estimate by using the Sequential Quadratic Programming (SQP) method (MATLAB 2000). However, this method was abandoned because the presence of multiple local minimums hindered the methods ability to obtain the global minimum.

The optimization was performed by running a pushover analysis for a broad range of modeling parameters and then selecting the scheme in which the mean total error (E_{total}, Equation 4.4) was minimized and the additional modeling accuracy terms (e.g., stiffness ratio) were reasonable. The range of values used for each calibration parameter are shown in Table 4.1, along with the step size between consecutive values within the range. The analysis consisted of every combination of the optimization parameters. Where c is equal to the column's neutral axis depth at a maximum

Table 4.1 Calibration parameter ranges for initial run

parameter	N_p	d_{comp}	γ
min	4	0.1 c	0.10
max	7	2.0 c	0.80
step size	1	0.1 c	0.10

compressive strain of 0.002 (c). In addition to the parameter values indicated in the table, the model without shear deformation was also considered in the optimization (i.e., $\gamma = \infty$).

The objective function for the optimization was a combination of the average pushover error and average strain errors at the two ranges of the column height. The total error, E_{total}, is defined as

$$E_{total} = \frac{1}{2}\text{mean}\left(E_{push}\right) + \frac{\kappa_1}{4}\text{mean}\left(E_{strain}^{(0-D/4)}\right) + \frac{\alpha_2}{4}\text{mean}\left(E_{strain}^{(D/4-D/2)}\right) \tag{4.4}$$

where:

$$\kappa_1 = \frac{\min\left(\text{mean}\left(E_{push}\right)\right)}{\min\left(\text{mean}\left(E_{strain}^{(0-D/4)}\right)\right)} \tag{4.5}$$

$$\kappa_2 = \frac{\min\left(\text{mean}\left(E_{push}\right)\right)}{\min\left(\text{mean}\left(E_{strain}^{(D/4-D/2)}\right)\right)} \tag{4.6}$$

where *mean* entails the average value over the eight Lehman and Moehle (2000) columns, and *min* entails the minimum value out of the total number of combinations. The α terms are included to ensure that the error terms are of similar magnitude.

4.5 OPTIMIZATION RESULTS

The optimization study described in the previous section was performed for the eight columns described by Lehman and Moehle (2000). The top 20 combinations from the optimization study are reported in Table 4.2. The accuracy measures reported in this table (e.g., E_{total} and S.R.) are average values for the eight columns.

Table 4.2 Distributed-plasticity optimization results

	Parameter Values			Measures of Accuracy						
Rank	Np	d_{comp}	γ	E_{total}	E_{push}	$E_{strain}^{0-D/4}$	$E_{strain}^{D/4-D/2}$	S.R.	M.R.	D.R
1	6	0.8 c	0.1	7.02	6.62	6.83	16.94	0.91	1.03	0.87
2	6	0.7 c	0.1	7.02	6.60	6.95	16.77	0.90	1.03	0.86
3	6	1 c	0.1	7.03	6.63	6.78	17.07	0.92	1.03	0.92
4	6	0.9 c	0.1	7.04	6.63	6.82	17.06	0.91	1.03	0.90
5	6	1.1 c	0.1	7.05	6.65	6.70	17.32	0.92	1.04	0.94
6	6	1.2 c	0.1	7.05	6.65	6.59	17.58	0.93	1.04	0.93
7	6	0.6 c	0.1	7.06	6.62	7.15	16.51	0.89	1.03	0.78
8	6	1.3 c	0.1	7.07	6.67	6.50	17.87	0.93	1.04	1.02
9	6	1.4 c	0.1	7.07	6.67	6.47	17.98	0.94	1.04	1.06
10	6	1.6 c	0.1	7.08	6.69	6.43	18.08	0.94	1.04	1.10
11	6	1.5 c	0.1	7.08	6.68	6.45	18.07	0.94	1.04	1.11
12	6	0.9 c	0.2	7.11	6.72	6.97	16.94	0.89	1.03	0.91
13	6	0.9 c	0.3	7.11	6.72	6.97	16.94	0.89	1.03	0.91
14	6	0.9 c	0.5	7.11	6.72	6.97	16.94	0.89	1.03	0.91
15	6	0.9 c	0.6	7.11	6.72	6.97	16.94	0.89	1.03	0.91
16	6	0.9 c	0.7	7.11	6.72	6.97	16.94	0.89	1.03	0.91
17	6	1.7 c	0.1	7.11	6.70	6.43	18.33	0.95	1.04	1.12
18	6	1.1 c	0.2	7.12	6.75	6.80	17.29	0.90	1.03	0.94
19	6	1.1 c	0.3	7.12	6.75	6.80	17.29	0.90	1.03	0.94
20	6	1.1 c	0.5	7.12	6.75	6.80	17.29	0.90	1.03	0.94

It was difficult to objectively select an optimal solution from this analysis because many combinations of parameters resulted in nearly identical values of E_{total}. The proposed modeling strategy was not sensitive to several of the optimization parameters, and the optimization results were dominated by several combinations that differed only by those parameters. For example, the only parameter that differs between the top 11 ranked combinations is the bond penetration depth (d_{comp}).

The effect of N_p on the optimization surface can be observed by sorting the optimization results first by N_p and then by E_{total}, and then plotting the normalized error $\left(\frac{E_{total}}{E_{total}^{min}} - 1\right)$ versus the normalized rank order (i.e., the ranking divided by the total number of combinations) (Figure 4.3). The normalized error varied from 0 ($E_{total} = 7.02$) to 0.92 ($E_{total} = 13.46$). As seen in the figure, the best results are obtained for $N_p = 6$. Nonetheless, as long as five integration points are used, similar minimum values of E_{total} can be obtained. This result can be explained by noting

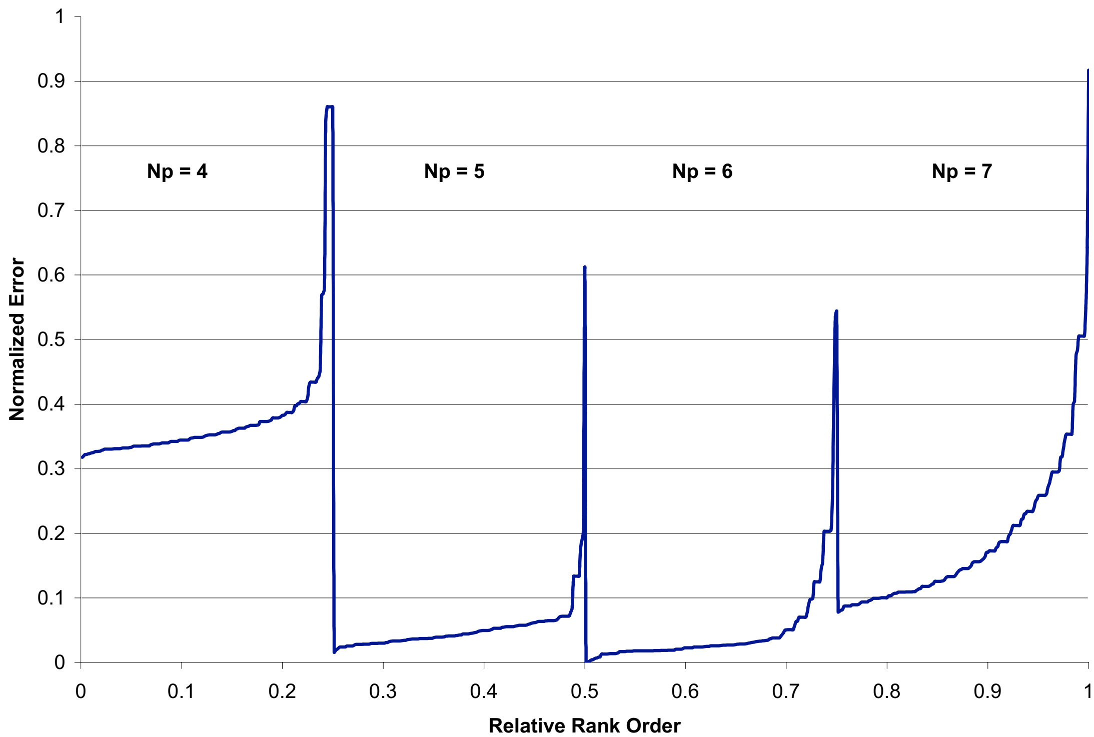

Fig. 4.3 Effect of n_p on optimization surface

that the columns being studied are well-confined columns with hardening section behavior. For such sections the number of integration points should not significantly affect the calculated global or local responses (Section 3.1.1). For modeling efficiency, the combinations with five integration points will be used to select the optimal solution.

Table 4.3 provides the top 20 combinations in which $N_p = 5$. As seen in the table, the combination that minimizes the total error ($E_{total} = 7.13$) is $d_{comp} = 0.4c$ and $\gamma = 0.1$. As seen in Table 4.3, γ does not significantly affect the accuracy of the model. The combination with $\gamma = 0.4$ (# 16, $d_{comp} = 0.5c$, $E_{total} = 7.21$) will be chosen as the optimal solution to remain consistent with previous research Park and Paulay (1975).

Table 4.3 Distributed-plasticity optimization results ($n_p = 5$, $\gamma = 0.4$ and $d_{comp} = c$)

	Parameter Values			Measures of Accuracy						
Rank	Np	d_{comp}	γ	E_{total}	E_{push}	$E_{strain}^{0-D/4}$	$E_{strain}^{D/4-D/2}$	S.R.	M.R.	D.R
1	5	0.4 c	0.1	7.13	6.85	6.57	17.52	0.87	1.04	0.35
2	5	0.5 c	0.1	7.15	6.83	6.52	17.87	0.88	1.04	0.42
3	5	0.3 c	0.1	7.16	6.91	6.78	17.02	0.86	1.04	0.31
4	5	0.6 c	0.1	7.17	6.82	6.49	18.22	0.89	1.04	0.44
5	5	0.4 c	0.2	7.19	6.96	6.62	17.37	0.85	1.04	0.36
6	5	0.4 c	0.3	7.19	6.96	6.62	17.37	0.85	1.04	0.36
7	5	0.4 c	0.5	7.19	6.96	6.62	17.37	0.85	1.04	0.36
8	5	0.4 c	0.6	7.19	6.96	6.62	17.37	0.85	1.04	0.36
9	5	0.4 c	0.7	7.19	6.96	6.62	17.37	0.85	1.04	0.36
10	5	0.5 c	0.2	7.20	6.96	6.52	17.73	0.86	1.04	0.40
11	5	0.5 c	0.3	7.20	6.96	6.52	17.73	0.86	1.04	0.40
12	5	0.5 c	0.5	7.20	6.96	6.52	17.73	0.86	1.04	0.40
13	5	0.5 c	0.6	7.20	6.96	6.52	17.73	0.86	1.04	0.40
14	5	0.5 c	0.7	7.20	6.96	6.52	17.73	0.86	1.04	0.40
15	5	0.7 c	0.1	7.20	6.84	6.46	18.47	0.90	1.04	0.48
16	5	0.5 c	0.4	7.21	7.02	6.51	17.61	0.85	1.04	0.38
17	5	0.6 c	0.2	7.21	6.94	6.44	18.14	0.87	1.04	0.43
18	5	0.6 c	0.3	7.21	6.94	6.44	18.14	0.87	1.04	0.43
19	5	0.6 c	0.5	7.21	6.94	6.44	18.14	0.87	1.04	0.43
20	5	0.6 c	0.6	7.21	6.94	6.44	18.14	0.87	1.04	0.43

The selected optimal solution is as follows.

Strain-Hardening Ratio, $b = 0.01$**.**

Bond-Strength Ratios, $\lambda_e = 0.9$ **and** $\lambda_i = 0.45$**.**

Development Bar Stress, $\sigma_d = 0.25\sigma_y$.

Number of Integration Points, $N_p = 5$**.**

Bond-Model Compression Depth, $d_{comp} = 0.5c$ (Half the N.A. Depth at $\varepsilon_c = 0.002$).

Shear-Stiffness Ratio, $\gamma = 0.4$**.**

This combination of parameters resulted in the following mean measures of accuracy: $E_{total} = 7.22$, $E_{push} = 7.02$, $E_{strain}^{(0-D/4)} = 6.51$, $E_{strain}^{(D/4-D/2)} = 17.73$, stiffness ratio = 0.85, moment ratio = 1.04 and degradation error ratio = 0.38. The corresponding coefficients of variation (%) for these measures were 20, 43, 44, 44, 11, 8, and -.

In a pilot study, a similar optimization was run without including the tensile strength of the concrete, and using the bond-strength ratios proposed by Lehman and Moehle (2000) ($\lambda_e = 1.0$, $\lambda_i = 0.5$). This optimization resulted in $d_{comp} = 1.0c$, $\gamma = 0.4$, and $N_p = 5$. This combination of parameters resulted in the following mean measures of accuracy: $E_{total} = 7.45$, $E_{push} = 6.73$, $E_{strain}^{(0-D/4)} = 7.78$, $E_{strain}^{(D/4-D/2)} = 14.40$, stiffness ratio = 1.02, moment ratio = 1.03, and degradation error ratio = 2.04.

4.6 MODEL EVALUATION

The selected optimal solution from the previous section will be evaluated in this section. First, the measured and calculated force-displacement envelopes are compared, and the various components of the total calculated deflection are studied. Then, the measured and calculated tensile steel strain-displacement envelopes are compared.

4.6.1 Force-Displacement Envelopes

The measured and calculated (using the optimal solution) force-displacement envelopes are shown in Figure 4.4. The proposed modeling strategy accurately predicts the stiffness ratio for all eight columns. However, the proposed modeling strategy overestimates the stiffness of all eight of the columns beyond 3% drift. It is difficult to observe trends in model accuracy with only these plots. Trends in the accuracy of the proposed modeling strategy is studied in greater detail later in this report.

The percentage of total deflection due to flexure, bond slip, and shear are plotted versus displacement ductility in Figure 4.5. As seen in Figure 4.5, the calculated shear component of total deflection is negligible, ranging from 2.5% to 0.3% of the total column deflection. Additionally, as expected, the component of total deflection due to bond slip decreases with increasing aspect ratio, and increases slightly with the level of column deformation.

4.6.2 Strain-Displacement Envelopes

The measured and average calculated strains for two ranges of column height are compared up to a displacement ductility ($\frac{\Delta}{\Delta_y}$) of 8 in Figure 4.6, and up to a displacement ductility of 3 in Figure 4.7. The vertical lines in figures 4.6 and 4.7 represent the ductility level at which the researchers reported the onset of cover spalling. As seen in the figures, the proposed modeling strategy accurately predicts the strains at low levels of column deformation, but is less accurate at higher levels. In general, shortly after the onset of spalling, the measured strain values at $D/4 - D/2$ increase rapidly and the measured strain values at $0 - D/4$ dip below the calculated values and begin approaching the strains at $D/4 - D/2$. This pattern, which was observed for 6 of the 8 columns, suggests that the discrepancies in measured and calculated strains at higher levels of column deformation may be due to the debonding of the longitudinal reinforcement up the height of the column.

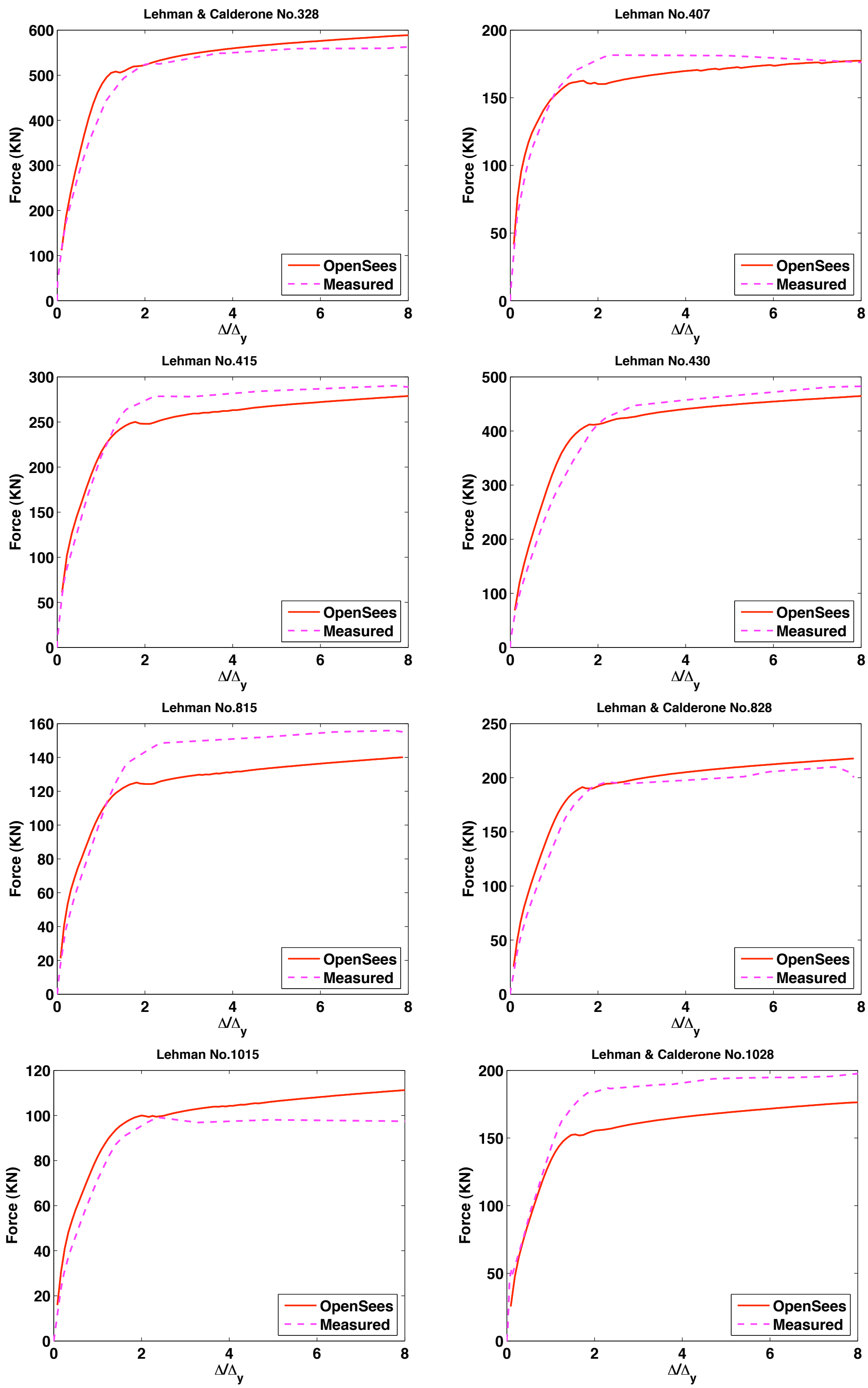

Fig. 4.4 Measured and calculated force-Δ envelopes

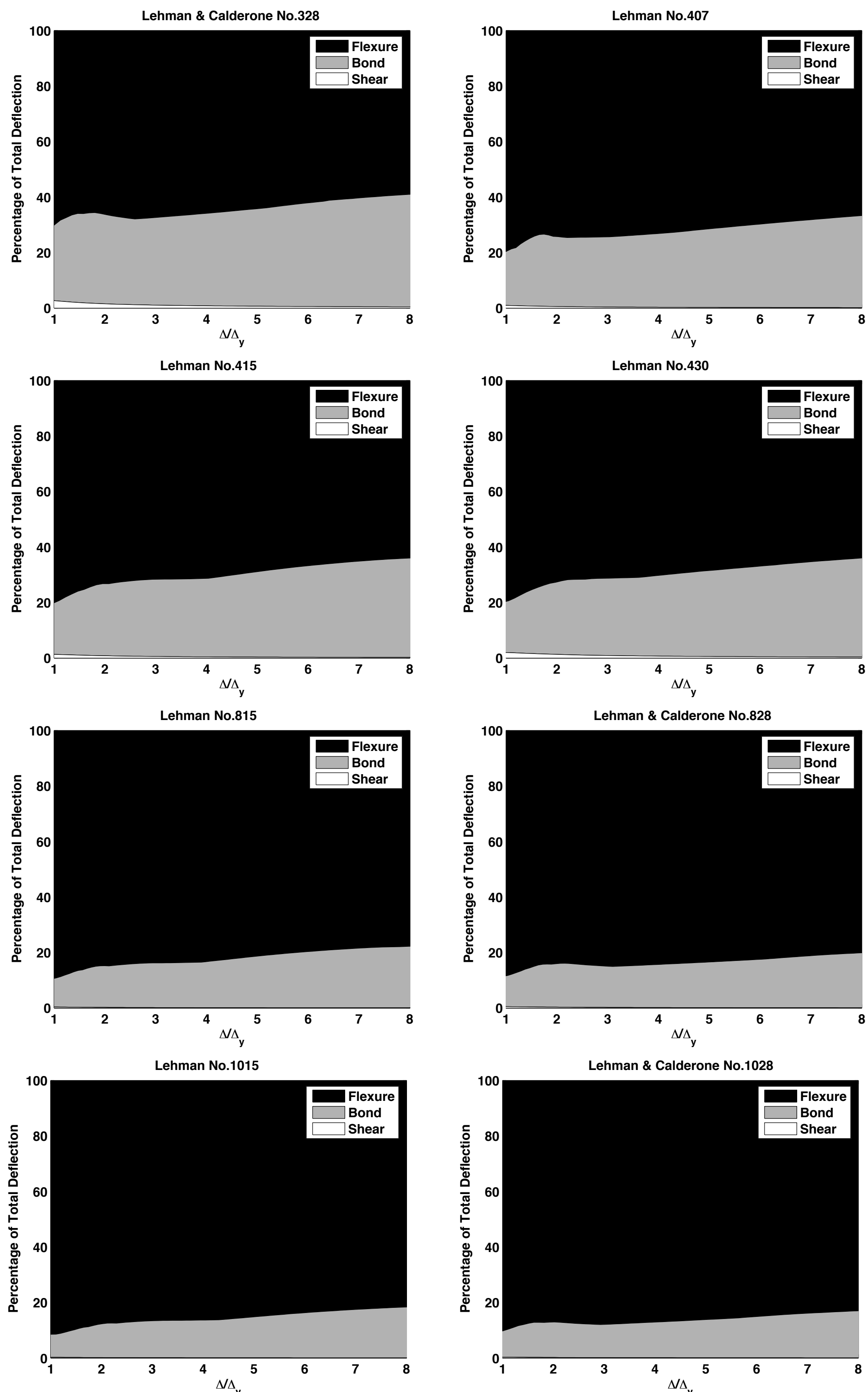

Fig. 4.5 Components of total deflection

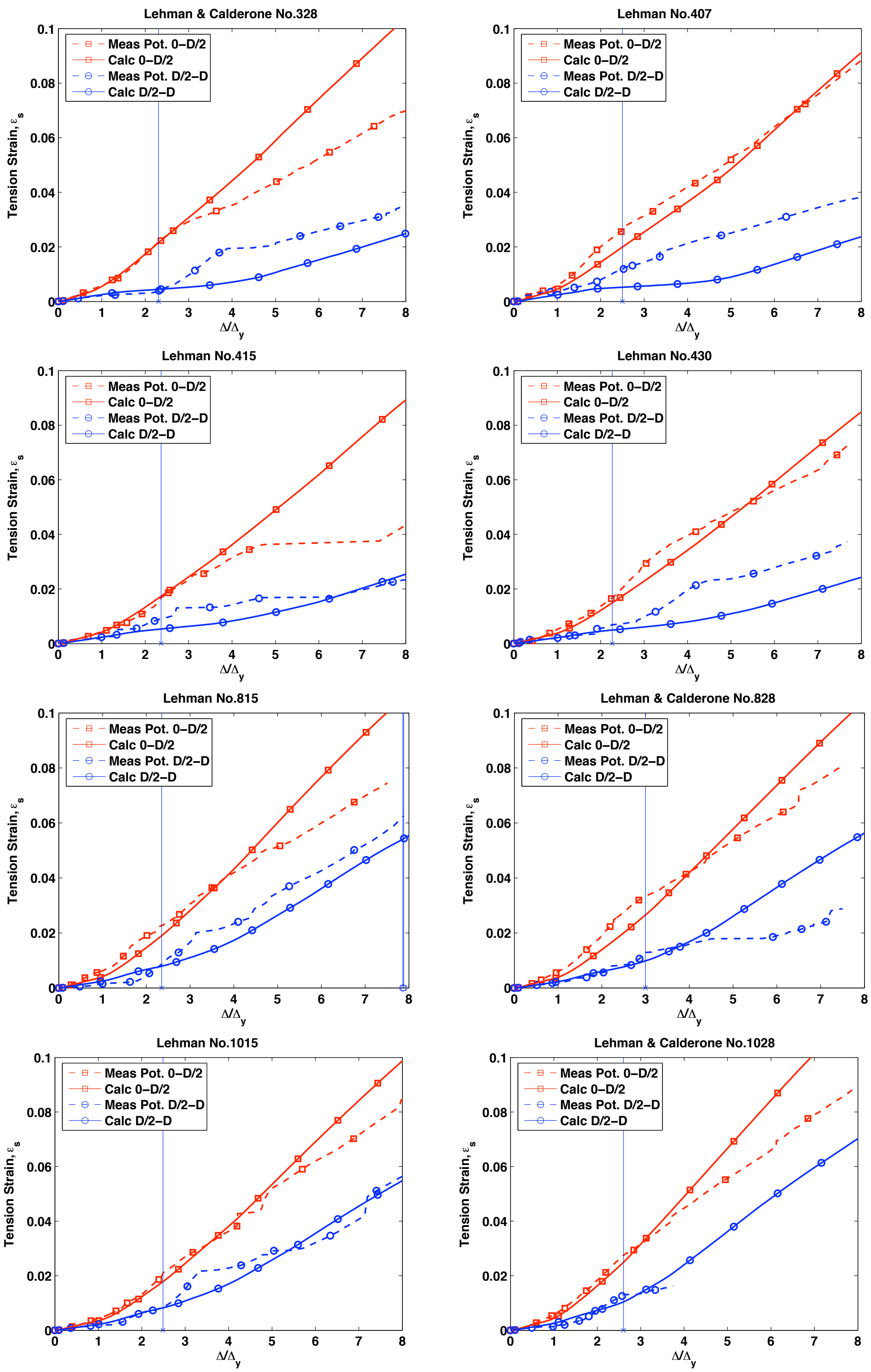

Fig. 4.6 Measured and calculated average strains (up to $\frac{\Delta}{\Delta_y} = 8$)

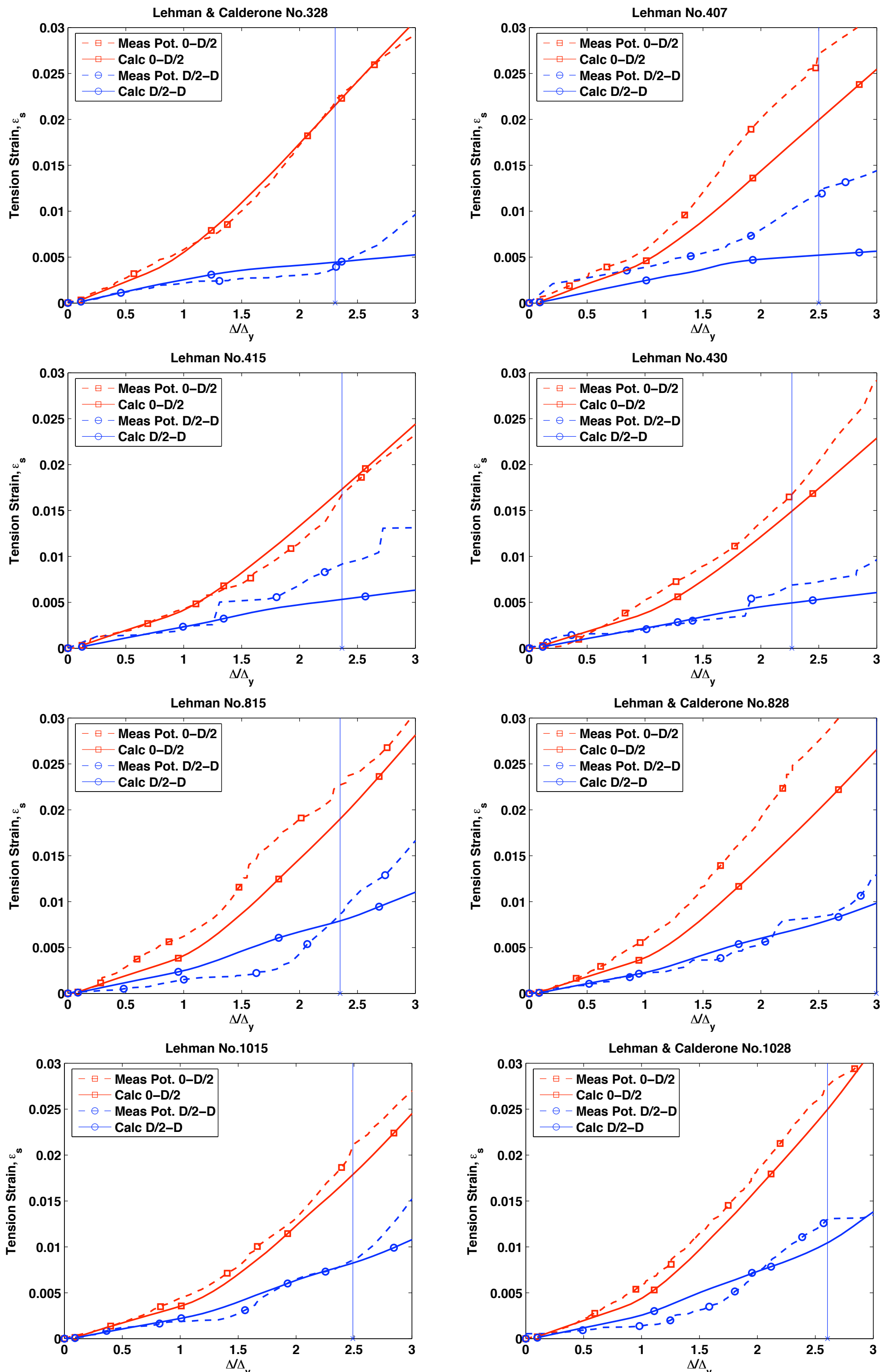

Fig. 4.7 Measured and calculated average strains (up to $\frac{\Delta}{\Delta_y} = 3$)

4.7 SENSITIVITY ANALYSES

A parametric study was performed to verify the results of the optimization analysis and to demonstrate the effect of the key modeling parameters on model accuracy. In this study, the measures of accuracy were plotted versus the five modeling parameters to demonstrate the effect of each parameter (figures 4.8 through 4.12). The optimal solution ($b = 0.01$, $N_p = 5$, $d_{comp} = c$, $\lambda = 1.0$, and $\gamma = 0.4$) was used as a basis, and each parameter was varied individually.

In Figure 4.8 the effect of the strain hardening ratio is studied by plotting the maximum, minimum, and mean values of E_{total}, $S.R.$, $M.R.$, and $D.R.$ versus the strain-hardening ratio (b). As seen in the figure, a b value near 1% minimizes the mean E_{total}. This result is consistent with the results of the previous section. As expected, increasing b does not affect the stiffness ratio, but decreases the $M.R.$ and increases the $D.R.$

Similarly, the effect of the number of integration points is shown in Figure 4.9. As seen here, slightly better values of E_{total}, $M.R.$, and $D.R$ can be obtained by using 6 or 7 integration points, but the increase in accuracy does not outweigh the loss of efficiency. As expected, the stiffness ratio is not affected by N_p.

The effect of the bond-strength ratio (λ) on pushover accuracy is shown in Figure 4.10. As expected, as λ increases, the stiffness ratios and moment ratios decrease and the degradation error ratios increase. A negligibly better value of E_{total} can be obtained by using $\lambda = 0.5$ than $\lambda = 1.0$; however, the stiffness ratio and moment ratio are better using $\lambda = 1.0$. The best moment ratio is obtained by using $\lambda = \infty$, which represents no bar slip.

The effect of the bond compression depth (d_{comp}) on pushover accuracy is shown in Figure 4.11. The stiffness ratios, moment ratios, and degradation error ratios increase as d_{comp} increases. The best E_{total} value was obtained for $d_{comp} = c$, but similar values were obtained for $d_{comp} = 0.1$ and 0.2.

Finally, the effect of the shear-deformation ratio (γ) is shown in Figure 4.12. As discussed earlier, the shear ratio influences the accuracy little.

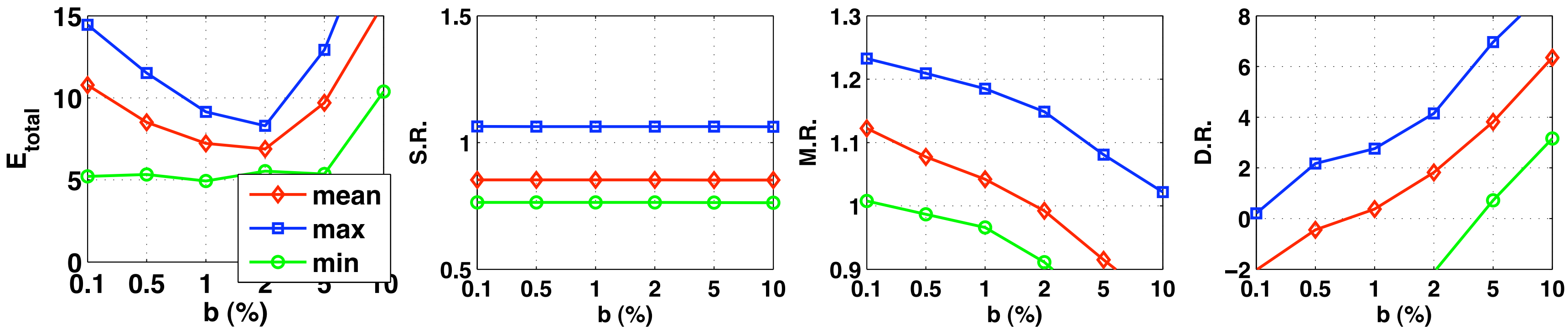

Fig. 4.8 Effect of varying strain-hardening ratio (b)

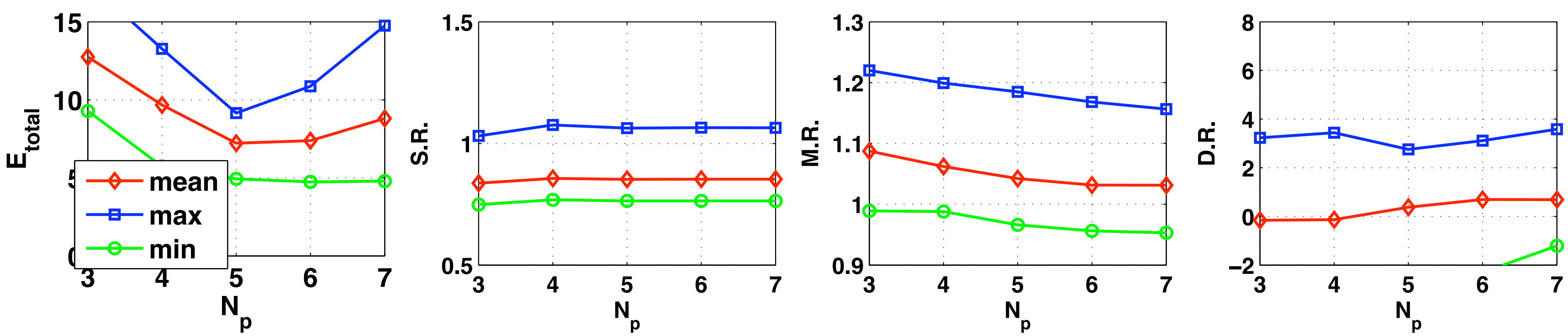

Fig. 4.9 Effect of varying number of integration points (n_p)

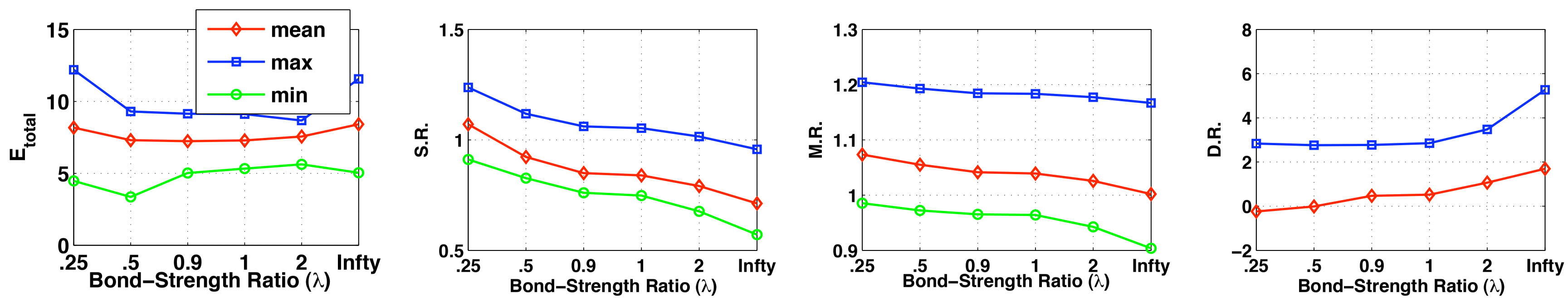

Fig. 4.10 Effect of varying bond-strength ratio (λ)

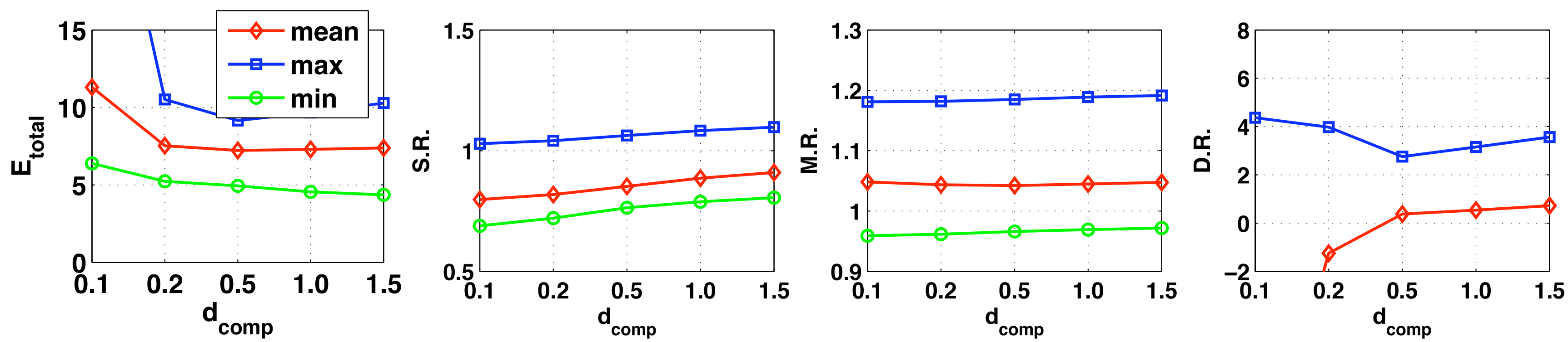

Fig. 4.11 Effect of varying bond compression depth (d_{comp})

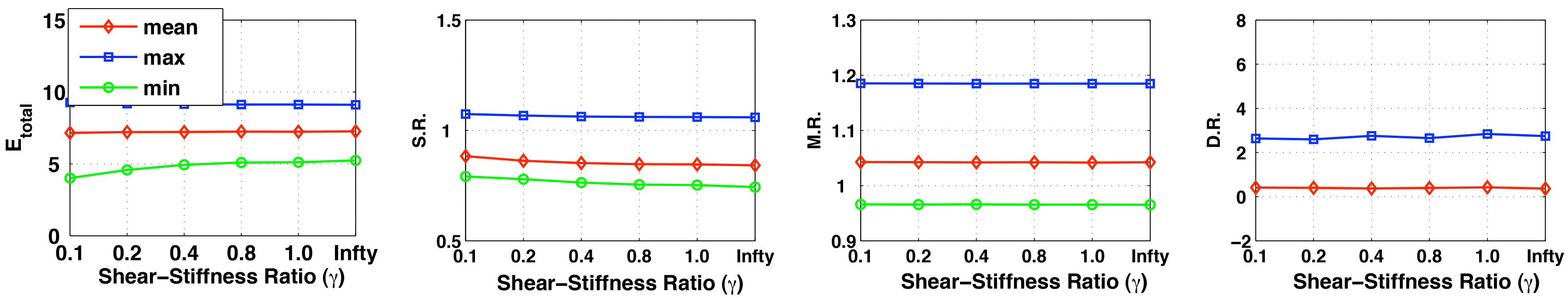

Fig. 4.12 Effect of varying shear-stiffness ratio (γ)

4.8 EVALUATION WITH DATABASE OF BRIDGE COLUMNS

The proposed modeling strategy was used to model the 37 bridge columns identified in Section 1.3. Key accuracy statistics of this evaluation are provided in Table 4.4. The mean value of the pushover error E_{push} was 7.4%. The mean values of the stiffness ratios ($S.R.$) and moment ratios ($M.R.$) were 0.85 and 1.03, with corresponding $c.o.v.$'s of 15.6% and 7.9%. The mean value of the degradation ratios ($D.R.$) was -0.51.

Table 4.4 Accuracy statistics for envelope response of distributed-plasticity model

Statistic	$E_{push}(\%)$	$S.R.$	$M.R.$	$D.R.$
Mean	7.4	0.84	1.03	-0.51
c.o.v. (%)	-	15.6	7.9	-

The measures of modeling accuracy are plotted versus key column properties to determine if the accuracy of the model is sensitive to these properties. In Figure 4.13, E_{push} is plotted versus, aspect ratio (L/D), longitudinal-reinforcement ratio (ρ_l), axial-load ratio (P/f'_cA_g), effective confinement ratio, concrete compressive strength, and the ratio of spiral spacing to longitudinal bar diameter (s/d_b). Included in the figure are the R^2 values, which indicate the magnitude of correlation between E_{push} and the property. As seen in the figure, there are no significant trends in the data.

Similarly, the stiffness ratio is plotted versus the key column properties in Figure 4.14. Slight trends can be observed in $S.R.$ versus L/D and f'_c, with R^2 values of 0.11 and 0.12.

The maximum moment ratio ($M.R.$) is plotted versus the key properties in Figure 4.15. As seen in the figure, only one trend can be observed. The moment ratio decreases with ab increase in effective confinement ratio.

The degradation ratio ($D.R.$) is plotted versus the key properties in Figure 4.16. There are no significant trends in the data.

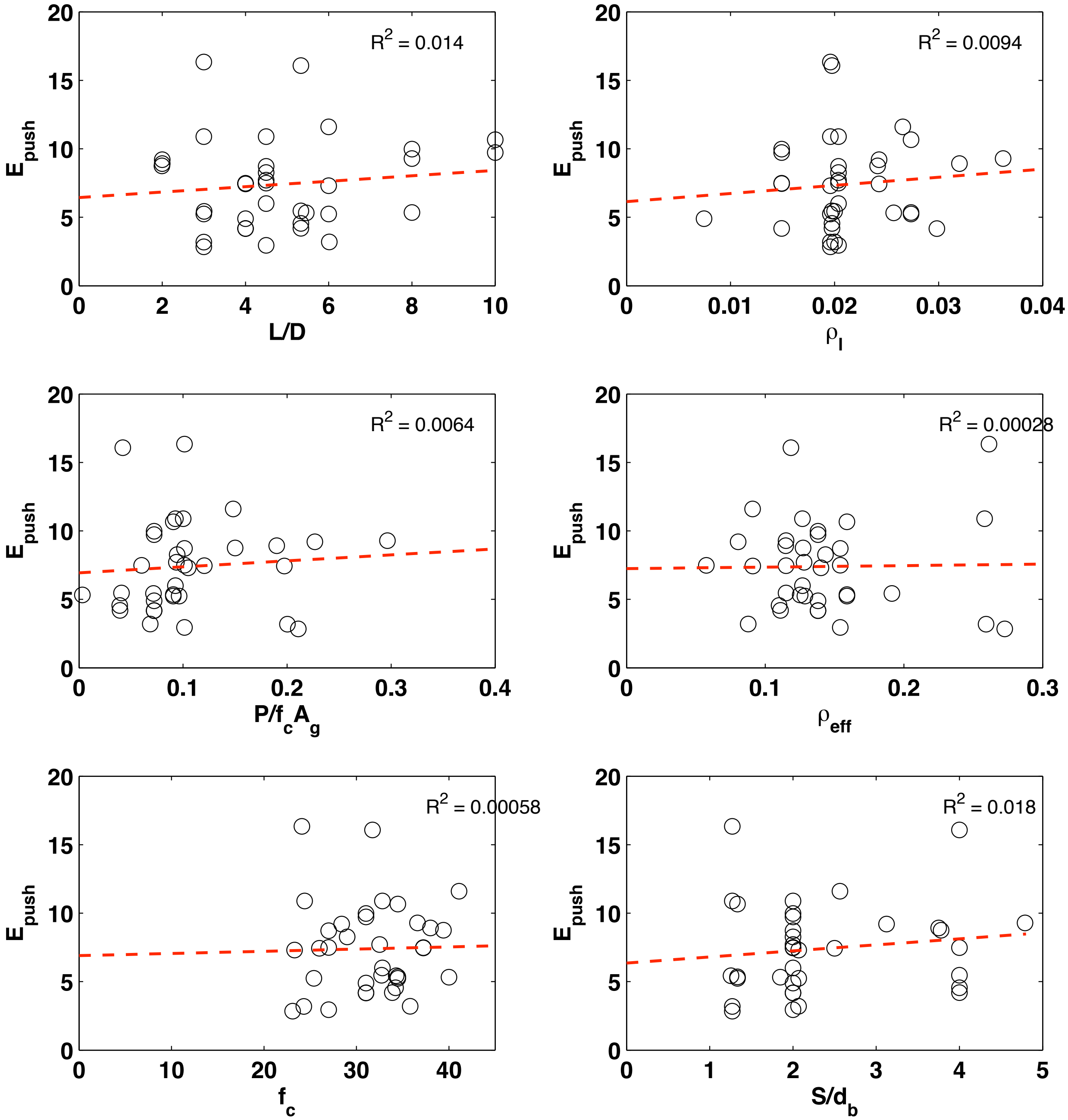

Fig. 4.13 Effect of key properties on pushover error

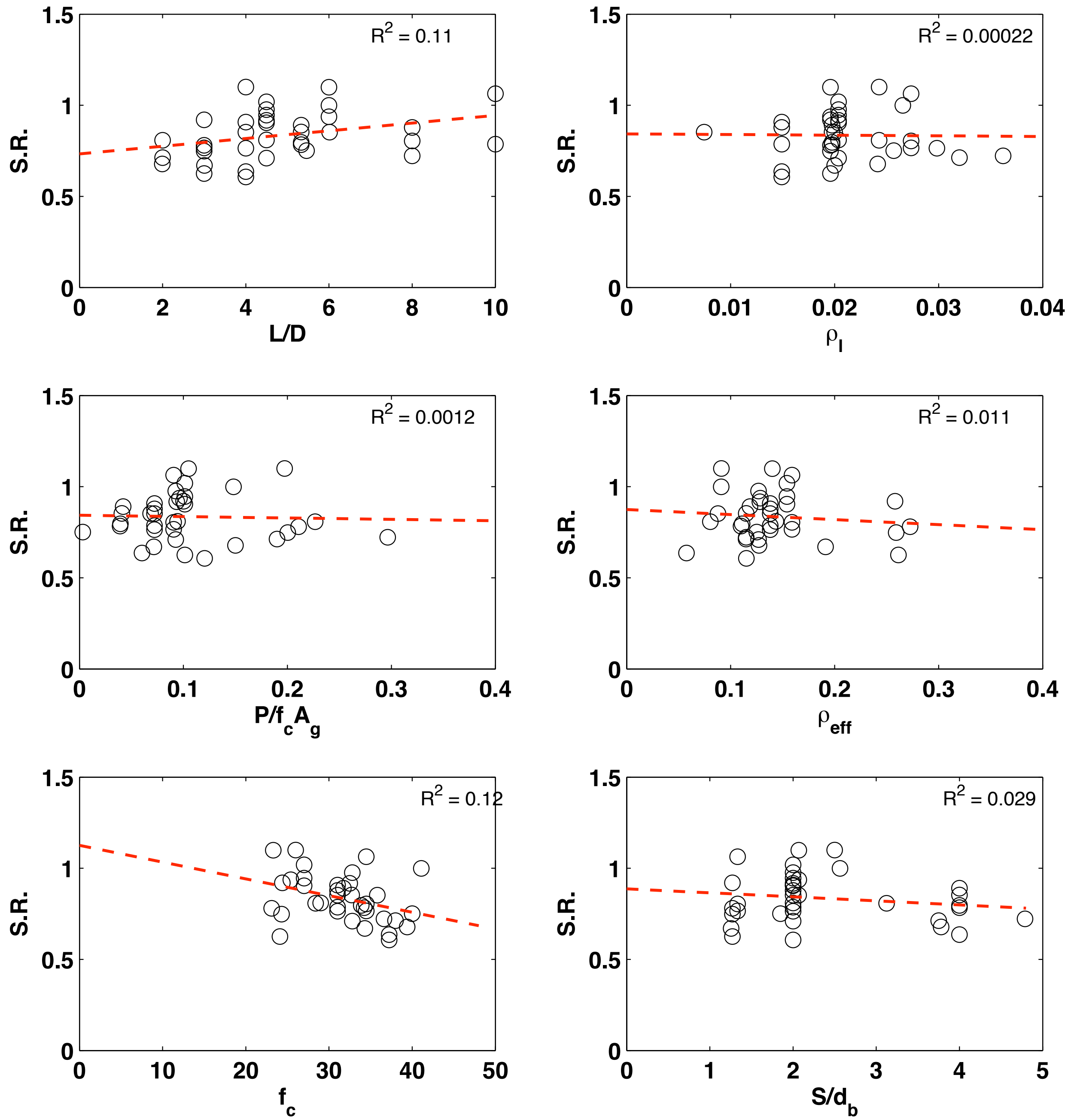

Fig. 4.14 Effect of key properties on stiffness ratio

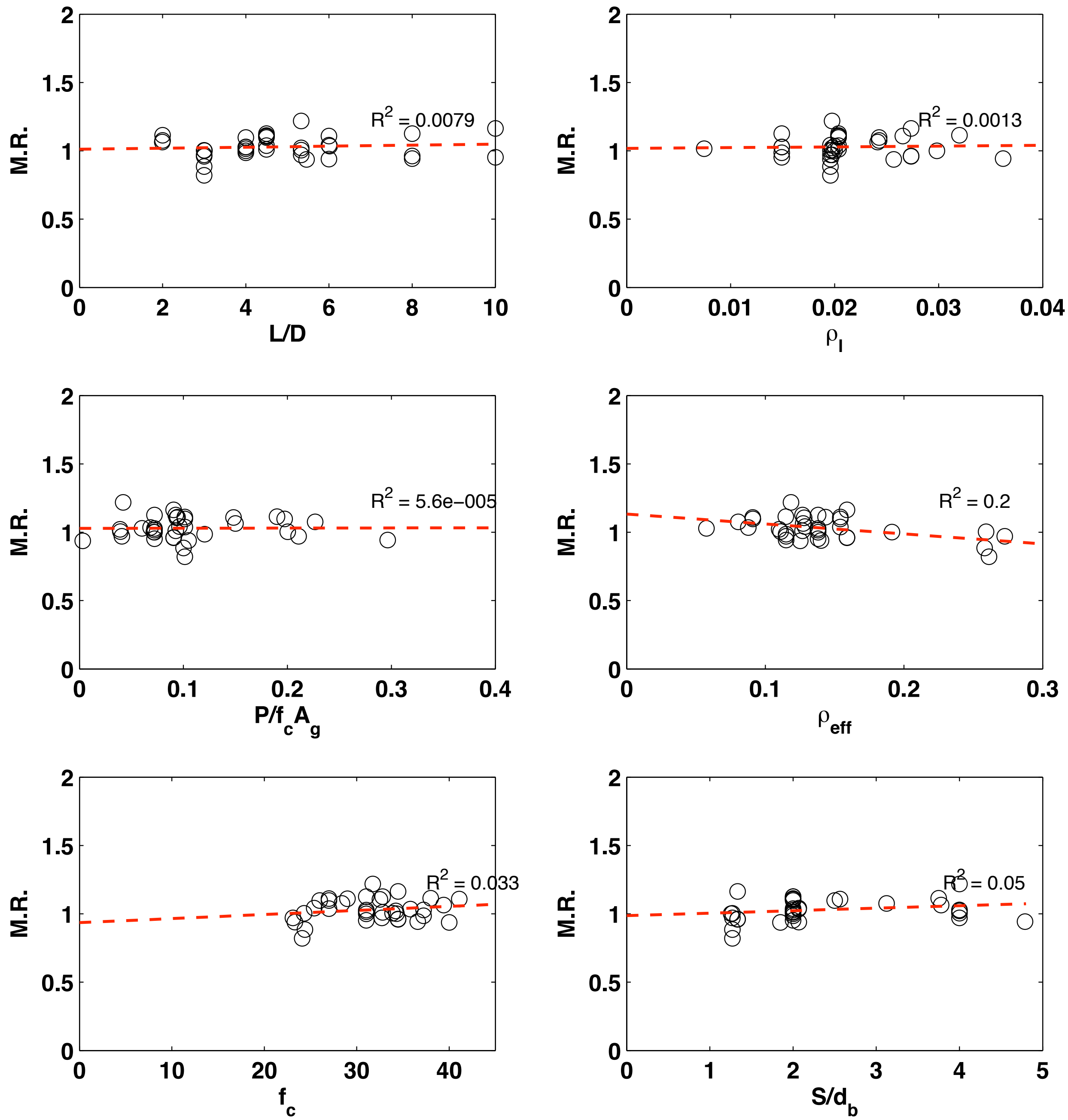

Fig. 4.15 Effect of key properties on moment ratio

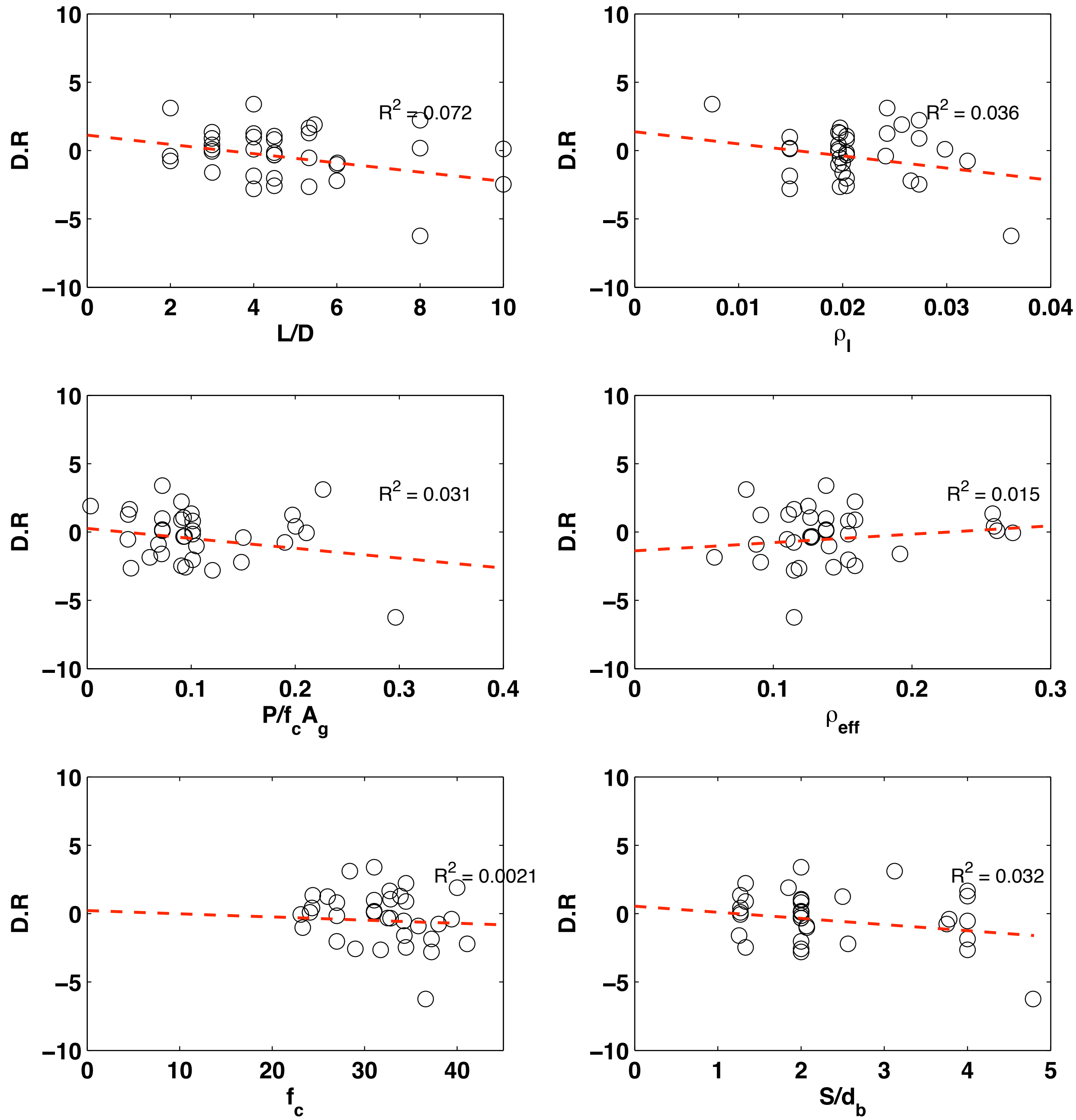

Fig. 4.16 Effect of key properties on degradation error ratio

4.9 SUMMARY

The measures of accuracy and optimization scheme utilized to calibrate the distributed-plasticity column model were presented in this chapter. The results of the optimization study were then presented and an optimal solution was selected. The optimal model parameters were as follows.

- Strain-Hardening Ratio, $b = 0.01$.
- Bond-Strength Ratios, $\lambda_e = 0.9$ and $\lambda_i = 0.45$.
- Development Bar Stress, $\sigma_d = 0.25\sigma_y$.
- Number of Integration Points, $N_p = 5$.
- Bond-Model Compression Depth, d_{comp} =1/2 neutral axis depth at $\varepsilon_c = 0.002$.
- Shear-Stiffness Ratio, $\gamma = 0.4$.

This combination of parameters resulted in the following mean measures of accuracy when applied to the dataset of 8 column tests by Lehman and Moehle (2000): $E_{total} = 7.22$, $E_{push} = 7.02$, $E_{strain}^{(0-D/4)} = 6.51$, $E_{strain}^{(D/4-D/2)} = 17.73$, stiffness ratio = 0.85, moment ratio = 1.04 and degradation error ratio = 0.38. The corresponding coefficients of variation for the stiffness ratio and moment ratio were 11% and 8%. When applied to the bridge dataset, the mean value of E_{push} was 7.4%. The mean values of the stiffness ratios and moment ratios were 0.85 and 1.03 with corresponding *c.o.v.*'s of 15.6% and 7.9%. The mean value of the degradation ratios (*D.R.*) was -0.51.

5 Development of Lumped-Plasticity Column Model

The spread-plasticity, force-based fiber beam-column element is susceptible to strain localization and loss of objectivity in degrading members (Section 3.1.1). A lumped-plasticity column-modeling strategy is developed to overcome this limitation, and to provide a less complex modeling strategy. In this chapter, a lumped-plasticity model formulation is presented, and key modeling parameters are identified for calibration.

5.1 MODEL FORMULATIONS

The widespread implementation of nonlinear analysis methods in software to support analysis and design has led to the development of a variety of plastic-hinge model formulations. In this chapter, two model formulations are presented, one that is commonly employed in design, and a more complicated formulation that can be implemented in a standard displacement-based finite element framework (e.g., OpenSees). Figure 5.1 shows a typical cantilever column subjected to a lateral load. The figure also shows the moment and actual curvature distributions, and the idealized curvature distributions that are the basis for the two lumped-plasticity models presented in this chapter.

The formulation of the plastic-hinge model employed in design uses the idealized distribution shown in Figure 5.1(d) to develop an expression for the post-yield displacement at the top of the column, Δ. The curvature is assumed to be linear above the plastic hinge, and the plastic curvature is assumed to be constant over the height of the plastic hinge. The resulting post-yield

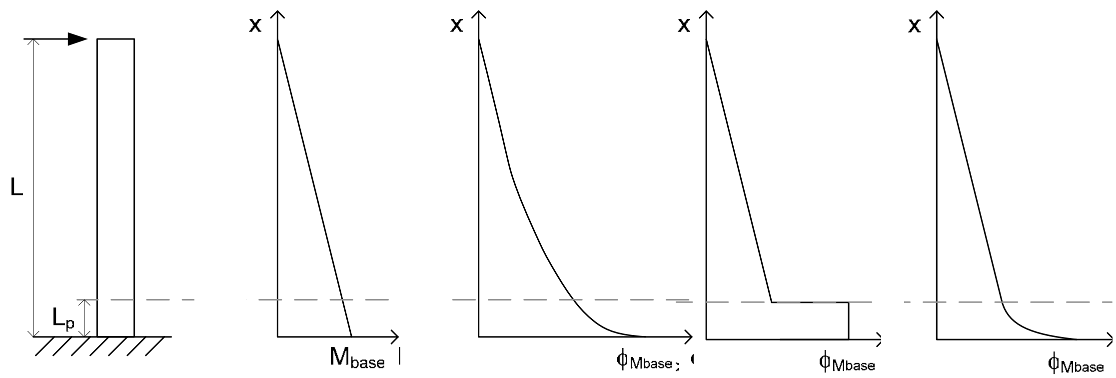

(a) Idealized Column

(b) Moment Distribution

(c) Actual Curvature Distribution

(d) Idealized Curvature Distribution for Formulation 1

(e) Idealized Curvature Distribution for Formulation 2

Fig. 5.1 Moment and curvature distributions

total displacement can be expressed as follows.

$$\Delta = \Delta_y + (\phi_{base} - \phi_y)\, L_p \left(L - \frac{L_p}{2}\right) \tag{5.1}$$

where: ϕ_y is the column curvature at first yield, ϕ_{base} is the curvature associated with the moment at the base of the column, L is the distance from the base of the column to the point of contraflexure, L_p is the plastic-hinge length, and Δ_y is the yield displacement of the column.

Scott and Fenves (2006) developed a lumped-plasticity formulation suitable for implementation in a standard displacement-based finite-element environment. The formulation utilizes the force-based fiber beam-column element formulation, and introduces a modified integration scheme in which inelastic deformations are confined to an assigned plastic-hinge length. This formulation, which is available in OpenSees, results in the curvature distribution shown in Figure 5.1(e). The curvature distribution is linear above the plastic hinge, and within the plastic hinge the curvature is calculated with moment-curvature analysis. Implementation of this method for a cantilever column results in the following expression for the post-yield tip displacement.

$$\Delta = \frac{M_{base}}{(EI)_{eff}} \left(\frac{L^2}{3} - LL_p\right) + \phi_{base} LL_p \tag{5.2}$$

where: M_{base} and ϕ_{base} are the moment and associated curvature at the base of the column, and

$(EI)_{eff}$ is the effective section stiffness of the elastic portion of the column. If $(EI)_{eff} = \frac{M_y}{\phi_y}$ is substituted into Equation 5.2, the following equation can be obtained.

$$\Delta = \phi_y \left(\frac{M_{base}}{M_y}\right)\left(\frac{L^2}{3} - LL_p\right) + \phi_{base} LL_p \tag{5.3}$$

where M_y is the moment at first yield.

The OpenSees environment was used in this report to model column behavior because it is capable of modeling cyclic and bidirectional loading, and variable axial loads. The lumped-plasticity model formulation proposed by Scott and Fenves (2006) was used within OpenSees. The OpenSees implementation is discussed in greater detail in Section 5.5.

Computing the tip displacement with either of these methods requires estimating the yield displacement, computing the moment-curvature response of the column cross section (i.e., ϕ_{base} and ϕ_y), and an expression for the plastic-hinge length. The following sections discuss each of these parameters individually.

5.2 YIELD DISPLACEMENT

The calculated yield displacement (Δ_y^{calc}) is typically computed in accordance to elastic theory as

$$\Delta_y^{calc} = \frac{F_y L^3}{3(EI)_{eff}} \tag{5.4}$$

where $(EI)_{eff}$ is the effective stiffness of the cross section, which can be calculated with several methods. Two methods are discussed in the following subsections.

5.2.1 Gross Section Properties

A simple approach for calculating $(EI)_{eff}$ is to use the gross-section stiffness as follows.

$$(EI)_{eff} = E_c I_g \tag{5.5}$$

where E_c is the modulus of elasticity of the concrete and I_g is the second moment of inertia of the gross cross-sectional area ($I_g = \frac{\pi D^4}{64}$).

Equations 5.4 and 5.5 provide a convenient means of predicting the yield displacement, but they neglect the effects of shear deformation, anchorage slip, and axial load (cracking). A factor can be introduced to account for these shortcomings of this methodology.

$$\Delta_y^{calc} = \frac{1}{\alpha_g}\frac{F_y L^3}{3EI_g} \tag{5.6}$$

where α_g is the stiffness modification ratio that is to be calibrated with experimental results. This parameter is studied and calibrated in Section 6.2.

5.2.2 Section Secant Stiffness

Alternatively, $(EI)_{eff}$ can also be taken as the secant stiffness ($(EI)_{sec}$) of the column cross section. The secant stiffness is the slope of the moment-curvature plot up to the yield moment, M_y.

$$(EI)_{eff} = (EI)_{sec} = \frac{M_y}{\phi_y} \tag{5.7}$$

This method accounts for the cracking of the column cross section, but assumes that the column is cracked over the entire height of the column.

Equations 5.4 and 5.7 provide a convenient means of predicting the yield displacement, but they neglect the effects of shear deformation and anchorage slip. A factor is introduced to account for these shortcomings of this methodology.

$$\Delta_y^{calc} = \frac{1}{\alpha_{sec}}\frac{F_y L^3}{3(EI)_{sec}} \tag{5.8}$$

where α_{sec} is a stiffness modification ratio that is calibrated with the experimental data described in Section 6.2.

5.2.3 Expected Trends in α_g and α_{sec}

The component of total deformation due to shear is dependent on the aspect ratio of the column, $\frac{L}{D}$. Therefore, α_g and α_{sec} are expected to depend on the aspect ratio. The following calculations are carried out to demonstrate how shear deformation varies with aspect ratio.

The flexural component of the yield displacement (Δ_y^f) for a circular cantilever column ($I_g = \frac{\pi D^4}{64}$) can be calculated as

$$\Delta_y^f = \frac{\phi_y L^2}{3} = \frac{M_y L^2}{E_c I_g} = \frac{M_y L^2}{E_c \frac{\pi D^4}{64}} = \frac{64 L^2 M_y}{3 D^4 E_c \pi} \tag{5.9}$$

where L is the length of the column and ϕ_y is the yield curvature of the section. The component of the yield displacement due to shear (Δ_y^v) can be calculated as

$$\Delta_y^v = \frac{4 F_y L}{3 G A_G} = \frac{4 M_y}{3 G A_G} = \frac{4 M_y}{3 G \frac{\pi D^2}{4}} \tag{5.10}$$

where G is the modulus of rigidity of the concrete, F_y is the lateral shear force, and A_G is the gross area of the section. The ratio of Δ_y^v to Δ_y^f can be simplified to the following expression.

$$\frac{\Delta_y^v}{\Delta_y^f} = \frac{E_c}{4G\left(\frac{L}{D}\right)^2} \tag{5.11}$$

The ratio decreases with increasing aspect ratio, indicating that the fraction of deformation due to shear decreases with increasing aspect ratio. Therefore, the stiffness modification ratios (α_g and α_{sec}) are expected to increase with increasing aspect ratio.

The following calculations are carried out to study the component of total deformation due to bond slip. The component of deflection due to bond slip can be approximated as follows.

$$\Delta_y^b = \theta_b L \tag{5.12}$$

where: θ_b is base rotation of the column due to bond slip, which can be calculated as

$$\theta_y^b = \frac{(u_e + u_e')}{\gamma D} \tag{5.13}$$

where γ is the ratio of the core diameter (D') to total column diameter (D), $\gamma = \frac{D'}{D}$. u_e and u_e' are the vertical displacements of the tensile steel and compressive steel, which can be calculated as follows (Section 3.2.1).

$$u_e = \frac{L_d \varepsilon_y}{2} \tag{5.14}$$

$$u'_e = \frac{L'_d \varepsilon'_y}{2} \tag{5.15}$$

where: L_p and L'_p are the development lengths for the compressive and tensile steel, respectively. ε_y is the tensile strain of the reinforcement, and ε'_y is the strain in the compression reinforcement when the tensile reinforcement yields, that is

$$\varepsilon'_y = \phi_y \gamma D - \varepsilon_y \tag{5.16}$$

The development lengths (L_d and L'_d) of equations 5.14 and 5.15 can be calculated as follows.

$$L_d = \frac{d_b f_y}{4\tau} \tag{5.17}$$

$$L'_d = \frac{d_b f'_y}{4\tau} \tag{5.18}$$

where: τ is the bond stress ($\tau \approx 1.0\sqrt{f'_c}$, f'_c in MPa), and d_b and f_y are the diameter and yield stress of the longitudinal reinforcement, respectively. The yield strain ε_y in a column can be approximated as a function of yield curvature and column depth as follows (Priestley et al. 1996).

$$\varepsilon_y = \frac{D\phi_y}{\lambda} \tag{5.19}$$

where: $\lambda = 2.45$ for spiral-reinforced columns and 2.14 for rectangular-reinforced columns. If equations 5.13-5.19 are substituted into Equation 5.12 with the identities $f_y = E_s \varepsilon_y$ and $f'_y = E_s \varepsilon'_y$, the following expression is obtained for displacement due to bond slip.

$$\Delta_y^b = \frac{(\gamma\lambda(\gamma\lambda - 2) + 2) D E_s L d_b \phi_y^2}{8\gamma\lambda^2\tau} \tag{5.20}$$

The ratio of the component of yield displacement due to bond slip to that from flexural deformation (Equation 5.9) can be calculated as follows.

$$\frac{\Delta_y^b}{\Delta_y^f} = \frac{3(\gamma\lambda(\gamma\lambda - 2) + 2)}{8\gamma\lambda} \frac{d_b f_y}{\tau L} \tag{5.21a}$$

$$= \frac{3(\gamma\lambda(\gamma\lambda - 2) + 2)}{2\gamma\lambda} \frac{L_d}{L} \tag{5.21b}$$

This ratio increases with an increase in $\frac{f_y d_b}{\tau L}$; therefore the fraction of total deformation due to anchorage slip should increase with this parameter. α_g and α_{sec} are therefore expected to decrease with increasing $\frac{f_y d_b}{\tau L}$.

In addition to the expected trends discussed above, α_g is expected to vary with varying axial-load ratio ($\frac{P}{A_g f_c'}$) and longitudinal-reinforcement ratio (ρ_l). $E_c I_g$ assumes that there is no cracking in the section, and overestimates the section stiffness. Therefore, α_g will be less than 1.0 to reduce this stiffness. At higher axial loads, α_g would not need to reduce $E_c I_g$ as much because at high axial loads, the neutral axis depth will be large, and there will be less cracking. Therefore α_g is expected to increase with an increase in axial load. Similarly, there will be less cracking with higher longitudinal-reinforcement ratios, therefore $alpha_g$ is expected to increase with increase in ρ_l.

Table 5.1 summarizes the expected trends in the stiffness modification ratios.

Table 5.1 Expected trends in α

	$\frac{L}{D}$	$\frac{P}{A_g f_c'}$	$\frac{f_y d_b}{L\tau}$	ρ_l
α_g	$\uparrow$	$\uparrow$	$\downarrow$	$\uparrow$
α_{sec}	$\uparrow$	-	$\downarrow$	-

5.3 MOMENT-CURVATURE RESPONSE

For this study, the cross sections of the columns were modeled with fiber sections (Section 2.1). With a fiber section, the column cross section is divided into small fibers in which each fiber is assigned a particular stress-strain response depending on the material the fiber represents. The fiber-section discretization strategies developed in Section 2.3 and the material models described in Section 2.2 were used to model the moment-curvature response of the lumped-plasticity models.

5.4 PLASTIC-HINGE LENGTHS

Many models have been proposed to estimate the plastic-hinge length based on the column properties. Previous researchers (e.g., Priestley et al. (1996); Mattock (1967)) have proposed that the plastic-hinge length is proportional to the column length, L, column depth, D, and the longitudinal reinforcement properties, as in the following equation:

$$L_p = \xi_1 L + \xi_2 D + \xi_3 f_y d_b \tag{5.22}$$

where f_y and d_b are the yield stress and bar diameter of the tension reinforcement, respectively. The column length is included in Equation 5.22 to account for the moment gradient along the length of the cantilever, and the column depth is included to account for the influence of shear on the size of the plastic region. The properties of the longitudinal bars are included to account for additional rotation at the plastic hinge resulting from anchorage bond slip.

Priestley et al. (1996) proposed an equation to calculate the plastic-hinge length in columns, in which $\xi_1 = 0.08$, $\xi_2 = 0$, and $\xi_3 = 0.022$ (fy in MPa) with an upper limit on L_p of 0.044 $f_y d_b$. Mattock (1967) proposed an equation to calculate the plastic-hinge length in beams, in which $\xi_1 = \frac{1}{20}$, $\xi_2 = \frac{1}{2}$, and $\xi_3 = 0.0$.

Equation 5.23 provides a reasonable estimate of column plastic-hinge length; however it can be shown that the amount of deformation due to bond slip is expected to vary with $\frac{f_y d_b}{\sqrt{f'_c}}$ and not just $f_y d_b$. Therefore, the following modification to Equation 5.22 is proposed.

$$L_p = \xi_1 L + \xi_2 D + \xi_3 \frac{f_y d_b}{\sqrt{f'_c}} \tag{5.23}$$

Equation 5.23 is used in this research to represent the length of plastic hinges. The unknown parameters (ξ_1, ξ_2, and ξ_3) are calibrated with experimental results in Chapter 6. Upon completion of the calibration, the effect of using the general form of plastic-hinge length proposed by Equation 5.22 will be evaluated.

5.5 OPENSEES IMPLEMENTATION

The OpenSees implementation of the lumped-plasticity model was used in this report because OpenSees is capable of modeling cyclic and bidirectional loading, and variable axial loads. For this research, the lumped-plasticity integration scheme proposed by Scott and Fenves (2006) is used within OpenSees. The current version of OpenSees (version 1.6.2.f) has three formulations of lumped-plasticity models. The formulation discussed in Section 5.1 (Scott and Fenves 2006) is used with the *beamWithHinges3* command in OpenSees. This command takes as input the column's fiber section, plastic-hinge length, and the properties of the elastic portion of the column (i.e., E, I, and A).

The application of the stiffness modification ratios (α_g and α_{sec}) to the Scott and Fenves (2006) formulation of the lumped-plasticity model is complex. With this formulation, the pre-yield lateral stiffness of the column varies discretely along the length of the column. In the elastic portion of the column, the stiffness is defined by the user-assigned section stiffness value (i.e., $(EI)_{eff}$). In the plastic hinge, the pre-yield stiffness is determined from the moment-curvature response of the fiber element assigned to the plastic hinge. In this region, the pre-yield section stiffness will be close to $(EI)_{sec}$. Because of the two stiffnesses, and because the pre-yield stiffness of the plastic hinge is a product of moment-curvature analysis, the stiffness modification ratios cannot be applied directly to modify the pre-yield response of the column. However, it is possible to modify the elastic properties of the column ($(EI)_{eff}$) in such a way that the yield displacements calculated with this method are identical to the yield displacements calculated with equations 5.6 and 5.8. The following discusses this procedure.

Stiffness modification ratios were introduced in equations 5.6 and 5.8 to account for several shortcomings of elastic bending theory . For convenience, a similar equation is given here. α in this equation, could be α_g or α_{sec} depending on which $(EI)_{eff}$ value is used.

$$\Delta_y^{\alpha} = \frac{1}{\alpha}\frac{F_y L^3}{3(EI)_{eff}} = \frac{1}{\alpha}\frac{M_y L^2}{3(EI)_{eff}} \tag{5.24}$$

The yield displacement calculated with the Scott and Fenves (2006) formulation can be calculated with Equation 5.2 as in the following equation:

$$\Delta_y^{OS} = \frac{M_y}{(EI)_{eff}}\left(\frac{L^2}{3} - LL_p\right) + \phi_y LL_p \tag{5.25}$$

In this equation, $(EI)_{eff}$ is supplied by the user and ϕ_y is a product of the moment-curvature analysis of the cross section assigned to the plastic hinge. A new stiffness modification ratio, ($\hat{\alpha}$) is proposed to modify the user-supplied section stiffness properties as in the following equation.

$$\Delta_y^{OS\_\hat{\alpha}} = \frac{M_y}{\hat{\alpha}(EI)_{eff}}\left(\frac{L^2}{3} - LL_p\right) + \phi_y LL_p \tag{5.26}$$

An expression for $\hat{\alpha}$ can be obtained by setting equations 5.24 and 5.26 equal to each other and simplifying. The resulting equation is as follows.

$$\hat{\alpha} = \frac{\alpha (L - 3L_p) M_y}{LM_y - 3\alpha(EI)_{eff} L_p \phi_y} \tag{5.27}$$

This expression can be used for $\alpha = \alpha_g$ and $(EI)_{eff} = E_c I_g$, as well as for $\alpha = \alpha_{sec}$ and $(EI)_{eff} = (EI)_{sec}$. The expression for $\hat{\alpha}_{sec}$ can be simplified further by substituting the identities $\phi_y = \frac{M_y}{(EI)_{sec}}$ (see Equation 5.7) and $(EI)_{eff} = (EI)_{sec}$ into Equation 5.27.

$$\hat{\alpha}_{sec} = \frac{\alpha (L - 3L_p)}{L - 3\alpha L_p} \tag{5.28}$$

5.6 SUMMARY

In this chapter, two formulations of the lumped-plasticity column-modeling strategy were presented, and key modeling parameters were identified for calibration with experimental results. The following parameters were identified for calibration and are calibrated in Chapter 6.

Stiffness Modification Ratios, α_g, α_{sec}. The parameters that account for several shortcomings of elastic theory at predicting yield displacement, $\Delta_y^{calc} = \frac{\Delta_y^{elastic}}{\alpha_{g/sec}}$ (Section 5.2).

Plastic-Hinge-Length Parameters, ξ_1, ξ_2, and ξ_3. The parameters used in the plastic-hinge-length equation; $L_p = \xi_1 L + \xi_2 D + \xi_3 \frac{f_y d_b}{\sqrt{f'_c}}$ (Section 5.4).

6 Calibration of Lumped-Plasticity Column Model

To accurately model the force-deformation response of reinforced concrete columns with the lumped-plasticity modeling strategy, the modeling parameters identified in Chapter 5 were calibrated with experimental results. The modeling parameters identified for calibration were:

Stiffness Modification Ratios, α_g, α_{sec}. The parameters that account for several shortcomings of elastic theory at predicting yield displac $\Delta_y^{calc} = \frac{\Delta_y^{elastic}}{\alpha_{g/sec}}$ (Section 5.2).

Plastic-Hinge-Length Parameters, ξ_1, ξ_2, and ξ_3. The parameters used in the plastic-hinge-length equation: $L_p = \xi_1 L + \xi_2 D + \xi_3 \frac{f_y d_b}{\sqrt{f'_c}}$ (Section 5.4).

This chapter discusses the calibration of the stiffness modification ratios and presents the results of this study. The optimization strategy used to calibrate the plastic-hinge-length equation is then presented, and the results of the calibration are summarized. The results of a sensitivity analysis are then presented to identify the effects of varying key parameters.

6.1 MEASURES OF ACCURACY

The parameters used in this chapter to measure the accuracy of the lumped-plasticity modeling strategy are identical to the measures used for the distributed-plasticity model, with the exception that the distributed-plasticity model accounted for the strain error E_{strain}. The measures are as follows:

Pushover Error (E_{push}). The accuracy of the force-displacement envelope was accounted for with the pushover error, which is defined as

$$E_{push} = \sqrt{\frac{\sum_{i=1}^{n} \left(F_{meas}^{i} - F_{calc}^{i}\right)^2}{\left(\max\left(F_{meas}\right)\right)^2 n}} \tag{6.1}$$

where F_{meas} and F_{calc} are the measured and calculated forces at corresponding displacements up to a drift ratio of 4%, and n is the number of datapoints in the envelope ($n = 100$ for this study).

Stiffness Ratio (S.R.) is the ratio of measured stiffness to calculated stiffness $\frac{K_{meas}}{K_{calc}}$, where $K_{meas} = \frac{F_y}{\Delta_y^{meas}}$ and $K_{calc} = \frac{F_y}{\Delta_y^{calc}}$. F_y is the smaller of the calculated lateral force at first first yield of the tensile reinforcement and the lateral, effective force calculated at a concrete strain of 0.002. Δ_y^{meas} and Δ_y^{calc} are the measured and calculated displacements associated with F_y.

Moment Ratio (M.R) is the ratio of the maximum measured moment at or before 4% drift to the calculated moment at or before 4% drift, $\frac{M_{max}^{meas}}{M_{max}^{calc}}$.

Degradation Error Ratio (D.R.) is a parameter that captures the effectiveness of the model in predicting column degradation.

$$D.R. = \left(\frac{\left(F_{calc}^{4\%} - F_{calc}^{3\%}\right)}{F_{calc}^{3\%}} - \frac{\left(F_{meas}^{4\%} - F_{meas}^{3\%}\right)}{F_{meas}^{3\%}} \right) * 100 \tag{6.2}$$

A degradation error ratio close to zero means that the model accurately models degradation.

6.2 COLUMN STIFFNESS

The accuracy of Equation 5.4 at estimating column stiffness was studied by calculating the stiffness ratio for 37 well-confined columns from the UW-PEER database (Section 1.3). Table 6.1 presents the means, minimums, maximums, and coefficients of variation of the stiffness ratios calculated using elastic theory (Equation 5.4) in combination with $E_c I_g$ and $(EI)_{sec}$.

Using $E_c I_g$ in Equation 5.4 significantly overestimates the stiffness of the column, as expected. This method neglects the effects of axial-load ratio, shear deformation, and anchorage slip on yield displacement. The mean value of the $S.R.$ equals 0.39 with a coefficient of variation of 0.30. $(EI)_{sec}$ provides a better estimate of yield displacement because it accounts for the effects

Table 6.1 Statistics of $s.r.$

	mean	cov	min	max
$\frac{K_{meas}}{K_g}$	0.40	0.26	0.24	0.68
$\frac{K_{meas}}{K_{sec}}$	0.80	0.22	0.51	1.14

of axial-load ratio and longitudinal-reinforcement ratio, but still overestimates the stiffness of the column. The mean value of the $S.R.$ equals 0.85 and the coefficient of variation is 0.20.

Because Equation 5.4 inaccurately predicts column stiffness using either effective stiffness method, stiffness modification ratios (α_g and α_{sec}) were introduced to account for the effects of axial-load ratio, longitudinal-reinforcement ratio, shear deformation, and anchorage slip. Expressions for α_g and α_{sec} can be derived by setting equations 5.6 and 5.8 equal to the measured yield displacement Δ_y^{meas}, and solving for α as follows.

$$\alpha_g = \frac{1}{\Delta_y^{meas}} \frac{F_y L^3}{3EI_g} = \frac{\Delta_y^g}{\Delta_y^{meas}} = \frac{K_{meas}}{K_g} \tag{6.3a}$$

$$\alpha_{sec} = \frac{1}{\Delta_y^{meas}} \frac{F_y L^3}{3(EI)_{sec}} = \frac{\Delta_y^{sec}}{\Delta_y^{meas}} = \frac{K_{meas}}{K_{sec}} \tag{6.3b}$$

As seen in Equation 6.3, α_g and α_{sec} are equivalent to the stiffness ratios. The key statistics of these parameters are reported in Table 6.1.

The mean values of α_g and α_{sec} could be used with equations 5.6 and 5.8 to calculate yield displacement. This approach would adjust the mean values of the stiffness ratios, but would not decrease the coefficients of variation of the stiffness ratios. In order to provide a better estimate of yield displacement, the expected trends in α_g and α_{sec} with respect to aspect ratio, axial-load ratio, and $\frac{f_y d_b}{L\tau}$ are considered (Table 5.1).

To verify the expected trends, α_g is plotted versus axial-load ratio, aspect ratio, longitudinal-reinforcement ratio, and $\frac{f_y d_b}{L\tau}$ in Figure 6.1. The least-squares-best-fit lines are shown in the figures, and the R^2 values are reported. As expected, α_g increases with increasing axial-load ratio, aspect ratio, and longitudinal-reinforcement ratio, and decreases with increasing $\frac{f_y d_b}{L\tau}$.

Similarly, α_{sec} is plotted versus the key properties to verify the parameters sensitivity to the properties (Figure 6.2). As expected, α_{sec} is not significantly affected by increasing axial load

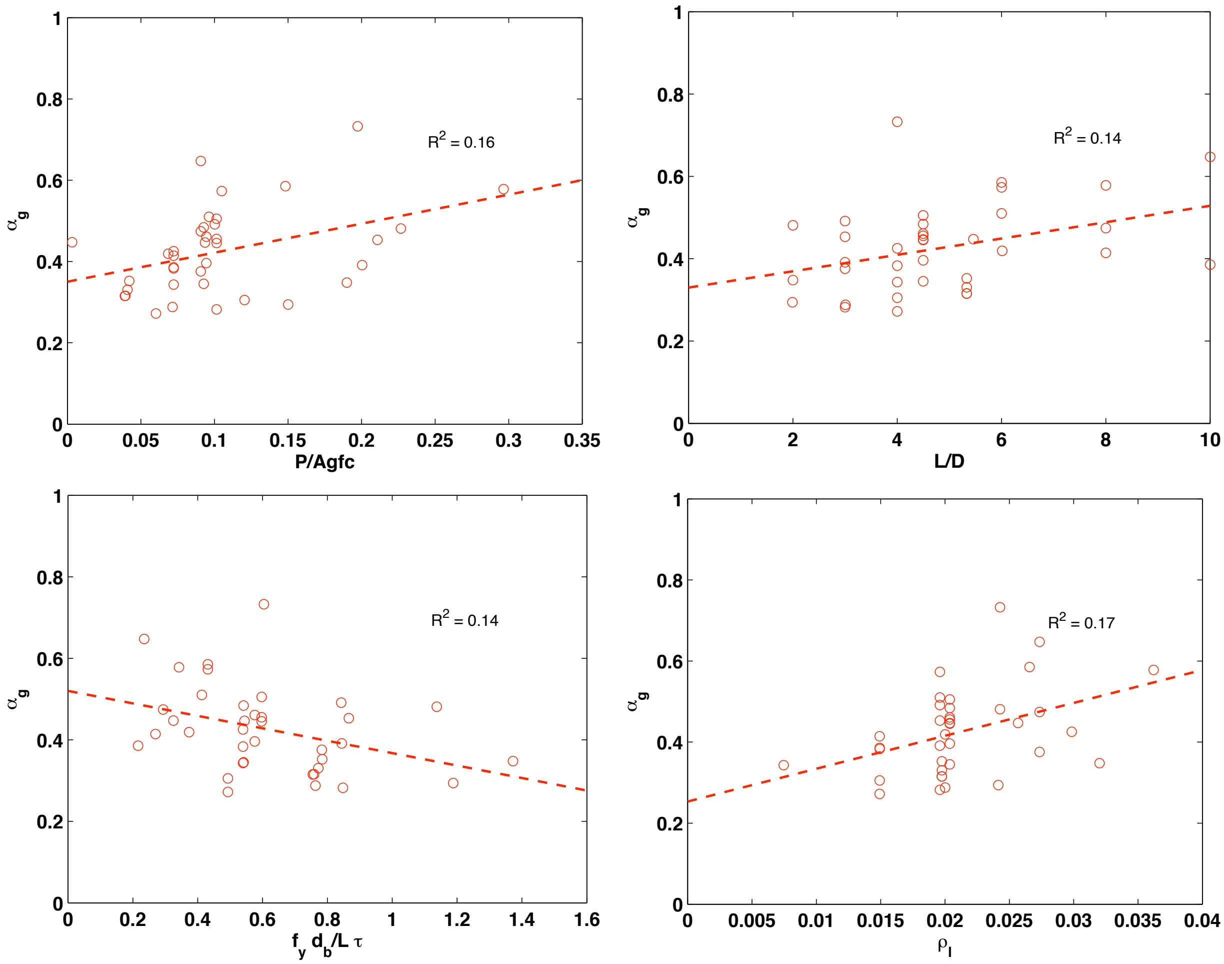

Fig. 6.1 α_g **versus key column properties**

and longitudinal-reinforcement ratio because $(EI)_{sec}$ already accounts for the effects of cracking. However, as expected, α_{sec} increases with increasing aspect ratio and decreases with increasing $\frac{f_y d_b}{L\tau}$.

Based on these trends, simple expressions were developed for α_g and α_{sec} as functions of aspect ratio, axial-load ratio, longitudinal-reinforcement ratio, and $\frac{f_y d_b}{L\tau}$. The general form of the expressions were as follows:

$$\alpha_{g/sec}^{calc} = \lambda_1 + \lambda_2 \frac{L}{D} + \lambda_3 \frac{P}{A_g f_c'} + \lambda_4 \frac{f_y d_b}{L\tau} + \lambda_5 \rho_l \leq 1.0 \tag{6.4}$$

The parameters λ_1-λ_5 were calibrated for both cross-section stiffness methods using the 37

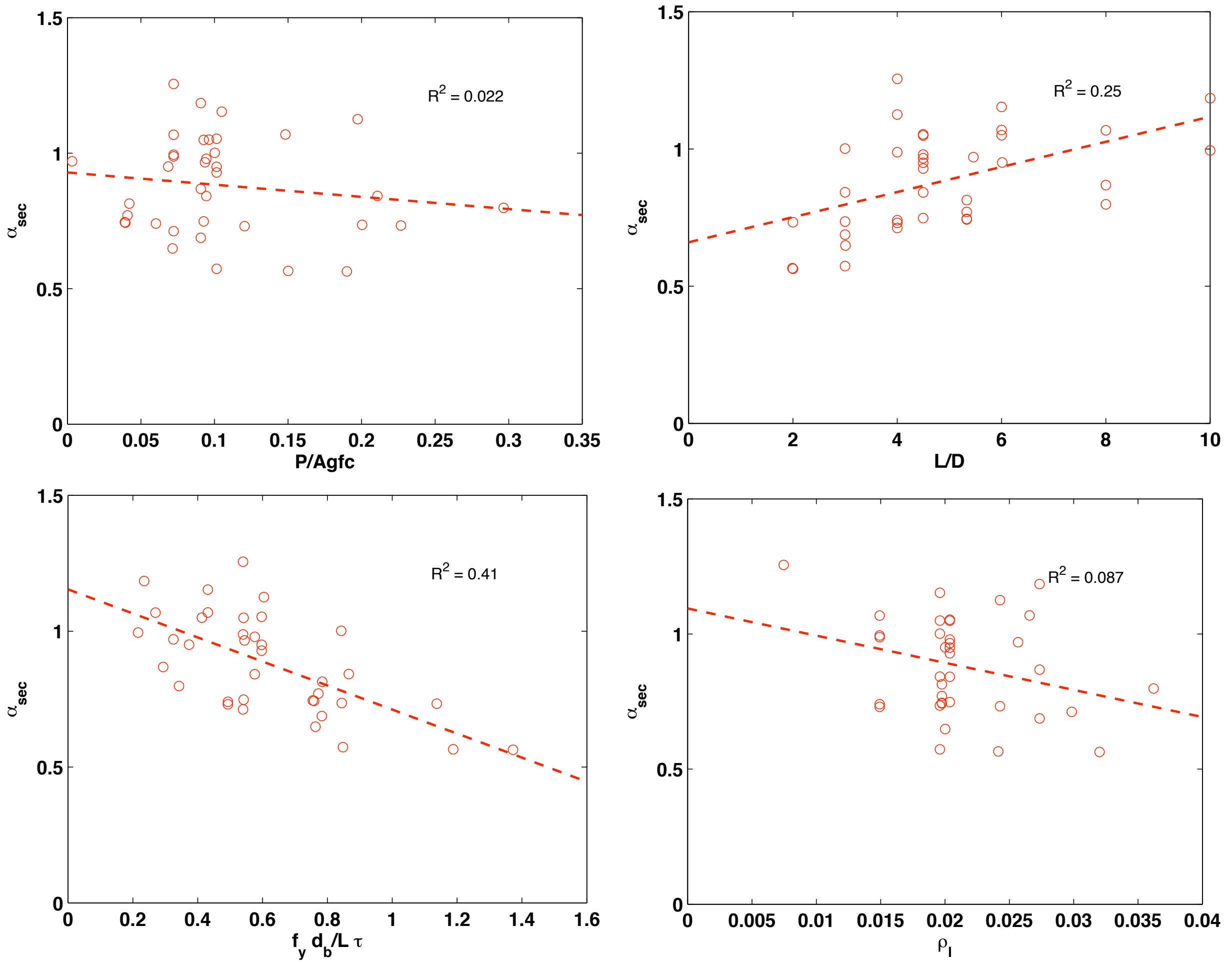

Fig. 6.2 α_{sec} versus key column properties

columns from the UW-PEER database. The parameters were calibrated by minimizing the coefficients of variation of the stiffness ratios calculated with equations 5.6, 5.8, and 6.4. Additionally, the mean value of the stiffness ratios were constrained to 1.0. For α_{sec}, λ_3 and λ_5 were fixed to 0.0 because α_{sec} is not affected by axial-load ratio and longitudinal-reinforcement ratio. The resulting equations for α_g^{calc} and α_{sec}^{calc} follow (equations 6.5 and 6.6), and the key statistics of the stiffness ratios calculated using these expressions are reported in Table 6.2.

$$\alpha_g^{calc} = 0.35 + 0.01\frac{L}{D} + 1.05\frac{P}{A_g f'_c} - 0.20\frac{f_y d_b}{L\tau} + 0.1\rho_l \leq 1.0 \tag{6.5}$$

$$\alpha_{sec}^{calc} = 0.85 + 0.03\frac{L}{D} - 0.3\frac{f_y d_b}{L\tau} \leq 1.0 \tag{6.6}$$

Table 6.2 Statistics of *s.r.* using α expressions

	Eqn #	mean	cov	min	max
$\frac{K_{meas}}{K_g}$	6.5	1.00	0.17	0.65	1.43
	6.7	1.00	0.19	0.70	1.49
$\frac{K_{meas}}{K_{sec}}$	6.6	1.00	0.14	0.77	1.30
	6.8	1.00	0.16	0.76	1.38

As seen in Table 6.2, equations 6.5 and 6.6 increase the accuracy of the yield displacement calculation. The mean values of the stiffness ratios are adjusted to 1.0, and the coefficients of variation have been reduced from 0.26 to 0.17 for $\frac{K_{meas}}{K_g}$, and from 0.22 to 0.14 for $\frac{K_{meas}}{K_{sec}}$.

Simpler equations can be obtained by considering the correlation between aspect ratio and $\frac{f_y d_b}{L\tau}$. In Figure 6.2, $\frac{L}{D}$ is plotted versus $\frac{f_y d_b}{L\tau}$ to demonstrate the correlation. Since these parameters have such a strong correlation, little is gained by including both effects in equations 6.5 and 6.6. The optimizations of α_g^{calc} and α_{sec}^{calc} were rerun using equation 6.4 with $\lambda_4 = 0.0$. The resulting equations follow (6.7 and 6.8), and the key statistics of using these simplified equations are reported in Table 6.2.

$$\alpha_g^{calc} = 0.15 + 0.03\frac{L}{D} + 0.95\frac{P}{A_g f_c'} + 0.08\rho_l \leq 1.0 \tag{6.7}$$

$$\alpha_{sec}^{calc} = 0.35 + 0.1\frac{L}{D} \leq 1.0 \tag{6.8}$$

Equations 6.7 and 6.8 are simpler than equations 6.5 and 6.6, and little accuracy is lost using these equations. Using the simplified equations results in only a 0.02 increase in the coefficients of variation of $\frac{K_{meas}}{K_g}$ and $\frac{K_{meas}}{K_{sec}}$.

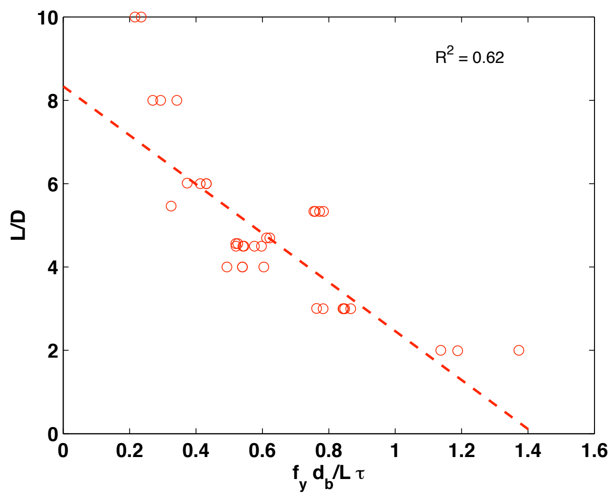

Fig. 6.3 Correlation between $\frac{l}{d}$ and $\frac{f_y d_b}{l\tau}$

6.3 CALIBRATION OF PLASTIC-HINGE LENGTH

The general form of an expression to estimate plastic-hinge length was proposed in Section 5.4 (Equation 5.23). The expression is given again here with a limit of $\frac{L}{4}$. The limit on the plastic-hinge length is from the lumped-plasticity model formulation proposed by Scott and Fenves (2006).

$$L_p = \xi_1 L + \xi_2 D + \xi_3 \frac{f_y d_b}{\sqrt{f'_c}} <= \frac{L}{4} \tag{6.9}$$

The parameters ξ_1, ξ_2, and ξ_3 are calibrated with experimental results in this section.

6.3.1 Optimization Scheme

The optimization was performed by running pushover analyses for a broad range of calibration parameters (ξ_1, ξ_2, ξ_3) and then selecting the scheme in which the total error (E_{total}, Equation 6.10) was minimized and the additional modeling accuracy terms (e.g., stiffness ratio) were reasonable. The range of values used for each calibration parameter are shown in Table 6.3, along with the step size between consecutive values within the range. The analysis consisted of every combination of the optimization parameters, which amounted to ∼5,000 combinations.

The optimization scheme used for this modeling strategy couples the accuracy of force-deformation predictions with the accuracy damage progression predictions. The total error, E_{total},

Table 6.3 Calibration parameter ranges for plastic-hinge length

parameter	ξ_1	ξ_2	ξ_3
min	0	0	0
max	0.2	0.8	0.15
step size	0.0125	0.0500	0.01

is defined as

$$E_{total} = \frac{\text{mean}\left(E_{push}\right)}{2} + \frac{\kappa_1}{4}\text{cov}\left(\frac{\Delta_{bb}^{meas}}{\Delta_{bb}^{calc}}\right) + \frac{\kappa_2}{4}\text{cov}\left(\frac{\Delta_{sp}^{meas}}{\Delta_{sp}^{calc}}\right) \tag{6.10}$$

where: Δ_{sp}^{meas} is the observed displacement at the onset of cover spalling, and Δ_{sp}^{calc} is the calculated displacement associated with the mean value of the maximum compressive strain in the concrete at cover spalling, ε_{sp}^{mean}. Δ_{bb}^{meas} is the observed displacement at the onset of bar buckling, and Δ_{bb}^{calc} is the calculated displacement associated with the calculated tensile strain in the longitudinal reinforcement at the onset of bar buckling, ε_{bb}^{calc}. This buckling strain is to be calculated as a function of the effective confinement ratio (ρ_{eff}) to account for the effect of spiral reinforcement on bar buckling, as in the following equation (Berry and Eberhard 2005).

$$\varepsilon_{bb}^{calc} = \chi_1 + \chi_2\rho_{eff} \leq 0.15 \tag{6.11}$$

where: $\rho_{eff} = \frac{\rho_s f_{ys}}{f_c'}$, and χ_1 and χ_2 are to be calibrated by minimizing the coefficient of variation of $\frac{\varepsilon_{bb}}{\varepsilon_{bb}^{calc}}$. ε_{bb} is the calculated tensile strain at the onset of bar buckling associated with the observed displacement of bar buckling.

The κ terms in Equation 6.10 are included to ensure that the error terms are of similar magnitude.

$$\kappa_1 = \frac{\min\left(\text{mean}\left(E_{push}\right)\right)}{\min\left(\text{cov}\left(\frac{\Delta_{bb}^{meas}}{\Delta_{bb}^{calc}}\right)\right)} \tag{6.12}$$

$$\kappa_2 = \frac{\min\left(\text{mean}\left(E_{push}\right)\right)}{\min\left(\text{cov}\left(\frac{\Delta_{sp}^{meas}}{\Delta_{sp}^{calc}}\right)\right)} \tag{6.13}$$

In equations 6.10, 6.12, and 6.13 *mean* entails the average value for the 37 bridge columns, *cov* is the coefficient of variation of for the columns in which the particular damage state is available (i.e., 33 columns for bar buckling and 31 columns for spalling), and *min* entails the minimum value out of the total number of combinations.

This optimization scheme did not account for the accuracy of the local deformations in the same manner as the optimization scheme used for the distributed-plasticity modeling strategy. This is because the local deformations in the plastic hinge are average values over the height of the plastic hinge. These average values do not correlate to available measured strain and rotation data.

OpenSees was used to model the the columns using the lumped-plasticity formulation proposed by Scott and Fenves (2006) (Section 5.1). The plastic hinges in this study were assigned fiber sections with the uniform-radial section discretization scheme described in Section 2.3. The steel was modeled with the Giufre-Menegotto-Pinto model described in Section 2.2.1. The strain-hardening ratio, b was set to 0.01. The Popovics curve with model parameters proposed by Mander et al. (1988) was used to model both the confined and unconfined concrete (Section 2.2.2). Additionally, the section stiffnesses of the elastic portion of the columns were calculated as the secant stiffnesses multiplied by the stiffness modification ratios (i.e., $(EI)_{eff} = \hat{\alpha}_{sec}(EI)_{sec}$, Section 6.2). α_{sec} was calculated with Equation 6.8, and $\hat{\alpha}_{sec}$ was then calculated with Equation 5.28.

6.3.2 Optimization Results

The optimization study described in the previous section was performed for 37 columns from the UW-PEER database (Section 4.1). The top 20 combinations from the optimization study are reported in Table 6.4. It should be noted that the stiffness ratios for all plastic-hinge lengths were 1.0 because the stiffness modification ratio $\hat{\alpha}_{sec}$ was used in this study to adjust the elastic stiffness properties of the column ($(EI)_{eff}$).

The combination that minimized E_{total} was $\xi_1 = 0.0375$, $\xi_2 = 0$, and $\xi_3 = 0.12$ ($E_{total} =$ 8.05). However, for simplicity, the combination in which $\xi_1 = 0.05$, $\xi_2 = 0$, and $\xi_3 = 0.1$ ($E_{total} =$ 8.09) was chosen as the optimal solution (combination #13). In Table 6.5, the chosen optimal solution is compared to the overall optimal solution, and the plastic-hinge models proposed by Priestley et al. (1996), Mattock (1967), and Corley (1966).

Table 6.4 Lumped-plasticity optimization results

	Parameter Values				Pushover Accuracy			Damage Estimates							
Rank	ξ_1	ξ_2	ξ_3	E_{total}	E_{push}	M.R.	D.R.	ε_{bb}		ε_{bb}^{calc}		$\frac{\Delta_{bb}^{meas}}{\Delta_{bb}^{calc}}$	ε_{sp}		$\frac{\Delta_{sp}^{meas}}{\Delta_{sp}^{mean}}$
				mean	mean	mean	mean	mean	cov	χ_1	χ_2	cov	mean	cov	cov
1	0.04	0.00	0.10	8.533	8.461	1.058	-0.638	0.091	0.297	0.054	0.256	0.244	0.009	0.483	0.338
2	0.04	0.00	0.11	8.537	8.460	1.062	-0.563	0.086	0.296	0.052	0.236	0.245	0.009	0.476	0.338
3	0.04	0.00	0.12	8.552	8.473	1.065	-0.601	0.082	0.296	0.050	0.220	0.246	0.008	0.470	0.338
4	0.04	0.00	0.09	8.560	8.500	1.053	-0.700	0.096	0.299	0.056	0.277	0.245	0.010	0.492	0.339
5	0.04	0.05	0.09	8.566	8.443	1.061	-0.598	0.087	0.298	0.053	0.234	0.249	0.009	0.477	0.338
6	0.04	0.05	0.08	8.571	8.450	1.058	-0.640	0.091	0.300	0.055	0.253	0.249	0.009	0.484	0.339
7	0.05	0.00	0.09	8.572	8.460	1.062	-0.780	0.085	0.302	0.048	0.260	0.244	0.009	0.486	0.344
8	0.05	0.00	0.10	8.574	8.477	1.066	-0.704	0.081	0.300	0.046	0.241	0.244	0.008	0.479	0.344
9	0.04	0.00	0.13	8.575	8.492	1.068	-0.695	0.078	0.296	0.049	0.205	0.247	0.008	0.463	0.338
10	0.04	0.05	0.10	8.579	8.465	1.065	-0.589	0.082	0.297	0.051	0.218	0.249	0.008	0.470	0.338
11	0.05	0.00	0.11	8.580	8.496	1.069	-0.728	0.078	0.297	0.045	0.225	0.244	0.008	0.471	0.344
12	0.05	0.00	0.12	8.583	8.517	1.072	-0.844	0.074	0.296	0.044	0.210	0.243	0.008	0.465	0.343
13	0.03	0.00	0.12	8.595	8.475	1.057	-0.436	0.092	0.301	0.059	0.229	0.254	0.009	0.477	0.333
14	0.05	0.00	0.13	8.597	8.551	1.075	-0.978	0.071	0.295	0.043	0.197	0.243	0.007	0.459	0.342
15	0.04	0.00	0.14	8.598	8.519	1.071	-0.849	0.075	0.296	0.047	0.192	0.249	0.008	0.458	0.338
16	0.05	0.00	0.08	8.600	8.473	1.059	-0.791	0.090	0.306	0.049	0.282	0.246	0.009	0.495	0.345
17	0.04	0.05	0.11	8.600	8.487	1.069	-0.714	0.079	0.297	0.049	0.204	0.250	0.008	0.464	0.339
18	0.03	0.00	0.11	8.603	8.509	1.052	-0.604	0.098	0.300	0.062	0.248	0.253	0.010	0.484	0.333
19	0.04	0.00	0.08	8.605	8.566	1.048	-0.738	0.102	0.301	0.058	0.304	0.245	0.010	0.501	0.340
20	0.04	0.05	0.07	8.608	8.487	1.053	-0.613	0.096	0.302	0.057	0.274	0.250	0.010	0.492	0.340

Table 6.5 Comparison of lumped-plasticity models

	Total Accuracy				Pushover Accuracy			Bar Buckling Estimates						Spalling Estimates		
Plastic-Hinge Length	E_{total}	(%) of E_{total}			E_{push}	M.R.	D.R.	ε_{bb}		$\frac{\Delta_{bb}^{meas}}{\Delta_{bb}^{mean}}$	χ_1	χ_2	$\frac{\Delta_{bb}^{meas}}{\Delta_{bb}^{calc}}$	ε_{sp}		$\frac{\Delta_{sp}^{meas}}{\Delta_{sp}^{mean}}$
	mean	E_{push}	E_{bb}	E_{sp}	mean	mean	mean	mean	cov	cov			cov	mean	cov	cov
Overall Optimal $0.0375L+0.11\frac{f_y d_b}{\sqrt{f'_c}} \leq L/4$	8.053	0.488	0.245	0.267	7.858	1.047	-1.150	0.083	0.294	0.277	0.050	0.224	0.239	0.008	0.471	0.344
Selected Optimal $0.05L+0.1\frac{f_y d_b}{\sqrt{f'_c}} \leq L/4$	8.089	0.486	0.243	0.272	7.856	1.048	-1.149	0.082	0.299	0.282	0.046	0.246	0.237	0.008	0.482	0.352
Priestley et al. (1996) $0.08L+0.022f_y d_b \leq 0.044 f_y d_b$	8.472	0.464	0.275	0.261	8.041	1.059	-1.235	0.070	0.349	0.322	0.040	0.205	0.281	0.007	0.455	0.355
Mattock (1967) $0.05L+0.5D$	8.900	0.441	0.318	0.241	8.047	1.051	-1.127	0.083	0.375	0.347	0.067	0.110	0.342	0.008	0.458	0.343
Corley (1966) $0.5D$	8.545	0.460	0.282	0.258	8.153	1.069	-1.364	0.058	0.323	0.305	0.041	0.119	0.291	0.006	0.422	0.354

As seen in the table, the measures of accuracy of the selected optimal solution are nearly identical to those of the overall optimal solution. Additionally, the selected optimal solution is more accurate than that of Priestley et al. (1996) and Corley (1966) for all measures of modeling accuracy, and is more accurate than Mattock (1967) for all measures of modeling accuracy except cover-spalling predictions.

6.4 MODEL EVALUATION

The proposed lumped-plasticity column-modeling strategy (including the selected optimal plastic-hinge length) is evaluated in this section. The measures of modeling accuracy are plotted versus key column properties to determine if the accuracy of the model is sensitive to these properties. In figure 6.4, E_{push} is plotted versus aspect ratio (L/D), longitudinal-reinforcement ratio (ρ_l), axial-load ratio ($P/f_c'A_g$), effective confinement ratio, concrete compressive strength, and the ratio of spiral spacing to longitudinal bar diameter (s/d_b). Included in the figure are the R^2 values, which indicate the magnitude of correlation between E_{push} and the property. As seen in the figure, there are no significant trends in the data.

Similarly, the stiffness ratio is plotted versus the key column properties in Figure 6.5. Slight trends can be observed in $S.R.$ versus ρ_l, f_c', and s/d_b, with R^2 values of 0.12, 0.11, and 0.15 respectively.

The maximum moment ratio ($M.R.$) is plotted versus the key properties in Figure 6.6. As seen in the figure, only one trend can be observed. The moment ratio decreases with an increase in effective-confinement ratio. The degradation ratio ($D.R.$) is plotted versus the key properties in Figure 6.7. There are no significant trends in the data.

The damage predictions from this modeling strategy will be studied later in this report. Trends in the predictions will be studied and the estimates will be compared to the predictions of other methods.

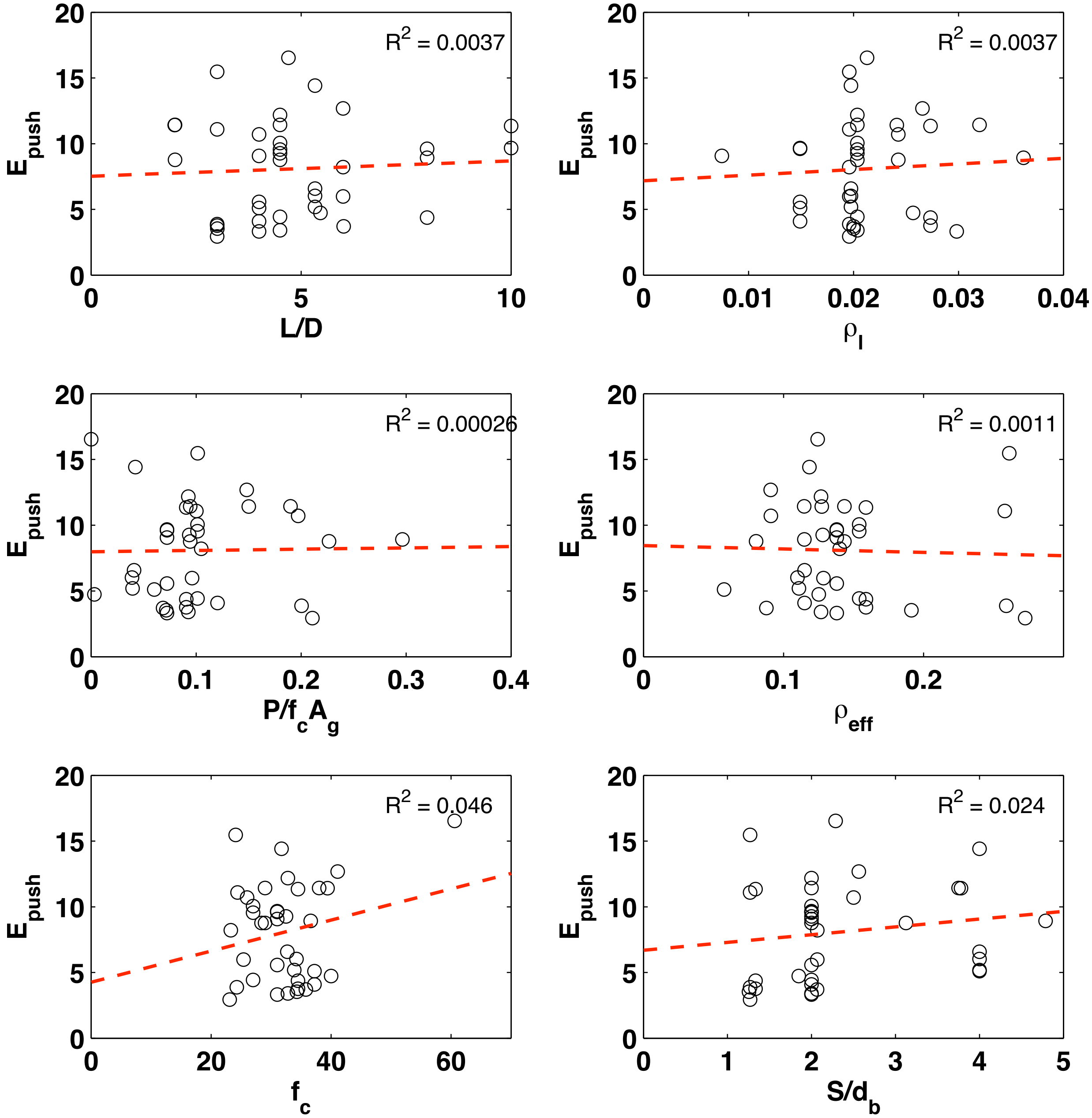

Fig. 6.4 Effect of key properties on pushover error

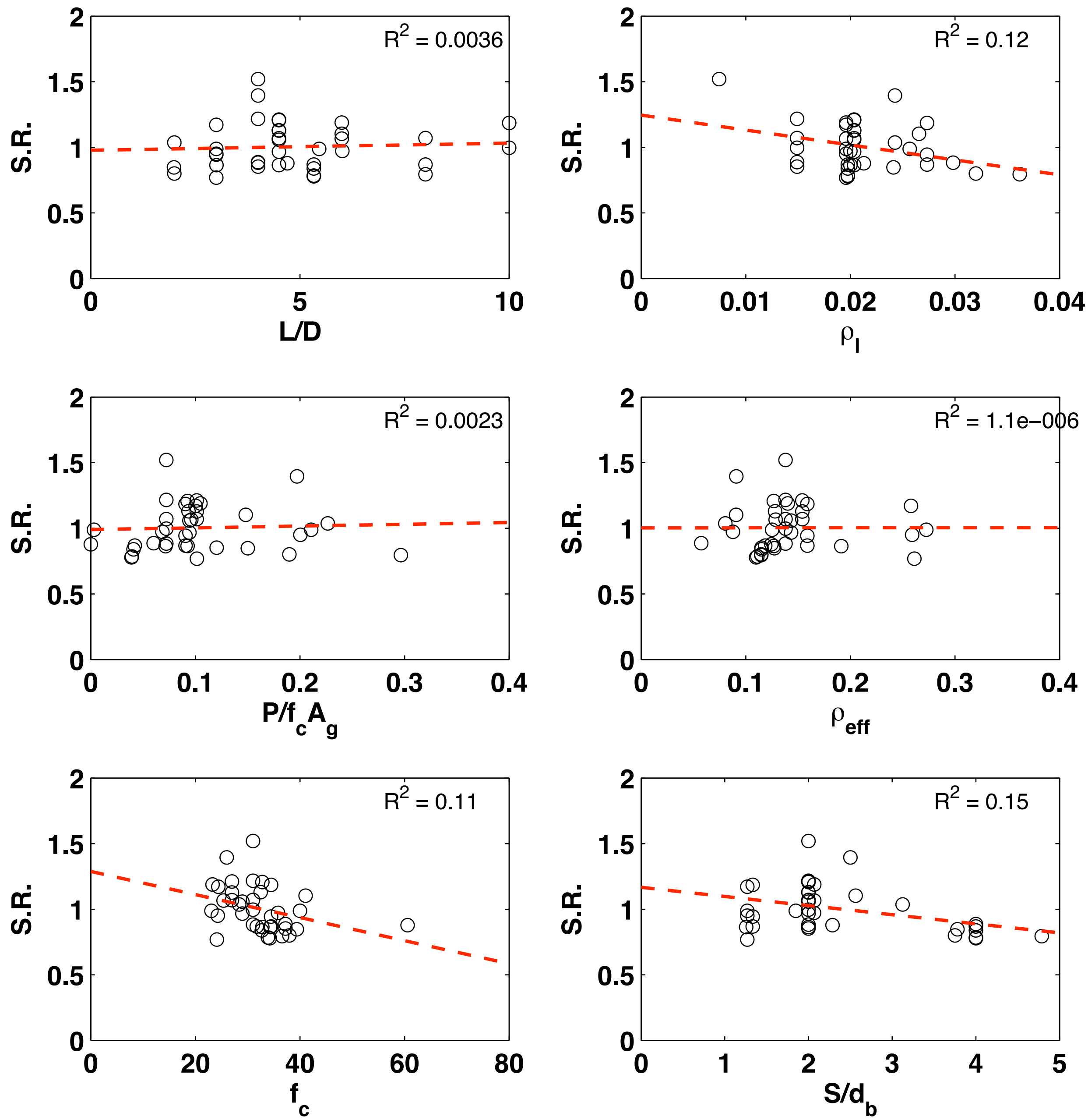

Fig. 6.5 Effect of key properties on stiffness ratio

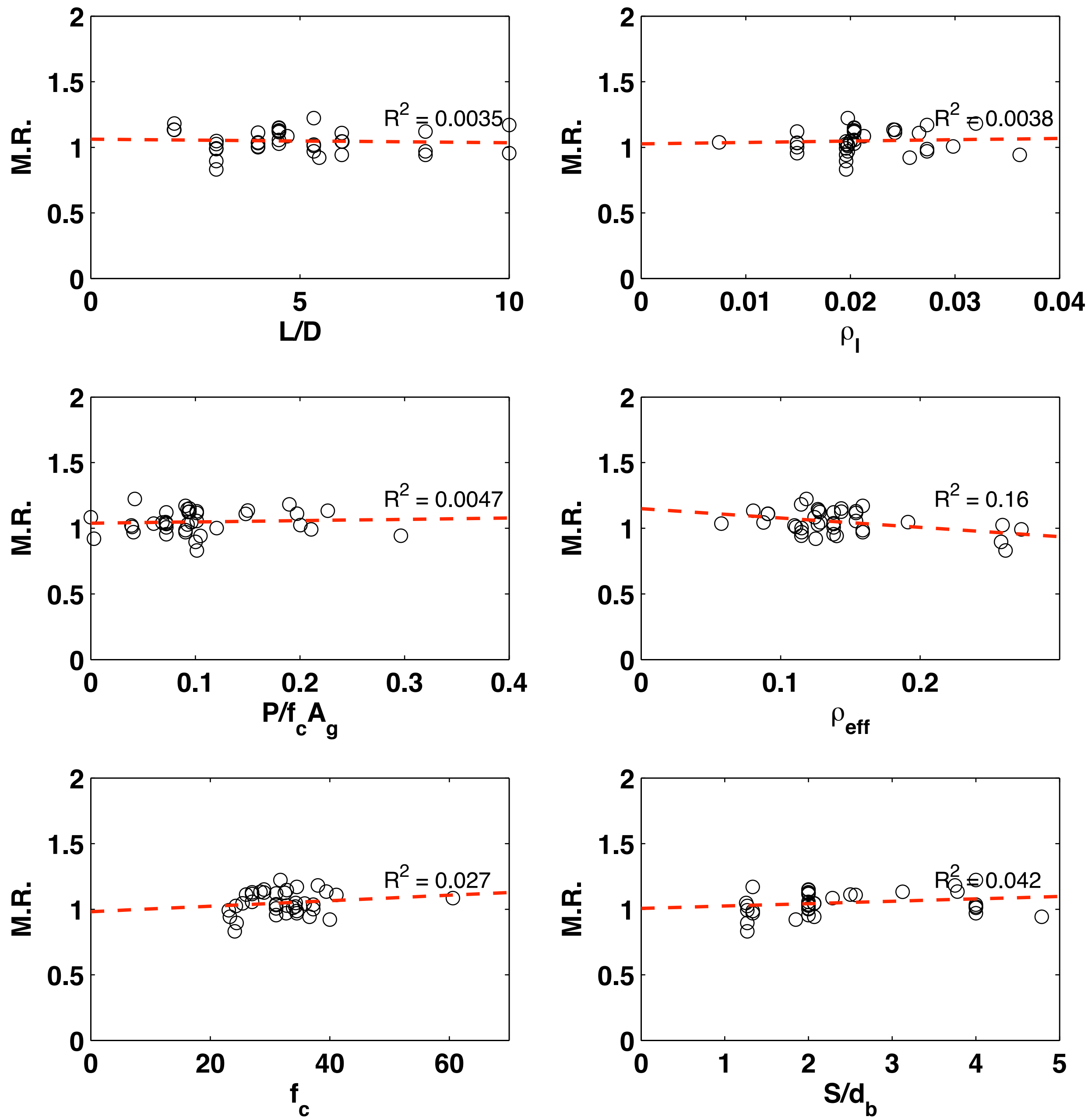

Fig. 6.6 Effect of key properties on moment ratio

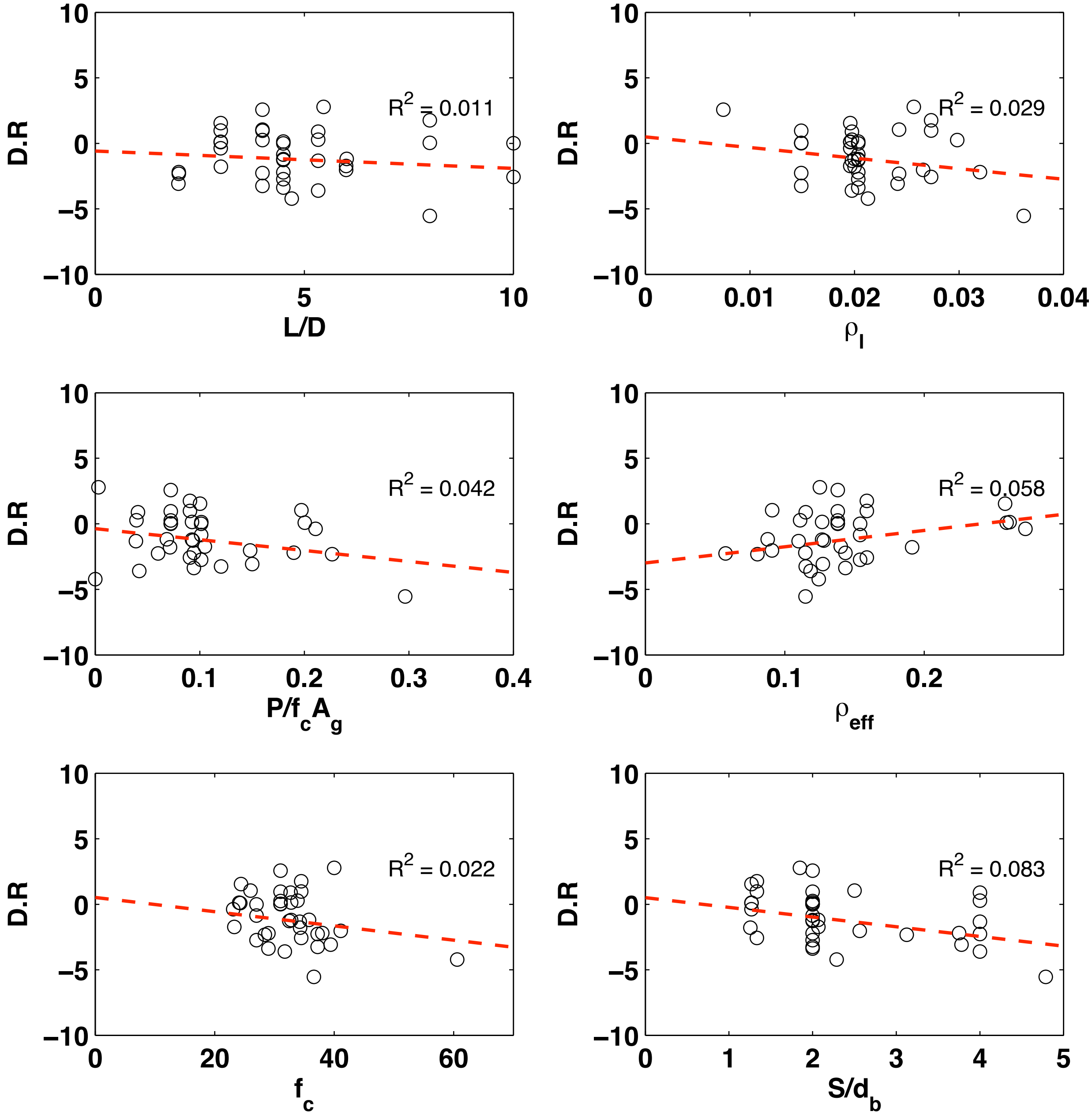

Fig. 6.7 Effect of key properties on degradation error ratio

6.5 SUMMARY

Elastic beam bending theory (Equation 5.4) with E_cI_g or $(EI)_{sec}$ alone inaccurately predicts column stiffness. The mean values of the stiffness ratios for 37 columns from the UW-PEER database were 0.39 using Equation 5.4 with E_cI_g, and 0.85 with $(EI)_{sec}$. The coefficients of variation were 0.30 and 0.20, respectively. Elastic theory neglects the effects of shear deformation and bond slip, and the use of E_cI_g will neglect the effects of axial load. A modification to traditional elastic theory is proposed in which stiffness modification ratios (α and α_{sec}) are included in the calculations (equations 5.6 and 5.8). Using the mean values of α_g (0.39) and α_{sec} (0.85) in these equations, adjusts the mean values of the stiffness ratios to 1.0, but does not reduce the coefficients of variation of the stiffness ratios. By accounting for the expected trends in α_g and α_{sec}, more accurate predictions of column stiffness can be obtained (equations 6.7 and 6.8). The coefficient of variation of the stiffness ratios can be reduced from 0.30 to 0.19 using α_g^{calc}, and from 0.20 to 0.16 using α_{sec}^{calc}.

The plastic-hinge-length proposed in Section 5.4 was calibrated in this chapter. The calibration considered the accuracy of the pushover analyses as well as the accuracy of damage predictions, namely bar buckling and cover spalling. The resulting plastic-hinge-length equation was

$$L_p = 0.05L + 0.1\frac{f_y d_b}{\sqrt{f'_c}} \leq \frac{L}{4} \tag{6.14}$$

The mean compressive strain in the cover at the onset of cover spalling was 0.008.

$$\varepsilon_{sp} = 0.008 \tag{6.15}$$

The strain at the onset of bar buckling can be predicted with the following equation.

$$\varepsilon_{bb}^{calc} = 0.046 + 0.25\rho_{eff} \leq 0.15 \tag{6.16}$$

where: L is the column length, f_y and d_b are the yield stress and bar diameter of the longitudinal reinforcement, f'_c is the concrete compressive strength, $\rho_{eff} = \frac{\rho_s f_{ys}}{f'_c}$, ρ_s is the spiral-reinforcement ratio, and f_{ys} is the yield stress of the spiral reinforcement.

7 Evaluation of Cyclic Response

The calibration of the proposed modeling strategies (chapters 4 and 6) considered only the envelope response of the columns. The full cyclic response must be considered for earthquake engineering applications. In this chapter, the cyclic response of the proposed modeling strategies are evaluated with experimental results from the UW-PEER database.

7.1 CYCLIC RESPONSE OF MATERIALS

The cyclic response of the proposed fiber-modeling strategies depend on the cyclic response of the material constitutive models. In this section, the cyclic responses of the concrete and steel are presented.

The cyclic response of the steel was defined by the Giuffre-Menegotto-Pinto steel model (Taucer et al. 1991), which accounts for the Bauschinger effect, but does not account for strength and stiffness degradation due to bar buckling and cycling. The cyclic response of the steel is illustrated in Figure 7.1.

The concrete model's stress-strain envelope is discussed in Section 2.2. As discussed in that section, the envelope response of the concrete includes the Popovic's curve in compression and a linear stress-strain response in tension until rupture. The cyclic response of the concrete in compression was defined by a model proposed by Karsan and Jirsa and modified by Professor Filippou at UC Berkeley (Mazzoni et al. 2006). As part of this report, this model was modified to incorporate tension. Upon unloading from tension, the stress-strain relationship passes through the origin. The cyclic responses of the concrete in both tension and compression are illustrated in Figure 7.2(a). A detailed view of the cyclic response of the concrete in tension is shown in Fig-

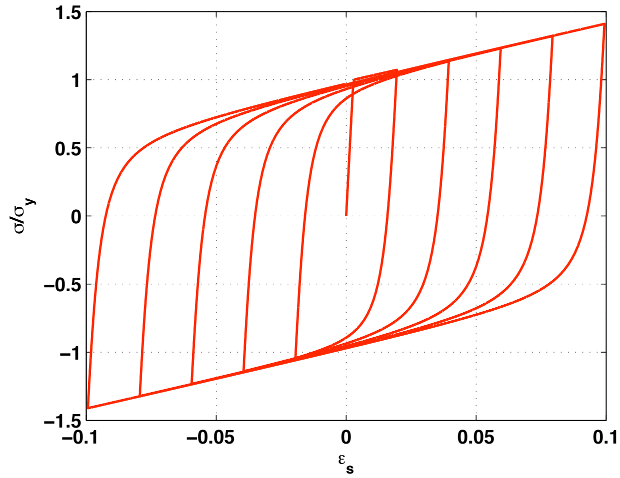

Fig. 7.1 Cyclic response of longitudinal reinforcing steel

ure 7.2(b).

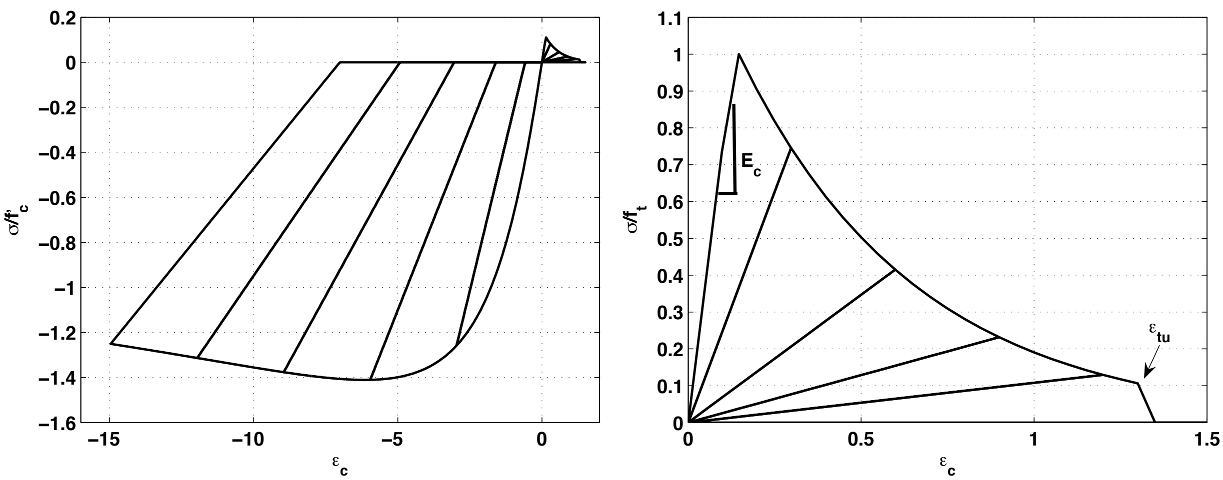

(a) Response in Compression and Tension

(b) Response in Tension

Fig. 7.2 Cyclic response of concrete

7.2 MEASURES OF ACCURACY

The cyclic response of the proposed modeling strategies will be evaluated with the following measures of model accuracy.

Normalized Hysteretic Force Error, E_{force}. The error between measured and calculated forces at corresponding displacements, as in the following equation.

$$E_{force} = \sqrt{\frac{\sum_{i=1}^{n}\left(F_{meas}^{i} - F_{calc}^{i}\right)^2}{\left(\max\left(F_{meas}\right)\right)^2 n}} \tag{7.1}$$

where F_{meas} and F_{calc} are the measured and calculated lateral forces at corresponding displacements, and n is the number of datapoints in the history.

Normalized Hysteretic Energy Error, E_{energy}. The error between measured and calculated hysteretic energies, Ω_{meas} and Ω_{calc}.

$$E_{energy} = \frac{\Omega_{meas} - \Omega_{calc}}{\Omega_{meas}} \tag{7.2}$$

Hysteretic energy is the area within the hysteresis loops and is calculated with the trapezoid numerical integration scheme as follows.

$$\Omega = \sum_{i=1}^{n-1} \frac{F_{i+1} - F_i}{2}\left(\Delta_{i+1} - \Delta_i\right) \tag{7.3}$$

where: F_i and Δ_i are the lateral force and displacement associated with the i^{th} step, and n is the total number of datapoints in the history. The closer to 0, the better the fit. The sign of E_{energy} is important. If $E_{energy} < 0$, the calculated response overestimates the amount of energy dissipated in the test, and in turn, if $E_{energy} > 0$ the amount of dissipated energy is underestimated.

7.3 EVALUATION OF DISTRIBUTED-PLASTICITY COLUMN-MODELING STRATEGY

7.3.1 Model Description

The total hysteretic response of the distributed-plasticity modeling strategy depends on the hysteretic responses of its various components (flexural, bond slip, shear). For this study, the shear component of the total deformation was assumed to remain elastic (linear). The hysteretic response of the flexural component (force-based beam-column element) relied on the cyclic response of the fiber section, which in turn depended on the material constitutive models (Section 7.1).

The hysteretic response of the zero-length bond-slip section also relied on the cyclic response of its material components. The cyclic responses of the concrete and anchorage steel were the same as those used in the flexural component of the model, with the exception that the relationships for the bond section were stress-displacement relationships and not stress-strain relationships. The details of the stress-displacement envelopes used for the cyclic response of the bond section are discussed in Section 3.2.

7.3.2 Evaluation with Lehman and Moehle (2000) Dataset

The ability of the proposed distributed-plasticity modeling strategy (Chapter 4) to model the cyclic response of columns was first evaluated by comparing the measured and calculated responses of the well-confined column tests performed by Lehman and Moehle (2000) (Section 4.1). Key statistics of this evaluation are provided in Table 7.1.

Table 7.1 Cyclic response statistics for distributed-plasticity model

	Lehman Subset			Bridge Columns		
	E_{force}	$abs(E_{energy})$	E_{energy}	E_{force}	$abs(E_{energy})$	E_{energy}
mean (%)	13.44	22.23	-19.09	16.13	26.02	-23.69
min (%)	7.69	3.11	-57.63	6.63	1.34	-109.97
max (%)	20.16	57.63	12.56	44.71	109.97	13.36
n	8	8	8	37	37	37

The measured and calculated force-deformation responses for the 8 columns tests in this dataset are shown in Figure 7.3. As seen in the figure, the calculated response accurately models column behavior at lower ductilities and low cycles. However, at larger deformations and increased cycling, the calculated response fails to capture the effect of column softening. In the standard implementation there is no parameter to account for this degradation. The influence of degradation is illustrated further in Figure 7.4. In this figure, the percentage of the total force error (E_{force}) attributed to cycles at various ductilities is plotted for the eight columns in the dataset. As seen in the figure, most of the error is attributed to the cycles beyond a ductility of 7. The total error could be significantly reduced by adding a modeling component that accounts for degradation due to cycling at high levels of ductility.

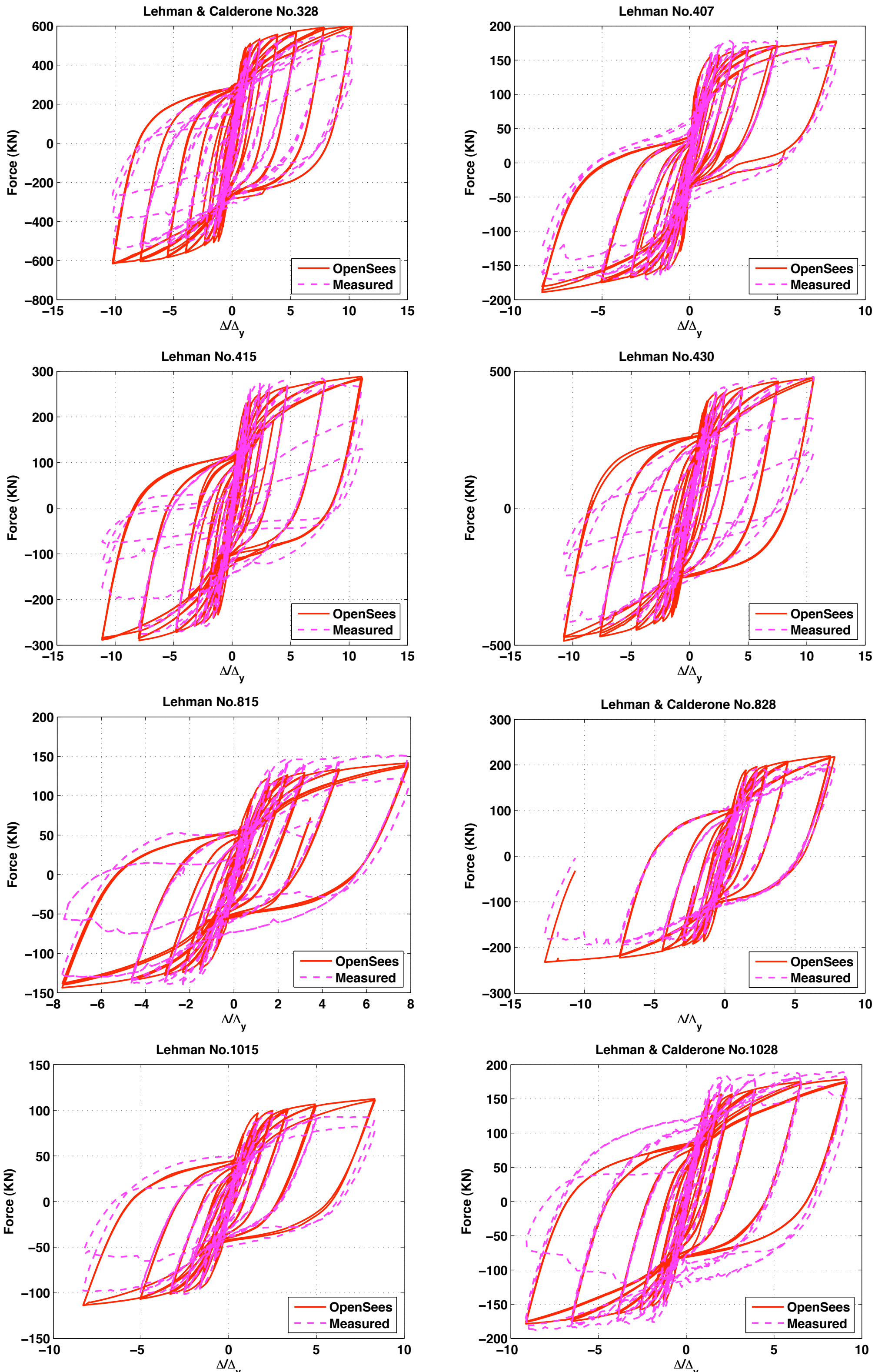

Fig. 7.3 Force-deformation responses for Lehman and Moehle dataset using distributed-plasticity column model and Giuffre-Menegotto-Pinto steel model

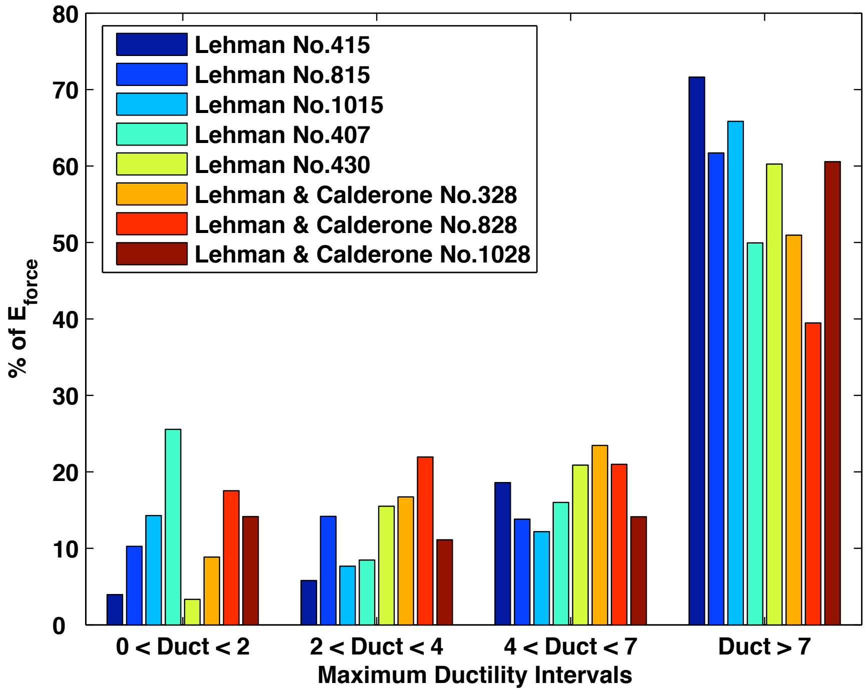

Fig. 7.4 Error distribution for distributed-plasticity model

7.3.3 Evaluation with Bridge Column Dataset

The ability of the proposed distributed-plasticity (Chapter 4) modeling strategy to model the cyclic response of columns was evaluated by comparing the measured and calculated responses of the bridge columns discussed in Section 1.3. The measures of model accuracy used in this evaluation are described in Section 7.2. Key statistics of this evaluation are provided in Table 7.1. The measured and calculated force-deformation histories for the the column tests with the minimum and maximum E_{force} values are provided in Figure 7.5.

To evaluate the effectiveness of the distributed-plasticity modeling strategy further, the error values (E_{force} and E_{energy}) were plotted versus maximum displacement ductility in Figure 7.6. Six outliers can be observed in the figure, and are highlighted by using a filled-in symbol. The outliers have E_{force} values greater than 25%, and are all from the same test series conducted by Cheok and Stone (1986). The force-displacement response of one of the outliers is presented in Figure 7.5. These column tests were subjected to cycling at high levels of ductility, resulting in significant strength and stiffness degradation. As discussed earlier, the proposed modeling strategy does not capture this effect.

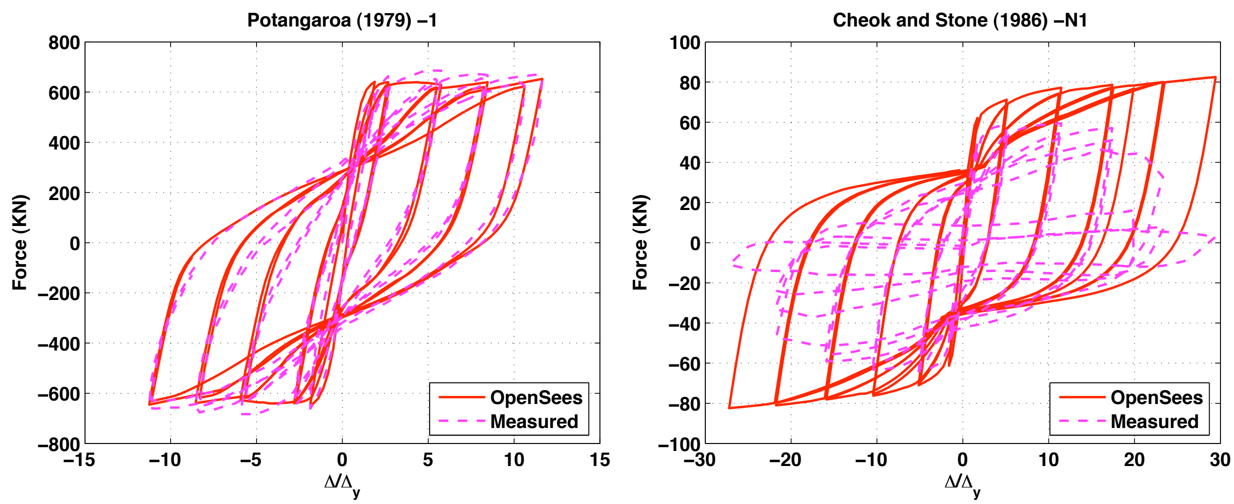

(a) $E_{force} = 6.63\%$ (b) $E_{force} = 44.71\%$

Fig. 7.5 Force-deformation histories for column tests with minimum and maximum E_{force} values using distributed-plasticity model

The accuracy measures were plotted versus key column properties to determine the influence of these parameters on model accuracy (figures 7.7 and 7.8). As seen in the figures, E_{force} appears to increase with an increase in ρ_{eff} and decrease with an increase in f_c'. The opposite trends are observed in the E_{energy} terms. However, these trends are governed by the outliers and are significantly less pronounced when the outliers are removed.

7.4 EVALUATION OF LUMPED-PLASTICITY COLUMN-MODELING STRATEGY

7.4.1 Model Description

The total hysteretic response of the lumped-plasticity modeling strategy (Chapter 6) depends on the cyclic response of the fiber section assigned to the plastic hinge. The response of the fiber section depends on the cyclic response of the material models (i.e., Giuffre-Menegotto-Pinto for steel, and Karsan and Jirsa for concrete) described in Section 7.1. The proposed lumped-plasticity column-modeling strategy does not include a zero-length bond-slip section or an added shear-deformation component; therefore the entire cyclic response of the column depends on the cyclic response of the material constitutive models.

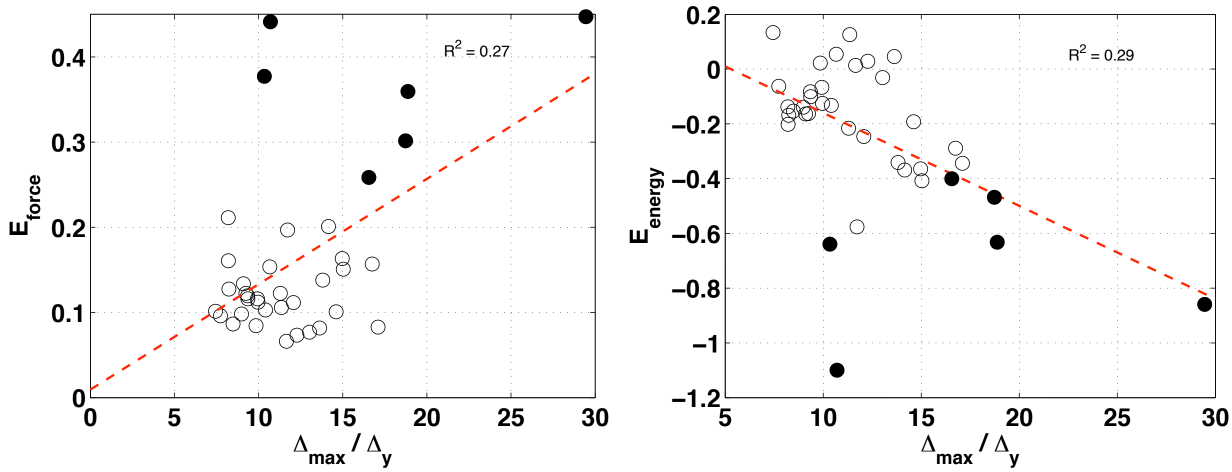

Fig. 7.6 Effect of maximum ductility on E_{force} and E_{energy} for distributed-plasticity model

7.4.2 Evaluation with Lehman and Moehle (2000) Dataset

The ability of the proposed lumped-plasticity modeling strategy to model the cyclic response of columns was first evaluated by comparing the measured and calculated responses of the well-confined column tests performed by Lehman and Moehle (2000) (Section 4.1). Key statistics of this evaluation are provided in Table 7.2.

Table 7.2 Cyclic response statistics for lumped-plasticity model

	Lehman Subset			Bridge Columns		
	E_{force}	$abs(E_{energy})$	E_{energy}	E_{force}	$abs(E_{energy})$	E_{energy}
mean (%)	13.17	21.36	-18.34	15.66	24.34	-21.37
min (%)	7.52	3.40	-50.26	6.47	0.42	-114.85
max (%)	20.11	50.26	8.68	46.05	114.85	20.14
n	8	8	8	37	37	37

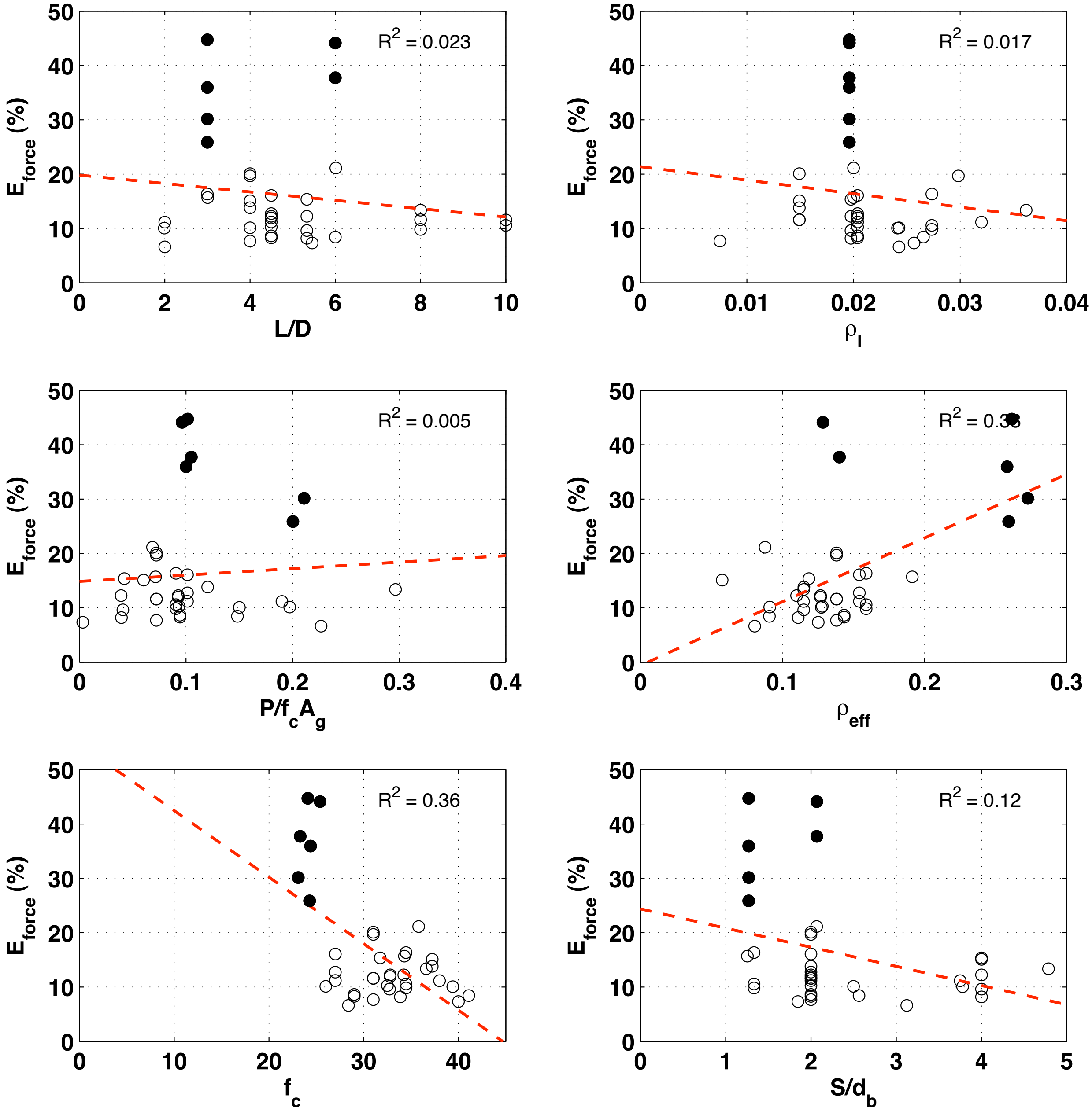

Fig. 7.7 Effect of key column properties on E_{force} using distributed-plasticity model

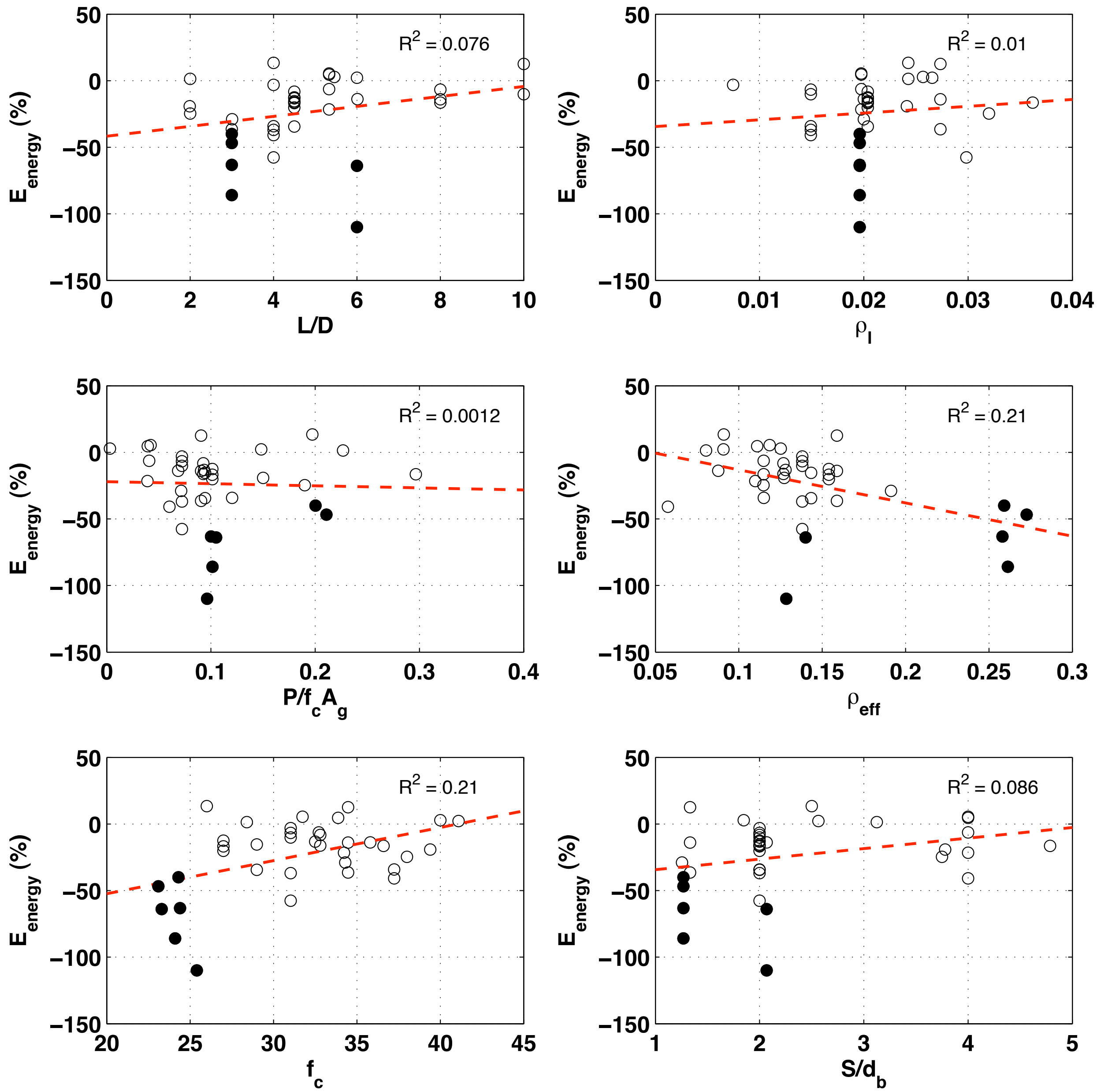

Fig. 7.8 Effect of key column properties on E_{energy} using distributed-plasticity model

The measured and calculated force-deformation responses for the 8 columns tests in this dataset are shown in Figure 7.9. Similar to the distributed-plasticity modeling strategy, the calculated response accurately models column behavior at lower ductilities and low cycles. However, at larger deformations and increased cycling, the calculated response fails to capture the effect of column softening. In the standard implementation there is no parameter to account for this degradation.

The model inaccuracy is illustrated further in Figure 7.10. In this figure, the percentage of the total force error (E_{force}) attributed to displacement cycles at various ductilities is plotted for the eight columns in the dataset. As seen in the figure, for all but one of the columns, most of E_{total} is attributed to the cycles beyond a ductility of 7. This suggests that the total error could be reduced if a modeling component was added that accounts for degradation due to cycling at high levels of ductility. The outlying column test (No. 407) did not degrade significantly, so the majority of the error was associated with initial cycles because the initial stiffness of this column is not accurately modeled.

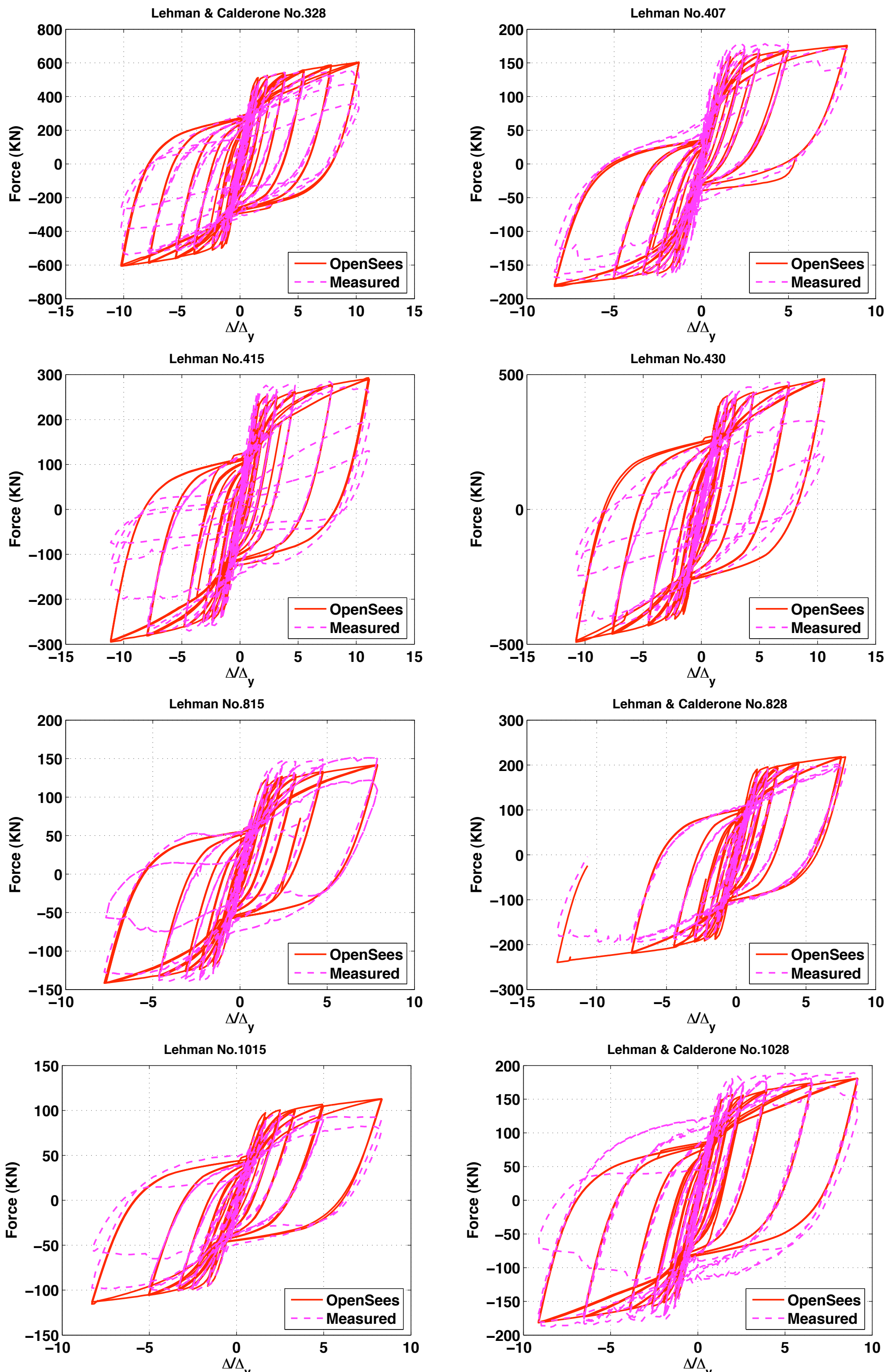

Fig. 7.9 Force-deformation responses for Lehman and Moehle dataset using lumped-plasticity column model and Giuffre-Menegotto-Pinto steel model

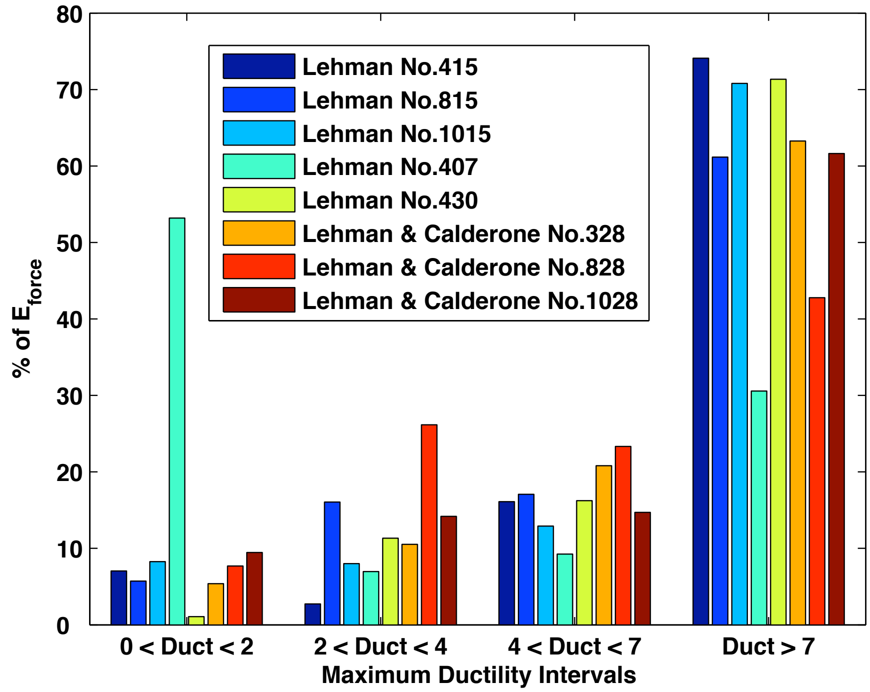

Fig. 7.10 Error distribution for lumped-plasticity model

7.4.3 Evaluation with Bridge Column Dataset

The ability of the proposed lumped-plasticity modeling strategy (Chapter 6) to model the cyclic response of columns was evaluated by comparing the measured and calculated responses of the bridge column dataset discussed in Section 1.3. Key statistics of this evaluation are provided in Table 7.2. The measured and calculated force-deformation histories for the the columns tests with the minimum and maximum E_{force} values are provided in Figure 7.11.

To evaluate the effectiveness of the lumped-plasticity modeling strategy further, the error values (E_{force} and E_{energy}) were plotted versus maximum displacement ductility in Figure 7.12. Six outliers can be observed in the figure, and are highlighted by using a filled-in symbol. The outliers have E_{force} values greater than 25%, and are all from the same test series conducted by Cheok and Stone (1986). The force-displacement response of one of the outliers is presented in Figure 7.11. These column tests were subjected to cycling at high levels of ductility, resulting in significant strength and stiffness degradation. As discussed earlier, the proposed modeling strategy does not capture this effect.

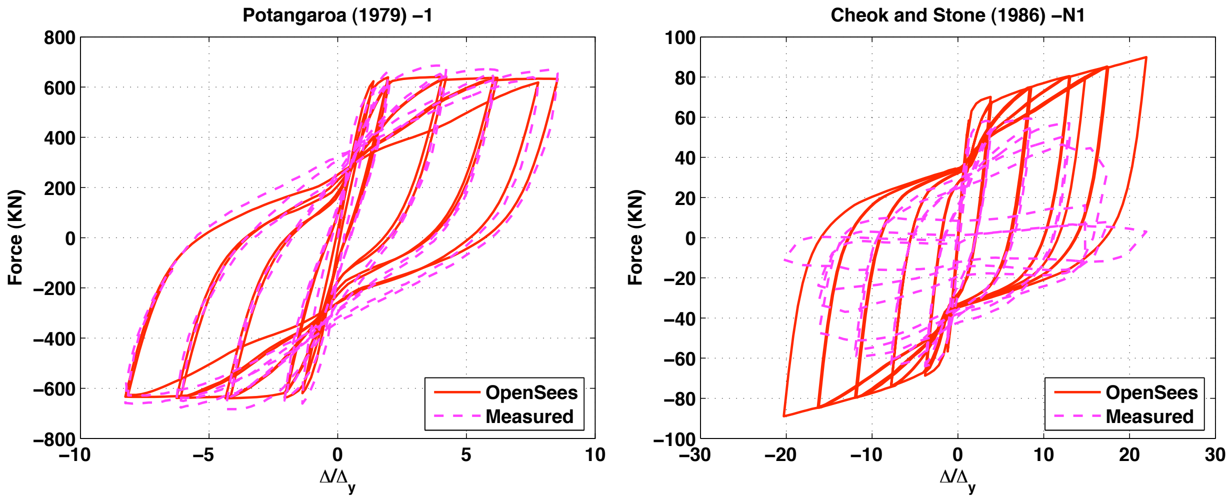

(a) $E_{force} = 6.47$ (b) $E_{force} = 46.05$

Fig. 7.11 Force-deformation histories for column tests with min and max E_{force} values using lumped-plasticity model

The accuracy measures were plotted versus key column properties to determine the influence of these parameters on model accuracy (figures 7.13 and 7.14). As seen in the figures, several trends can be observed. E_{force} appears to increase with an increase in ρ_{eff} and decrease with an increase in f'_c. The opposite trends are observed in the E_{energy} terms. However, these trends are governed by the outliers and are significantly less pronounced when the outliers are removed.

7.5 SUMMARY

The cyclic response of the proposed column-modeling strategies was considered in this chapter. The cyclic responses of the materials were presented first because the cyclic responses of the column models are governed by the cyclic responses of the material constitutive models. The cyclic response of the steel was modeled according to Giuffre-Menegotto-Pinto (Taucer et al. 1991), and the cyclic response of the compressive concrete was modeled according Karsan and Jirsa. These constitutive models do not model degradation due to repeated deformations at high ductility, and this is reflected in the accuracy of the column-modeling strategies at larger deformations. Modifications to the standard cyclic response of the steel are considered in Chapter 8.

The cyclic responses of the proposed column-modeling strategies were then evaluated by comparing the measured and calculated responses of the columns in the bridge column dataset

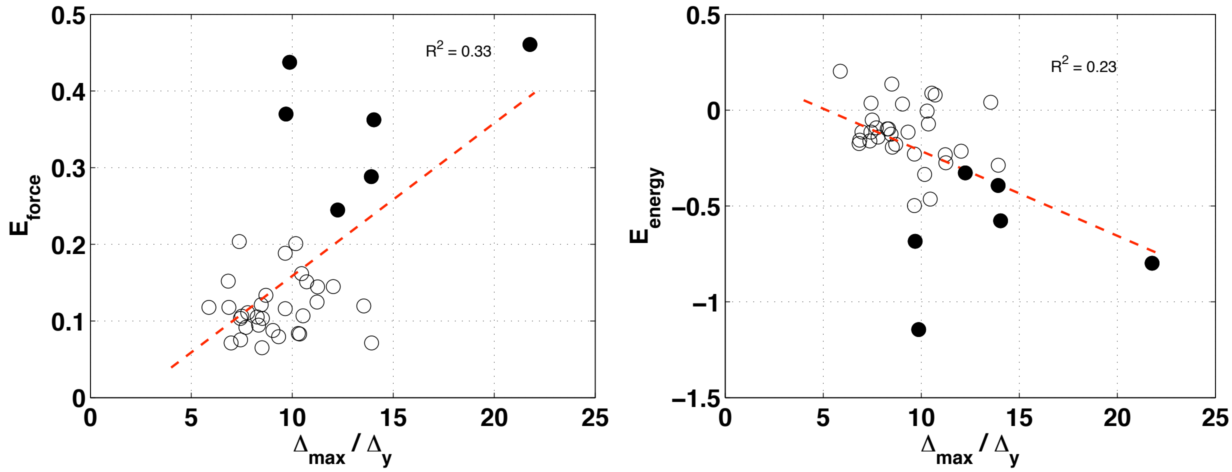

Fig. 7.12 Effect of maximum ductility on cyclic accuracy for lumped-plasticity model

(Section 1.3). Similar accuracy can be obtained using either of the distributed-plasticity or lumped-plasticity column-modeling strategies with standard cyclic material models. The mean values of the force errors (E_{force}) were 16.1% and 15.7% for the distributed-plasticity and lumped-plasticity models, respectively. The mean values of the energy errors (E_{energy}) were -23.7% and -19.9% for the distributed-plasticity and lumped-plasticity models, respectively.

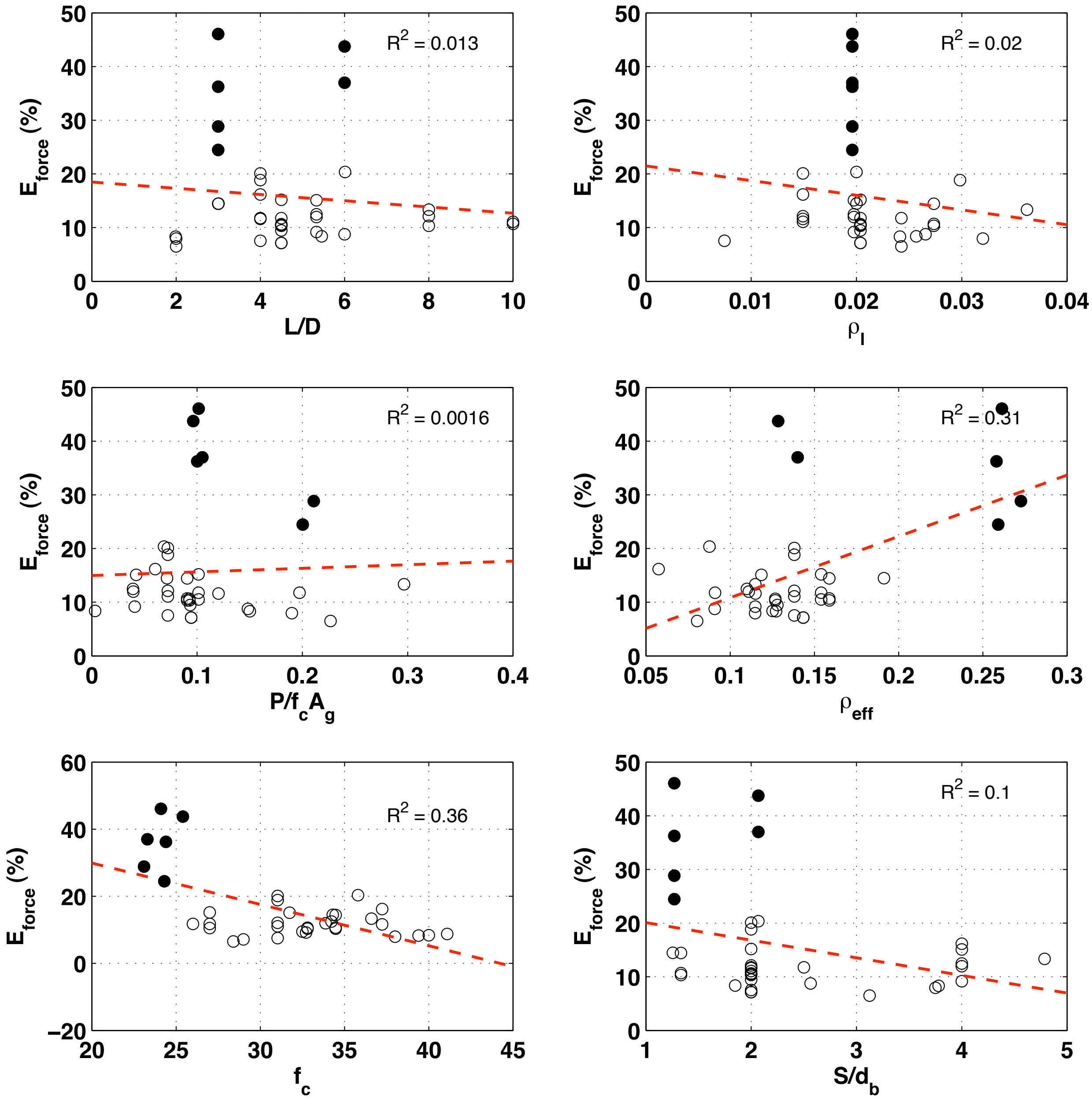

Fig. 7.13 Effect of key column properties on E_{force} using lumped-plasticity model

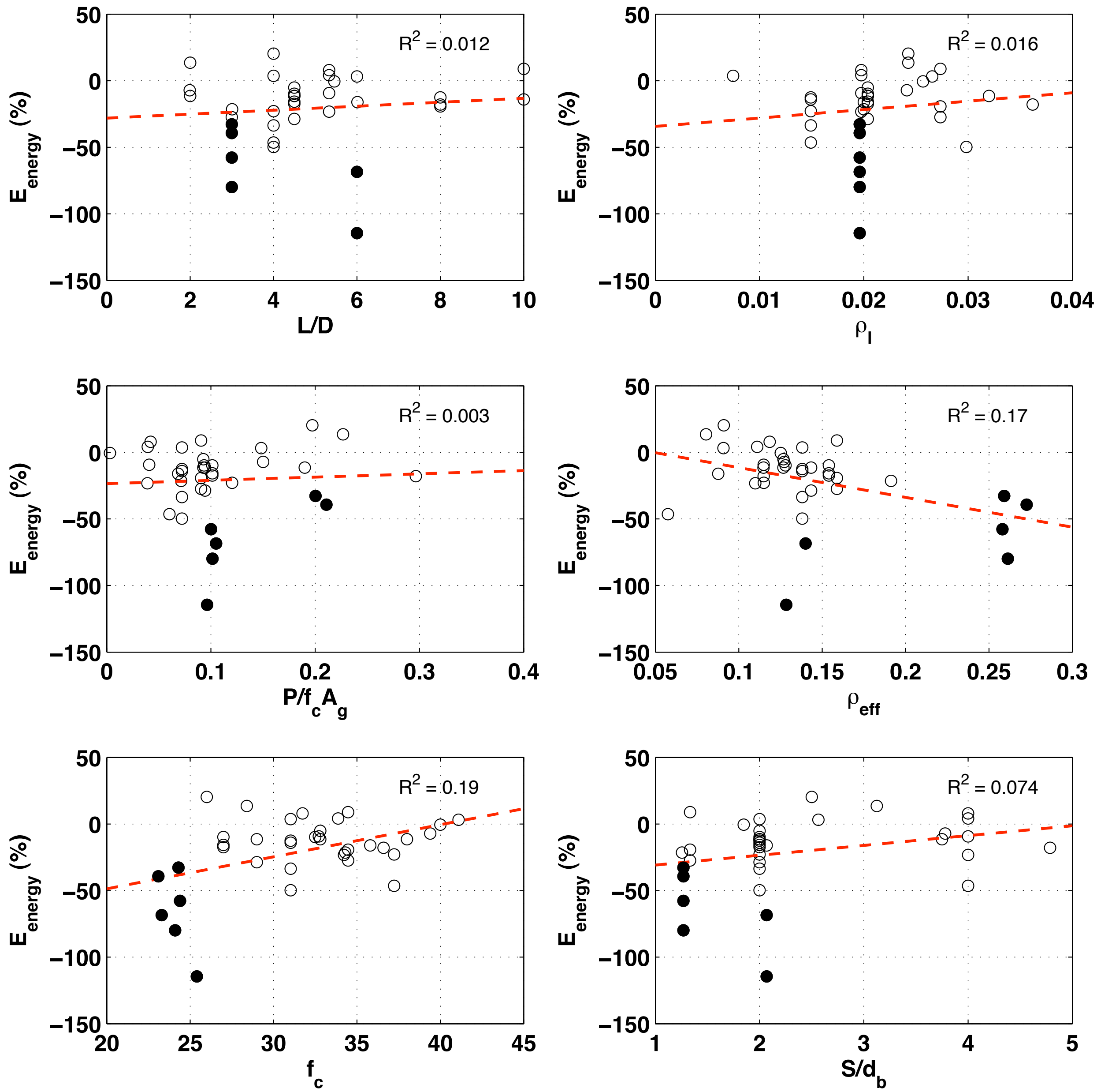

Fig. 7.14 Effect of key column properties on E_{energy} using lumped-plasticity model

8 Improved Cyclic Material Models

The cyclic responses of the fiber-model column-modeling strategies developed in this report depend on the cyclic responses of the material models. The proposed modeling strategies with standard cyclic material models (Karsan and Jirsa concrete, and Giuffre-Menegotto-Pinto steel) were evaluated in Chapter 7, and insufficiencies were identified. The cyclic response of the Giuffre-Menegotto-Pinto steel does not model degradation due to bar fracture and cycling, while the Karsan and Jirsa concrete model does not model imperfect crack closure.

In this chapter, a new steel model proposed by Mohle and Kunnath (2006) will be calibrated and evaluated. The Karsan and Jirsa concrete model will be modified to model imperfect crack closure, and a parametric study will be carried out to demonstrate the effects of this modification.

8.1 CALIBRATION OF MOHLE AND KUNNATH (2006) STEEL MODEL

To enhance the calculated cyclic response of the proposed modeling strategies, a more complex steel constitutive model that accounts for cyclic degradation (Mohle and Kunnath 2006) was implemented. In this section, the cyclic response of the Mohle and Kunnath (2006) steel model is demonstrated, and key cyclic modeling parameters are identified and calibrated. The response of the Mohle and Kunnath (2006) model depends on the calculated plastic-strain history of the bar, and the strains calculated with the distributed-plasticity strategy are inaccurate in columns with perfectly-plastic or degrading section behavior (Section 3.1.1). Therefore, the calibration and evaluation of this model was only carried out using the lumped-plasticity modeling strategy.

8.1.1 Cyclic Response of Model

The Mohle and Kunnath (2006) steel constitutive model is based on the steel model proposed by Chang and Mander (1994). The model can be used to account for isotropic hardening, diminishing yield plateau, the Bauschinger effect, degrading strength and stiffness due to bar buckling, and degrading strength and stiffness due to cycling. Within the model, bar buckling can be modeled according to models proposed by Dhakal and Maekawa (2002), or Gomes and Appleton (1997). The degradation of strength and stiffness due to cycling was calculated according to the Coffin and Manson fatigue model.

Because of numerical errors in the current implementation of the steel model in OpenSees (v.1.7.0), the isotropic hardening component and bar-buckling components were neglected. However, the Bauschinger effect and the degradation of the steel due to cycling were modeled. The Bauschinger effect was modeled using the model parameters suggested by Mohle and Kunnath (2006).

The Mohle and Kunnath (2006) steel model uses a cyclic fatigue model proposed by Coffin and Manson to model the effects of cycling on bar fracture. According to the Coffin and Manson theory, a bar is assumed to fracture when the damage factor D reaches a value of 1.0. The damage factor D is defined below.

$$D = \sum \left(\frac{\varepsilon_p}{C_f} \right)^{\frac{1}{\alpha}} \tag{8.1}$$

where: the half-cycle plastic-strain is defined as

$$\varepsilon_p = \varepsilon_t - \frac{\sigma_t}{E} \tag{8.2}$$

ε_t and σ_t are the total change in half-cycle strain and stress as illustrated in Figure 8.1(a). C_f and α are factors used to relate the number of half cycles till fracture to ε_p. This relationship is illustrated in Figure 8.1(b).

In addition to fracture fatigue, the Mohle and Kunnath (2006) model accounts for loss in strength due to cumulative damage. This degradation is controlled by the degradation parameter, ϕ_{SR}, as illustrated in Figure 8.1(c). This parameter is defined in the following equation, where C_d

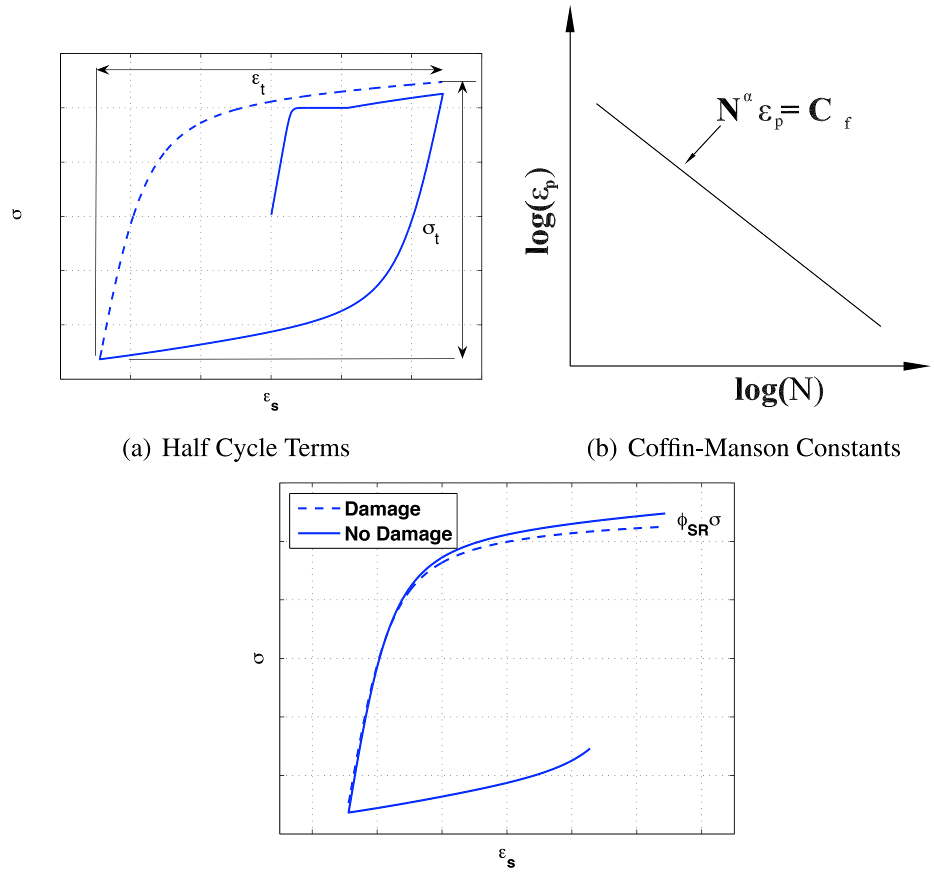

(a) Half Cycle Terms (b) Coffin-Manson Constants

(c) Strength Reduction Factor

Fig. 8.1 Coffin and Manson parameters (based on Mohle and Kunnath, 2006)

is a factor that is calibrated with experimental results.

$$\phi_{SR} = \sum \left(\frac{\varepsilon_p}{C_d} \right)^{\frac{1}{\alpha}} \tag{8.3}$$

The key modeling parameters identified in the previous discussion are presented below, and the effects of these parameters are demonstrated in Figure 8.2.

Damage Strain Range Constant, α is used to relate damage from one strain range to an equivalent damage at another strain range. This parameter is obtained from the calibration with material tests, and is usually constant for a material type. For this research the value proposed by Mohle and Kunnath (2006) is used, $\alpha = 0.506$.

Ductility Constant, C_f adjusts the number of cycles to bar failure. The effect of this parameter

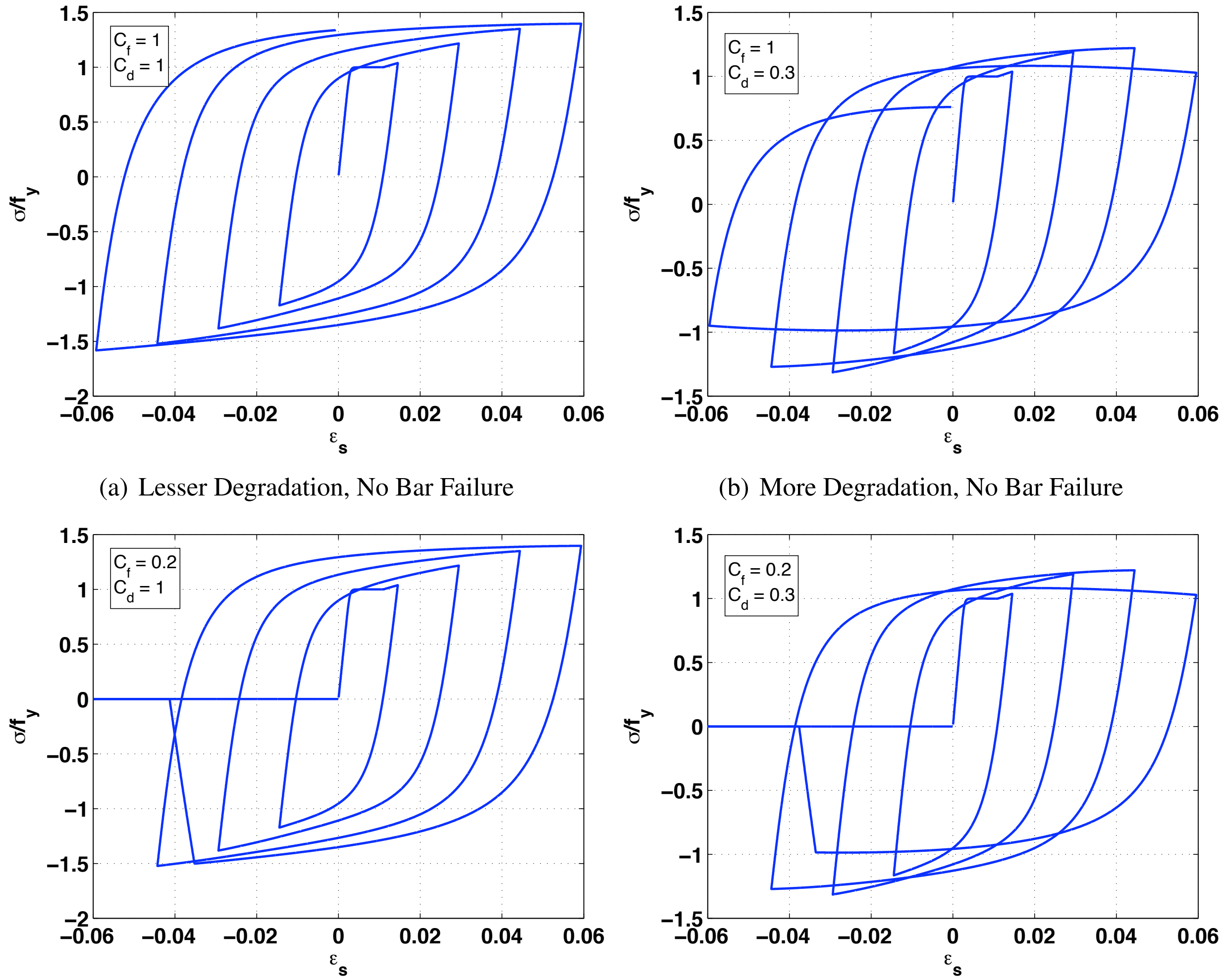

(a) Lesser Degradation, No Bar Failure

(b) More Degradation, No Bar Failure

(c) Lesser Degradation, Bar Failure

(d) More Degradation, Bar Failure

Fig. 8.2 Effect of Coffin and Manson parameters on cyclic response of steel

is demonstrated by comparing figures 8.2(a) with 8.2(c), and 8.2(b) with 8.2(d). A higher value for C_f results in a larger number of cycles to failure.

Strength Reduction Constant, C_d controls the amount of degradation per cycle. The effect of this parameter is demonstrated by comparing figures 8.2(a) with 8.2(b), and 8.2(c) with 8.2(d). A higher C_d value will result in a lower reduction of strength for each cycle.

8.1.2 Optimization Strategy and Results

The Mohle and Kunnath (2006) steel model assumes that bar fracture occurs when the damage index, D (Equation 8.1) reaches a value of 1.0. The bar-fracture component of the Mohle and

Kunnath (2006) steel model was calibrated with a subset of 20 columns from the bridge column dataset in which bar fractures were reported. C_f was calibrated with this dataset by (1) calculating the cyclic force-deformation responses of the 20 columns in the dataset for $C_d = \infty$ and a given C_f value, (2) calculating the mean value of the damage indices at the observed displacements at the onset of bar fracture, (3) adjusting C_f accordingly and repeating procedure until the mean value of the damage indices at the onset of bar fracture is 1.0. This procedure resulted in an optimal value of $C_f = 0.255$. This value is nearly identical to the value recommended by Mohle and Kunnath (2006), $C_f = 0.26$.

The strength reduction constant (C_d) was calibrated with the 37 column tests in the bridge column dataset by minimizing the mean value of the force error term E_{force} with $C_f = 0.26$. This procedure resulted in an optimal value of $C_d = 0.45$.

Key accuracy statistics of the lumped-plasticity modeling strategy with the optimized Mohle and Kunnath (2006) model, are provided in Table 8.1 for the 8 column tests performed by Lehman and Moehle (2000), and for the 37 bridge columns. For illustration, the measured and calculated cyclic force-deformation responses of the 8 columns are shown in Figure 8.3. The accuracy of the lumped-plasticity column-modeling strategy using the Mohle and Kunnath (2006) steel model is compared to the accuracy using the standard steel model in the summary of this chapter (Section 8.3).

Table 8.1 Cyclic response statistics (Kunnath steel with lumped-plasticity model)

	Lehman Subset			Bridge Columns		
	E_{force}	$abs(E_{energy})$	E_{energy}	E_{force}	$abs(E_{energy})$	E_{energy}
mean (%)	11.06	14.75	-7.42	11.98	12.88	-9.34
min (%)	7.37	0.32	-33.84	5.15	0.14	-69.68
max (%)	16.24	33.84	24.75	29.45	69.68	24.75

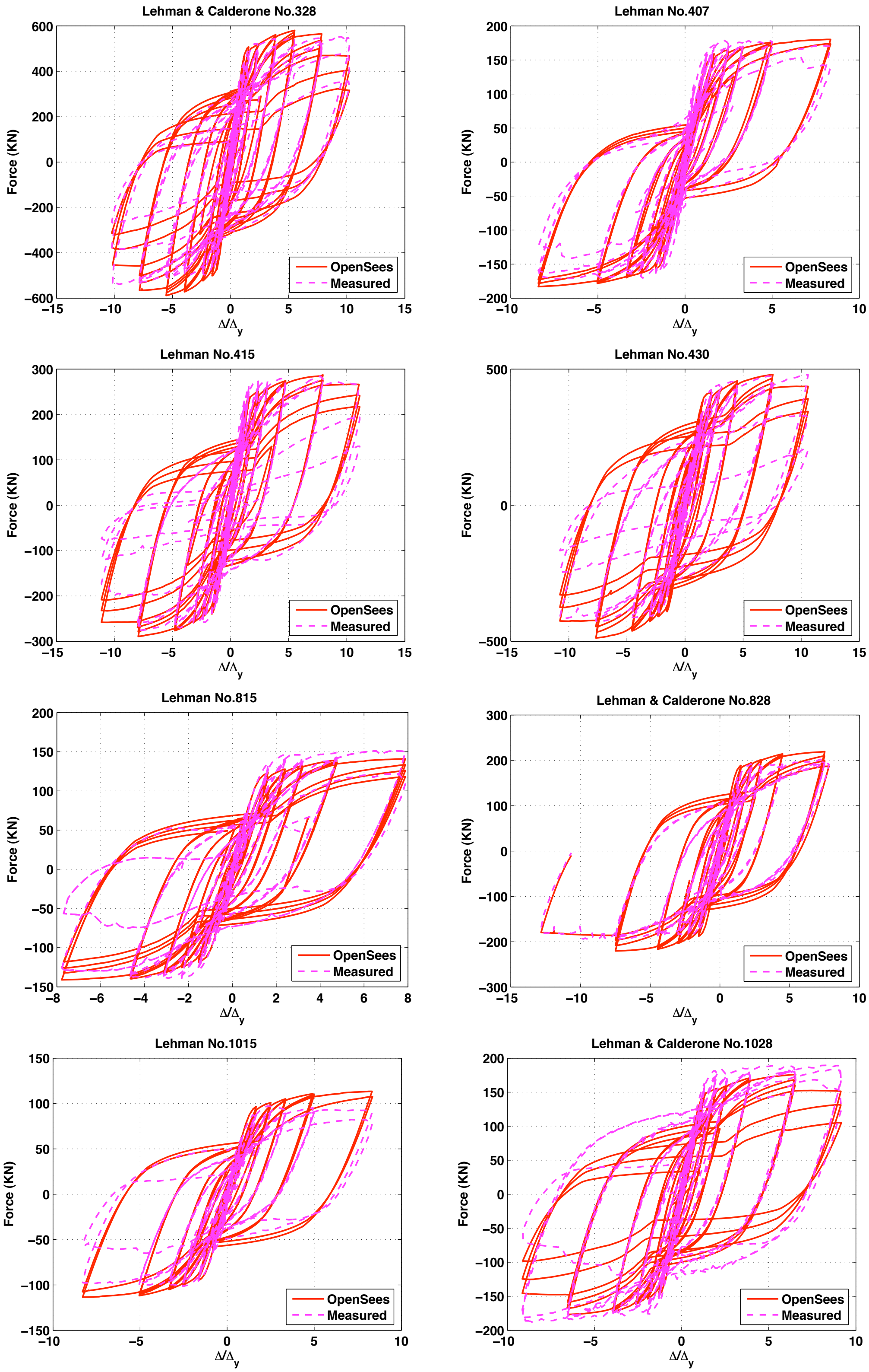

Fig. 8.3 Force-deformation response, Kunnath steel model

8.2 IMPERFECT CRACK CLOSURE

Tension cracks in concrete can become partially filled with small particles of concrete sediments and shear deformations in the column may result in misaligned cracks, causing some load to be transferred across the cracks before they fully close. The standard concrete model developed as part of this project (Popovic's curve with Mander constants, and Karsan and Jirsa cyclic properties) does not account for this phenomenon. The standard concrete model was modified to account for this increase in strength and stiffness. The component of the model that accounts for the early increase in strength is based on the model proposed by Stanton (1979).

8.2.1 Modified Concrete Model

The stress-strain response of the modified concrete model is illustrated in Figure 8.4, along with the strain history used for the demonstration, and the resulting stiffness history. This response is defined by the following rules.

1. The cyclic stress-strain curves in compression are contained within an envelope defined by the Popovic's curve. The concrete is assumed to have tension strength with exponentially decreasing strength beyond ultimate tensile stress. This envelope response is described in Section 2.2.2.
2. The unloading and reloading response of the concrete in tension is not modified from the standard implementation. This response is defined in Section 7.1.
3. The unloading and reloading response of the concrete in compression is governed by stiffnesses E_u and E_r, and strains ε_1, ε_2, ε_3, and ε_4. Each of these is illustrated in Figure 8.4(a), and described below.

   · E_u is the unloading stiffness defined by the Karsan and Jirsa concrete model.

   · E_r is the reloading stiffness. This value is calculated such that reloading follows a straight line from the reloading strain to (ε_1, f_1). This stiffness can be calculated as follows.

$$E_r = \frac{f_1}{\varepsilon_1 - \varepsilon_4} \tag{8.4}$$

- ε_1 and f_1 are the strain and stress at which the unloading curve departs from the envelope curve.
- ε_2 is the strain at which the stress becomes zero.
- ε_3 is the maximum strain reached during the unload-reload cycle.
- ε_4 is the strain at which reloading starts.

Opening and closing of cracks both occur at zero stress. When strains exceed ε_2, cracks are assumed to open. With perfect crack closure, they would close again when the strain returned to ε_2. However, with imperfect crack closure, compression would begin to be transmitted at a lower strain, ε_4. This reloading stress is calculated as follows.

$$\varepsilon_4 = \varepsilon_2 + r(\varepsilon_3 - \varepsilon_2) \tag{8.5}$$

where: r is the proportion of the crack filled by sediment, $0 \leq r \leq 1.0$, $(\varepsilon_3 - \varepsilon_2) \leq c_{max}$, and $\varepsilon_3 \leq 0.0$.

If reloading stops before reaching the envelope (Figure 8.4(a), point F), unloading occurs at a stiffness equal to the latest value of E_u. If unloading stops before the stress has reached zero (point G), then reloading follows a straight line from the reversal point to (ε_1, f_1).

The modeling parameters that can be varied to influence the reloading response of the concrete are r and c_{max}. The effect of varying r is illustrated in Figure 8.6. In this figure r is varied from 0.0 to 1.0, while c_{max} is held constant. A value of $r = 0.0$ assumes perfect crack closure and results in a model identical to the model described in Section 7.1. An increase in r assumes that cracks will begin closing sooner upon reversal. The crack is assumed to close immediately upon reversal when $r = 1.0$. Similarly, the effects of c_{max} are demonstrated in Figure 8.7. A value of $c_{max} = 0.0$ also assumes perfect crack closure.

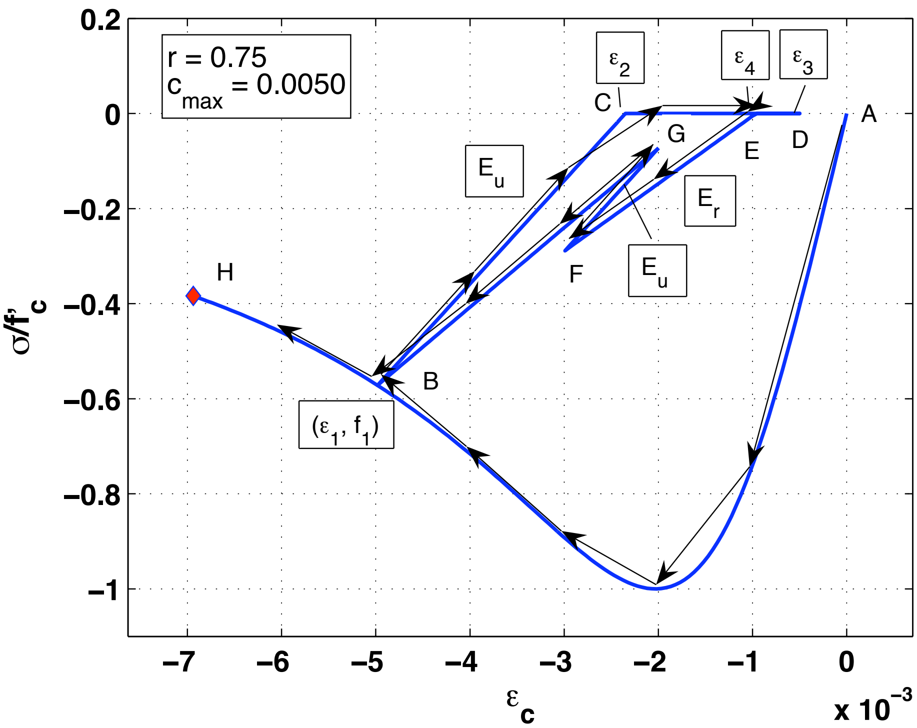

(a) Stress-strain response of concrete with imperfect crack Closure

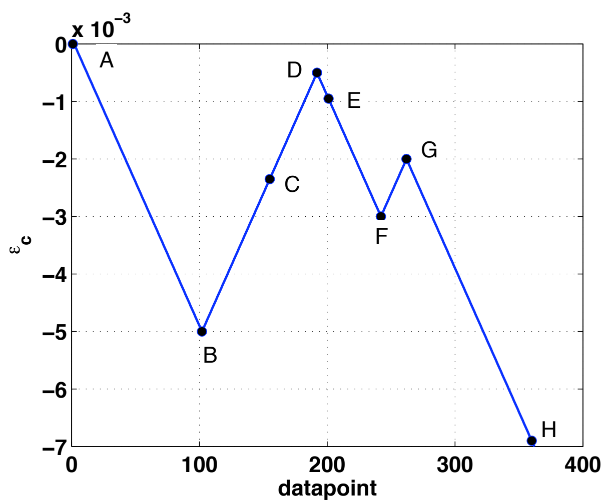

(b) Strain history for response

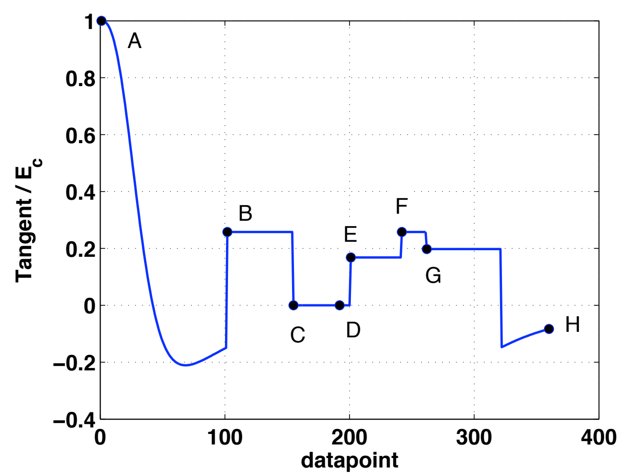

(c) Tangent history of response

Fig. 8.4 Cyclic response of concrete with imperfect crack closure

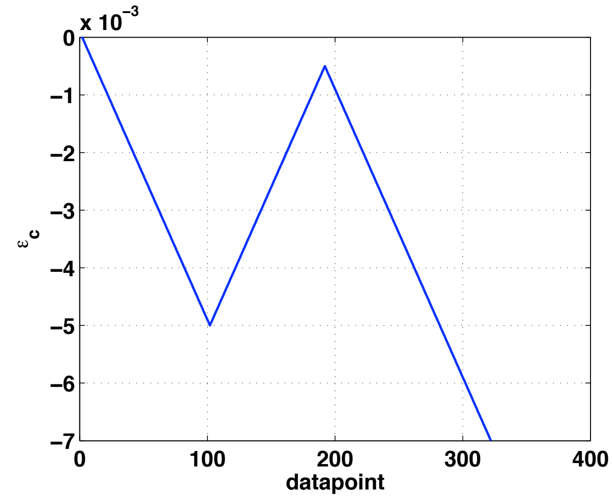

Fig. 8.5 Strain history for demonstration of imperfect crack closure properties

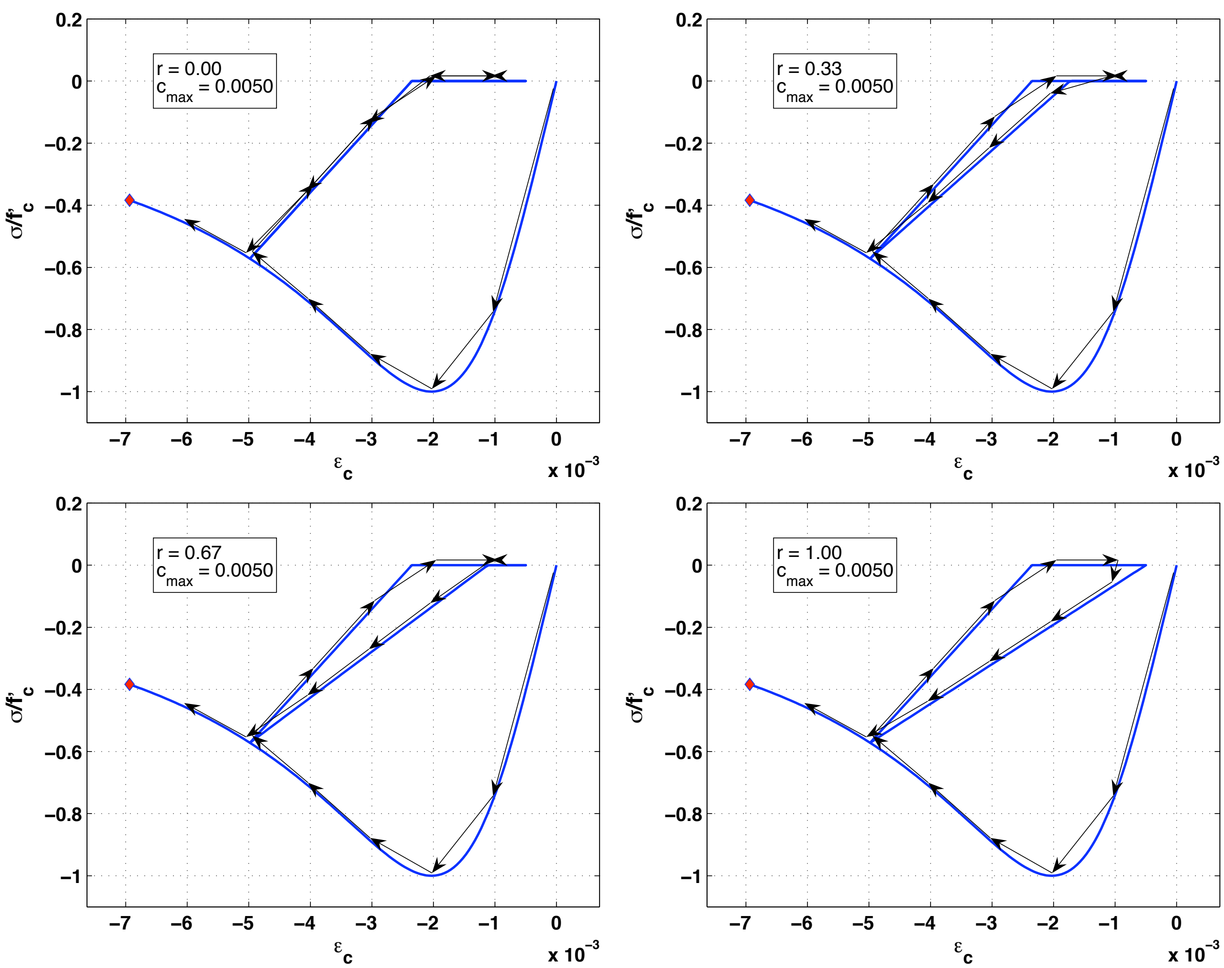

Fig. 8.6 Effect *r* on concrete stress-strain response

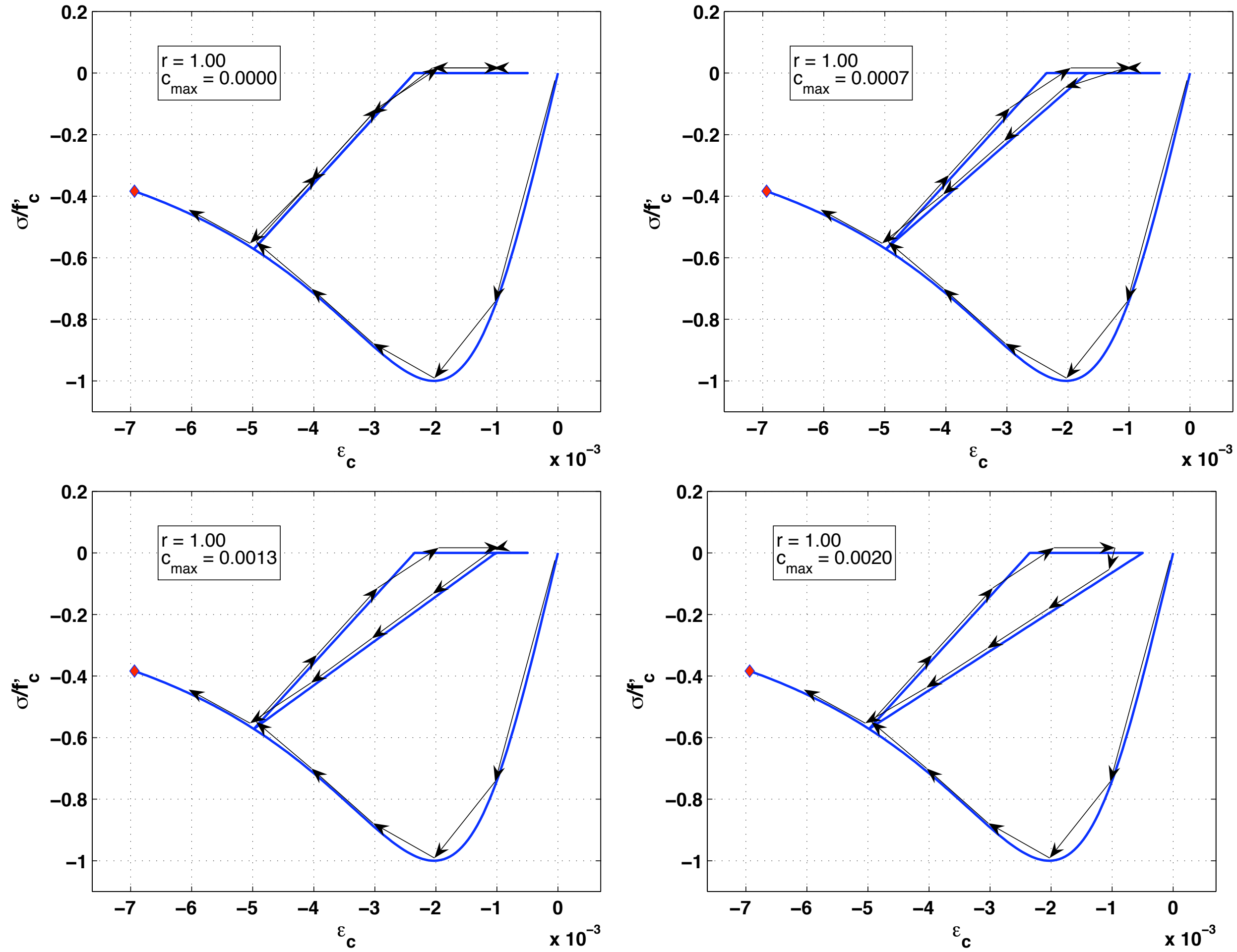

Fig. 8.7 Effect effect c_{max} on concrete stress-strain response

8.2.2 Parametric Study of Imperfect Crack Closure Parameters

For this project, a parametric study was carried out to demonstrate the effects of r and c_{max} on model accuracy. For this study, the lumped-plasticity column-modeling strategy was used with the Mohle and Kunnath (2006) steel to model the 8 column tests performed by Lehman and Moehle (2000). The modified concrete model was used, and the parameters r and c_{max} were systematically varied to demonstrate their influence. The effect of r is demonstrated in Figure 8.8. For this analyses c_{max} was set to 0.005. In this figure, the mean values of E_{force} and E_{energy} are plotted versus multiple values of r. As seen in this figure, r does not significantly affect E_{force}. In contrast, r does seem to affect E_{energy}. As r increases, E_{energy} gets further away from 0.0. At $r = 1.0$, E_{energy} is nearly 15% smaller (i.e., less accurate) than when $r = 0.0$.

In a similar fashion, the mean values of E_{force} and E_{energy} are plotted versus c_{max}. For this analysis $r = 0.5$. The parameter c_{max} does not significantly influence E_{force}; however it slightly affects E_{energy}. As c_{max} increases from 0.0 to 0.005, E_{energy} decreases by 15%.

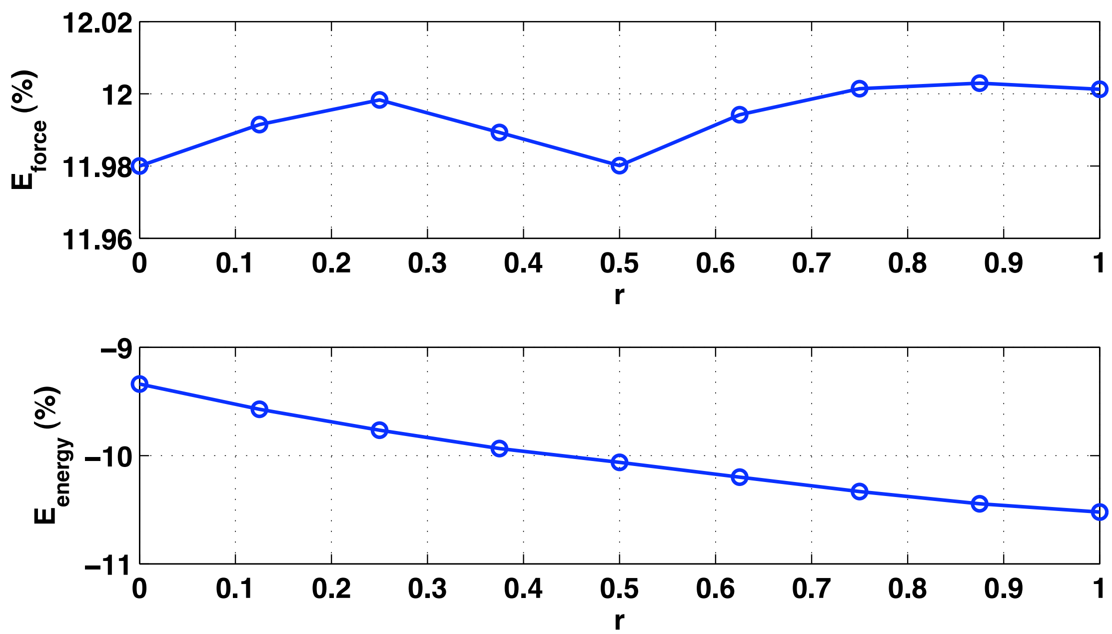

Fig. 8.8 Effect of *r* on overall model accuracy (lumped-plasticity, Kunnath steel)

This study indicates that imperfect crack closure does not have a significant effect on the accuracy of pseudo-static reinforced concrete column models. However, this phenomenon may affect the calculated dynamic response of columns more significantly. This will be studied further in a later chapter (Chapter 10).

8.3 SUMMARY

The cyclic modeling inaccuracies identified in Chapter 7 were addressed in this chapter. A steel material model proposed by Mohle and Kunnath (2006), which accounts for degradation due to cycling, was presented, calibrated, and evaluated. The use of this more complex steel constitutive model improved the accuracy of the lumped-plasticity column-modeling strategy. The mean force error (E_{force}) decreased from 15.7% with the standard steel model to 12.6% with the Mohle and Kunnath (2006) steel model and calibrated parameters ($C_f = 0.26$ and $C_d = 0.45$). The mean energy error (E_{energy}) was improved from -19.9% to -4.5%.

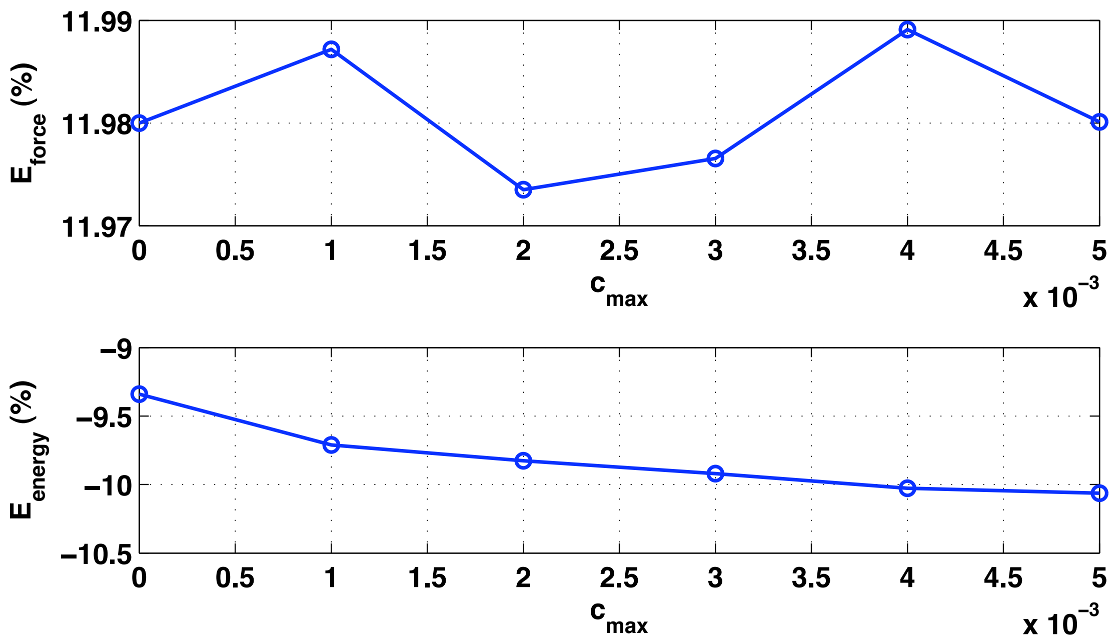

Fig. 8.9 Effect of c_{max} on overall model accuracy (lumped-plasticity, Kunnath steel)

A concrete model that accounts for imperfect crack closure was also developed and evaluated. The modifications to the standard Karsan and Jirsa cyclic material behavior to account for imperfect crack closure did not significantly affect the accuracy of the lumped-plasticity modeling strategy. It is possible that these modifications will affect the calculated residual displacements for shake-table tests (Chapter 10).

9 Column Flexural Damage

To implement performance-based earthquake engineering for reinforced concrete bridges, it is necessary to accurately predict column damage and assess the probability of reaching particular levels of damage. This chapter develops and evaluates several methods that correlate engineering demand parameters to damage measures. The engineering demand parameters considered in this chapter are drift ratio, plastic rotation, and longitudinal strain.

The damage measures considered in this report are cover spalling, longitudinal bar buckling, and longitudinal bar fracture. This report considered concrete cover spalling (Figure 9.1(a)) because it represents the first flexural damage state in which there are marginal safety implications, there may be a possible short-term loss of function, and the cost to repair concrete spalling could be significant. Buckling and fracture of the longitudinal bars (Figure 9.1(b)) were also considered because these levels of damage represent damage states in which safety implications are significant, partial replacement may be required, and a longer-term loss of function may occur.

9.1 ESTIMATES BASED ON DRIFT RATIO

Berry and Eberhard (2003) developed empirical equations to estimate deformations at bar buckling and cover concrete spalling based on theoretically expected trends in drift ratios, displacement ductilities, plastic rotations, and longitudinal strains. Because the drift-ratio equations are the simplest to use (e.g., no estimate of yield displacement), and because these equations were as accurate as the more complex methods, the drift-ratio equations were chosen as the most suitable for many practical situations. The bar-buckling equations were modified in Berry and Eberhard (2005). The resulting equations for the drift ratio at the onset of cover spalling ($\frac{\Delta_{spall}}{L}$) and bar

(a) Spalling of cover concrete

(b) Longitudinal bar buckling

(c) Longitudinal bar fracture

Fig. 9.1 Key flexural damage states (Ranf, 2006)

buckling ($\frac{\Delta_{bb}}{L}$) are provided below.

$$\frac{\Delta_{sp}^{calc}}{L}(\%) \cong 1.6\left(1-\frac{P}{A_g f_c'}\right)\left(1+\frac{L}{10D}\right) \tag{9.1}$$

$$\frac{\Delta_{bb}^{calc}}{L}(\%) = 3.25\left(1+k_e \rho_{eff}\frac{d_b}{D}\right)\left(1-\frac{P}{A_g f_c'}\right)\left(1+\frac{L}{10D}\right) \tag{9.2}$$

where k_e = 40 for rectangular columns and 150 for spiral-reinforced columns, $\rho_{eff} = \rho_s \frac{f_{ys}}{f_c'}$, ρ_s is the volumetric transverse reinforcement ratio, f_{ys} is the yield stress of the transverse reinforcement, f_c' is the concrete compressive strength, d_b is the diameter of the longitudinal reinforcement, D is the column depth, P is the axial load, A_g is the gross area of the cross section, and L is the distance from the column base to the point of contraflexure.

The dataset originally used in the calibration of the spalling equation contained 102 rectangular-reinforced columns and 40 spiral-reinforced columns. The ratios of the measured displacements at cover spalling to the displacements calculated with the proposed model (Equation 9.1) had a mean of 0.97 for rectangular columns with a c.o.v. of 43%, and a mean of 1.07 with a c.o.v. 35% for spiral-reinforced columns (Berry and Eberhard 2003).

The dataset originally used in the calibration of the buckling equation contained 62 rectangular-reinforced columns and 42 spiral-reinforced columns. The ratios of the measured displacements at bar buckling to the displacements calculated with the proposed model (Equation 9.2) had a mean of 1.01 and a coefficient of variation of 25% for rectangular-reinforced concrete columns. The corresponding mean and coefficient of variation for spiral-reinforced columns were 0.97 and 24%, respectively (Berry and Eberhard 2005).

The bridge column dataset used in this report is a subset of the dataset originally used to calibrate the drift-ratio equations described above. The accuracy statistics of the drift-ratio equations (9.1 and 9.2) applied to the bridge column dataset used in this report (29 observations of cover spalling and 33 observations of bar buckling) are presented in Table 9.1. In this table and throughout this chapter, the subscript *dam* is used to indicate a general damage state. For example, Δ_{dam}^{meas} would be Δ_{sp}^{meas} for the cover-spalling damage state. For the bridge dataset, the ratios

Table 9.1 Key accuracy statistics of drift-ratio equations with bridge column dataset

		Statistics of $\Delta_{dam}^{meas}/L\%$				Statistics of $\Delta_{dam}^{meas}/\Delta_{dam}^{calc}$			
Dataset	Damage State	min	max	mean	cov (%)	min	max	mean	cov (%)
Original Dataset	Cover Spalling	0.61	4.51	2.30	44.2	0.48	1.75	1.07	34.9
	Bar Buckling	2.31	14.62	6.59	43.2	0.46	1.62	0.97	24.0
Bridge Columns	Cover Spalling	0.75	4.17	2.34	38.9	0.48	1.75	1.07	34.9
	Bar Buckling	3.75	14.58	7.39	37.1	0.64	1.62	1.01	24.7
	Bar Fracture	3.75	12.30	7.63	25.9	0.60	1.48	0.97	20.0

of the measured displacements at cover spalling to the displacements calculated with the proposed model (Equation 9.1) have a mean of 1.07 and a coefficient of variation of 35%. The corresponding mean and coefficient of variation for bar buckling is 1.01 and 25%, respectively. The accuracy of equations 9.1 and 9.2 are nearly identical when applied to the smaller bridge column dataset.

As part of this project, an equation was developed to predict the drift ratio at the onset of bar buckling by recalibrating the coefficients of Equation 9.2 with the bridge column subset. The resulting equation is as follows.

$$\frac{\Delta_{bf}^{calc}}{L}(\%) = 3.5 \left(1 + 150\rho_{eff}\frac{d_b}{D}\right)\left(1 - \frac{P}{A_g f_c'}\right)\left(1 + \frac{L}{10D}\right) \tag{9.3}$$

The coefficient of variation of the ratios of measured to calculated (from Equation 9.3) displacements at the onset of bar fracture was 20.0% (Table 9.1).

Fragility curves are helpful in the design and assessment in performance-based earthquake engineering. Fragility curves help a designer answer the following question:

> *For a particular level of column deformation, what is the likelihood that the longitudinal reinforcement will have begun to buckle?*

Figure 9.2 shows the fragility curves for cover spalling, bar buckling, and bar fracture in spiral-reinforced columns for the dataset used in this project. In these figures, the Y-axis is the cumulative probability of cover spalling or bar buckling, and the X-axis is the ratio of $\frac{\Delta_{dam}^{meas}}{\Delta_{dam}^{calc}}$. If the database is assumed to be representative of the entire population of spiral-reinforced columns, this ratio can be interpreted as $\frac{\Delta_{dam}^{demand}}{\Delta_{dam}^{calc}}$. These plots also show the normal cumulative distribution functions (CDF) and the lognormal cumulative distribution functions.

In some situations, the normal CDF may fit the data better than the lognormal CDF. However, the normal CDF allows negative values of $\Delta_{dam}^{demand}/\Delta_{dam}^{calc}$ at low probabilities.

The ratios of measured to calculated displacements at the onset of cover spalling, bar buckling, and bar fracture are plotted versus key column properties in figures 9.3 and 9.5 to evaluate the effect of these properties on the accuracy of the proposed equations. As seen in Figure 9.3, the ratios of measured to calculated displacements increase with an increase in effective confinement ratio and decrease with an increase in concrete compressive strength. The effect of confinement on cover spalling is addressed later in this chapter. With respect to bar buckling (Figure 9.4), the ratios increase slightly with an increase in aspect ratio, longitudinal-reinforcement ratio, and concrete compressive strength. No significant trends are observed in the bar-fracture ratios.

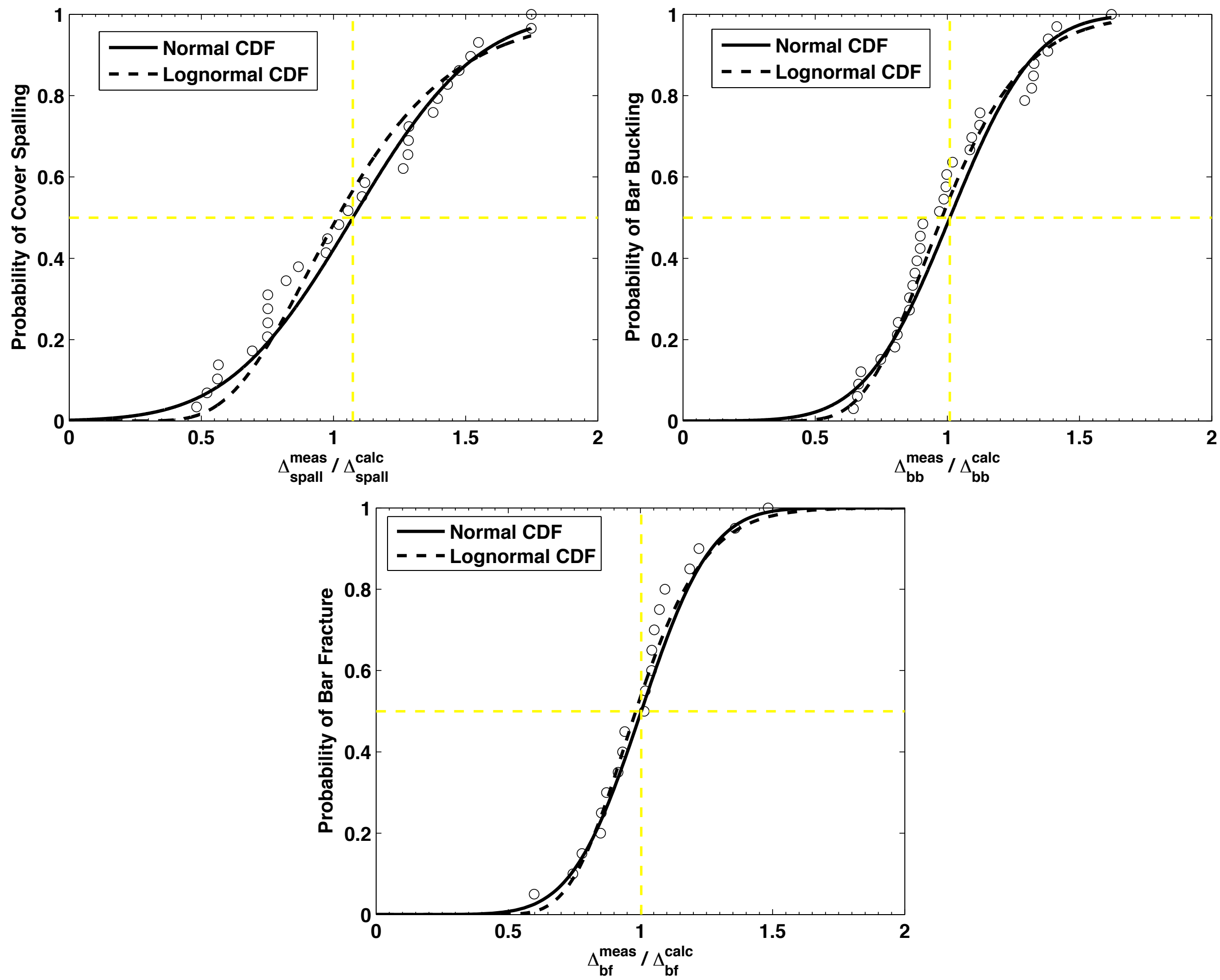

Fig. 9.2 Fragility curves for cover spalling, bar buckling, and bar fracture using drift-ratio equations

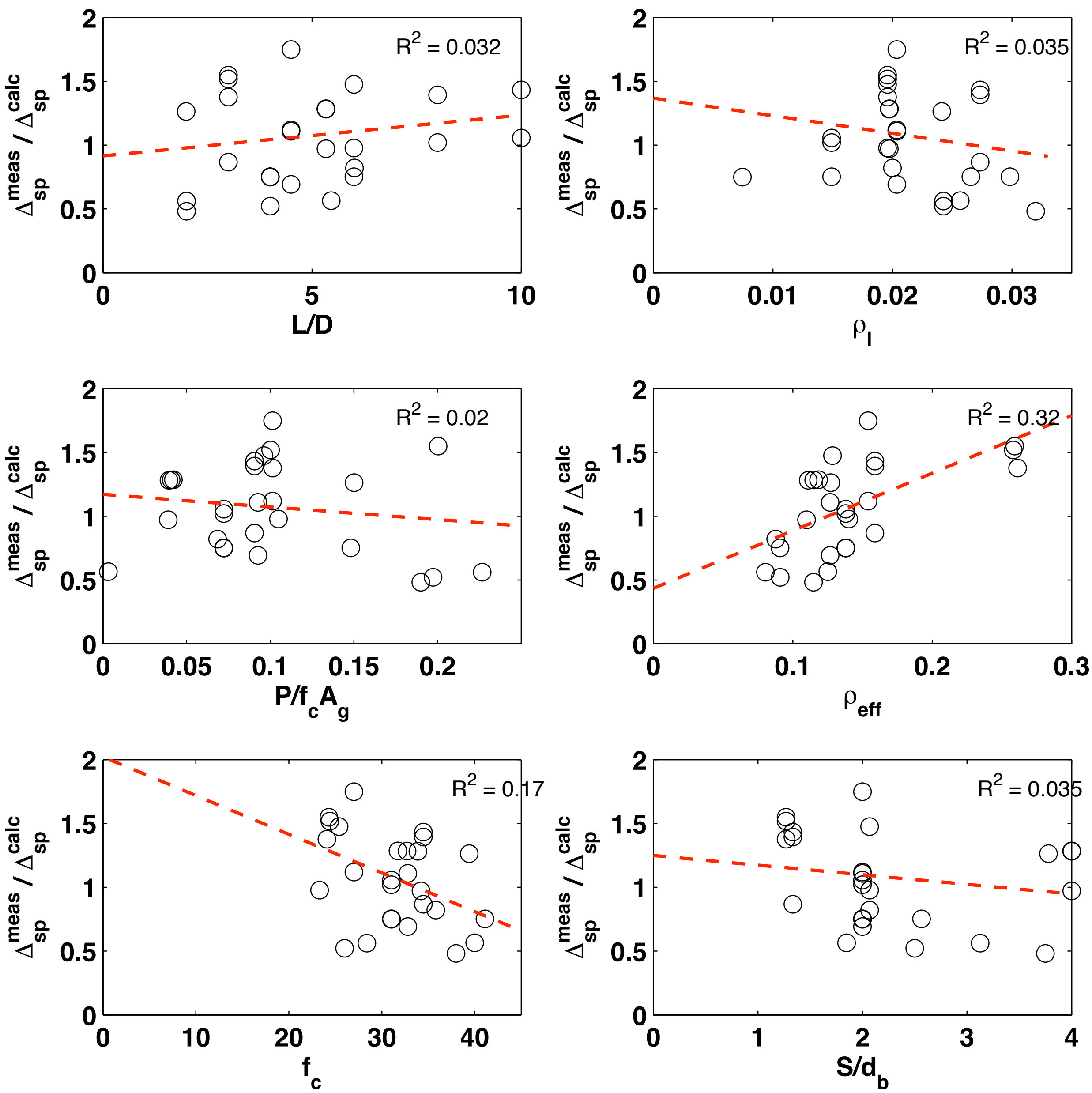

Fig. 9.3 Effect of key column properties on accuracy of drift-ratio cover-spalling equations

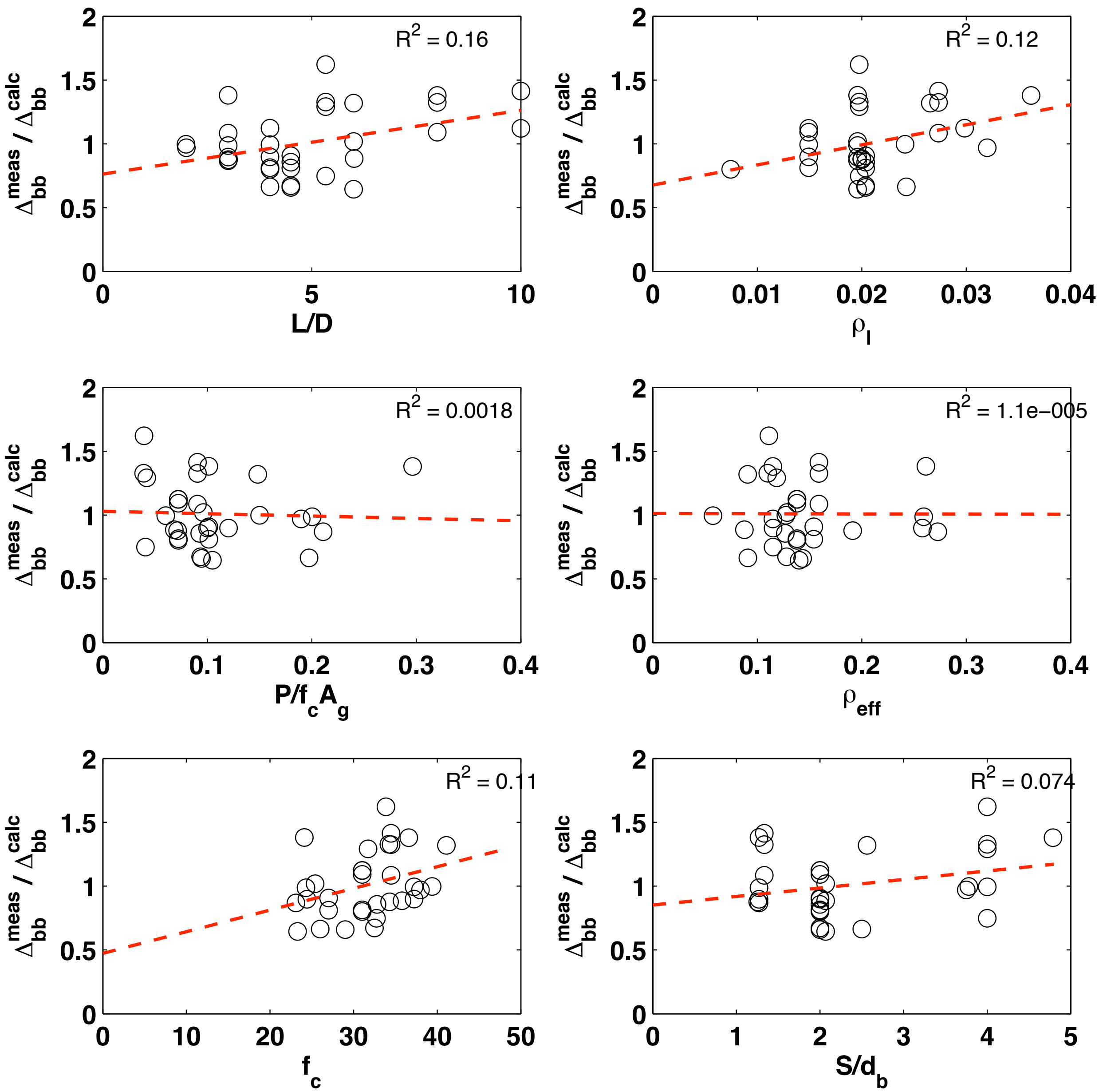

Fig. 9.4 Effect of key column properties on accuracy of drift-ratio bar-buckling equations

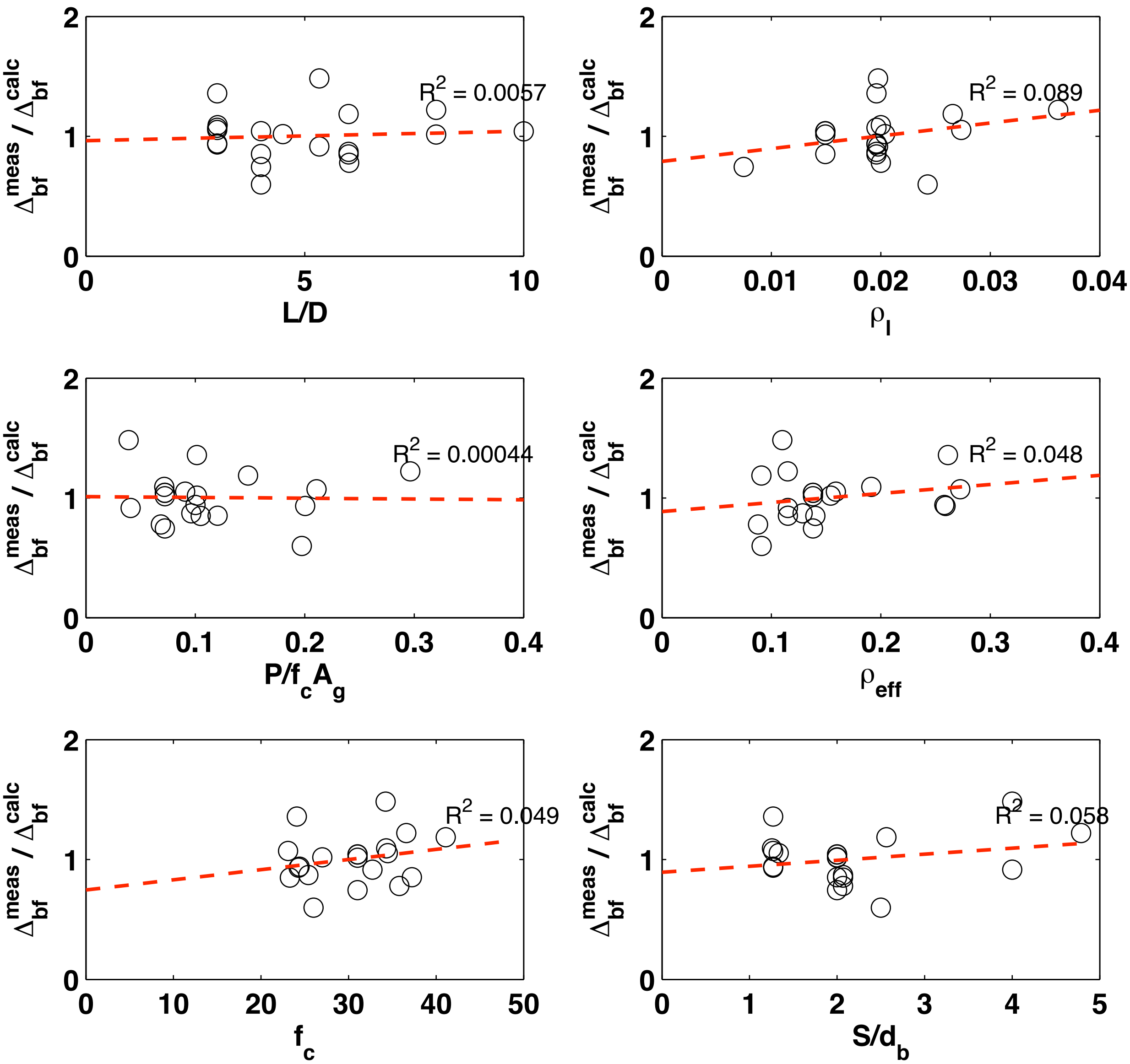

Fig. 9.5 Effect of key column properties on accuracy of drift-ratio bar-fracture equations

The drift-ratio equations provide a practical correlation between an engineering demand parameter and key damage states. However, the drift-ratio equations may not always be applicable, such as cases in which the distance to the point of contraflexure is unknown or varies. Therefore, similar damage estimates will be developed for other, more versatile engineering damage parameters: plastic rotations and longitudinal strain.

9.2 DAMAGE ESTIMATES BASED ON PLASTIC ROTATION

Empirical equations, similar to the drift-ratio equations, can be developed for the plastic rotation at the onset of particular damage states. This engineering demand parameter may be more versatile than drift ratio because plastic rotations can be calculated in a complex model more easily. The plastic rotations calculated with the distributed-plasticity modeling strategy (with no bond slip component) should be identical to the plastic rotations calculated with the lumped-plasticity formulation if the plastic curvatures calculated from the distributed-plasticity strategy are adjusted to account for localization in accordance to the method presented in Section 3.1.1. If the zero-length bond-slip section is used in the distributed-plasticity modeling strategy, the rotation due to bond slip must be added to the rotations recorded at the integration points, because these rotations will be relative rotations, and the following equations were developed for total rotations.

Berry and Eberhard (2003) demonstrated that the plastic rotation at the onset of damage ($\theta_{p\_dam}^{calc}$) should increase with an increase in aspect ratio (L/D) and key longitudinal-reinforcement properties ($f_y d_b/D$), and decrease with an increase in axial-load ratio ($P/A_g f'_c$), as indicated in Equation 9.4.

$$\theta_{p\_dam}^{calc} = C_0\left(\varepsilon_{dam}\right)\left(1+C_1\frac{P}{A_g f'_c}\right)^{-1}\left(1+C_2\frac{L}{D}+C_3\frac{f_y d_b}{D}\right) \tag{9.4}$$

where ε_{dam} is the strain at the onset of cover spalling (ε_{sp}) or bar buckling (ε_{bb}), and $C_0 - C_3$ are constants to be calibrated with experimental results.

In the following subsections, Equation 9.4 will be calibrated for cover spalling, bar buckling, and bar fracture. The corresponding equations were calibrated by obtaining values of $C_0 - C_3$ such that the coefficients of variation of the ratios of measured to calculated displacements at the onset of the particular damage states ($\Delta_{dam}^{meas}/\Delta_{dam}^{calc}$) were minimized. The calculated displacements at the onset of the damage states are the displacements associated with the calculated values of $\theta_{p\_dam}^{calc}$ from Equation 9.4.

9.2.1 Cover Spalling

The observed plastic rotations at the onset of cover spalling, $\theta_{p\_sp}^{meas}$, (calculated from the observed displacements at cover spalling) have a mean value of 1.50% with a coefficient of variation of 49.7% (Table 9.2). The mean value of the ratios of the measured displacements to the calculated displacements associated with the mean value of $\theta_{p\_sp}^{meas}$ is 0.98 with a coefficient of variation of 33.9%.

This estimate of the plastic rotation at the onset of cover spalling can be improved by considering the trends proposed in Equation 9.4. For cover spalling, ε_{sp} is not expected to vary with the amount of traverse or longitudinal reinforcement; therefore the plastic rotation at the onset of cover spalling can be approximated with the following simplified expression.

$$\theta_{p\_sp}^{calc} = C_0 \left(1 + C_1 \frac{P}{A_g f'_c}\right)^{-1} \left(1 + C_2 \frac{L}{D} + C_3 \frac{f_y d_b}{D}\right) \tag{9.5}$$

This equation was calibrated with the method discussed previously. The resulting coefficients and accuracy statistics are presented in Table 9.2. For comparison, the table includes the estimates based on the displacements calculated with the mean value of the plastic rotation at the onset of the particular damage states. This method is equivalent to setting C_0 in Equation 9.5 to the mean value of $\theta_{p\_sp}^{meas}$, and setting the other coefficients to zero.

Table 9.2 Results of plastic-rotation calibration

	Coefficients					$\theta_{p\_sp}^{meas}/\theta_{p\_sp}^{calc}$		$\Delta_{dam}^{meas}/\Delta_{dam}^{calc}$	
Methodology	C_0	C_1	C_2	C_3	C_4	mean	cov (%)	mean	cov (%)
mean θ_{p_sp}	0.015	-	-	-	-	1.00	49.7	0.98	33.9
Eq (9.5)	0.0095	0.001	0.08	0.015	-	0.99	48.1	0.99	33.3

Little accuracy is gained by utilizing the expected trends in plastic rotation at the onset of cover spalling (Equation 9.5). The coefficient of variation of $\Delta_{sp}^{meas}/\Delta_{sp}^{calc}$ with Equation 9.5 was 33.3%, which is only slightly more accurate than using the mean value of θ_{p_sp} (1.50%) to calculate the displacement at the onset of cover spalling, Δ_{sp}^{mean} (33.9%). Additionally, a slightly smaller coefficient of variation can be obtained using a constant plastic rotation of 1.20% (32.5%). Therefore, this value recommended for calculating the plastic rotation at the onset of cover spalling.

Fragility curves for estimates of the plastic rotations at the onset of cover spalling are shown in Figure 9.6. The figure on the left is the fragility curve for $\theta_{p\_sp}^{meas}/\theta_{p\_sp}^{calc}$, where $\theta_{p\_sp}^{calc} = 1.20\%$. The fragility curve on the right is for $\Delta_{sp}^{meas}/\Delta_{sp}^{calc}$, where Δ_{sp}^{calc} is the calculated displacement associated with $\theta_{p\_sp}^{calc} = 1.20\%$.

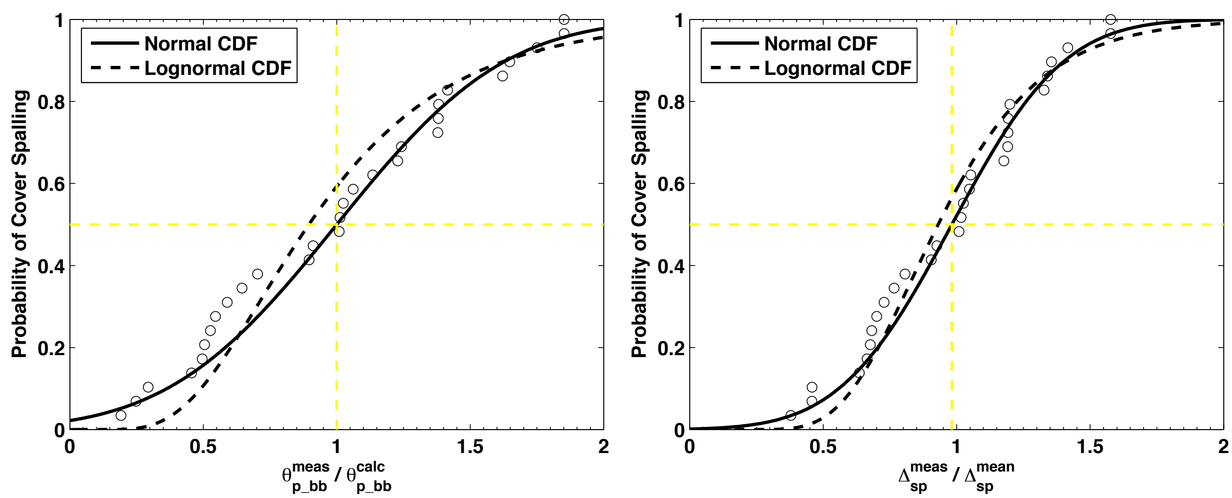

Fig. 9.6 Fragility curves for cover spalling and bar buckling using plastic rotation

The ratios of measured to calculated displacements (at the calculated plastic rotation) at the onset of cover spalling are plotted versus key column properties in Figure 9.7 to evaluate the effect of these properties on the accuracy of the proposed damage estimate. As seen in the drift-ratio estimates, the ratios of measured to calculated displacements increase with an increase in effective confinement ratio and decrease with an increase in concrete compressive strength.

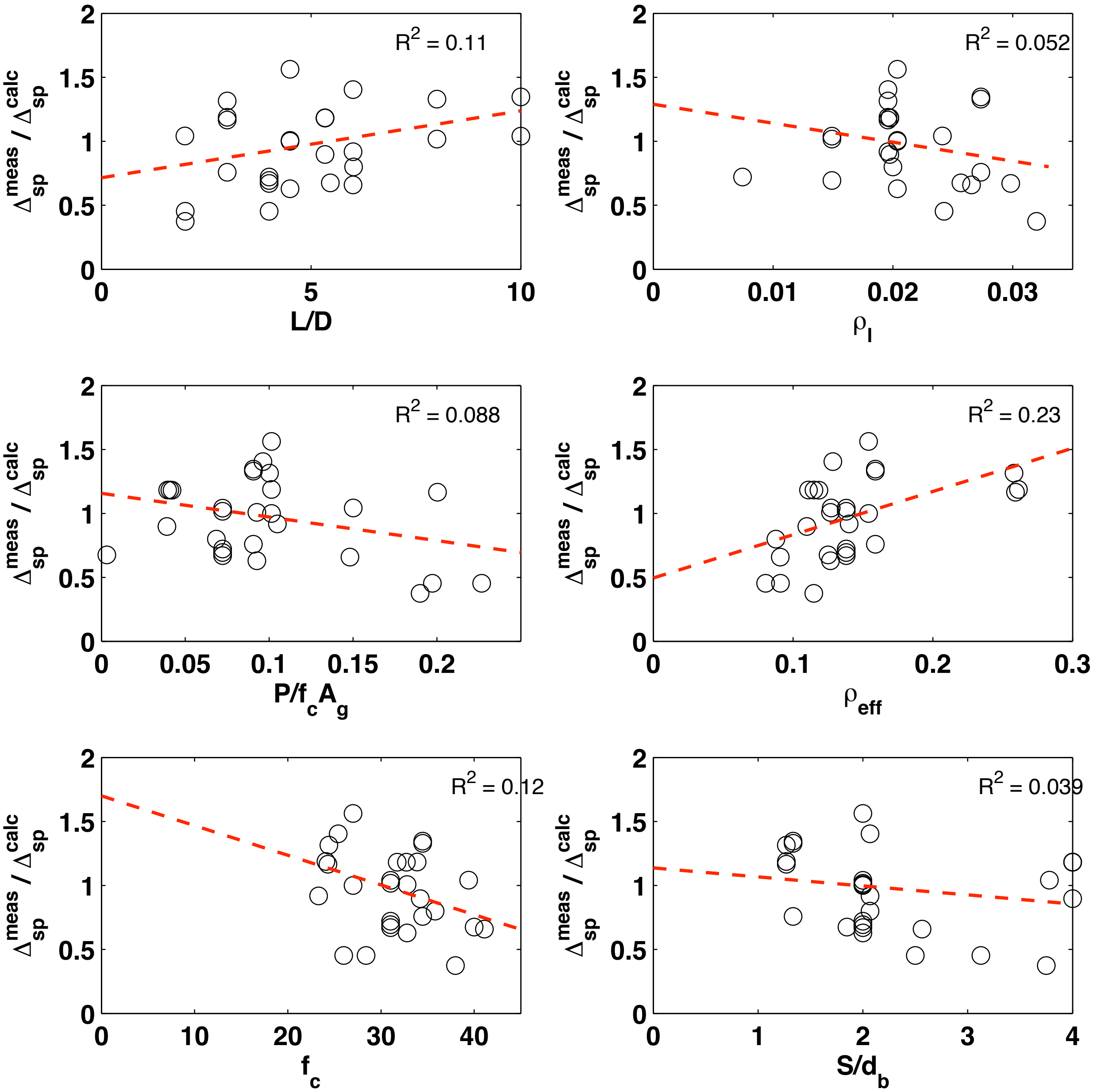

Fig. 9.7 Effect of key column properties on accuracy of plastic-rotation cover-spalling equations

9.2.2 Bar Buckling

The mean value and coefficient of variation of the observed plastic rotations at the onset of bar buckling ($\theta_{p\_bb}^{meas}$) were 6.50% and 39.1%, respectively. The mean and coefficient of variation of the ratios of measured displacements at the onset of bar buckling to the displacements associated with the mean value of $\theta_{p\_bb}^{meas}$ were 0.99 and 34.4%, respectively.

Estimates of the plastic rotation at the onset of bar buckling can be improved by considering the trends proposed in Equation 9.4. The plastic-rotation equation can be extended further for bar buckling by considering the effect of the confining steel on the strain at bar buckling. The strain at the onset of bar buckling is expected to increase with an increase in effective confinement ratio ($\rho_{eff} = \rho_s f_{ys}/f_c'$) as in the following equation.

$$\varepsilon_{bb} = \chi_1 + \chi_2 \rho_{eff} \tag{9.6}$$

By combining Equation 9.6 with Equation 9.4, simplifying, and combining constants, the following equation for the plastic rotation at the onset of bar buckling is obtained.

$$\theta_{p\_bb} = C_0 \left(1 + C_4 \rho_{eff}\right) \left(1 + C_1 \frac{P}{A_g f_c'}\right)^{-1} \left(1 + C_2 \frac{L}{D} + C_3 \frac{f_y d_b}{D}\right) \tag{9.7}$$

The coefficients in the bar-buckling equation (Equation 9.7) were previously calibrated by Berry and Eberhard (2005). However the coefficients obtained in their study were developed for a different model formulation and dataset. Therefore, the equations were recalibrated as part of this study with the bridge column dataset and new model formulation.

The resulting coefficients and accuracy statistics are presented in Table 9.3. For comparison, the table includes the estimates based on the displacements calculated with the mean value of $\theta_{p\_bb}^{meas}$. This method is equivalent to setting C_0 in equation 9.7 to the mean value of $\theta_{p\_bb}^{meas}$, and setting the other coefficients to zero. The coefficients for Equation 9.7 previously calibrated by Berry and Eberhard (2005) are also included in the table.

As seen in Table 9.3, Equation 9.7 provides an accurate means of estimating bar buckling. The coefficient of variation of the ratios of measured to calculated displacements at the onset of bar buckling was 21.1%. This is an improvement to the 25% coefficient of variation obtained using

Table 9.3 Results of plastic-rotation calibration

Methodology	Coefficients					$\theta_{p\_bb}^{meas}/\theta_{p\_bb}^{calc}$		$\Delta_{dam}^{meas}/\Delta_{dam}^{calc}$	
	C_0	C_1	C_2	C_3	C_4	mean	cov (%)	mean	cov (%)
mean $\theta_{p\_bb}^{meas}$	0.0650	-	-	-	-	1.00	39.1	0.99	34.4
Berry and Eberhard, 2005	0.006	3.1	0.65	0.23	7.19	0.93	24.9	0.94	22.1
Eq (9.7)	0.0010	1.30	1.30	3.00	7.30	0.98	23.3	1.02	21.1
Eq (9.8)	0.0009	-	1.30	3.00	7.30	1.01	24.1	1.01	21.6

the drift-ratio equations in the previous section (Equation 9.2).

Equation 9.7, with the previously calibrated coefficients from Berry and Eberhard (2005), does not accurately predict (on average) the displacement at the onset of bar buckling for the smaller bridge column dataset used in this report. The mean value of ratios of measured to calculated displacements is 0.94 with a coefficient of variation of 22.1%. This is similar to the coefficient of variation obtained for the recalibrated equation, but the mean is not 1.00. The reason for this difference is because the smaller dataset used in this project does not include high axial load tests, whereas the previous dataset did. All of the columns in the smaller dataset have $\frac{P}{A_g f_c'} \leq 0.30$ (Section 1.3). By removing the higher axial load tests, the previously calibrated equation is less accurate because the influence of the axial-load ratio term was so significant. The axial-load coefficient in the recalibrated coefficients is smaller than in the original equation, and does not significantly affect the calculated rotation. Therefore, for column with axial-load ratios less than 0.30, a simpler equation in which the axial-load term is neglected can be developed.

$$\theta_{p\_bb} = C_0 \left(1 + C_4 \rho_{eff}\right) \left(1 + C_2 \frac{L}{D} + C_3 \frac{f_y d_b}{D}\right) \tag{9.8}$$

The accuracy statistics and calibrated coefficients for this equation are provided in Table 9.3. Little accuracy is lost using this equation. The coefficient of variation of measured to calculated displacements increased slightly from 21.1% using Equation 9.7 to 21.6% using Equation 9.8. Simpler equations including only one and two column properties were also studied. The best estimate of $\theta_{p\_bb}^{calc}$ using only two column properties included the effects of L/D and ρ_{eff}, as in the following equation.

$$\theta_{p\_bb} = C_0 \left(1 + C_4 \rho_{eff}\right) \left(1 + C_2 \frac{L}{D}\right) \tag{9.9}$$

The accuracy statistics and calibrated coefficients for this equation are also provided in Table 9.3.

As seen in the table, if only two column properties are used in the estimate, the accuracy of the damage estimate is reduced. The coefficient of variation of the measured to calculated displacements are reduced from 21.6% using Equation 9.8 to 27.3% using Equation 9.9.

The best one property estimate of $\theta_{p\_bb}^{calc}$ included the effects of the column aspect ratio (L/D) as in the following equation.

$$\theta_{p\_bb} = C_0\left(1 + C_2\frac{L}{D}\right) \tag{9.10}$$

The calibrated coefficients and accuracy statistics for this equation are also provided in Table 9.3. In this case, the coefficient of variation of the ratios of measured to calculated displacements is 29.5%, significantly larger than the 21.6% using three column properties.

Equation 9.8 provides a practical compromise between simplicity and accuracy; this estimate is simpler than Equation 9.7, and little accuracy is lost when using this simpler equation. However, this equation was developed for columns with axial-load ratios less than 0.30. This should be considered when applying this equation because previous research (Berry and Eberhard 2005) indicates that axial load influences the plastic rotation at the onset of damage.

For comparison and simplicity, an equation was developed that has a similar form to the simplified drift-ratio equations of the previous section (Equation 9.2). The resulting equation is as follows.

$$\theta_{p\_bb}^{calc}(\%) = 2.75\ \left(1 + 150\rho_{eff}d_b/D\right)\left(1 - P/A_g f_c'\right)\ (1 + L/10D) \tag{9.11}$$

Using this equation, the mean and coefficient of variation of the ratios of measured to calculated plastic rotations were 1.01 with a coefficient of variation of 28.3%, whereas the mean and coefficient of variation of the ratios of measured displacements to calculated displacements associated with the rotations calculated with Equation 9.12 were 1.01 with a coefficient of variation of 24.3%.

Fragility curves for estimates of the plastic rotations at the onset of bar buckling are shown in Figure 9.8. The figure on the left is the fragility curve for $\theta_{p\_bb}^{meas}/\theta_{p\_bb}^{calc}$, where $\theta_{p\_bb}^{calc}$ is calculated with Equation 9.8 and coefficients in Table 9.3. The fragility curve on the right is for $\Delta_{bb}^{meas}/\Delta_{bb}^{calc}$, where Δ_{bb}^{calc} is the calculated displacement associated with $\theta_{p\_bb}^{calc}$.

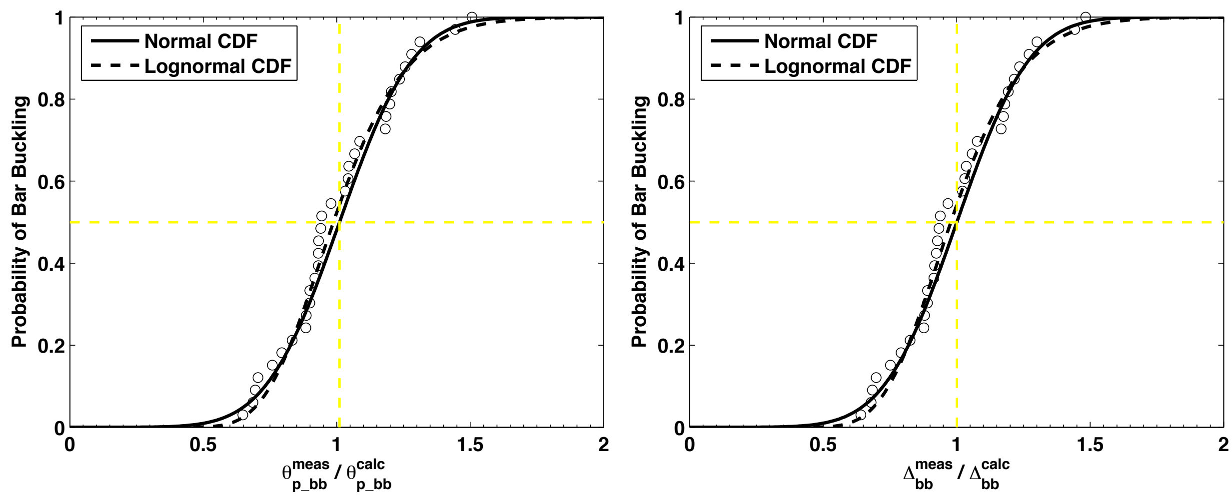

Fig. 9.8 Fragility curves for bar buckling using plastic rotation

The ratios of measured to calculated displacements (from the calculated plastic rotation) at the onset of bar buckling are plotted versus key column properties in Figure 9.9 to evaluate the effect of these properties on the accuracy of the proposed damage estimate. No significant trends are observed in the data.

9.2.3 Bar Fracture

The plastic-rotation equations developed for the onset of bar buckling (equations 9.7 and 9.8) were calibrated to estimate the onset of bar fracture. The results of this calibration are presented in Table 9.4.

Table 9.4 Results of plastic-rotation calibration

	Coefficients					$\theta^{meas}_{p\_bf}/\theta^{calc}_{p\_bf}$		$\Delta^{meas}_{dam}/\Delta^{calc}_{dam}$	
Methodology	C_0	C_1	C_2	C_3	C_4	mean	cov (%)	mean	cov (%)
mean θ_{p_bf}	0.0650	-	-	-	-	1.00	39.1	0.99	34.4
Eq (9.7)	0.0010	1.0	2.4	1.7	6.7	1.00	17.5	0.98	15.2
Eq (9.8)	0.0009	-	2.4	1.7	6.7	0.99	18.3	0.99	16.0

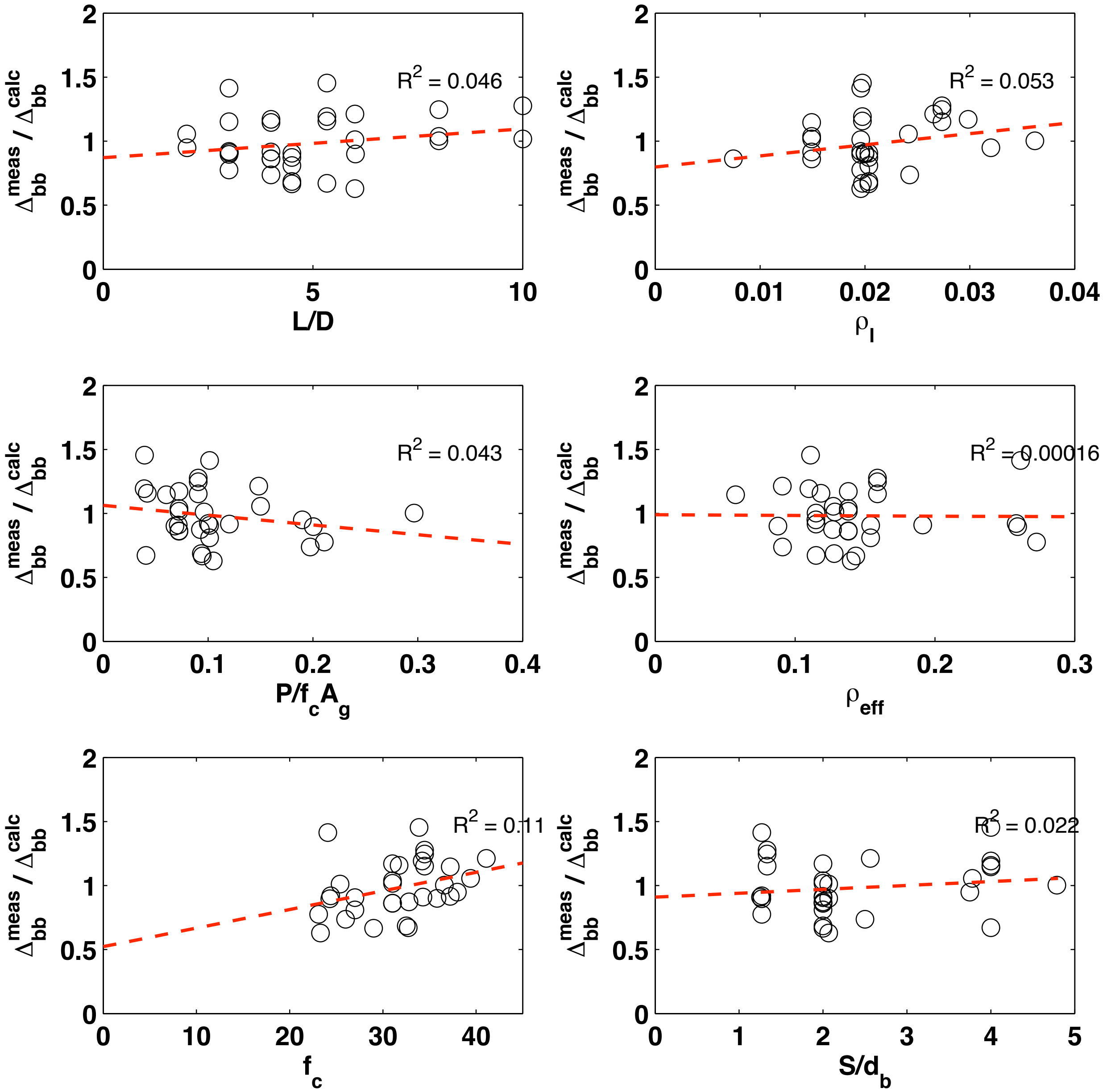

Fig. 9.9 Effect of key column properties on accuracy of plastic-rotation bar-buckling equation

As seen in this table, estimates of plastic rotations at the onset of bar fracture are significantly improved by considering the effects of the key column properties. The coefficient of variation of measured to calculated displacements is reduced from 34.4% using the mean value of $\theta_{p\_bf}^{meas}$ to 15.2% using Equation 9.7, and 16.0% using Equation 9.8. Little accuracy is gained by considering the axial load term in the bar-fracture estimates. Therefore, Equation 9.8 is recommended for columns with axial ratios ≤ 0.30.

A simplified equation similar to the equation developed for the drift ratio at the onset of bar fracture (Equation 9.3) was developed for the plastic rotation as follows.

$$\theta_{p\_bf}^{calc}(\%) = 3.0\ \left(1+150\rho_{eff}d_b/D\right)\left(1-P/A_g f_c'\right)\ (1+L/10D) \tag{9.12}$$

The mean value of the ratios of measured to calculated plastic rotations were 0.97 with a coefficient of variation of 22.7%, whereas the corresponding mean and coefficient of variation for the ratios of measured to calculated displacements were 0.97 and 19.6%.

Fragility curves for this damage state and engineering demand parameter are provided in Figure 9.10, and the ratios of measured to calculated displacements are plotted versus key column properties in Figure 9.11. The only significant trend observed in the data is a slight increase in the ratios of measured to calculated displacements with an increase in concrete compressive strength.

9.3 DAMAGE ESTIMATES BASED ON STRAIN

Longitudinal strains introduce more information into the prediction process, and thus may provide more versatile and accurate predictions of damage. Additionally, the empirical equations based on drift ratio and plastic rotation developed in the previous sections may not be applicable to some modeling situations, such as cases where the distance to the point of contraflexure varies, the axial load varies, or there is biaxial bending. This section will focus on developing and evaluating damage predictions based on longitudinal strain.

Tests show that the onset of cover spalling correlates to the maximum compressive strain in the cover concrete (Lehman and Moehle 2000), therefore this parameter is chosen as the local engineering demand parameter for this damage state. The tensile strain in the extreme reinforcing bar was chosen as the local engineering demand parameter for longitudinal bar buckling; this

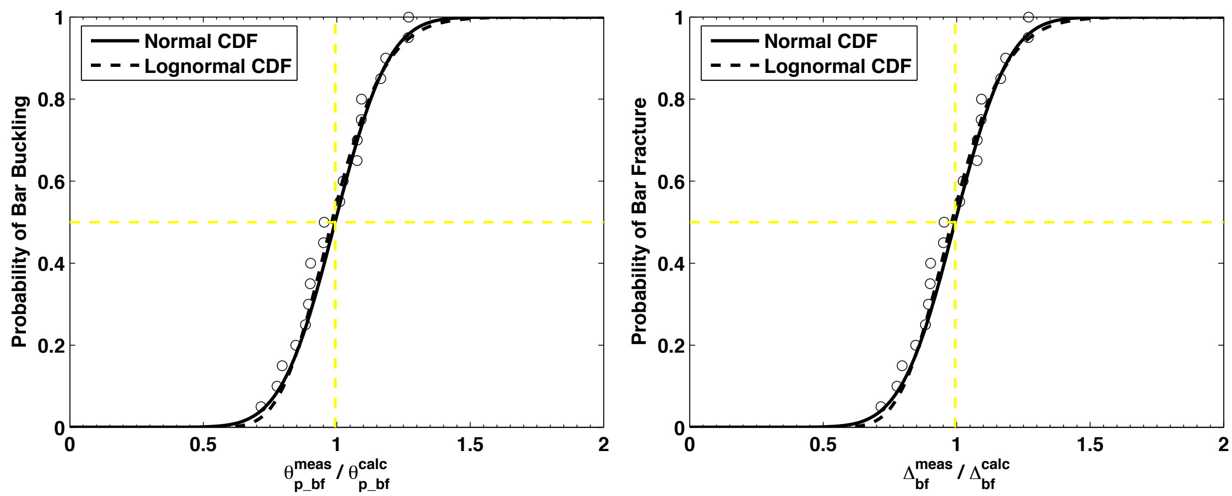

Fig. 9.10 Fragility curves for bar fracture using plastic rotation

parameter is suggested by multiple researchers including Moyer and Kowalsky (2001), Priestley et al. (1996), and Lehman and Moehle (2000). Tensile strain is chosen for bar fracture because bar fracture often occurs immediately after buckling of the longitudinal reinforcement.

The lumped-plasticity modeling strategy developed in this report will be used to evaluate the effectiveness of using maximum concrete compressive strain to estimate cover spalling, and maximum longitudinal-reinforcement tensile strain to estimate bar buckling and bar fracture. Key statistics and fragility curves will be presented. The calibration of the proposed plastic-hinge length in this report considered the estimation of these damage states, and the reader is referred to Section 6.3 for details on this procedure.

The evaluation will not be carried out for both modeling strategies proposed in this report because the longitudinal strains calculated with the distributed-plasticity method are subject to strain concentrations in columns with perfectly-plastic or degrading behavior, as indicated in Section 3.1.1. Strain estimates based on this methodology are only valid for columns with hardening responses, and all of the columns in the bridge dataset do not portray this type of response, whereas the strains estimated with the lumped-plasticity formulation are objective for all section responses.

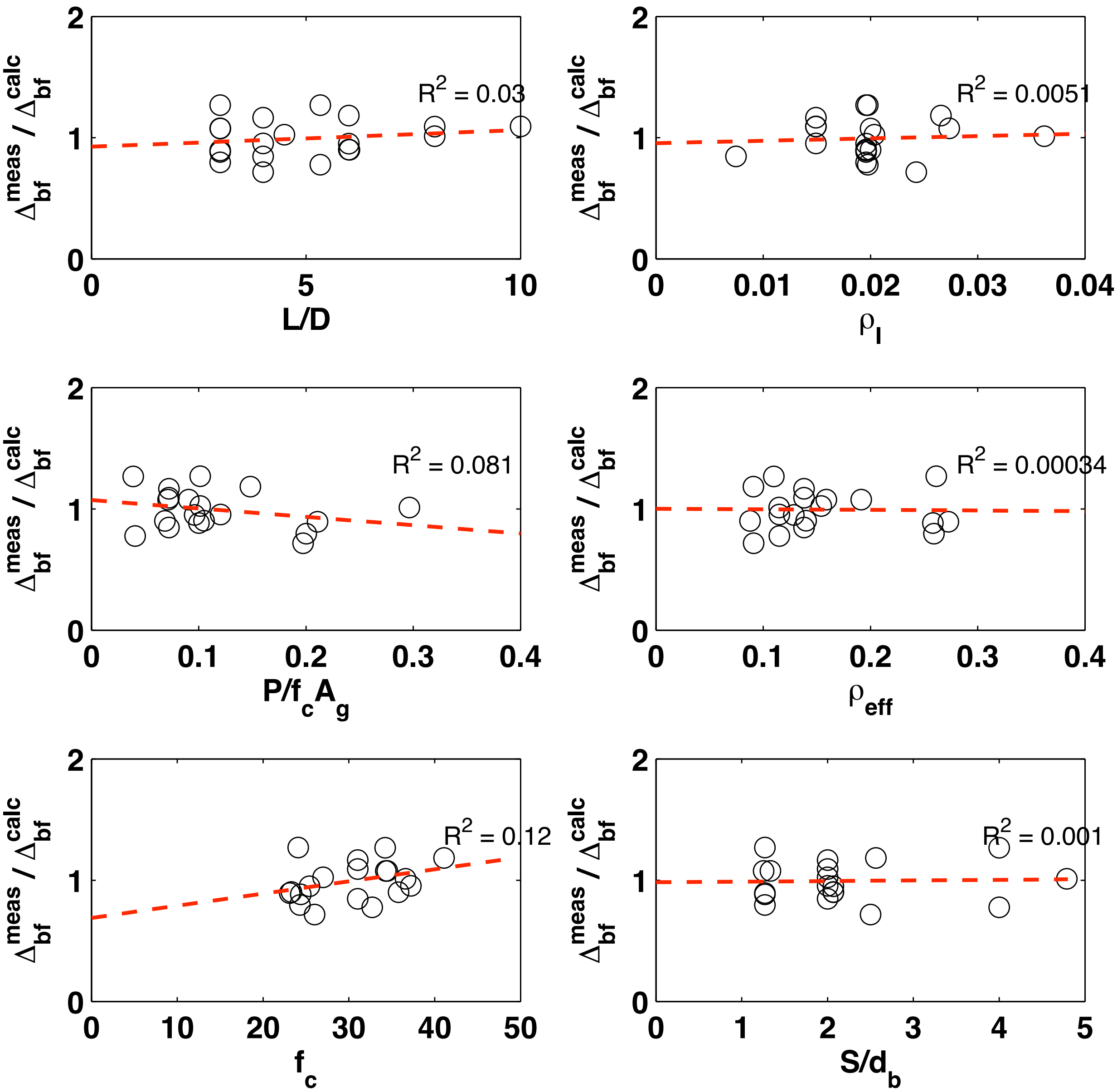

Fig. 9.11 Effect of key column properties on accuracy of plastic-rotation bar-fracture equation

9.3.1 Cover Spalling

The mean value of the compressive strains at the onset of cover spalling (ε_{sp}^{meas}) was 0.008 with a coefficient of variation of 48.6%. The mean value of the ratios of observed spalling displacements to the displacement associated with the mean value of ε_{sp}^{meas} was 0.99 with a coefficient of variation of 34.7% (Table 9.5).

Table 9.5 Cover-spalling estimates based on longitudinal compressive strain

	$\varepsilon_{sp}^{meas}/\varepsilon_{sp}^{calc}$		$\Delta_{sp}^{meas}/\Delta_{sp}^{calc}$	
Methodology	mean	cov (%)	mean	cov (%)
mean $\varepsilon_{sp} = 0.008$	1.00	48.6	0.99	34.7
Eq (9.13)	0.99	39.6	1.0	27.5

The strain at the onset of cover spalling is not expected to increase with an increase of effective confinement ratio. However, if ε_{sp} is plotted versus ρ_{eff}, a significant trend can be observed (Figure 9.12). The best fit line for this trend is as follows.

$$\varepsilon_{sp}^{calc} = 0.0004 + 0.045\rho_{eff} \tag{9.13}$$

The R^2 value for this correlation is 0.42. The effective confinement ratio may be affecting the compressive strain at the onset of cover spalling by confining the lateral expansion of the concrete core and longitudinal reinforcement. If this trend is included in the estimate of the displacement at the onset of cover spalling (Δ_{sp}^{calc}), a significantly better estimate can be obtained. As seen in Table 9.5, the coefficient of variation of the ratios of measured to calculated displacements at the onset of spalling can be reduced from 34.5% to 27.5%. This phenomenon requires a more thorough investigation before this method is recommended for use.

Fragility curves for estimates of the compressive strain at the onset of cover spalling are shown in Figure 9.13. The figure on the left is the fragility curve for $\varepsilon_{sp}^{meas}/\varepsilon_{sp}^{calc}$, where ε_{sp}^{calc} is the mean value of the observed strain 0.008. The fragility curve on the right is for $\Delta_{sp}^{meas}/\Delta_{sp}^{calc}$, where Δ_{sp}^{calc} is the calculated displacement associated with the mean value of ε_{sp} (0.008).

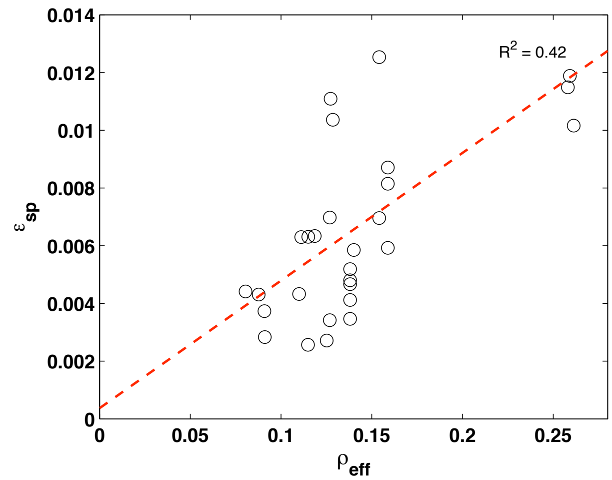

Fig. 9.12 Effect of effective confinement ratio on ε_{sp}

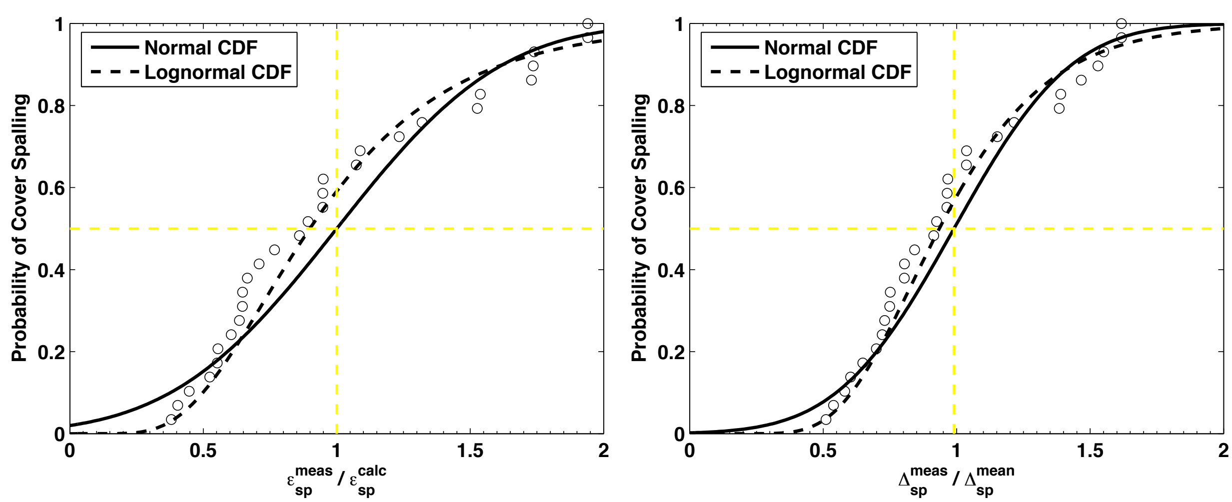

Fig. 9.13 Fragility curves for cover spalling and bar buckling using longitudinal strain

The ratios of measured to calculated displacements (from the calculated compressive strain) at the onset of cover spalling are plotted versus key column properties in Figure 9.14 to evaluate the effect of these properties on the accuracy of the proposed damage estimates. As mentioned earlier in this section and in previous sections of this chapter, the ratio of measured to calculated displacements increase with an increase in effective confinement ratio. As noted for the drift ratio and plastic-rotation estimates, the ratios decrease with an increase in concrete compressive strength.

9.3.2 Bar Buckling

The mean value of the tensile strains at the onset of bar buckling (ε_{bb}^{meas}) was 0.081 with a coefficient of variation of 30.1%. The mean and coefficient of variation of the ratios of observed displacements to displacements associated with the mean value of ε_{bb}^{meas} were 1.00 and 28.1%, respectively (Table 9.6).

Table 9.6 Buckling estimates based on longitudinal-reinforcement tensile strain

	$\varepsilon_{bb}^{meas}/\varepsilon_{bb}^{calc}$		$\Delta_{bb}^{meas}/\Delta_{bb}^{calc}$	
Methodology	mean	cov (%)	mean	cov (%)
mean $\varepsilon_{bb} = 0.081$	1.00	30.1	1.00	28.1
Eq 9.14	1.00	25.4	1.0	23.6

Berry and Eberhard (2005) proposed that the strain at the onset of bar buckling should increase with an increase in effective confinement ratio, as in Equation 9.14.

$$\varepsilon_{bb}^{calc} = \chi_1 + \chi_2 \rho_{eff} \leq 0.15 \tag{9.14}$$

To verify this expected trend, ε_{bb} is plotted versus the effective confinement ratio in Figure 9.15.

Equation 9.14 was calibrated in Section 6.3, and the following equation was obtained.

$$\varepsilon_{bb}^{calc} = 0.045 + 0.25\rho_{eff} \leq 0.15 \tag{9.15}$$

The accuracy of predicting the displacement at the onset of bar buckling as a function of strain can be increased by including this trend in the estimate. To include this trend, the calculated displacements at the onset of bar buckling could be determined by (1) calculating ε_{bb}^{calc} for each column using Equation 9.15, and then (2) calculating the displacements associated with these calculated strain values (Δ_{bb}^{calc}).

Key accuracy statistics for estimating the displacement at the onset of bar buckling utilizing this method are presented in Table 9.6. The coefficient of variation of the ratios of measured to calculated displacements can be reduced from 28.1% using the mean value of ε_{bb} (0.08) to 23.6% using the ε_{bb}^{calc} from Equation 9.15.

Fragility curves for estimates of the tensile strain at the onset of cover spalling are shown in Figure 9.16. The figure on the left is the fragility curve for $\varepsilon_{bb}^{meas}/\varepsilon_{bb}^{calc}$, where ε_{bb}^{calc} is calculated from Equation 9.15. The fragility curve on the right is for $\Delta_{bb}^{meas}/\Delta_{bb}^{calc}$, where Δ_{bb}^{calc} is the calculated displacement associated with ε_{bb}^{calc}.

The ratios of measured to calculated displacements (from the ε_{bb}^{calc}) at the onset of bar buckling are plotted versus key column properties in Figure 9.17 to evaluate the effect of these properties on the accuracy of the proposed damage estimates. As seen in the figures, the ratios decrease slightly with an increase in axial-load ratio, and increase slightly with an increase in concrete compressive strength.

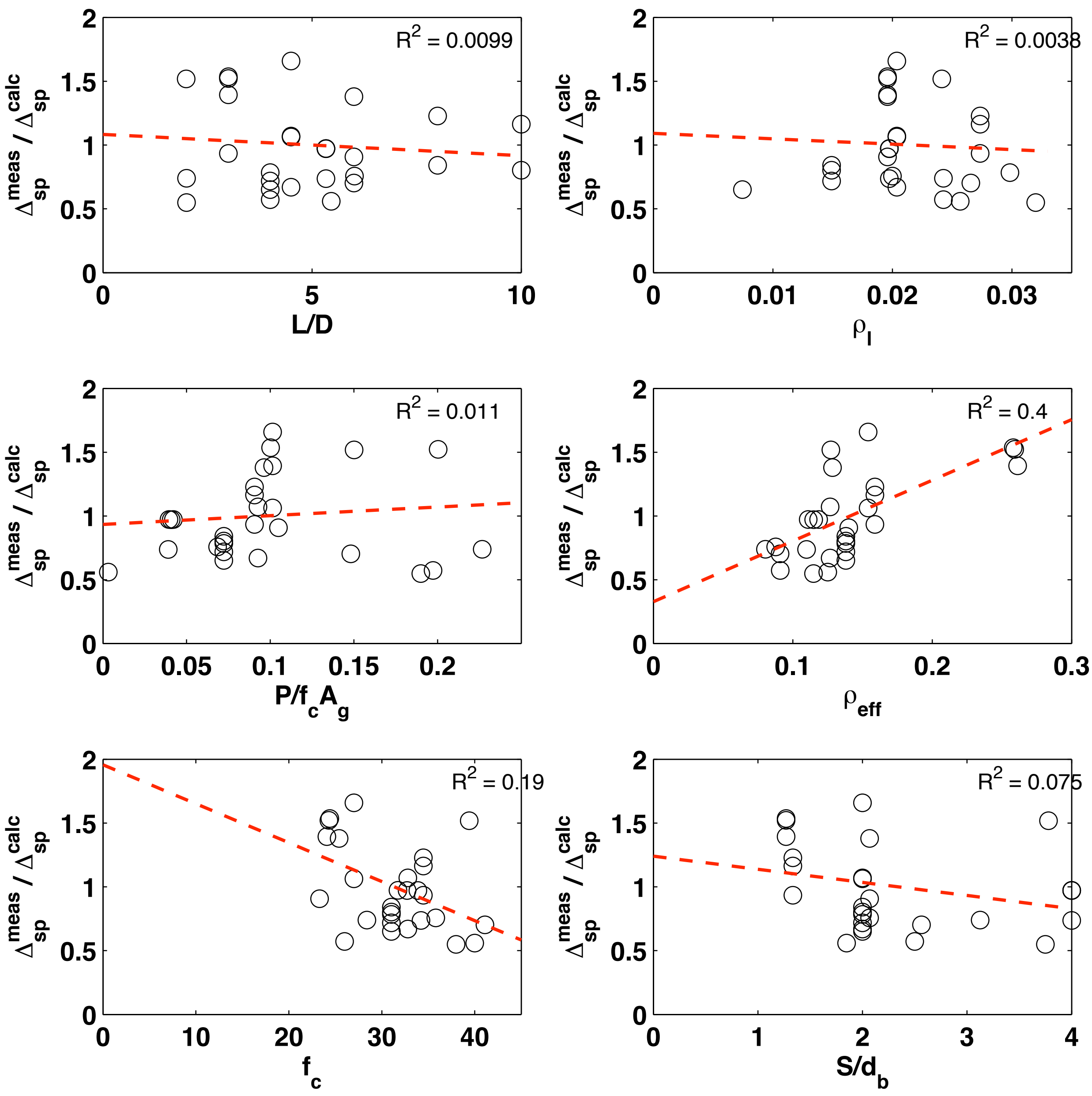

Fig. 9.14 Effect of key column properties on accuracy of strain estimates of cover spalling

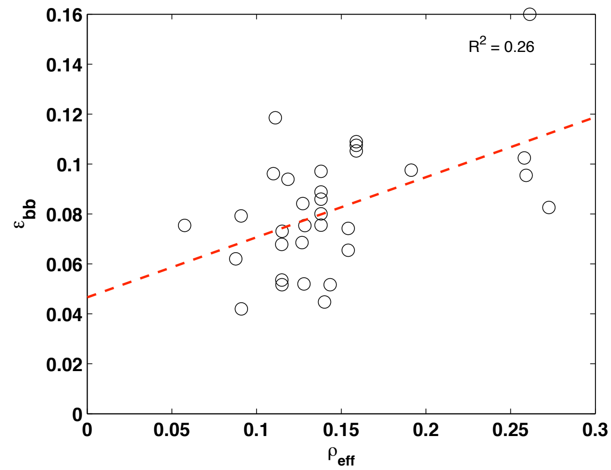

Fig. 9.15 Effect of effective confinement ratio on ε_{bb}

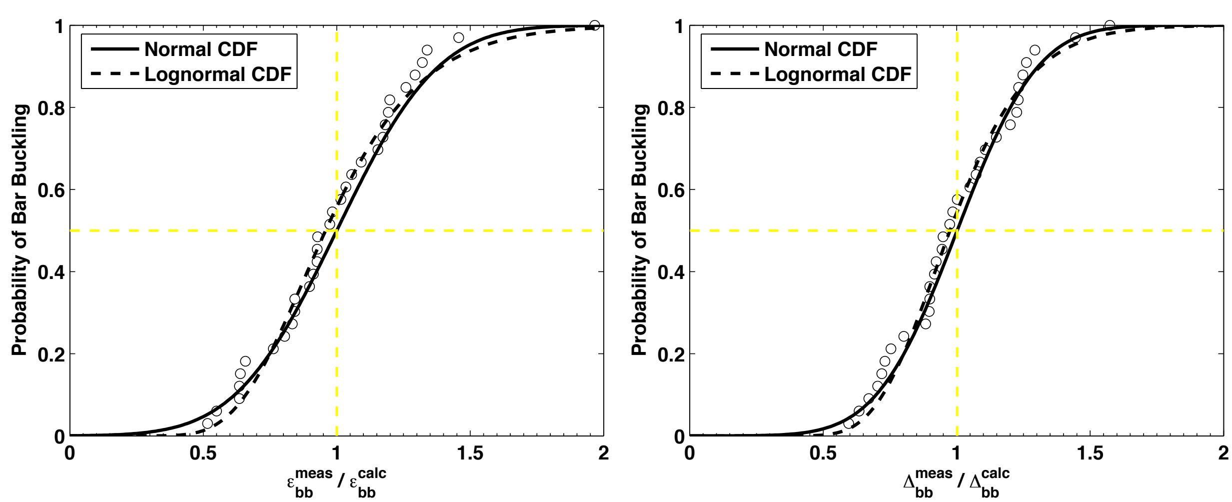

Fig. 9.16 Fragility curves for bar buckling using longitudinal tensile strain

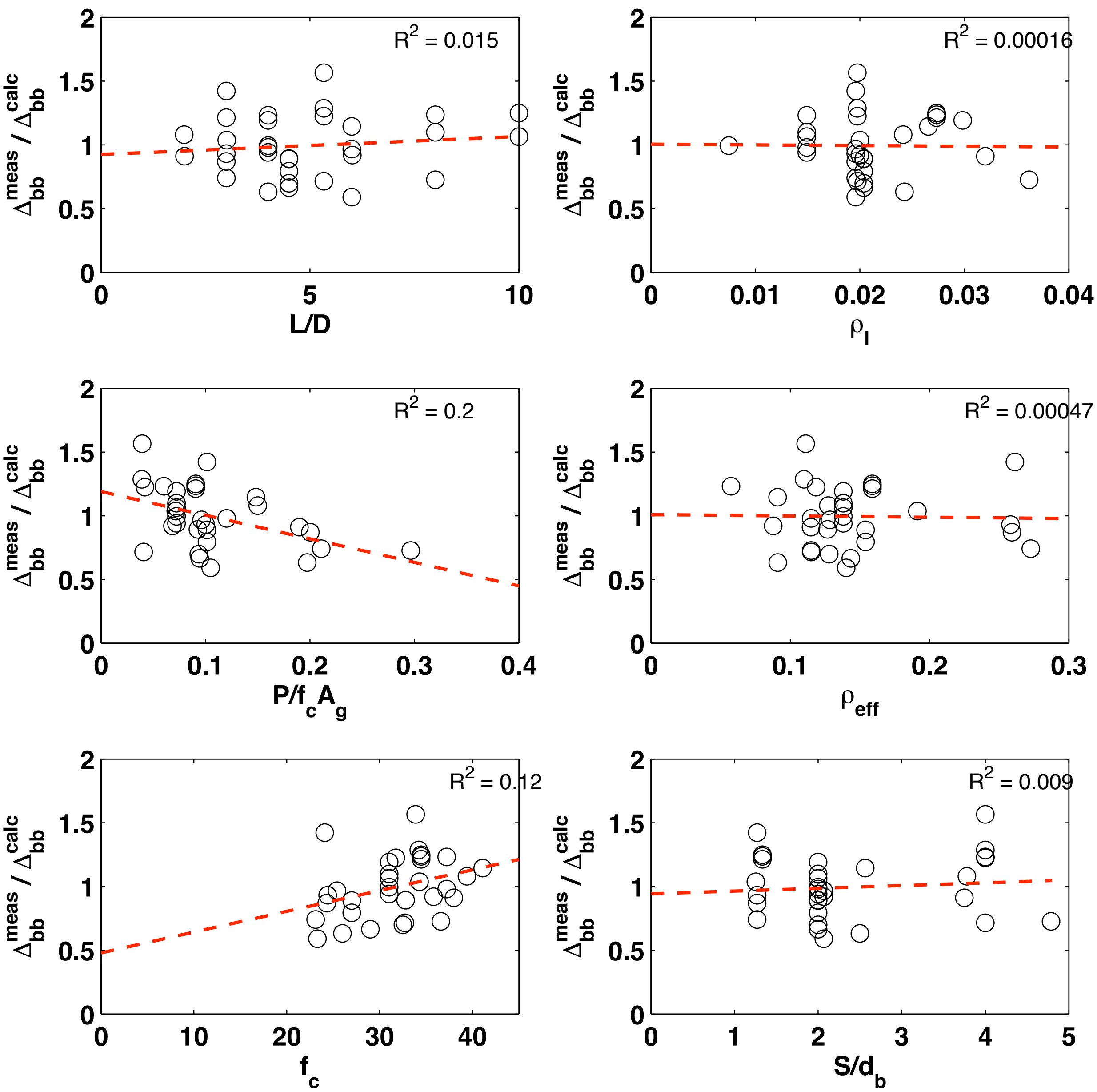

Fig. 9.17 Effect of key column properties on accuracy of strain estimates of bar buckling

9.3.3 Bar Fracture

The mean value of the tensile strain at the onset of bar fracture (ε_{bf}^{meas}) was 0.087 with a coefficient of variation of 28.8%. The mean value and coefficient of variation of the ratios of measured displacements to calculated displacements associated with the mean value of ε_{bf}^{meas} were 1.00 and 27.5%, respectively.

Table 9.7 Bar-fracture estimates based on longitudinal-reinforcement tensile strain

	$\varepsilon_{bf}^{meas}/\varepsilon_{bf}^{calc}$		$\Delta_{bf}^{meas}/\Delta_{bf}^{calc}$	
Methodology	mean	cov (%)	mean	cov (%)
mean $\varepsilon_{bf} = 0.087$	1.00	28.8	1.00	27.5
Eq (9.16)	1.00	22.5	1.00	21.2

The tensile strain at the onset of bar fracture is expected to increase with an increase in effective confinement ratio. This trend is verified in Figure 9.18. In a similar fashion as the bar-

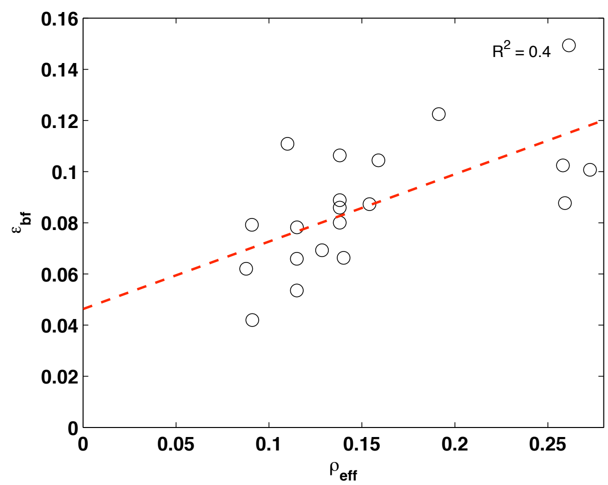

Fig. 9.18 Effect of effective confinement ratio on ε_{bf}

buckling damage level, an equation was developed to predict the tensile strain at the onset of longitudinal bar fracture as a function of effective confinement ratio (Equation 9.18). The resulting equation is nearly identical to the equation developed for bar buckling; therefore the same equation will be used for both damage states for simplicity.

$$\varepsilon_{bf}^{calc} = 0.045 + 0.30\rho_{eff} \leq 0.15 \tag{9.16}$$

By accounting for the effect of effective confinement ratio with Equation 9.16, the accuracy of the bar-fracture estimates are improved (Table 9.7). The coefficient of variation for $\varepsilon_{bf}^{meas}/\varepsilon_{bf}^{calc}$ is reduced from 28.8% using the mean value of ε_{bf}^{meas}, to 21.8% using Equation 9.16. Similarly, the ratio of measured to calculated displacements are reduced from 27.5% to 20.5%. Fragility curves for this damage state and engineering demand parameter are provided in Figure 9.19.

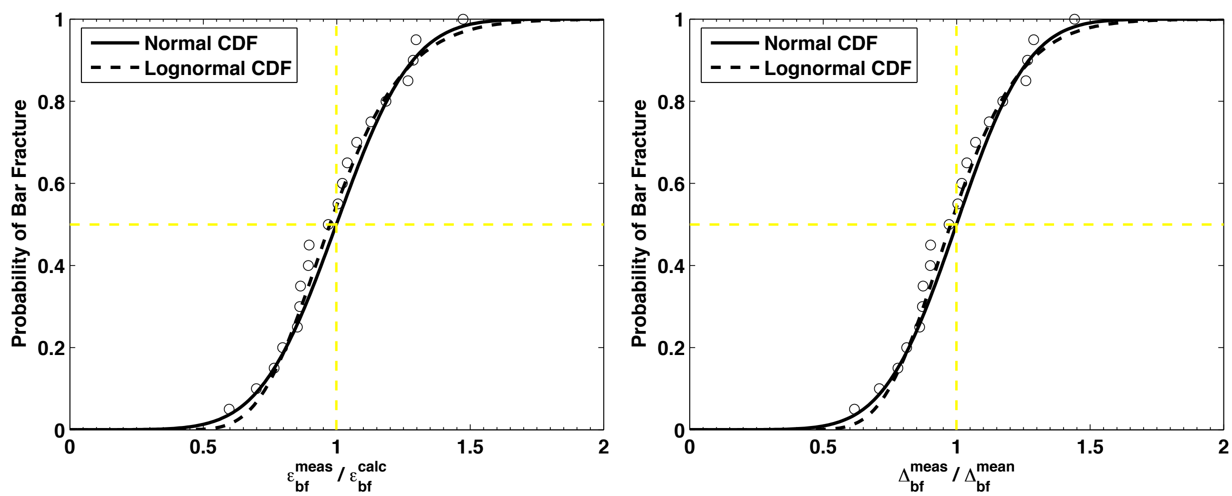

Fig. 9.19 Fragility curves for bar fracture using longitudinal tensile strain

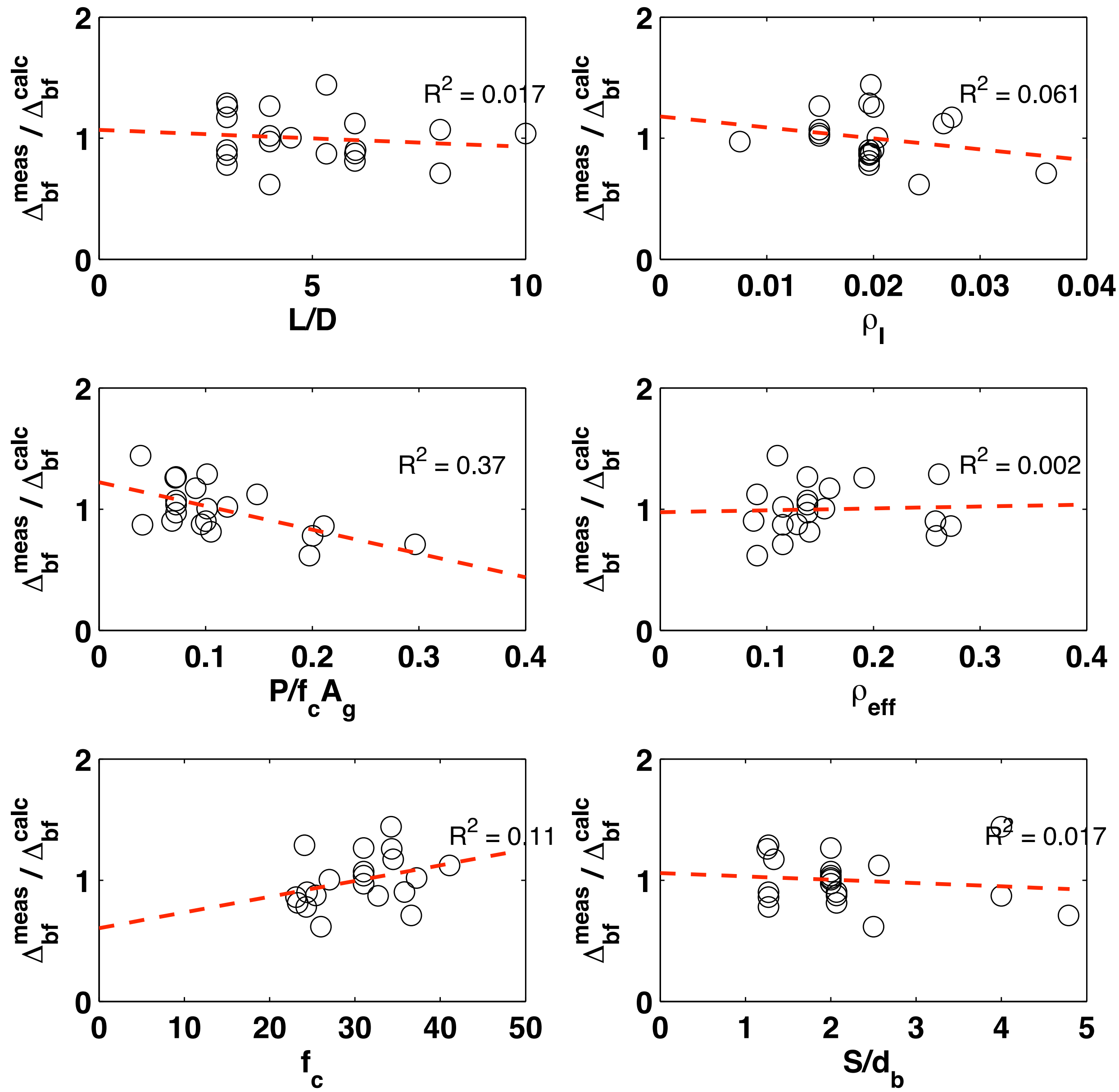

Fig. 9.20 Effect of key column properties on accuracy of strain estimates of bar fracture

9.4 COMPARISON OF DAMAGE ESTIMATES

Damage estimates based on three engineering demand parameters (i.e., drift ratio, plastic rotation, and longitudinal strain) were evaluated in the previous sections. In Table 9.8, this study is summarized and the accuracy of using the various engineering parameters are compared.

Table 9.8 Comparison of damage estimates

Damage State	E.D.P.	Equation	$\Delta_{dam}^{meas}/\Delta_{dam}^{calc}$ mean	cov (%)
Cover Spalling (29 columns)	$\Delta_{sp}^{calc}/L\,(\%)$	$1.6\ (1-P/A_g f_c')\ (1+L/10D)$	1.07	34.9
	$\theta_{p\_sp}^{calc}\,(\%)$	1.20	0.98	33.9
	ε_{sp}	0.008	0.99	34.7
Bar Buckling (33 columns)	$\Delta_{bb}^{calc}/L\,(\%)$	$3.25\ \left(1+150\rho_{eff}d_b/D\right)(1-P/A_g f_c')\ (1+L/10D)$	1.01	24.7
	$\theta_{p\_bb}^{calc}\,(\%)$	$0.0009\left(1+7.3\rho_{eff}\right)(1+1.3L/D+3f_y d_b/D)$	1.01	21.6
	$\theta_{p\_bb}^{calc}\,(\%)$	$2.75\ \left(1+150\rho_{eff}d_b/D\right)(1-P/A_g f_c')\ (1+L/10D)$	1.01	24.3
	ε_{bb}^{calc}	$0.045+0.25\rho_{eff}\leq 0.15$	1.00	23.6
Bar Fracture (20 columns)	$\Delta_{bf}^{calc}/L\,(\%)$	$3.5\ \left(1+150\rho_{eff}d_b/D\right)(1-P/A_g f_c')\ (1+L/10D)$	0.97	20.0
	$\theta_{p\_bf}^{calc}\,(\%)$	$0.0009\left(1+6.7\rho_{eff}\right)(1+2.4L/D+1.7f_y d_b/D)$	0.99	16.0
	$\theta_{p\_bf}^{calc}\,(\%)$	$3.0\ \left(1+150\rho_{eff}d_b/D\right)(1-P/A_g f_c')\ (1+L/10D)$	0.97	19.6
	ε_{bf}^{calc}	$0.045+0.30\rho_{eff}\leq 0.15$	0.96	20.5

As seen in the table, similar levels of accuracy can be obtained by estimating the onset of damage using drift ratio, plastic rotation, or longitudinal strain. The coefficient of variation for the ratios of measured to calculated displacements at the onset of spalling was approximately 34% for all three methods. The coefficient of variations for the onset of bar buckling using the three methods were 22-25%. For bar fracture, slightly better accuracy can be obtained by using plastic rotation (coefficient of variation of 16.0%) than drift ratio or longitudinal strain ($\approx 21\%$).

The drift-ratio equations provide a practical correlation between an engineering demand parameter and key damage states. However, the application of this method is limited to tests in which the the distance to the point of contraflexure does not vary, the axial load does not vary, and there is only uniaxial bending. Although estimates based on plastic rotation suffer from the same limitations, plastic rotation is a more versatile engineering demand parameter because it is more easily calculated in a complex model. The damage estimates based on longitudinal strain overcome the limitations of the drift-ratio and plastic-rotation equations; however they require a more detailed model in which strains can be monitored.

10 Application of Column-Modeling Strategy to More Complex Structural Models

The column-modeling strategies developed in this report were calibrated and evaluated with experimental tests of single, equivalent cantilever bridge columns, loaded pseudo-statically in one dimension. In this chapter, the proposed column-modeling strategies are applied to two more complex modeling situations. First, the column-modeling strategies are employed to model the columns of a single bridge bent. The modeling strategies are then used to model shake-table tests of columns subjected to unidirectional and bidirectional base motions.

10.1 COLUMN BENT TESTS

The proposed distributed-plasticity and lumped-plasticity modeling strategies were used to model the response of a bridge bent test performed by Makido (2006) at Purdue University (Figure 10.1). The geometric and material properties of the specimen are provided in tables 10.1 and 10.2, respectively.

10.1.1 Distributed-Plasticity Model

The distributed-plasticity model of the column-bent is illustrated in Figure 10.2. The columns were modeled with the proposed distributed-plasticity modeling strategy and standard material models (Chapter 4), with a slip-section at both ends of the column and with 6 integration points, which is recommended for columns under double curvature (Section 3.1.1). The cross-beam was modeled as a rectangular force-based beam-column element with six integrations points. However, upon

Fig. 10.1 Test setup

the completion of the analysis, it was observed that the cross member did not crack, and therefore could have been modeled as an elastic section with gross section properties.

Accuracy statistics for this modeling strategy are provided in Table 10.3, and the calculated envelope response is compared to the measured envelope response in Figure 10.3(a). The basic distributed-plasticity modeling strategy accurately predicts the maximum moment ($M.R. = 1.02$), but the model overestimates the initial stiffness ($S.R. = 0.69$), and does not model the envelope degradation. The calculated and measured cyclic responses are compared in Figure 10.3(b). As seen in this figure, this method does not model the strength and stiffness degradation due to cycling at large deformations.

Ranf (2006) analyzed the same bridge bent in detail. Based on strain measurements in the bent footing, he recommended bond-strength ratios of $\lambda_e = 0.6$ (compared with $\lambda_e = 0.9$) and $\lambda_i = 0.3$ (compared with $\lambda_i = 0.45$), and a larger bond-compression depth of $d_{comp} = 0.5D$ (compared with 1/2 the neutral axis depth at concrete compressive strain of 0.002). Using these values in the bond-model provides a better estimate of the stiffness ratio (0.94) and therefore a better E_{push}

Table 10.1 Geometric properties of the Purdue bent

Category	Property	
Column Dimensions	Gross Diameter (*mm*)	304.8
	Clear Cover (*mm*)	26.6
	Core Diameter (*mm*)	261.6
	Column Height (*mm*)	1524.0
	Intra-Bent Column Spacing (*mm*)	1828.8
Column Reinforcement	No. of Longitudinal Bars	16
	Bar No.	3
	Longitudinal Steel Ratio (%)	1.56
	Spiral Bar	W2.9
	Spiral Spacing (*mm*)	31.8
	Spiral Bar Diameter (*mm*)	4.9
	Spiral Bar Area (mm^2)	18.7
	Transverse Volumetric Steel Ratio (%)	0.90
Beam Dimensions	Length (*mm*)	3149.6
	Width (*mm*)	812.8
	Depth (*mm*)	457.2
	Clear Cover (*mm*)	25.4
Beam Reinforcement	No. of Longitudinal Bars	12
	Longitudinal Bar No.	5
	Transverse Bar No.	3
	Transverse Spacing (*mm*)	152.4

Table 10.2 Measured material properties for the Purdue bent

Member	Property	
Column	f'_c (MPa)	29.8
	f_y (MPa)	482.6
	E_s (MPa)	2.00e5
Beam	f'_c (MPa)	46.9
	f_y (MPa)	434.32
	E_s (MPa)	2.00e5

value (8.43). The strength estimates did not change, but E_{force} and E_{energy} improved slightly (Table 10.3).

To capture the strength and stiffness degradation due to cycling at large deformations, a material model that accounts for this phenomenon is needed. A steel model that accounts for cyclic degradation is proposed in Chapter 8 (Mohle and Kunnath 2006). However, this model can not be used reliably in combination with this modeling strategy because the distributed-plasticity modeling strategy is susceptible to strain concentrations in columns with degrading behavior.

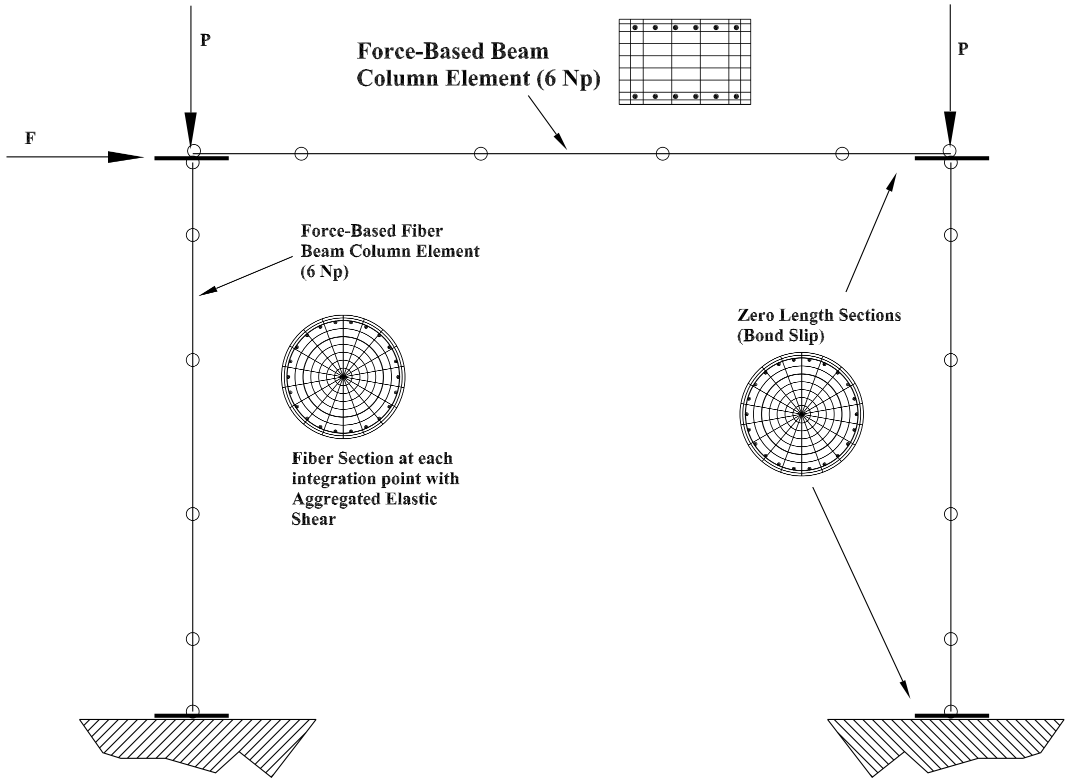

Fig. 10.2 Bent model with distributed-plasticity column-modeling strategy

10.1.2 Lumped-Plasticity Model

The modeling strategy for the bridge bent using the proposed lumped-plasticity column-modeling strategy (Chapter 6) is illustrated in Figure 10.4. A plastic hinge is assumed to form at both ends of each column, and the length of the plastic hinge was calculated as $L_p = 0.05L_s + 0.1f_y d_b/\sqrt{f_c'}$, where L_s is the distance from column fixity to point of contraflexure ($L/2$). For these columns, the calculated plastic-hinge length was 122.3 *mm*, which is equal to 40% of the column diameter. The effective stiffness of the elastic portion of the columns was calculated as $(EI)_{eff} = \hat{\alpha}_{sec}(EI)_{sec}$,

Table 10.3 Accuracy statistics for column-modeling strategies

Strategy	Steel Model	$E_{push}(\%)$	$S.R.$	$M.R.$	$D.R.(\%)$	$E_{force}(\%)$	$E_{energy}(\%)$
Distr.	Standard	11.9	0.7	1.0	8.8	21.0	-63.9
Distr., Ranf Bond	Standard	8.4	0.9	1.0	8.9	19.3	-50.0
Lumped	Standard	7.6	0.9	1.1	8.2	19.8	-56.3
Lumped	Mohle and Kunnath	8.5	0.9	1.0	8.1	13.4	-33.5

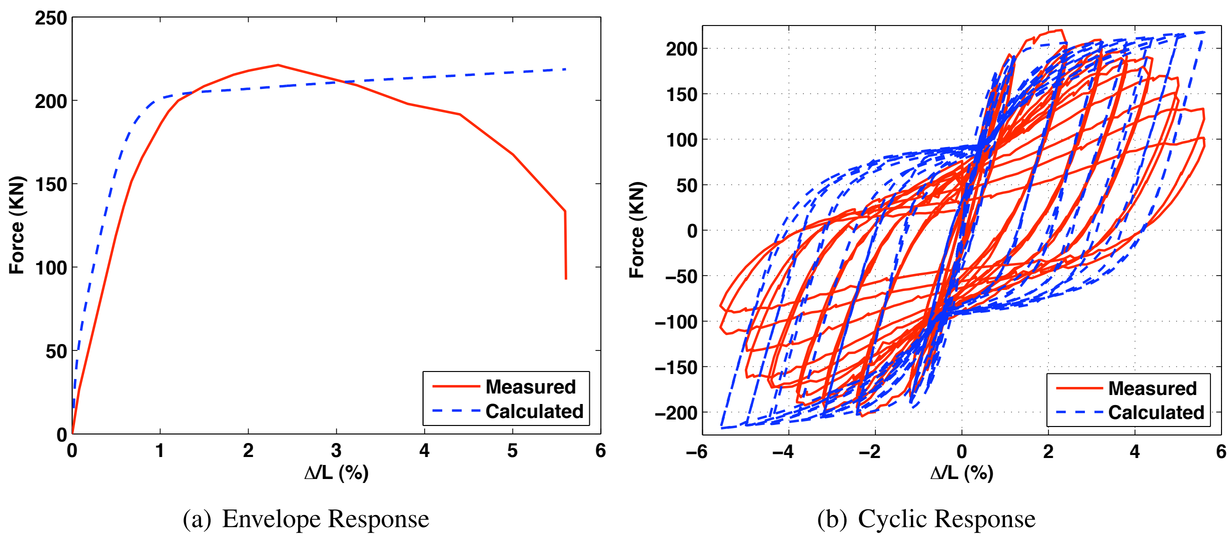

Fig. 10.3 Force-deformation response of bridge bent with distributed-plasticity model and standard steel

where $\hat{\alpha}_{sec} = \frac{\alpha(L-3L_p)}{L-3\alpha L_p}$, and $\alpha_{sec} = 0.35 + 0.1L_s/D$ (sections 6.2 and 5.5). For these columns $(EI)_{eff} \approx 0.15E_cI_g$. As in the distributed-plasticity model, the cross beam was modeled as a rectangular, force-based beam-column element with six integrations points. However, upon the completion of the analysis it was observed that the cross member did not crack, and therefore could have been modeled as an elastic section with gross section properties.

Accuracy statistics for this modeling strategy are provided in Table 10.3, and the calculated and measured envelopes are compared in Figure 10.5(a). The proposed modeling strategy accurately models the response of the bridge bent at low levels of deformation; the initial stiffness is calculated within 15% of the measured response, and the maximum moment is calculated within 5% of the measured response. However, as with the distributed-plasticity method, the lumped-plasticity method does not model the degrading envelope accurately. The calculated and measured cyclic responses are compared in Figure 10.5(b). As seen in the figure, this method does not account for the degradation due to cycling at large deformations.

To overcome this limitation, the more complex steel model (Mohle and Kunnath 2006) described in Chapter 8 was used to model the reinforcing steel. The envelope curves and hysteresis loops for this analysis are presented in Figure 10.6(a) and 10.6(b), and the accuracy statistics are provided in Table 10.3. As seen in the figures and the table, the Mohle and Kunnath (2006) steel

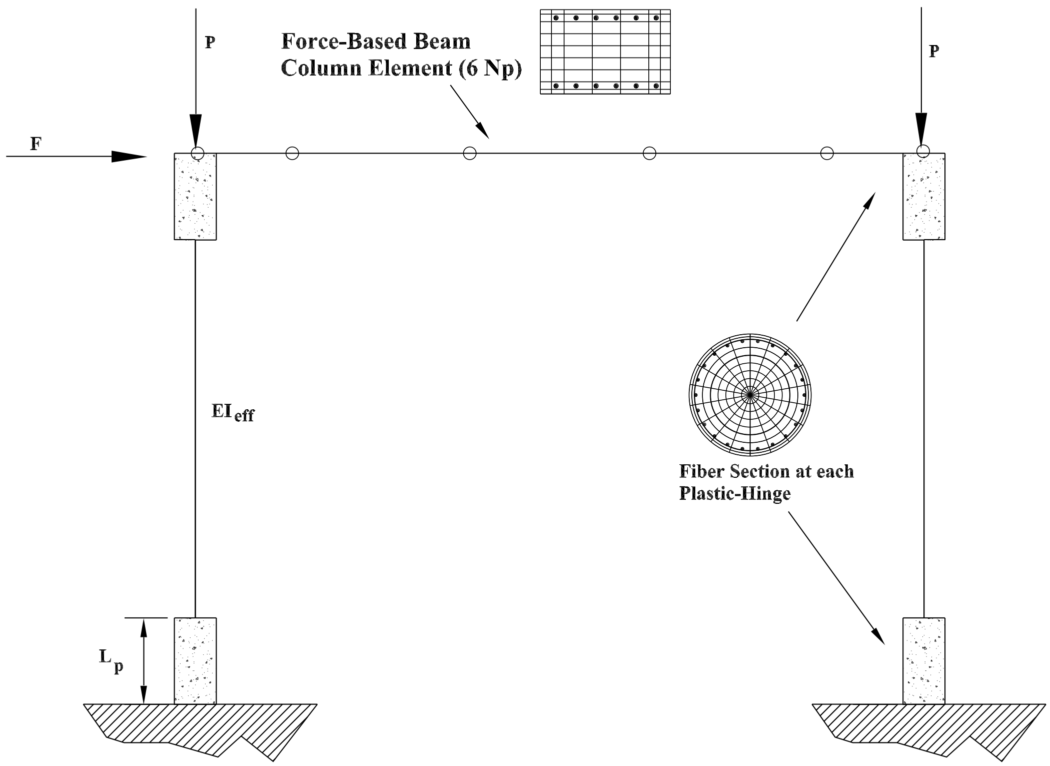

Fig. 10.4 Bent model with lumped-plasticity column-modeling strategy

model significantly improves the estimates of the cyclic response of the bent. The values of E_{force} and E_{energy} (13.4% and -33.5%) using the Mohle and Kunnath (2006) steel model are approximately 60% of the values using the standard steel model (19.8% and -56.3%).

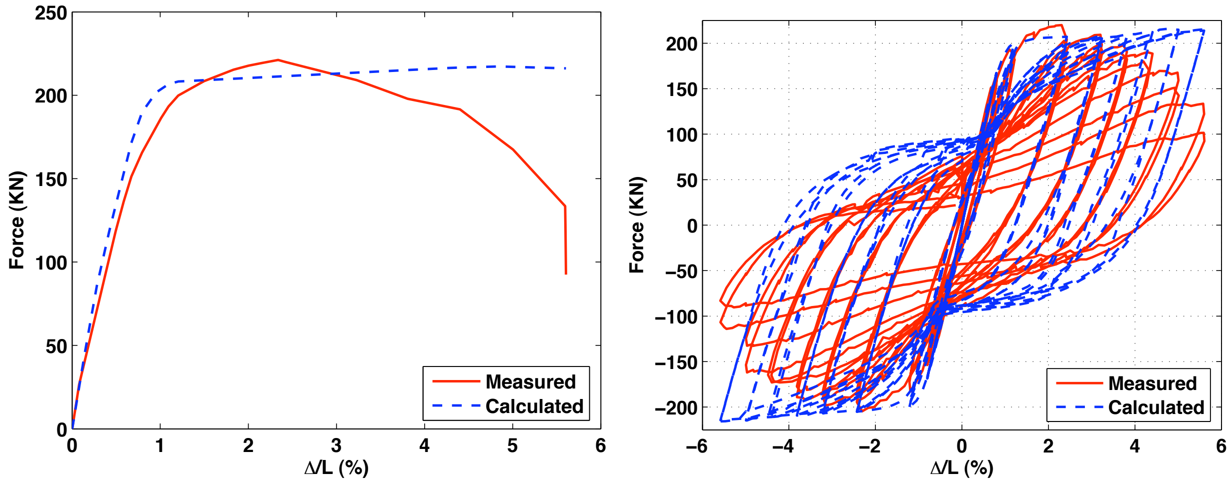

(a) Envelope Response (b) Cyclic response

Fig. 10.5 Force-deformation response of bridge bent with lumped-plasticity model and standard steel

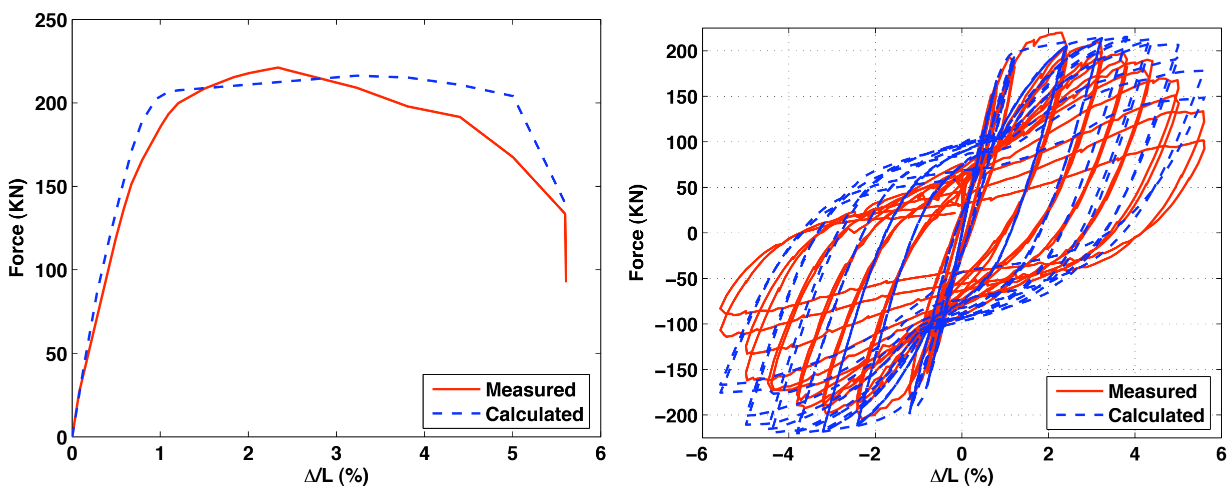

(a) Envelope response (b) Cyclic response

Fig. 10.6 Force-deformation response of bridge bent with lumped-plasticity model and Mohle and Kunnath (2006) steel

10.1.3 Flexural Damage

The estimates of cover spalling and bar buckling proposed in Chapter 9 will be applied to the Purdue bent test in this section. The lumped-plasticity formulation with the standard steel model was used for this study. The measured drift ratios at the onset of cover spalling and bar buckling were 1.2%, 3.8% and 4.4% respectively. The calculated engineering demand parameters (drift ratio, plastic rotation, and longitudinal strain) are reported in Table 10.4. The calculated drift ratios associated with the calculated engineering demand parameters are also reported along with the ratios of measured to calculated displacements. As seen in the table, the proposed methodologies

Table 10.4 Damage estimates for purdue bent test

Damage State	E.D.P.	E.D.P. (%)	$\Delta_{dam}^{calc}/L(\%)$	$\Delta_{dam}^{meas}/\Delta_{dam}^{calc}$
Cover Spalling	Drift Ratio	1.1	1.1	1.1
	Plastic-Rotation	1.5	0.93	1.29
	Compressive Strain	0.8	1.24	0.96

accurately predict the onset of cover spalling and bar buckling. For this test specimen, longitudinal strain was the most accurate means of predicting the displacement at the onset of cover spalling ($\Delta_{sp}^{meas}/\Delta_{sp}^{calc} = 0.96$), whereas drift ratio and plastic-rotation were the most effective means for predicting bar buckling ($\Delta_{sp}^{meas}/\Delta_{sp}^{calc} = 1.05$ and 0.95, respectively).

10.2 SHAKE-TABLE TESTS

The proposed column-modeling strategies were used to model shake-table tests performed by Hachem et al. (2003) at the University of California at Berkeley.

10.2.1 Test Setup and Procedure

The shake-table tests consisted of four identical columns subjected to unidirectional and bidirectional earthquake excitations. The column specimens are illustrated in Figure 10.7, and key geometric and material properties are provided in Table 10.5. Hachem et al. (2003) provides details of the tests.

Specimens A1 and B1 were subjected to unidirectional excitations, whereas A2 and B2 were subjected to excitations in two directions (Table 10.6). Two horizontal ground motion time histories

Table 10.5 Properties of shake-table specimens

Category	Property	
Column	Gross Diameter (*mm*)	406.0
	Clear Cover (*mm*)	13.0
	Column Height (*mm*)	1630.0
Column Reinforcement	No. of Longitudinal Bars	16
	Longitudinal Bar Diameter (*mm*)	12.7
	Longitudinal Steel Ratio (%)	1.17
	Spiral Bar Diameter	4.5
	Spiral Spacing (*mm*)	31.8
	Spiral Bar Diameter (*mm*)	4.9
	Transverse Volumetric Steel Ratio (%)	0.53
Material Properties	f'_c (MPa)	39.3
	f_y (MPa)	499.9
	f_{ys} (MPa)	620.5

were used in the tests, and for simplicity, no vertical accelerations were considered. Specimens A1 and A2 were subjected to variations of the Olive View record of the 1994 Northridge earthquake, whereas columns B1 and B2 were subjected to the 1985 Chile earthquake recorded at the Llolleo station. Each specimen was initially subjected to runs at or below the yield level to help identify the elastic response of the specimens. The specimens were then subjected to runs with accelerations at the *design* level. Following these runs, the accelerations were amplified to the *maximum* level, which matched the capacity of the simulator. The amplitude of the runs at the *maximum* level were 1.5-2.0 times the amplitude of the design level. The *design* and *maximum* level runs were repeated (in pairs) until failure. The base-acceleration histories of the specimens in the longitudinal and lateral directions at the *design* level are presented in Figure 10.8. Table 10.6 lists the peak ground accelerations (PGA) for the first design level and the first maximum level. The Northridge record represents a near-fault ground motion with a high-velocity pulse, whereas the Chile record was chosen to be representative of a long-duration earthquake. The response spectra for the four *design* level excitations are presented in Figure 10.9 (damping ratio of 5%).

Table 10.6 Test matrix with pga for 1^{st} design level and 1^{st} maximum level

		Peak Ground Accelerations (g)			
Specimen	History	design long.	design lat.	max long.	max lat.
A1	Northridge	0.58	-	0.9	-
A2	Northridge	0.58	0.65	0.91	0.95
B1	Chile	0.48	-	0.87	-
B2	Chile	0.47	0.36	0.9	0.67

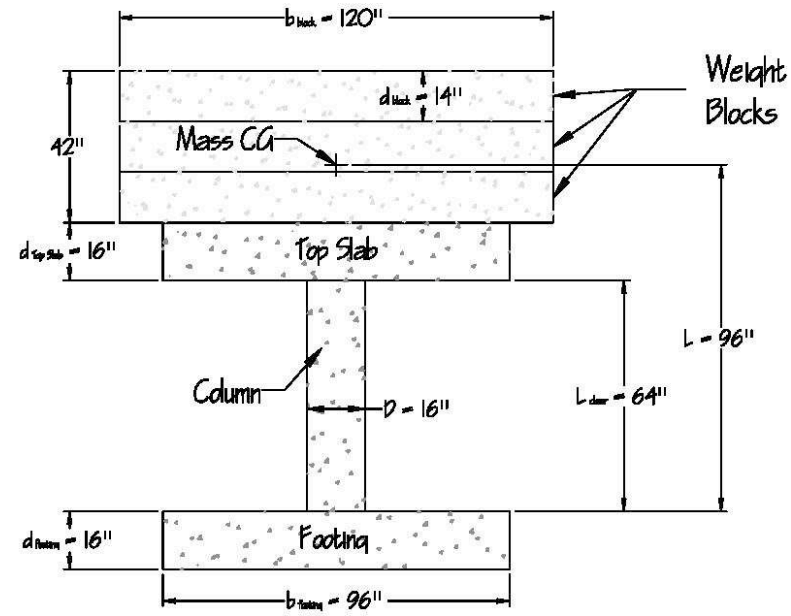

Fig. 10.7 Column specimen and key dimensions (Hachem et al. 2003)

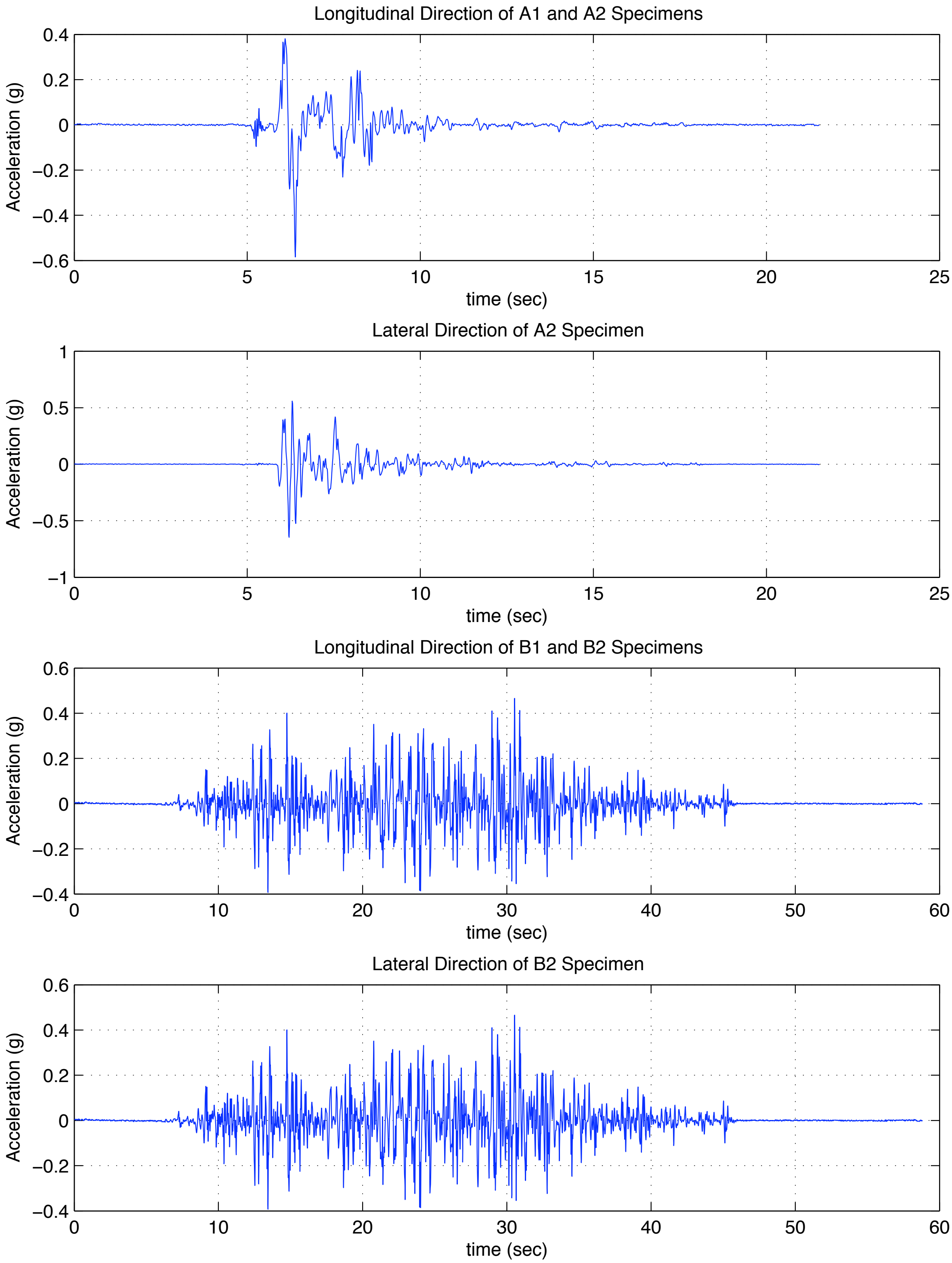

Fig. 10.8 Base-acceleration records for test specimens

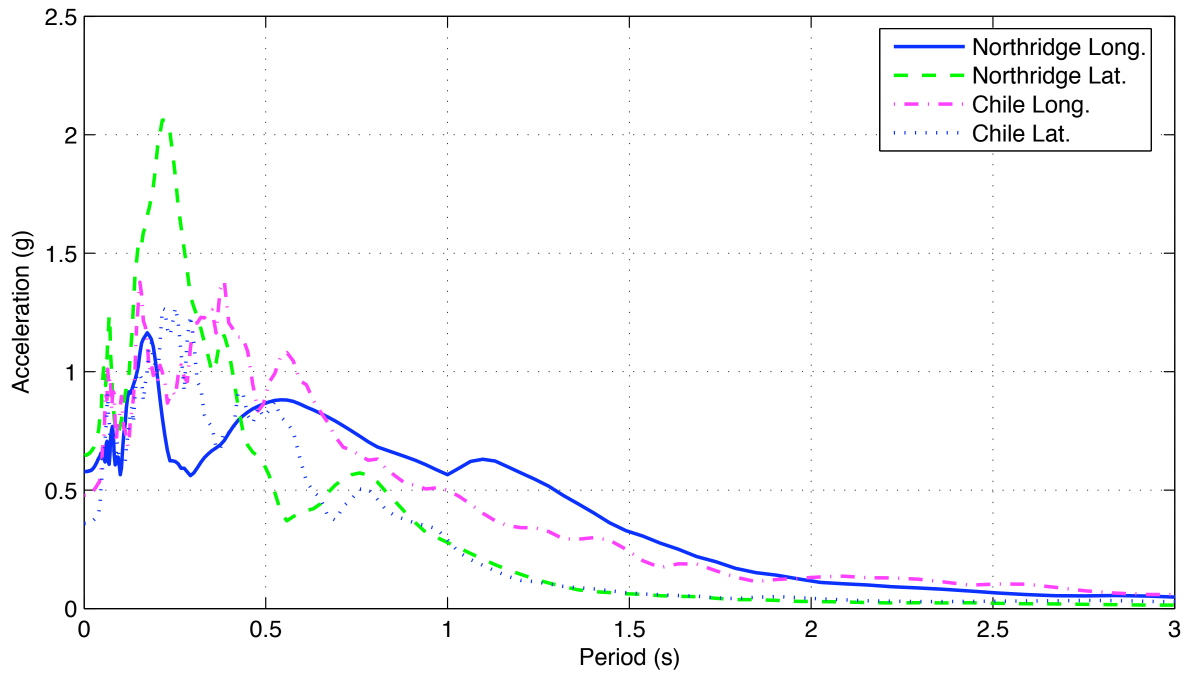

Fig. 10.9 Response spectra for base accelerations with a damping ratio of 5%

10.2.2 Modeling Strategies

The distributed-plasticity and lumped-plasticity modeling strategies for the shake-table tests are illustrated in Figure 10.10. In both modeling strategies, the mass of the block was lumped with its center of gravity at a distance (L_{CG}) of 812 *mm* (32 *in.*) above the top of the column. The mass of the block (m) was 296 Mg (0.169 $kip \cdot s^2/in.$), and the rotational moment of inertia of the mass (m_R) was 26 $Mg \cdot m^2$ (234 $kip \cdot in. \cdot s^2$). A rigid beam was used to link the top of the column to the lumped mass. The columns of the specimens were modeled with the strategies proposed in chapters 4 (distributed-plasticity) and 6 (lumped-plasticity). Rayleigh damping was used in the model. Based on the damping observed in the shake-table tests, the Raleigh coefficients α and β were selected such that the damping ratio was 3.5% at periods of 0.1 and 1.0 seconds ($\alpha = 0.4$ and $\beta = 0.001$).

The models described above were evaluated at the first *design* level and the first *maximum* level with the standard cyclic material models, and the modified material models proposed in Chapter 8. To account for the effects of preliminary ground motions, all runs prior to the first *d*esign

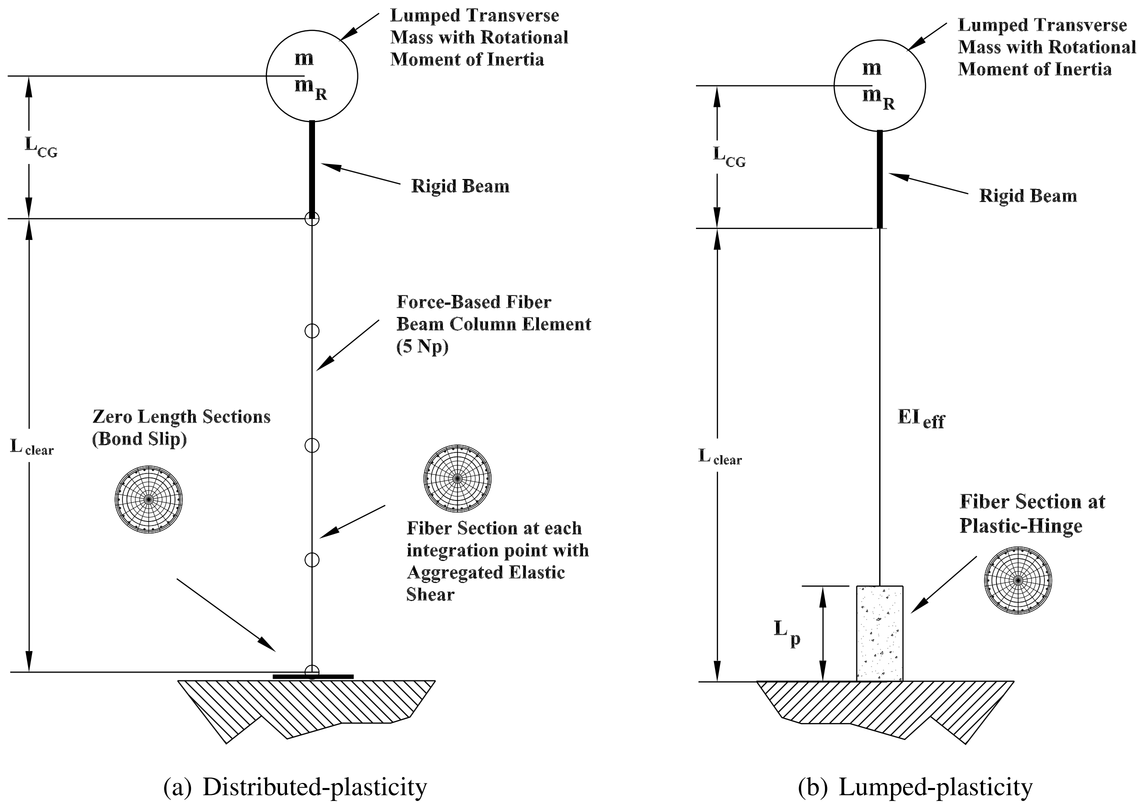

Fig. 10.10 Modeling strategies for shake-table tests

level and *m*aximum level were considered in the analysis. Table 10.7 describes the six modeling variations evaluated in this study. The distributed-plasticity model was evaluated with perfect crack closure ($r = 0.0$) and imperfect crack closure ($r = 1.0$) and the standard steel model. The lumped-plasticity method was evaluated with both variations of crack closure assumptions, and the two proposed steel models: Menegotto-Pinto and Mohle and Kunnath (2006) ($C_f = 0.26$ and $C_d = 0.45$).

10.2.3 Response Maxima and Hysteretic Energy

Maximum tip displacement, maximum base moment, maximum base shear, and hysteretic energy were used to evaluate the six modeling strategies. The hysteretic energy is the area within the hysteretic force-deformation curves and is calculated with Equation 7.3.

The accuracy of each model is shown graphically in Figure 10.11 (*design* level-lateral), Figure 10.12 (*design* level-longitudinal), Figure 10.13 (*maximum* level-lateral), and Figure 10.14

Table 10.7 Modeling variations for shake-table specimens

Modeling Strategy	Steel Model	Crack Closure	Name
Distributed	Standard	r = 0.0 cmax = 0.0	DP-S-PC
	Standard	r = 1.0 cmax = 0.01	DP-S-IC
Lumped	Standard	r = 0.0 cmax = 0.0	LP-S-PC
	Standard	r = 1.0 cmax = 0.01	LP-S-IC
	Mohle	r = 0.0 cmax = 0.0	LP-M-PC
	Mohle	r = 1.0 cmax = 0.01	LP-M-IC

(*maximum* level-longitudinal). As seen in the figures, all column-modeling variations predict the maximum displacement, shear force, and hysteretic energy within 30% of the measured response for both earthquake records at both levels of excitation in the longitudinal and lateral directions. However, the modeling variations were less accurate when predicting the maximum base moments, especially the lumped-plasticity methods in the lateral direction. Also seen in the figures, the crack closure variations do not significantly affect any of the response maxima, which leaves two strategies to compare: distributed plasticity to lumped plasticity (both with standard steel), and the lumped-plasticity variation with standard steel to the lumped-plasticity variation with degrading steel.

No significant trends can be observed in the maximum displacements, and hysteretic energy estimates calculated with the distributed-plasticity and lumped-plasticity estimates (both with standard steel) at either earthquake record or excitation level. However, the ratios of measured to calculated base moments are larger for the distributed-plasticity methodology for both earthquake records at both levels of excitation in the longitudinal direction. However the opposite trend is observed in the lateral direction. Similarly, the ratios of measured to calculated shear forces are larger (on average) for the distributed-plasticity methodology for both earthquake records and both excitation levels in both directions.

On average, the ratios of measured to calculated base moments and shear forces are greater for the lumped-plasticity methodology with standard steel than with the degrading steel model. No other significant trends are observed when comparing these two variations.

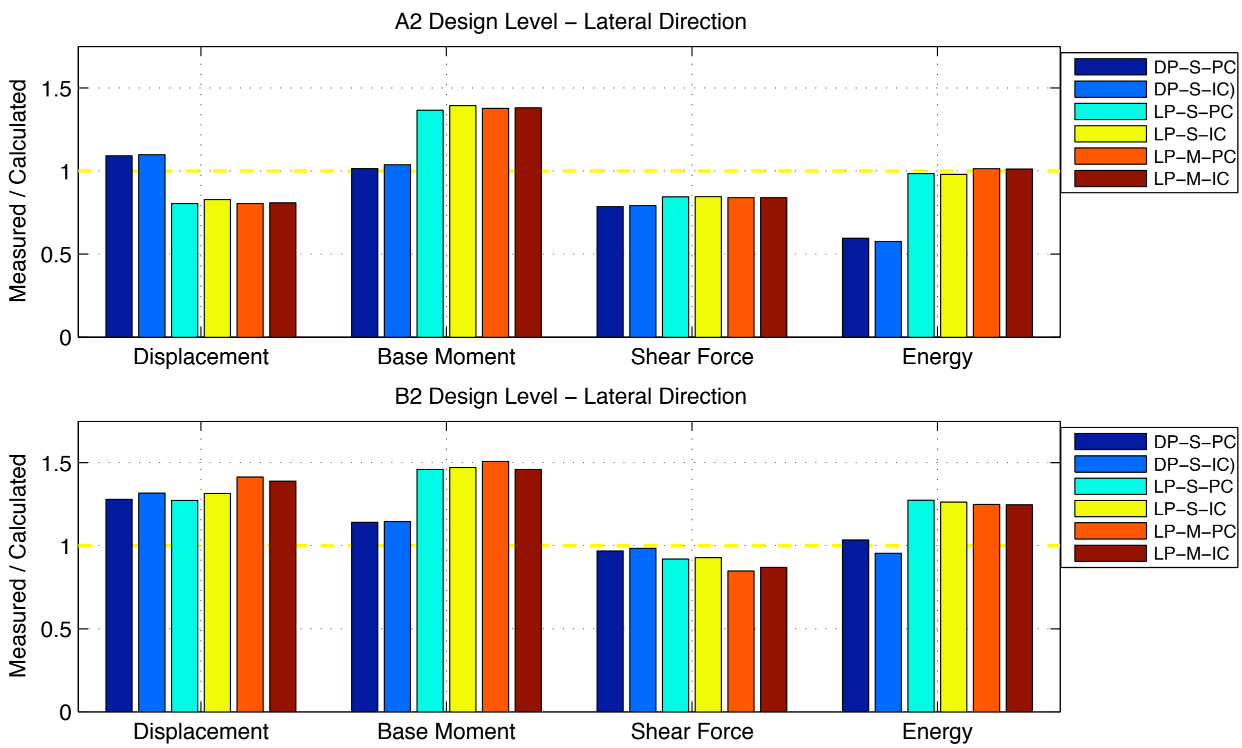

Fig. 10.11 Ratio of measured to calculated results for various response maxima in the lateral direction at first design level

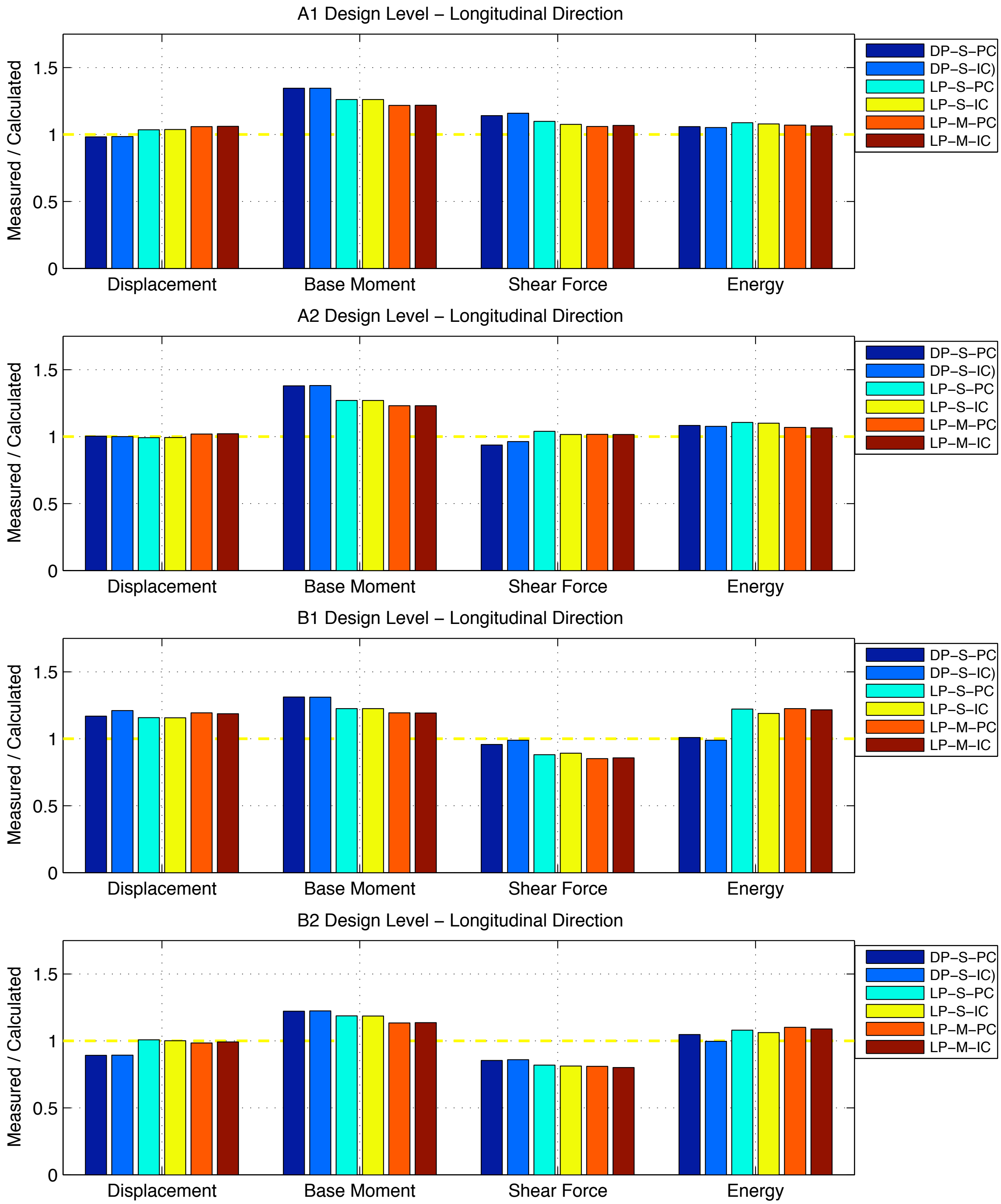

Fig. 10.12 Ratio of measured to calculated results for various response maxima in the longitudinal direction at first design level

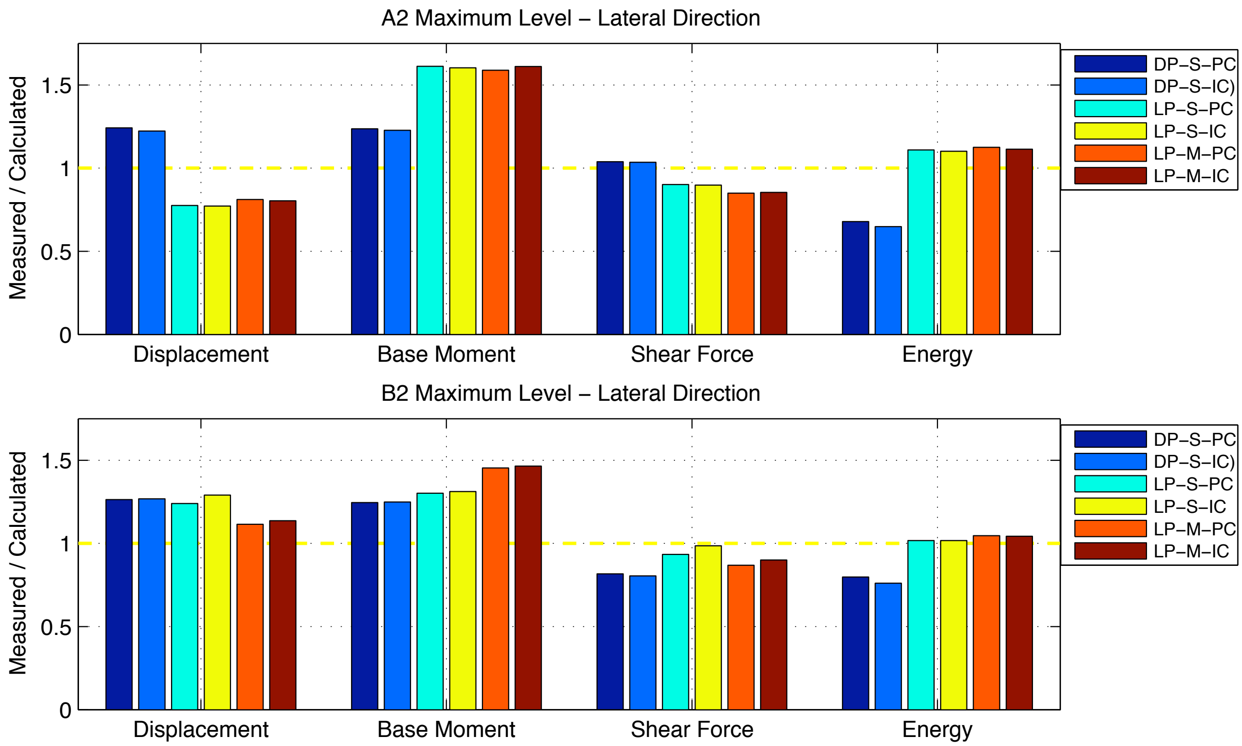

Fig. 10.13 Ratio of measured to calculated results for various response maxima in the lateral direction at first maximum level

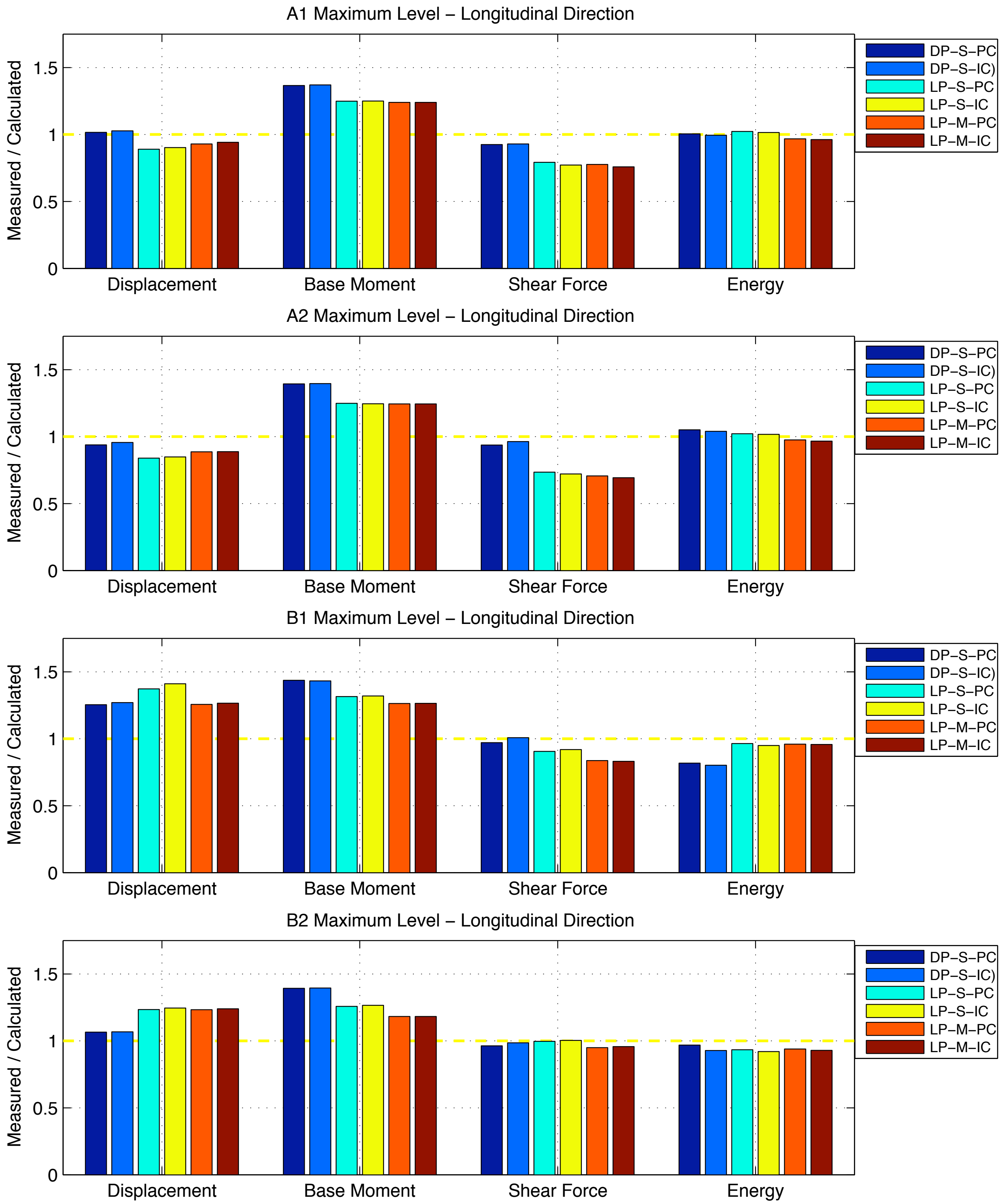

Fig. 10.14 Ratio of measured to calculated results for various response maxima in the longitudinal direction at first maximum level

10.2.4 Residual Displacements

To evaluate the accuracy of the residual displacements calculated with the six modeling variations, the calculated residual displacements (Δ_{rc}/L) in the longitudinal direction are plotted versus the measured residual displacements (Δ_{rm}/L) for both earthquake records at both levels of excitation (*design* and *maximum*) in Figure 10.15.

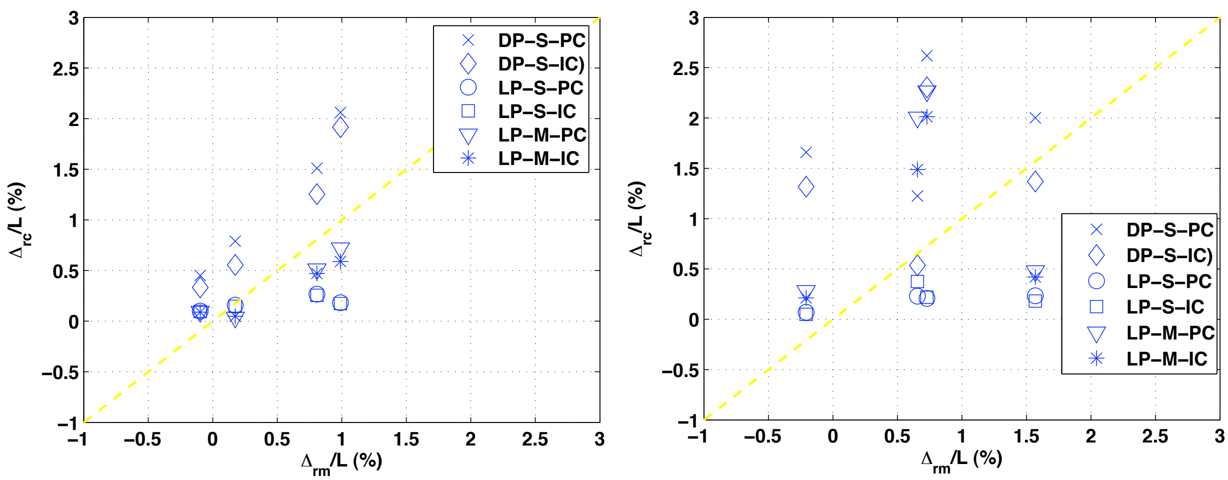

Fig. 10.15 Comparison of measured and calculated residual displacements

The following can be observed in the figure.

1. The model variations are more accurate at predicting the residual displacements at the *design* level than at the *maximum* level.
2. The distributed-plasticity variations overestimate (on average) the residual displacements for both earthquake records and both levels of excitation.
3. The imperfect crack closure variation improves the estimates of residual displacements for the distributed-plasticity model.
4. The imperfect crack closure assumption does not improve the residual displacements calculated with the lumped-plasticity variations with standard steel or degrading steel.

The normalized residual displacement error (E_{rd}) is used to further evaluate the effectiveness of the modeling strategies' abilities to predict residual displacements. This error measure is defined as the difference between measured (Δ_{res}^{meas}) and calculated (Δ_{res}^{calc}) residual displacements normalized by the maximum measured displacement, as follows.

$$E_{rd} = abs\left(\frac{\Delta_{res}^{meas} - \Delta_{res}^{calc}}{\Delta_{max}^{meas}}\right) \tag{10.1}$$

E_{rd} is plotted for each modeling strategy and each column for the first *design* level and first *maximum* level in Figure 10.16. As noted previously, the imperfect crack closure assumption improves the estimate of residual displacements for the distributed-plasticity strategy. However, the same can not be said for the lumped-plasticity methodology; there is no significant trend for this methodology. The effect of the crack closure variations may be more evident in the distributed-plasticity methodology because the stress-deformation response of the concrete in the bond-slip section was modeled with the the crack closure variations, and a significant portion of the total deformation is attributed to this section. Therefore, the model is more sensitive to this parameter. No other significant trends can be observed in the data.

More work is needed to improve estimates of residual displacements. One possible improvement would be to remove the limitation on the imperfect crack closure concrete model that does not allow compression stress in the concrete while it still has tensile strain. This would amplify the effect of imperfect crack closure, and may improve estimates of residual displacements.

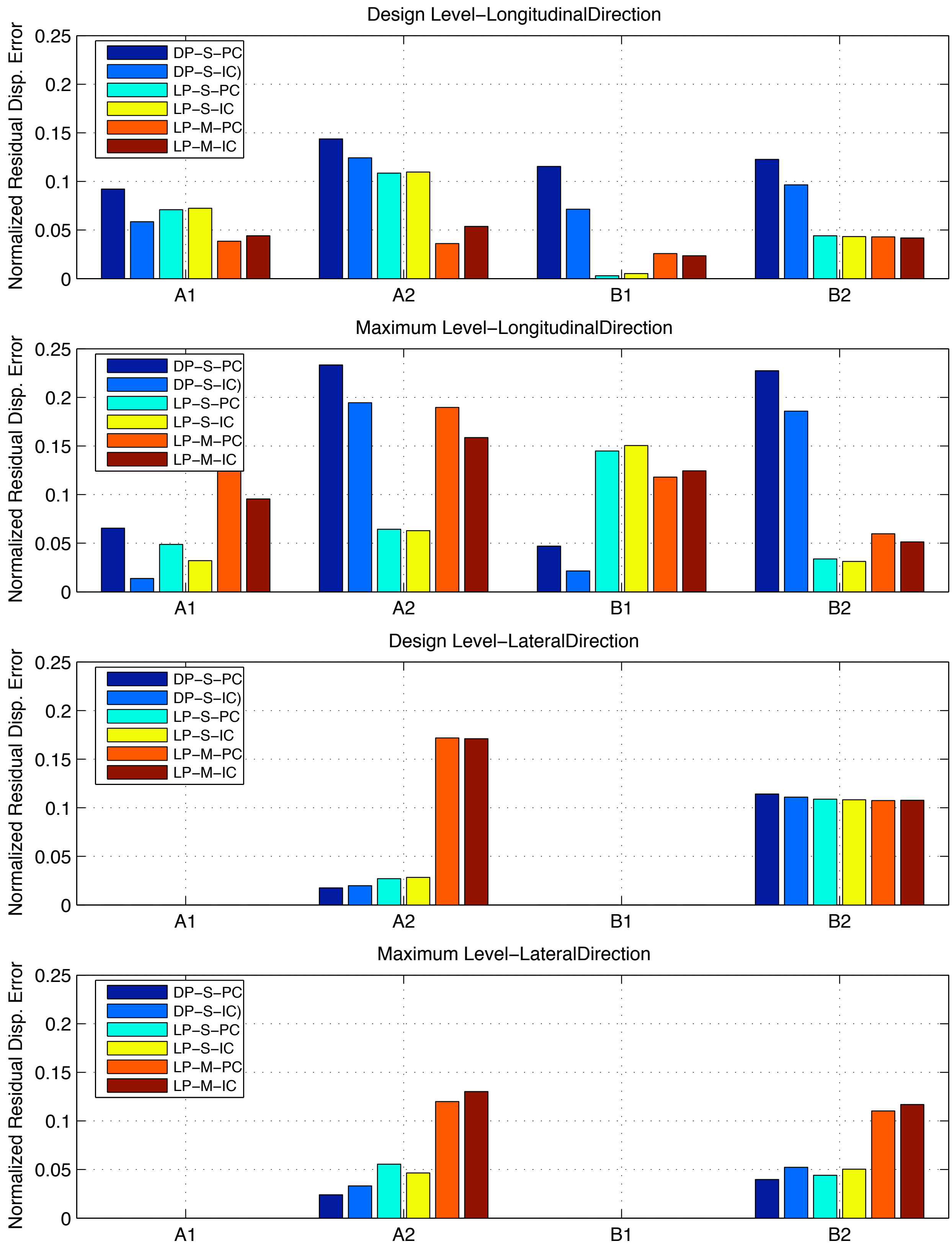

Fig. 10.16 Normalized residual displacement errors at first design level and first maximum level in longitudinal and lateral directions

10.2.5 Flexural Damage

In Chapter 9, equations were developed to predict the drift ratio (Δ_{dam}/L), plastic rotation (θ_{p_dam}), and longitudinal strain (ε_{dam}) at the onset of cover spalling and bar buckling. In this section, these damage equations are applied to the shake-table tests to evaluate their accuracy. The following analysis was carried out with only one model variation from the previous section: the lumped-plasticity variation with standard steel and perfect crack closure.

Application of the drift-ratio equations to this structural model is difficult because the distance from the base of the column to the point of contraflexure varies throughout the duration of the earthquake. This phenomenon complicates the calculation of the demand drift ratio, as well as the calculated drift ratios at the onset of cover spalling and bar buckling (from the damage equations). The varying inflexion point also complicates the calculation of the plastic rotation at the onset of bar buckling. Some simplifications must be made to apply the drift-ratio and plastic-rotation methodologies to this structural system. For a preliminary analysis, the system is assumed to act as a cantilever system, where the distance to the point of contraflexure is constant and is equal to the height of the column. This assumption is not accurate, but is performed here to demonstrate the process of applying the methodologies. The damage estimates based on strain overcome this limitation, and should provide a more effective means of estimating damage in more complicated systems.

The results of the preliminary study are summarized in tables 10.8 (cover spalling) and 10.9 (bar buckling). In these tables the calculated engineering demand parameters (from the damage equations) at the onset of the damage states are reported, along with the maximum calculated engineering demand parameters before ("pre") and immediately after ("post") the run where the damage state was observed. The probability (based on statistics from Chapter 9) that cover spalling or bar buckling will have occurred before and after the observed damage run are also provided.

As seen in Table 10.8, the onset of cover spalling is accurately predicted with the proposed drift-ratio and plastic-rotation methodologies (with current inflexion point assumption). Whereas, the strain estimates accurately predict cover spalling in specimens A1 and A2, but only estimate a 10% probability of spalling in B1 and 30% probability in B2.

The bar buckling estimates were not as clean. Although some methods calculate a 50% probability of bar buckling after the reported damage run, the same probability is calculated for the runs prior to the observed damage run. These results suggest that estimates of bar buckling may be improved if cycling is considered.

Table 10.8 Summary of spalling estimates

	Δ_{sp}/L (%)					θ_{p_sp} (%)					ε_{sp} (%)				
		pre		post			pre		post			pre		post	
col.	calc	max	pr.	max	pr.	calc	max	pr.	max	pr.	calc	max	pr.	max	pr.
A1	2.1	0.9	4%	4.9	100%	1.5	0.0	0%	3.8	100%	0.8	0.1	1%	1.5	100%
A2	2.1	0.9	5%	4.9	100%	1.5	0.0	0%	3.8	100%	0.8	0.1	1%	1.4	99%
B1	2.1	1.1	7%	3.0	81%	1.5	0.1	0%	1.9	78%	0.8	0.1	1%	0.4	10%
B2	2.1	1.3	12%	3.0	83%	1.5	0.3	1%	2.0	85%	0.8	0.2	1%	0.6	30%

Table 10.9 Summary of bar-buckling estimates

	Δ_{bb}/L (%)					θ_{p_bb} (%)					ε_{bb} (%)				
		pre		post			pre		post			pre		post	
col.	calc	max	pr.	max	pr.	calc	max	pr.	max	pr.	calc	max	pr.	max	pr.
A1	6.0	6.2	54%	6.2	54%	5.9	5.2	27%	5.2	27%	6.7	4.5	8%	5.9	32%
A2	6.0	5.5	36%	5.5	36%	5.9	4.5	13%	4.5	13%	6.7	6.7	50%	6.7	50%
B1	6.0	3.0	2%	4.5	15%	5.9	1.9	0%	3.4	3%	6.7	3.4	2%	5.9	30%
B2	6.0	4.5	14%	4.5	14%	5.9	3.4	2%	3.4	2%	6.7	5.0	15%	5.0	15%

11 Summary and Conclusions

It is important to characterize the performance of bridges during earthquakes because they are integral components of transportation networks. Loss of bridge function can have severe economic consequences, and and consequences to life safety when bridges are critical links in lifelines to emergency facilities, which are particularly important after a disasters. Although damage to other bridge elements can have economic and life-safety impacts, reinforced concrete columns are often the most vulnerable elements in a bridge, and column failure can have catastrophic consequences. Excessive deformations can result in spalling of cover concrete, buckling of longitudinal reinforcement, bar fracture, reduction of flexural capacity, and eventually, structural collapse.

The objective of this project was to develop, calibrate, and evaluate column-modeling strategies to accurately model column behavior under seismic loading, including global forces and local deformations, as well as progression of damage. The models were calibrated using the observed cyclic force-deformation responses and damage progression observations of 37 tests of spiral-reinforced columns, representative of modern bridge construction (Section 1.3). This effort is an important step toward implementing performance-based earthquake engineering for modern reinforced concrete bridges.

11.1 CROSS-SECTION MODELING

The accuracy of the column-modeling strategies presented in this report depend on the accuracy of the cross-section model, and in turn the accuracy of the material constitutive models and the cross-section discretization strategy. Uniform and nonuniform radial discretization strategies were presented in Chapter 2. Based on convergence considerations, the following conclusions were drawn.

1. A uniform radial discretization scheme with 10 radial core divisions, 20 transverse core divisions, 1 radial cover division, and 20 transverse cover divisions provides a sufficient mesh (220 total fibers) for modeling the section response of a reinforced concrete column.
2. A nonuniform discretization scheme with a coarser mesh near the center of the column can be used with an insignificant loss of accuracy. The recommended nonuniform discretization strategy has 140 total fibers. The coarse mesh at the center of the column has a radius of half the column depth with 10 transverse divisions and 2 radial divisions. The denser core concrete mesh has 20 transverse divisions and 5 radial divisions, while the cover concrete has 20 transverse divisions and 1 radial division.

11.2 ENVELOPE RESPONSE OF DISTRIBUTED-PLASTICITY COLUMN-MODELING STRATEGY

A distributed-plasticity modeling strategy was described, calibrated, and evaluated based on the envelope response of the element in chapters 3 and 4. In the proposed distributed-plasticity modeling strategy, a nonlinear force-based fiber beam-column element, a zero-length bond section, and an aggregated elastic-shear section were combined to model the flexural, bond slip and shear components of the total tip deflection of a column. In this formulation, nonlinear deformations are allowed to form anywhere along the height of the column. The following conclusions are made about the envelope response of the proposed distributed-plasticity modeling strategy.

1. The proposed distributed-plasticity column-modeling strategy provided an accurate means of estimating envelope response of the bridge columns. Key accuracy statistics are presented in Table 11.1.
2. The optimal model parameters were as follows.
   - Strain-Hardening Ratio, $b = 0.01$.
   - Elastic and Inelastic Bond-Strength Ratios, $\lambda_e = 0.9$ and $\lambda_i = 0.45$.
   - Development Bar Stress, $\sigma_d = 0.25\sigma_y$.
   - Number of Integration Points, $N_p = 5$ (Cantilever Columns), $N_p = 6$ (Double Curvature).
   - Bond-Model Effective Compression Depth, d_{comp} =1/2 neutral axis depth at $\varepsilon_c = 0.002$.

· Shear-Stiffness Ratio, $\gamma = 0.4$.

3. The calculated response of the distributed-plasticity modeling strategy is not sensitive to the integration scheme for columns with hardening section behavior. However, the calculated local deformations varied with the integration scheme for columns with perfectly-plastic section responses. For columns with degrading section responses, both the local deformations and global forces vary with the integration scheme. This subjectivity is due to strain localizations that occur at the integration point with the maximum moment.

Table 11.1 Accuracy statistics for envelope response of column-modeling strategies

	Distributed-Plasticity				Lumped-Plasticity			
Statistic	$E_{push}(\%)$	$S.R.$	$M.R.$	$D.R.$	$E_{push}(\%)$	$S.R.$	$M.R.$	$D.R.$
Mean	7.4	0.84	1.03	-0.51	7.9	1.00	1.05	-1.11
c.o.v. (%)	-	15.6	7.9	-	-	16.1	8.4	-

11.3 ENVELOPE RESPONSE OF LUMPED-PLASTICITY COLUMN-MODELING STRATEGY

The envelope response of a lumped-plasticity column-modeling strategy was presented, calibrated, and evaluated in chapters 5 and 6. In this approach, the nonlinear deformations of the lumped-plasticity formulation are assumed to be concentrated in the prescribed plastic-hinge region of the column. In the lumped-plasticity formulation, there are not separate model components to account for the shear and bond slip components of the total tip deflection. The effects of these deformation components are accounted for in the plastic-hinge length. The following conclusions were drawn about the envelope response of the proposed lumped-plasticity formulation.

1. The envelope response of modern reinforced concrete bridge columns can modeled accurately with the proposed lumped-plasticity modeling strategy. Key accuracy statistics are provided in Table 11.1.
2. The effective cross-section stiffness, $(EI)_{eff}$, of the elastic portion of the lumped-plasticity column model can be estimated as a function of the gross cross-section stiffness, E_cI_g, or secant stiffness, $(EI)_{sec} = M_y/\phi_y$, with the following equations.

$$(EI)_{eff} = \alpha_g^{calc} E_c I_g \tag{11.1}$$

$$(EI)_{eff} = \alpha_{sec}^{calc}(EI)_{sec} \tag{11.2}$$

where E_c is the modulus of elasticity of the concrete, I_g is the moment of inertia of the gross cross section. The parameters α_g and α_{sec} are stiffness modification ratios that account for the effects of bar slip, shear deformation, and axial load. These parameters can be calculated with the following equations.

$$\alpha_g^{calc} = 0.15 + 0.03\frac{L}{D} + 0.95\frac{P}{A_g f_c'} + 0.08\rho_l \leq 1.0 \tag{11.3}$$

$$\alpha_{sec}^{calc} = 0.35 + 0.1\frac{L}{D} \leq 1.0 \tag{11.4}$$

where L is the distance from the point of maximum moment to the point of contraflexure, D is the depth of the column, f_y and d_b are the yield stress and diameter of the longitudinal reinforcement, P is the axial load, A_g is the gross area of the cross section, f_c' is the concrete compressive strength, and ρ_l is the longitudinal-reinforcement ratio.

3. The length of the plastic-hinge region of the lumped-plasticity column-modeling strategy can be calculated with the following equation.

$$L_p = 0.05L + 0.1\frac{f_y d_b}{\sqrt{f_c'}} \leq \frac{L}{4} \tag{11.5}$$

11.4 CYCLIC RESPONSE OF MODELING STRATEGIES WITH STANDARD MATERIAL MODELS

The initial calibration and evaluation of the proposed distributed-plasticity (Chapter 4) and lumped-plasticity (Chapter 6) modeling strategies were based on the envelope response of the columns. In Chapter 7, the cyclic response of the modeling strategies (with standard material models) was evaluated, and inaccuracies were identified. Based on this study, the following conclusions were made.

1. Similar accuracy can be obtained using either of the distributed-plasticity or lumped-plasticity column-modeling strategies with standard cyclic material models (Giuffre-Menegotto-Pinto steel and Karsan-Jirsa concrete). Key accuracy statistics are presented in Table 11.2. The mean values of the force errors (E_{force}) were 16.1% and 15.7% for both the distributed-plasticity and lumped-plasticity models, respectively. The mean values of the energy errors

(E_{energy}) were -23.7% and -19.9% for the distributed-plasticity and lumped-plasticity models, respectively.

2. The proposed modeling strategies with standard cyclic material models accurately predict the cyclic response of the columns at low levels of ductility and cycling. However, the models failed to capture the effects of degradation due to cycling at high levels of ductility.

Table 11.2 Accuracy statistics for cyclic response of column-modeling strategies

	E_{force} (%)			E_{energy} (%)		
Modeling Strategy (Steel Model)	mean	min	max	mean	min	max
Distributed-Plasticity (Standard)	16.1	6.6	44.7	-23.7	-109.7	13.4
Lumped-Plasticity (Standard)	15.7	6.5	45.1	-19.9	-112.7	20.7
Lumped-Plasticity (Mohle and Kunnath)	12.6	5.9	23.9	-4.5	-47.2	31.6

11.5 IMPROVED CYCLIC MATERIAL MODELS

The cyclic modeling inaccuracies identified in Chapter 7 were addressed in Chapter 8. A steel material model proposed by Mohle and Kunnath (2006), which accounts for degradation due to cycling, was presented, calibrated, and evaluated. A concrete model that accounts for imperfect crack closure was also developed and evaluated in this chapter. The following conclusions were made based on the results of this study.

1. The use of a more complex steel constitutive model (Mohle and Kunnath 2006), which includes degradation due to cycling, improved the accuracy of the lumped-plasticity column-modeling strategy (Table 11.2). The mean force error (E_{force}) decreased from 15.7% with the standard steel model to 12.6% with the Mohle and Kunnath (2006) steel model and calibrated parameters ($C_f = 0.26$ and $C_d = 0.45$). The mean energy error (E_{energy}) improved from -19.9% to -4.5%.
2. The distributed-plasticity modeling strategy is susceptible to strain concentrations in perfectly-plastic or degrading members (Section 11.2). Therefore, the Mohle and Kunnath (2006) steel constitutive model should be used to model degradation due to cycling only in the lumped-plasticity column-modeling strategy.
3. The modification to the standard Karsan and Jirsa cyclic material behavior to account for imperfect crack closure did not significantly affect the accuracy of the proposed modeling

strategies.

11.6 COLUMN FLEXURAL DAMAGE

In Chapter 9, a series of damage models were developed that link three engineering demand parameters (drift ratio, plastic rotation, longitudinal strain) with three damage states (cover spalling, bar buckling, and bar fracture). Table 11.3 summarizes this study and provides key accuracy statistics.

Table 11.3 Comparison of damage estimates

Damage State	E.D.P.	Equation	$\Delta_{dam}^{meas}/\Delta_{dam}^{calc}$ mean	cov (%)
Cover Spalling (29 columns)	$\Delta_{sp}^{calc}/L\,(\%)$	$1.6\ (1-P/A_g f'_c)\ (1+L/10D)$	1.07	34.9
	$\theta_{p\_sp}^{calc}\ (\%)$	1.20	0.98	33.9
	ε_{sp}	0.008	0.99	34.7
Bar Buckling (33 columns)	$\Delta_{bb}^{calc}/L\,(\%)$	$3.25\ \left(1+150\rho_{eff}d_b/D\right)(1-P/A_g f'_c)\ (1+L/10D)$	1.01	24.7
	$\theta_{p\_bb}^{calc}\ (\%)$	$2.75\ \left(1+150\rho_{eff}d_b/D\right)(1-P/A_g f'_c)\ (1+L/10D)$	1.01	24.3
	ε_{bb}^{calc}	$0.045+0.25\rho_{eff}\leq 0.15$	1.00	23.6
Bar Fracture (20 columns)	$\Delta_{bf}^{calc}/L\,(\%)$	$3.5\ \left(1+150\rho_{eff}d_b/D\right)(1-P/A_g f'_c)\ (1+L/10D)$	0.97	20.0
	$\theta_{p\_bf}^{calc}\ (\%)$	$3.0\ \left(1+150\rho_{eff}d_b/D\right)(1-P/A_g f'_c)\ (1+L/10D)$	0.97	19.6
	ε_{bf}^{calc}	$0.045+0.30\rho_{eff}\leq 0.15$	0.96	20.5

1. Similar levels of accuracy can be obtained by estimating the onset of damage using drift ratio, plastic rotation, or longitudinal strain (Table 11.3). The coefficients of variation for the ratios of measured to calculated displacements at the onset of spalling were approximately 35% for all three methods. The coefficients of variation for the onset of bar buckling using the three methods were approximately 24%. For bar fracture, the coefficient of variations were approximately 21% for all three methods.
2. The drift-ratio equations provide a practical correlation between an engineering demand parameter and key damage states. However, the application of this method is limited to tests in which the the distance to the point of contraflexure does not vary, the axial load does not vary, and there is only uniaxial bending. Although estimates based on plastic rotation suffer

from the same limitations, plastic rotation is a more versatile engineering demand parameter because it is more easily calculated in a complex model. The damage estimates based on longitudinal strain overcome the limitations of the drift-ratio and plastic-rotation equations, however they require a more detailed model in which strains can be monitored, and the calculated strains depend on the assumed plastic-hinge length.

11.7 APPLICATION OF COLUMN-MODELING STRATEGIES TO MORE COMPLEX STRUCTURES

The proposed modeling strategies were evaluated for use in more complex structures in Chapter 10. The models were first used to model the columns of a two-column bent test performed at Purdue University (Makido 2006). The modeling strategies were then used to model the dynamic response of shake-table specimens tested at the University of California at Berkeley (Hachem, Mahin, and Moehle 2003). The following conclusions were drawn from this study.

1. The proposed modeling strategies provided an accurate means of predicting the force-deformation response and damage progression of the column bent tests (Table 11.4). The stiffness estimates improved by using the bond properties identified by Ranf (2006). The Mohle and Kunnath (2006) steel constitutive model provided a more accurate estimate of cyclic response.

Table 11.4 Accuracy statistics for bent specimen

Strategy	Steel Model	$E_{push}(\%)$	$S.R.$	$M.R.$	$D.R.(\%)$	$E_{force}(\%)$	$E_{energy}(\%)$
Distr.	Standard	11.9	0.7	1.0	8.8	21.0	-63.9
Distr., Ranf Bond	Standard	8.4	0.9	1.0	8.9	19.3	-50.0
Lumped	Standard	7.6	0.9	1.1	8.2	19.8	-56.3
Lumped	Mohle and Kunnath	8.5	0.9	1.0	8.1	13.4	-33.5

2. The proposed column-modeling strategies provided an accurate means of estimating response maxima, hysteretic energy dissipation, and cover spalling in the shake-table specimens tested at the University of California at Berkeley. However, the models were not successful at predicting residual displacements nor the effect of cumulative deformation on bar buckling.

3. Similar accuracy can be obtained by using either the distributed-plasticity or lumped-plasticity column-modeling strategies. It is necessary to use the distributed-plasticity modeling strategy when the location of the yielding is unknown (e.g., modeling a column partially embedded in the soil). In situations in which the location of the plastic hinge is known (e.g., cantilever column), the lumped-plasticity method is preferred. This method is more efficient (only one nonlinear integration point) and the localization issues are governed by a calculated plastic hinge (which has a physical interpretation), rather than a selected integration scheme.

11.8 RECOMMENDATIONS FOR FURTHER WORK

The following suggestions are made for further work.

1. The effect of cycling on cover spalling, bar buckling, and bar fracture should be evaluated further.
2. The return drift and return strain models proposed by Freytag (2006) to estimate bar buckling should be used to evaluate the column tests in the bridge column dataset used in this report.
3. The effect of varying the damping ratio on the calculated response of the shake-table specimens should be evaluated.
4. The imperfect crack closure model proposed in Chapter 10 should be improved to allow compressive stress while the concrete is still in the tensile strain region.

REFERENCES

ACI 318 (2002). *Building Code Requirements for Structural Concrete*. American Concrete Institute.

Berry, M. and M. Eberhard (2003). *Performance Models for Flexural Damage in Reinforced Concrete Columns,*. PEER 2003/18, Pacific Earthquake Engineering Research Center, Berkeley, CA.

Berry, M. and M. Eberhard (2005, July). Practical performance model for bar buckling. *Journal of the Structural Engineering ASCE 131*(7), 1060–70.

Berry, M., M. Parish, and M. O. Eberhard (2004). *PEER Structural Performance Database*. Pacific Earthquake Engineering Research Center, Berkeley, CA.

Chang, G. and J. Mander (1994). NCEER Technical Report 94-0006.

Cheok, G. S. and W. C. Stone (1986). *Behavior of 1/6-scale model bridge columns subjected to cycle inelastic loading, NBSIR 86-3494*. U.S. National Institute of Standards and Technology, Gaithersburg, Md.

Coleman, J. and E. Spacone (2001, November). Localization issues in force-based frame elements. *Journal of the Structural Engineering ASCE 127*(11), 1257–1265.

Corley, G. W. (1966). Rotational capacity of reinforced concrete beams. *Journal of the Structural Division ASCE 92*(ST5), 121–146.

Dhakal, R. and K. Maekawa (2002). Modeling for postyield buckled of reinforcement. *Journal of the Structural Engineering ASCE 128*(9), 1139–1147.

Freytag, D. (2006). Bar buckling in reinforced concrete bridge columns. Master's thesis, University of Washington.

Ghee, A. B., M. J. N. Priestley, and R. Park (1981). *Ductility of reinforced concrete bridge piers under seismic loading, Report 81-3*. Department of Civil Engineering, University of Canterbury, Christchurch, New Zealand.

Gomes, A. and J. Appleton (1997). Nonlinear cyclic stress-strain relationship of reinforcing bars including buckling. *Journal of the Structural Engineering ASCE 19*(10).

Hachem, M. M., S. A. Mahin, and J. P. Moehle (2003). *Performance of Circular Reinforced Concrete Bridge Columns under Bidirectional Earthquake Loading*. PEER 2003/06, Pacific Earthquake Engineering Research Center, Berkeley, CA.

Henry, L. and S. A. Mahin (1999). *Study of buckling of longitudinal bars in reinforced concrete bridge columns*. Report to the California Dept. of Transportation.

Hose, Y. D., F. Seible, and M. J. N. Priestley (1997). *Strategic relocation of plastic hinges in bridge columns, Structural Systems Research Project, 97/05*. University of California, San Diego.

Johnson, N., R. T. Ranf, M. Saiidi, D. Sanders, and M. Eberhard (2006, August). Shake table studies of a large scale two-span reinforced concrete bridge frame. *Proceedings from the Eighth National Conference on Earthquake Engineering*.

Kowalsky, M., M. Priestley, and F. Seible (1999). Shear and flexural behavior of lightweight concrete bridge columns in seismic regions. *ACI Structural Journal*.

Kunnath, S., A. El-Bahy, A. Taylor, and W. Stone (1997). *Cumulative seismic damage of reinforced concrete bridge piers, NCEER-97-0006*. National Center for Earthquake Engineering Research, Buffalo, N.Y.

Lehman, D. E. and J. P. Moehle (2000). *Seismic Performance of Well-Confined Concrete Bridge Columns*. PEER 1998/01, Pacific Earthquake Engineering Research Center, Berkeley, CA.

Makido, A. (2006). Pseudo-static tests of bridge components. Master's thesis, Purdue University.

Mander, J., M. Priestley, and R. Park (1988, August). Theoretical stress-strain model for confined concrete. *Journal of the Structural Division ASCE 114*(8), 1804–1826.

MATLAB (2005). *Version 7.01*. The Mathworks, www.mathworks.com.

Mattock, A. (1967). Rotational capacity of reinforced concrete beams. *Journal of Structural Division, ASCE 93*(ST2).

Mazzoni, S., F. McKenna, G. L. Fenves, and et al (2006). Open system for earthquake engineering simulation user manual. *www.opensees.berkeley.edu*.

Mohle, J. and S. Kunnath (2006). Reinforcing steel. *OpenSEES User's Manual, www.opensees.berkeley.edu*.

Moyer, M. and M. Kowalsky (2001). Influence of tension strain on buckling of reinforcement in rc bridge columns. Master's thesis, North Carolina State University.

Munro, I., R. Park, and M. Priestley (1976). *Seismic Behaviour of Reinforced Concrete Bridge Piers, Report 76-9*. Department of Civil Engineering, University of Canterbury, Christchurch, New Zealand.

OpenSees Development Team (2002). Opensees: Open system for earthquake engineering simulations. Version 1.5, Berkeley, CA.

Parish, M. (2001). Accuracy of seismic performance methodologies for rectangular reinforced concrete columns. Master's thesis, University of Washington.

Park, R. and T. Paulay (1975). *Reinforced Concrete Structures*. New York: John Wiley and Sons, Inc.

Pontangaroa, R., M. Priestley, and R. Park (1979). *Ductility of Spirally Reinforced Concrete Columns Under Seismic Loading, Report 79-8*. Department of Civil Engineering, University of Canterbury, Christchurch, New Zealand.

Priestley, M., F. Seible, and G. Calvi (1996). *Seismic Design and Retrofit of Bridges*. New York: John Wiley and Sons, Inc.

Ranf, R. (2006). *Performance Based Evaluation of Seismic Modeling Strategies for Bridges*. Ph. D. thesis, Univeristy of Washington, Seattle.

Sachem, M. (2003). *Performance of Circular Reinforced Concrete Bridge Columns Under Bidirectional Earthquake Loading*. PEER 2003/06, Pacific Earthquake Engineering Research Center, Berkeley, CA.

Scott, M. and G. Fenves (2006, February). Plastic hinge integration methods for force-based beam-column elements. *Journal of the Structural Engineering ASCE 132*(2), 244–252.

Stanton, J. (1979). *The Development of a Mathematical Model to Predict the Flexural Response of Reinforced Concrete Beams to Cyclic Loads, Using System Identification*. Ph. D. thesis, University of California at Berkeley, Berkeley, California.

Stone, W. C. and G. S. Cheok (1989). *Inelastic behavior of full-scale bridge columns subjected to cyclic loading, NIST Building Science Series 166*. U.S. National Institute of Standards and Technology, Gaithersburg, Md.

Taucer, F., E. Spacone, and F. Filippou (1991). *A Fiber Beam-Column Element for Seismic Response Analysis of Reinforced Concrete Structures*. UCB/EERC-91/17, Earthquake Engineering Research Center, Berkeley, CA.

Vu, N. D., M. J. N. Priestley, F. Seible, and G. Benzoni (1998). *Seismic response of well confined circular reinforced concrete columns with low aspect ratios, 97/05*. Proc., 5th Caltrans Seismic Research Workshop, Sacramento, California.

Wong, Y. L., T. Paulay, and M. J. N. Priestley (1990). *Squat circular bridge piers under multi-directional seismic attack, Report 90-4*. Department of Civil Engineering, University of Canterbury, Christchurch, New Zealand.

PEER REPORTS

PEER reports are available from the National Information Service for Earthquake Engineering (NISEE). To order PEER reports, please contact the Pacific Earthquake Engineering Research Center, 1301 South 46th Street, Richmond, California 94804-4698. Tel.: (510) 665-3405; Fax: (510) 665-3420.

PEER 2007/11 *Bar Buckling in Reinforced Concrete Bridge Columns.* Wayne A. Brown, Dawn E. Lehman, and John F. Stanton. February 2008.

PEER 2007/09 *Integrated Probabilistic Performance-Based Evaluation of Benchmark Reinforced Concrete Bridges.* Kevin R. Mackie, John-Michael Wong, and Božidar Stojadinović. January 2008.

PEER 2007/08 *Assessing Seismic Collapse Safety of Modern Reinforced Concrete Moment-Frame Buildings.* Curt B. Haselton and Gregory G. Deierlein. February 2008.

PEER 2007/07 *Performance Modeling Strategies for Modern Reinforced Concrete Bridge Columns.* Michael P. Berry and Marc O. Eberhard. April 2008.

PEER 2007/06 *Development of Improved Procedures for Seismic Design of Buried and Partially Buried Structures.* Linda Al Atik and Nicholas Sitar. June 2007.

PEER 2007/05 *Uncertainty and Correlation in Seismic Risk Assessment of Transportation Systems.* Renee G. Lee and Anne S. Kiremidjian. July 2007.

PEER 2007/02 *Campbell-Bozorgnia NGA Ground Motion Relations for the Geometric Mean Horizontal Component of Peak and Spectral Ground Motion Parameters.* Kenneth W. Campbell and Yousef Bozorgnia. May 2007.

PEER 2007/01 *Boore-Atkinson NGA Ground Motion Relations for the Geometric Mean Horizontal Component of Peak and Spectral Ground Motion Parameters.* David M. Boore and Gail M. Atkinson. May. May 2007.

PEER 2006/12 *Societal Implications of Performance-Based Earthquake Engineering.* Peter J. May. May 2007.

PEER 2006/11 *Probabilistic Seismic Demand Analysis Using Advanced Ground Motion Intensity Measures, Attenuation Relationships, and Near-Fault Effects.* Polsak Tothong and C. Allin Cornell. March 2007.

PEER 2006/10 *Application of the PEER PBEE Methodology to the I-880 Viaduct.* Sashi Kunnath. February 2007.

PEER 2006/09 *Quantifying Economic Losses from Travel Forgone Following a Large Metropolitan Earthquake.* James Moore, Sungbin Cho, Yue Yue Fan, and Stuart Werner. November 2006.

PEER 2006/08 *Vector-Valued Ground Motion Intensity Measures for Probabilistic Seismic Demand Analysis*. Jack W. Baker and C. Allin Cornell. October 2006.

PEER 2006/07 *Analytical Modeling of Reinforced Concrete Walls for Predicting Flexural and Coupled–Shear-Flexural Responses.* Kutay Orakcal, Loenardo M. Massone, and John W. Wallace. October 2006.

PEER 2006/06 *Nonlinear Analysis of a Soil-Drilled Pier System under Static and Dynamic Axial Loading.* Gang Wang and Nicholas Sitar. November 2006.

PEER 2006/05 *Advanced Seismic Assessment Guidelines.* Paolo Bazzurro, C. Allin Cornell, Charles Menun, Maziar Motahari, and Nicolas Luco. September 2006.

PEER 2006/04 *Probabilistic Seismic Evaluation of Reinforced Concrete Structural Components and Systems.* Tae Hyung Lee and Khalid M. Mosalam. August 2006.

PEER 2006/03 *Performance of Lifelines Subjected to Lateral Spreading.* Scott A. Ashford and Teerawut Juirnarongrit. July 2006.

PEER 2006/02 *Pacific Earthquake Engineering Research Center Highway Demonstration Project.* Anne Kiremidjian, James Moore, Yue Yue Fan, Nesrin Basoz, Ozgur Yazali, and Meredith Williams. April 2006.

PEER 2006/01 *Bracing Berkeley. A Guide to Seismic Safety on the UC Berkeley Campus.* Mary C. Comerio, Stephen Tobriner, and Ariane Fehrenkamp. January 2006.

PEER 2005/16 *Seismic Response and Reliability of Electrical Substation Equipment and Systems.* Junho Song, Armen Der Kiureghian, and Jerome L. Sackman. April 2006.

PEER 2005/15 *CPT-Based Probabilistic Assessment of Seismic Soil Liquefaction Initiation.* R. E. S. Moss, R. B. Seed, R. E. Kayen, J. P. Stewart, and A. Der Kiureghian. April 2006.

PEER 2005/14 *Workshop on Modeling of Nonlinear Cyclic Load-Deformation Behavior of Shallow Foundations.* Bruce L. Kutter, Geoffrey Martin, Tara Hutchinson, Chad Harden, Sivapalan Gajan, and Justin Phalen. March 2006.

PEER 2005/13 *Stochastic Characterization and Decision Bases under Time-Dependent Aftershock Risk in Performance-Based Earthquake Engineering.* Gee Liek Yeo and C. Allin Cornell. July 2005.

PEER 2005/12 *PEER Testbed Study on a Laboratory Building: Exercising Seismic Performance Assessment.* Mary C. Comerio, editor. November 2005.

PEER 2005/11 *Van Nuys Hotel Building Testbed Report: Exercising Seismic Performance Assessment.* Helmut Krawinkler, editor. October 2005.

PEER 2005/10 *First NEES/E-Defense Workshop on Collapse Simulation of Reinforced Concrete Building Structures.* September 2005.

PEER 2005/09 *Test Applications of Advanced Seismic Assessment Guidelines.* Joe Maffei, Karl Telleen, Danya Mohr, William Holmes, and Yuki Nakayama. August 2006.

PEER 2005/08 *Damage Accumulation in Lightly Confined Reinforced Concrete Bridge Columns.* R. Tyler Ranf, Jared M. Nelson, Zach Price, Marc O. Eberhard, and John F. Stanton. April 2006.

PEER 2005/07 *Experimental and Analytical Studies on the Seismic Response of Freestanding and Anchored Laboratory Equipment.* Dimitrios Konstantinidis and Nicos Makris. January 2005.

PEER 2005/06 *Global Collapse of Frame Structures under Seismic Excitations.* Luis F. Ibarra and Helmut Krawinkler. September 2005.

PEER 2005//05 *Performance Characterization of Bench- and Shelf-Mounted Equipment.* Samit Ray Chaudhuri and Tara C. Hutchinson. May 2006.

PEER 2005/04 *Numerical Modeling of the Nonlinear Cyclic Response of Shallow Foundations.* Chad Harden, Tara Hutchinson, Geoffrey R. Martin, and Bruce L. Kutter. August 2005.

PEER 2005/03 *A Taxonomy of Building Components for Performance-Based Earthquake Engineering.* Keith A. Porter. September 2005.

PEER 2005/02 *Fragility Basis for California Highway Overpass Bridge Seismic Decision Making.* Kevin R. Mackie and Božidar Stojadinović. June 2005.

PEER 2005/01 *Empirical Characterization of Site Conditions on Strong Ground Motion.* Jonathan P. Stewart, Yoojoong Choi, and Robert W. Graves. June 2005.

PEER 2004/09 *Electrical Substation Equipment Interaction: Experimental Rigid Conductor Studies.* Christopher Stearns and André Filiatrault. February 2005.

PEER 2004/08 *Seismic Qualification and Fragility Testing of Line Break 550-kV Disconnect Switches.* Shakhzod M. Takhirov, Gregory L. Fenves, and Eric Fujisaki. January 2005.

PEER 2004/07 *Ground Motions for Earthquake Simulator Qualification of Electrical Substation Equipment.* Shakhzod M. Takhirov, Gregory L. Fenves, Eric Fujisaki, and Don Clyde. January 2005.

PEER 2004/06 *Performance-Based Regulation and Regulatory Regimes.* Peter J. May and Chris Koski. September 2004.

PEER 2004/05 *Performance-Based Seismic Design Concepts and Implementation: Proceedings of an International Workshop.* Peter Fajfar and Helmut Krawinkler, editors. September 2004.

PEER 2004/04 *Seismic Performance of an Instrumented Tilt-up Wall Building.* James C. Anderson and Vitelmo V. Bertero. July 2004.

PEER 2004/03 *Evaluation and Application of Concrete Tilt-up Assessment Methodologies.* Timothy Graf and James O. Malley. October 2004.

PEER 2004/02 *Analytical Investigations of New Methods for Reducing Residual Displacements of Reinforced Concrete Bridge Columns.* Junichi Sakai and Stephen A. Mahin. August 2004.

PEER 2004/01 *Seismic Performance of Masonry Buildings and Design Implications.* Kerri Anne Taeko Tokoro, James C. Anderson, and Vitelmo V. Bertero. February 2004.

PEER 2003/18 *Performance Models for Flexural Damage in Reinforced Concrete Columns.* Michael Berry and Marc Eberhard. August 2003.

PEER 2003/17 *Predicting Earthquake Damage in Older Reinforced Concrete Beam-Column Joints.* Catherine Pagni and Laura Lowes. October 2004.

PEER 2003/16 *Seismic Demands for Performance-Based Design of Bridges.* Kevin Mackie and Božidar Stojadinović. August 2003.

PEER 2003/15 *Seismic Demands for Nondeteriorating Frame Structures and Their Dependence on Ground Motions.* Ricardo Antonio Medina and Helmut Krawinkler. May 2004.

PEER 2003/14 *Finite Element Reliability and Sensitivity Methods for Performance-Based Earthquake Engineering.* Terje Haukaas and Armen Der Kiureghian. April 2004.

PEER 2003/13 *Effects of Connection Hysteretic Degradation on the Seismic Behavior of Steel Moment-Resisting Frames.* Janise E. Rodgers and Stephen A. Mahin. March 2004.

PEER 2003/12 *Implementation Manual for the Seismic Protection of Laboratory Contents: Format and Case Studies.* William T. Holmes and Mary C. Comerio. October 2003.

PEER 2003/11 *Fifth U.S.-Japan Workshop on Performance-Based Earthquake Engineering Methodology for Reinforced Concrete Building Structures.* February 2004.

PEER 2003/10 *A Beam-Column Joint Model for Simulating the Earthquake Response of Reinforced Concrete Frames.* Laura N. Lowes, Nilanjan Mitra, and Arash Altoontash. February 2004.

PEER 2003/09 *Sequencing Repairs after an Earthquake: An Economic Approach.* Marco Casari and Simon J. Wilkie. April 2004.

PEER 2003/08 *A Technical Framework for Probability-Based Demand and Capacity Factor Design (DCFD) Seismic Formats*. Fatemeh Jalayer and C. Allin Cornell. November 2003.

PEER 2003/07 *Uncertainty Specification and Propagation for Loss Estimation Using FOSM Methods.* Jack W. Baker and C. Allin Cornell. September 2003.

PEER 2003/06 *Performance of Circular Reinforced Concrete Bridge Columns under Bidirectional Earthquake Loading*. Mahmoud M. Hachem, Stephen A. Mahin, and Jack P. Moehle. February 2003.

PEER 2003/05 *Response Assessment for Building-Specific Loss Estimation.* Eduardo Miranda and Shahram Taghavi. September 2003.

PEER 2003/04 *Experimental Assessment of Columns with Short Lap Splices Subjected to Cyclic Loads*. Murat Melek, John W. Wallace, and Joel Conte. April 2003.

PEER 2003/03 *Probabilistic Response Assessment for Building-Specific Loss Estimation.* Eduardo Miranda and Hesameddin Aslani. September 2003.

PEER 2003/02 *Software Framework for Collaborative Development of Nonlinear Dynamic Analysis Program.* Jun Peng and Kincho H. Law. September 2003.

PEER 2003/01 *Shake Table Tests and Analytical Studies on the Gravity Load Collapse of Reinforced Concrete Frames.* Kenneth John Elwood and Jack P. Moehle. November 2003.

PEER 2002/24 *Performance of Beam to Column Bridge Joints Subjected to a Large Velocity Pulse.* Natalie Gibson, André Filiatrault, and Scott A. Ashford. April 2002.

PEER 2002/23 *Effects of Large Velocity Pulses on Reinforced Concrete Bridge Columns.* Greg L. Orozco and Scott A. Ashford. April 2002.

PEER 2002/22 *Characterization of Large Velocity Pulses for Laboratory Testing.* Kenneth E. Cox and Scott A. Ashford. April 2002.

PEER 2002/21 *Fourth U.S.-Japan Workshop on Performance-Based Earthquake Engineering Methodology for Reinforced Concrete Building Structures*. December 2002.

PEER 2002/20 *Barriers to Adoption and Implementation of PBEE Innovations.* Peter J. May. August 2002.

PEER 2002/19 *Economic-Engineered Integrated Models for Earthquakes: Socioeconomic Impacts.* Peter Gordon, James E. Moore II, and Harry W. Richardson. July 2002.

PEER 2002/18 *Assessment of Reinforced Concrete Building Exterior Joints with Substandard Details.* Chris P. Pantelides, Jon Hansen, Justin Nadauld, and Lawrence D. Reaveley. May 2002.

PEER 2002/17 *Structural Characterization and Seismic Response Analysis of a Highway Overcrossing Equipped with Elastomeric Bearings and Fluid Dampers: A Case Study.* Nicos Makris and Jian Zhang. November 2002.

PEER 2002/16 *Estimation of Uncertainty in Geotechnical Properties for Performance-Based Earthquake Engineering.* Allen L. Jones, Steven L. Kramer, and Pedro Arduino. December 2002.

PEER 2002/15 *Seismic Behavior of Bridge Columns Subjected to Various Loading Patterns.* Asadollah Esmaeily-Gh. and Yan Xiao. December 2002.

PEER 2002/14 *Inelastic Seismic Response of Extended Pile Shaft Supported Bridge Structures.* T.C. Hutchinson, R.W. Boulanger, Y.H. Chai, and I.M. Idriss. December 2002.

PEER 2002/13 *Probabilistic Models and Fragility Estimates for Bridge Components and Systems.* Paolo Gardoni, Armen Der Kiureghian, and Khalid M. Mosalam. June 2002.

PEER 2002/12 *Effects of Fault Dip and Slip Rake on Near-Source Ground Motions: Why Chi-Chi Was a Relatively Mild M7.6 Earthquake.* Brad T. Aagaard, John F. Hall, and Thomas H. Heaton. December 2002.

PEER 2002/11 *Analytical and Experimental Study of Fiber-Reinforced Strip Isolators*. James M. Kelly and Shakhzod M. Takhirov. September 2002.

PEER 2002/10 *Centrifuge Modeling of Settlement and Lateral Spreading with Comparisons to Numerical Analyses***.** Sivapalan Gajan and Bruce L. Kutter. January 2003.

PEER 2002/09 *Documentation and Analysis of Field Case Histories of Seismic Compression during the 1994 Northridge, California, Earthquake.* Jonathan P. Stewart, Patrick M. Smith, Daniel H. Whang, and Jonathan D. Bray. October 2002.

PEER 2002/08 *Component Testing, Stability Analysis and Characterization of Buckling-Restrained Unbonded Braces™.* Cameron Black, Nicos Makris, and Ian Aiken. September 2002.

PEER 2002/07 *Seismic Performance of Pile-Wharf Connections.* Charles W. Roeder, Robert Graff, Jennifer Soderstrom, and Jun Han Yoo. December 2001.

PEER 2002/06 *The Use of Benefit-Cost Analysis for Evaluation of Performance-Based Earthquake Engineering Decisions*. Richard O. Zerbe and Anthony Falit-Baiamonte. September 2001.

PEER 2002/05 *Guidelines, Specifications, and Seismic Performance Characterization of Nonstructural Building Components and Equipment*. André Filiatrault, Constantin Christopoulos, and Christopher Stearns. September 2001.

PEER 2002/04 *Consortium of Organizations for Strong-Motion Observation Systems and the Pacific Earthquake Engineering Research Center Lifelines Program: Invited Workshop on Archiving and Web Dissemination of Geotechnical Data, 4–5 October 2001*. September 2002.

PEER 2002/03 *Investigation of Sensitivity of Building Loss Estimates to Major Uncertain Variables for the Van Nuys Testbed.* Keith A. Porter, James L. Beck, and Rustem V. Shaikhutdinov. August 2002.

PEER 2002/02 *The Third U.S.-Japan Workshop on Performance-Based Earthquake Engineering Methodology for Reinforced Concrete Building Structures*. July 2002.

PEER 2002/01 *Nonstructural Loss Estimation: The UC Berkeley Case Study.* Mary C. Comerio and John C. Stallmeyer. December 2001.

PEER 2001/16 *Statistics of SDF-System Estimate of Roof Displacement for Pushover Analysis of Buildings.* Anil K. Chopra, Rakesh K. Goel, and Chatpan Chintanapakdee. December 2001.

PEER 2001/15 *Damage to Bridges during the 2001 Nisqually Earthquake.* R. Tyler Ranf, Marc O. Eberhard, and Michael P. Berry. November 2001.

PEER 2001/14 *Rocking Response of Equipment Anchored to a Base Foundation.* Nicos Makris and Cameron J. Black. September 2001.

PEER 2001/13 *Modeling Soil Liquefaction Hazards for Performance-Based Earthquake Engineering.* Steven L. Kramer and Ahmed-W. Elgamal. February 2001.

PEER 2001/12 *Development of Geotechnical Capabilities in OpenSees.* Boris Jeremi . September 2001.

PEER 2001/11 *Analytical and Experimental Study of Fiber-Reinforced Elastomeric Isolators*. James M. Kelly and Shakhzod M. Takhirov. September 2001.

PEER 2001/10 *Amplification Factors for Spectral Acceleration in Active Regions.* Jonathan P. Stewart, Andrew H. Liu, Yoojoong Choi, and Mehmet B. Baturay. December 2001.

PEER 2001/09 *Ground Motion Evaluation Procedures for Performance-Based Design.* Jonathan P. Stewart, Shyh-Jeng Chiou, Jonathan D. Bray, Robert W. Graves, Paul G. Somerville, and Norman A. Abrahamson. September 2001.

PEER 2001/08 *Experimental and Computational Evaluation of Reinforced Concrete Bridge Beam-Column Connections for Seismic Performance*. Clay J. Naito, Jack P. Moehle, and Khalid M. Mosalam. November 2001.

PEER 2001/07 *The Rocking Spectrum and the Shortcomings of Design Guidelines.* Nicos Makris and Dimitrios Konstantinidis. August 2001.

PEER 2001/06 *Development of an Electrical Substation Equipment Performance Database for Evaluation of Equipment Fragilities*. Thalia Agnanos. April 1999.

PEER 2001/05 *Stiffness Analysis of Fiber-Reinforced Elastomeric Isolators.* Hsiang-Chuan Tsai and James M. Kelly. May 2001.

PEER 2001/04 *Organizational and Societal Considerations for Performance-Based Earthquake Engineering.* Peter J. May. April 2001.

PEER 2001/03 *A Modal Pushover Analysis Procedure to Estimate Seismic Demands for Buildings: Theory and Preliminary Evaluation.* Anil K. Chopra and Rakesh K. Goel. January 2001.

PEER 2001/02 *Seismic Response Analysis of Highway Overcrossings Including Soil-Structure Interaction.* Jian Zhang and Nicos Makris. March 2001.

PEER 2001/01 *Experimental Study of Large Seismic Steel Beam-to-Column Connections.* Egor P. Popov and Shakhzod M. Takhirov. November 2000.

PEER 2000/10 *The Second U.S.-Japan Workshop on Performance-Based Earthquake Engineering Methodology for Reinforced Concrete Building Structures.* March 2000.

PEER 2000/09 *Structural Engineering Reconnaissance of the August 17, 1999 Earthquake: Kocaeli (Izmit), Turkey.* Halil Sezen, Kenneth J. Elwood, Andrew S. Whittaker, Khalid Mosalam, John J. Wallace, and John F. Stanton. December 2000.

PEER 2000/08 *Behavior of Reinforced Concrete Bridge Columns Having Varying Aspect Ratios and Varying Lengths of Confinement.* Anthony J. Calderone, Dawn E. Lehman, and Jack P. Moehle. January 2001.

PEER 2000/07 *Cover-Plate and Flange-Plate Reinforced Steel Moment-Resisting Connections.* Taejin Kim, Andrew S. Whittaker, Amir S. Gilani, Vitelmo V. Bertero, and Shakhzod M. Takhirov. September 2000.

PEER 2000/06 *Seismic Evaluation and Analysis of 230-kV Disconnect Switches.* Amir S. J. Gilani, Andrew S. Whittaker, Gregory L. Fenves, Chun-Hao Chen, Henry Ho, and Eric Fujisaki. July 2000.

PEER 2000/05 *Performance-Based Evaluation of Exterior Reinforced Concrete Building Joints for Seismic Excitation.* Chandra Clyde, Chris P. Pantelides, and Lawrence D. Reaveley. July 2000.

PEER 2000/04 *An Evaluation of Seismic Energy Demand: An Attenuation Approach.* Chung-Che Chou and Chia-Ming Uang. July 1999.

PEER 2000/03 *Framing Earthquake Retrofitting Decisions: The Case of Hillside Homes in Los Angeles.* Detlof von Winterfeldt, Nels Roselund, and Alicia Kitsuse. March 2000.

PEER 2000/02 *U.S.-Japan Workshop on the Effects of Near-Field Earthquake Shaking.* Andrew Whittaker, ed. July 2000.

PEER 2000/01 *Further Studies on Seismic Interaction in Interconnected Electrical Substation Equipment.* Armen Der Kiureghian, Kee-Jeung Hong, and Jerome L. Sackman. November 1999.

PEER 1999/14 *Seismic Evaluation and Retrofit of 230-kV Porcelain Transformer Bushings*. Amir S. Gilani, Andrew S. Whittaker, Gregory L. Fenves, and Eric Fujisaki. December 1999.

PEER 1999/13 *Building Vulnerability Studies: Modeling and Evaluation of Tilt-up and Steel Reinforced Concrete Buildings.* John W. Wallace, Jonathan P. Stewart, and Andrew S. Whittaker, editors. December 1999.

PEER 1999/12 *Rehabilitation of Nonductile RC Frame Building Using Encasement Plates and Energy-Dissipating Devices.* Mehrdad Sasani, Vitelmo V. Bertero, James C. Anderson. December 1999.

PEER 1999/11 *Performance Evaluation Database for Concrete Bridge Components and Systems under Simulated Seismic Loads.* Yael D. Hose and Frieder Seible. November 1999.

PEER 1999/10 *U.S.-Japan Workshop on Performance-Based Earthquake Engineering Methodology for Reinforced Concrete Building Structures.* December 1999.

PEER 1999/09 *Performance Improvement of Long Period Building Structures Subjected to Severe Pulse-Type Ground Motions.* James C. Anderson, Vitelmo V. Bertero, and Raul Bertero. October 1999.

PEER 1999/08 *Envelopes for Seismic Response Vectors.* Charles Menun and Armen Der Kiureghian. July 1999.

PEER 1999/07 *Documentation of Strengths and Weaknesses of Current Computer Analysis Methods for Seismic Performance of Reinforced Concrete Members.* William F. Cofer. November 1999.

PEER 1999/06 *Rocking Response and Overturning of Anchored Equipment under Seismic Excitations.* Nicos Makris and Jian Zhang. November 1999.

PEER 1999/05 *Seismic Evaluation of 550 kV Porcelain Transformer Bushings.* Amir S. Gilani, Andrew S. Whittaker, Gregory L. Fenves, and Eric Fujisaki. October 1999.

PEER 1999/04 *Adoption and Enforcement of Earthquake Risk-Reduction Measures.* Peter J. May, Raymond J. Burby, T. Jens Feeley, and Robert Wood.

PEER 1999/03 *Task 3 Characterization of Site Response General Site Categories*. Adrian Rodriguez-Marek, Jonathan D. Bray, and Norman Abrahamson. February 1999.

PEER 1999/02 *Capacity-Demand-Diagram Methods for Estimating Seismic Deformation of Inelastic Structures: SDF Systems*. Anil K. Chopra and Rakesh Goel. April 1999.

PEER 1999/01 *Interaction in Interconnected Electrical Substation Equipment Subjected to Earthquake Ground Motions.* Armen Der Kiureghian, Jerome L. Sackman, and Kee-Jeung Hong. February 1999.

PEER 1998/08 *Behavior and Failure Analysis of a Multiple-Frame Highway Bridge in the 1994 Northridge Earthquake.* Gregory L. Fenves and Michael Ellery. December 1998.

PEER 1998/07 *Empirical Evaluation of Inertial Soil-Structure Interaction Effects.* Jonathan P. Stewart, Raymond B. Seed, and Gregory L. Fenves. November 1998.

PEER 1998/06 *Effect of Damping Mechanisms on the Response of Seismic Isolated Structures.* Nicos Makris and Shih-Po Chang. November 1998.

PEER 1998/05 *Rocking Response and Overturning of Equipment under Horizontal Pulse-Type Motions.* Nicos Makris and Yiannis Roussos. October 1998.

PEER 1998/04 *Pacific Earthquake Engineering Research Invitational Workshop Proceedings, May 14–15, 1998: Defining the Links between Planning, Policy Analysis, Economics and Earthquake Engineering.* Mary Comerio and Peter Gordon. September 1998.

PEER 1998/03 *Repair/Upgrade Procedures for Welded Beam to Column Connections.* James C. Anderson and Xiaojing Duan. May 1998.

PEER 1998/02 *Seismic Evaluation of 196 kV Porcelain Transformer Bushings.* Amir S. Gilani, Juan W. Chavez, Gregory L. Fenves, and Andrew S. Whittaker. May 1998.

PEER 1998/01 *Seismic Performance of Well-Confined Concrete Bridge Columns.* Dawn E. Lehman and Jack P. Moehle. December 2000.

ONLINE REPORTS

The following PEER reports are available by Internet only at http://peer.berkeley.edu/publications/peer_reports.html

PEER 2007/101 *Generalized Hybrid Simulation Framework for Structural Systems Subjected to Seismic Loading.* Tarek Elkhoraibi and Khalid M. Mosalam. July 2007.

PEER 2007/100 *Seismic Evaluation of Reinforced Concrete Buildings Including Effects of Masonry Infill Walls.* Alidad Hashemi and Khalid M. Mosalam. July 2007.